Trinity College Dublin
Coláiste na Tríonóide, Baile Átha Cliath
The University of Dublin

Design of Novel Magnetic Materials with Machine-Learning and High-Throughput Techniques

by

Michail Minotakis

A thesis submitted for the degree of

Doctor of Philosophy

School of Physics
Trinity College Dublin, the University of Dublin

February 14, 2024

Declaration

I declare that this thesis has not been submitted as an exercise for a degree at this or any other university and it is entirely my own work. I agree to deposit this thesis in the University's open access institutional repository or allow the Library to do so on my behalf, subject to Irish Copyright Legislation and Trinity College Library conditions of use and acknowledgement. I consent to the examiner retaining a copy of the thesis beyond the examining period, should they so wish (EU GDPR May 2018).

Signature: . . . . . .

Abstract

The importance of magnetic materials in modern applications is unquestionable. They are used in a wide range of applications, going from data storage devices to green energy production. This class of materials is well known since antiquity; yet the number of materials known to be magnetic has been limited to ~ 5000. A magnetic material is considered to be useful for applications if the Curie temperature T_C (the temperature at which a ferromagnetic material ceases to be magnetic) is well above room temperature. If we enforce this constraint on the known materials then the number of useful ones reduces dramatically, this implies the need for the design of novel magnetic materials.

Traditionally, the search for suitable candidates is done experimentally. This task is not only time-consuming, reducing the throughput so much that it is impossible to explore the vast chemical spaces available, but is also expensive both in workforce and in resources.

Advances in computational materials science and artificial intelligence make the theoretical discovery of magnetic materials increasingly accessible. Tools like machine learning and high-throughput ab-initio calculations give us the ability to scan large chemical spaces in search of novel compounds that exhibit desired properties in a fraction of time. Moreover, the stability of these compounds can be assessed with high confidence. Suitable candidates can be studied with state-of-the-art ab initio simulations, and their properties can be predicted before they are synthesized experimentally.

This thesis is divided into 3 parts. In the first two chapters, we introduce our workflow for material exploration. This uses a combination of machine-learning and ab-initio methods for the search of thermodynamically stable ternary alloy materials. To

achieve the needed throughput, we diminish the use of expensive ab-initio simulations by utilising Machine Learning Interatomic Potentials, MLIAPs. Using them as energy predictors, the exploration of large materials spaces becomes reachable. Then a methodology is explored for the creation of possible ternary candidates. Providing us with viable material candidates as a starting point is crucial for materials exploration workflows.

In the third chapter of this thesis, we will solely use high-throughput ab-initio methods to explore the Heusler family of materials. Heusler ternaries are well known for their magnetic properties, and interestingly, several high-performance magnets are discovered among them. Thoroughly, we use density functional theory, DFT, to search for antiferromagnetic and tetragonal distorted materials. The former are known to be used for spintronics applications, and the latter exhibit large magnetic crystalline anisotropy.

In the first part of this thesis, the reader will be introduced to the scope underpinning this work and the computational tools used. Then the main part of the work is divided into three chapters where the results of each project will be presented and discussed. The last part is focused on discussing the main findings of this work and presenting the future outlook.

Keywords: Machine Learning, High-Throughput Calculations, Density Functional Theory, Ternary Phase Diagrams, Crystal Structure Generator, Heusler Alloys.

To my family.

Thank you.

The First Step

The young poet Evmenis
complained one day to Theocritus:
"I've been writing for two years now
and I've composed only one idyll.
It's my single completed work.
I see, sadly, that the ladder
of Poetry is tall, extremely tall;
and from this first step I'm standing on now
I'll never climb any higher."
Theocritus retorted: "Words like that
are improper, blasphemous.
Just to be on the first step
should make you happy and proud.
To have reached this point is no small achievement:
what you've done already is a wonderful thing.
Even this first step
is a long way above the ordinary world.
To stand on this step
you must be in your own right
a member of the city of ideas.
And it's a hard, unusual thing
to be enrolled as a citizen of that city.
Its councils are full of Legislators
no charlatan can fool.
To have reached this point is no small achievement:
what you've done already is a wonderful thing."

C.P. Cavafy

Acknowledgements

First and foremost, I would like to express my gratitude to Professor Stefano Sanvito, my supervisor, whose unwavering support has been instrumental throughout my PhD journey. Stefano's generosity with his time and his ability to foster a positive working environment have significantly impacted my research. His profound knowledge spanning various fields has been a constant source of inspiration over the past four years.

I extend my heartfelt thanks to Hugo Rossignol, whose invaluable contributions have made three of the four chapters of this thesis possible. His consistent cooperation and adept problem-solving skills were instrumental in overcoming the challenges we encountered during the past four years.

My journey would have been considerably less enjoyable without the friendship and support of Matteo, Luke, Laura, Michelangelo, and Bruno (in random order). I truly appreciate their willingness to share countless wonderful moments with me, which have truly enriched my overall experience.

I have had the pleasure of working alongside many exceptional colleagues at Trinity. In particular, I want to acknowledge Dr. Rajarshi Tiwari and Dr. Urvesh Patil for their consistent technical support. My gratitude also extends to the entire Computational Spintronics Group for their support over the past four years.

I would like to express my appreciation to Stefania Negro for her valuable administrative assistance, which played a significant role in my seamless integration into this group. Additionally, I acknowledge TCHPC (Research IT, Trinity College Dublin) and the Irish Center for High-End Computing (ICHEC) for providing computational facilities and assistance.

Outside of my direct scientific environment, I have had the pleasure of meeting

numerous individuals from various walks of life who have assisted me in their unique ways. While I wish I could thank each one individually, space constraints limit me here.

Last but not least, I would like to express my gratitude to my family and friends for their support during my Ph.D. journey. Finally, and most importantly, I want to thank my parents, without whom none of this would have been possible.

List of Publications

1. *M. Minotakis*, H. Rossignol, M. Cobelli, S. Sanvito, *Machine learning surrogate model for acellerating the search of stable ternary alloys.* Phys. Rev. Materials **7**, 093802 (2023)

2. H. Rossignol, *M. Minotakis*, M. Cobelli, S. Sanvito, *Machine learning assisted construction of ternary phase diagrams.* Journal of Chemical Information and Modeling (2024)

3. *M. Minotakis*, S. Sanvito, *High-throughput study of tetragonal and antiferromagnetic Heusler alloys.* (in preparation)

Contents

The First Step . . . iii

1 Introduction **1**

1.1 Materials Science has shaped the World . . . 1

1.2 Magnetic Materials . . . 2

1.3 High-throughput and Machine-Learning Techniques . . . 4

1.4 Inverse Design . . . 5

1.5 Our contribution . . . 7

2 Theoretical Background **9**

2.1 Density Functional Theory . . . 10

2.1.1 Hohenberg and Kohn Theorems . . . 10

2.1.2 Kohn-Sham DFT . . . 13

2.1.3 Kohn-Sham Variational Equations . . . 15

2.1.4 Solution to the Kohn-Sham Equations . . . 16

2.1.5 Exchange and Correlation Functionals . . . 17

2.2 Machine Learning Interatomic Potentials . . . 19

2.2.1 Machine-Learning and Types of Learning . . . 19

2.2.2 Ridge Regression and Model Training . . . 20

2.2.3 Matrix Notation and Gradient Descent . . . 22

2.2.4 Interatomic Potentials . . . 24

2.2.5 Machine Learning Interatomic Potentials, the Case of SNAP . . . 25

2.2.6 Applications . . . 31

2.3 Prototype Creation Strategies . . . 32

2.3.1 AFLOW Dictionary Method 34
2.3.2 Enumlib 36
2.4 Thermodynamic Stability 40
2.5 AFLOW and AFLOWLIB 44
2.5.1 RESTful API and AFLOW-CHULL 45
2.5.2 AFLOW standards 46
2.5.3 Thesis overview 47

3 MLIAP for ternary phase diagrams 49
3.1 Introduction 49
3.2 Results 53
3.2.1 Learning Curve 53
3.2.2 Hyperparameter Optimisation 54
3.2.3 Binary Phases Trained Models 56
3.2.4 Testing over the ternary phases 58
3.2.5 Testing on Novel Ternaries 60
3.2.6 Model Benchmark: Cd-Hf-Rh and Ti-Mo-Pt 66
3.3 Discussion and Conclusion 68

4 SNAP-based Workflow 71
4.1 Introduction 71
4.2 Ternary Phase Diagram Workflow 73
4.2.1 The Prototype Generation stage 74
4.2.2 Ensemble of Models 78
4.2.3 Screening of the Prototypes 82
4.3 Results 87
4.3.1 Cu-Ag-Au ternary convex hull 88
4.3.2 Mo-Ta-W ternary convex hull 94
4.4 Conclusion 104

5 M3gnet-Based Workflow **107**

5.1 Introduction . . . 107

5.2 Graph Neural Networks: MEGNet and M3gnet . . . 109

5.3 M3gnet-based workflow : M3GW . . . 116

5.4 Results . . . 120

5.4.1 Mo-Ta-W ternary system . . . 121

5.4.2 Al-Fe-Ni ternary system . . . 127

5.4.3 Bi-Fe-X ternary system . . . 137

5.5 Conclusions . . . 140

6 HT study of Tet. and AF Heusler Alloys **143**

6.1 Introduction . . . 143

6.2 Computational details . . . 147

6.2.1 Tetragonal Distortion and Antiferromagnetic configurations . . . 147

6.2.2 DFT details . . . 149

6.2.3 Convex hull Distance Correction . . . 150

6.2.4 Workflow . . . 151

6.3 Results . . . 153

6.3.1 Correcting the Convex Hull Distance . . . 153

6.3.2 Band Structure Calculations . . . 166

6.4 Conclusions and Discussion . . . 170

7 Conclusions and Future Work **171**

7.1 Conclusions . . . 171

7.2 Future Work . . . 177

Appendices **179**

A PCA plot for Cu and Au **181**

B Candidates Selection for the AgAu **184**

C Convex hull analysis Mo-Ta-W **185**

D Heusler Alloys **187**

List of Figures

1.1 Common Magnetic Orders - Ferromagnetic and Antiferromagnetic . . . 3

1.2 The Inverse Design Workflow 6

2.1 Self-consistent field (SCF) loop for the solution of the KS equations . . 17

2.2 Schematic representation of the main steps of a machine-learning workflow. 20

2.3 Illustrations of Underfitting, Overfitting and Proper Fitting 22

2.4 Comparison of Supercell Structures for Binary Alloys $A_{0.5}B_{0.5}$, $Cu_{0.5}Au_{0.5}$, and $Fe_{0.5}Pt_{0.5}$ 35

2.5 Different views of the AuCu phase diagram 42

2.6 Phase Diagrams and Convex Hull Analysis of AgCu and Ternary Systems 43

3.1 HfRh Binary Phase Diagram Convex Hull: Stable Phases and Intermetallics 50

3.2 Learning Curve for Models Trained on Ag-Au, Cu-Au, and Cu-Ag Binary Phase Diagram Data 54

3.3 SNAP Predicted vs. DFT Calculated Energies: Ag-Au, Cu-Ag, Cu-Au Binary Systems 57

3.4 SNAP vs. DFT Energies: Cu-Ag-Au Binary and Ternary Compounds . 59

3.5 SNAP vs. DFT Energies: Cu-Ag-Au Binary and Ternary Compounds . 61

3.6 Energy Comparison: SNAP Relaxed vs. Unrelaxed Structures 63

3.7 Principal Components Analysis Plot for Ag Local Chemical Environments 64

3.8 SNAP vs. DFT Energies: Ti-Mo-Pt and Cd-Hf-Rh Binary and Ternary Compounds 67

4.1 Convex Hull Prediction Workflow: From Initialization to Phase Diagram Update 74
4.2 Energy Window Selection for Cu-Au and Cu-Ag Parent Structures . . . 76
4.3 Sample of parent structures 77
4.4 Prototype A and B: Varied Decorations for Compound Creation 81
4.5 Energy distribution for $Cu_1Ag_1Au_1$ structures. 83
4.6 Volume Comparison for $Cu_2Ag_1Au_1$ Ternary Prototypes: Initial vs. Equilibrium 84
4.7 Relaxation Workflow for Single Prototype: SNAP Model Ensemble Approach 85
4.8 Cu-Ag-Au Ternary System Predictions: Workflow vs. AFLOWlib Method 90
4.9 Crystal Structure of $Cu_1Ag_1Au_3$ Unit Cell Views 91
4.10 Convex Hull of Cu-Ag-Au Ternary System: AFLOW-CHULL Analysis 92
4.11 Convex Hull of Cu-Ag-Au Ternary System: Workflow Predictions . . . 93
4.12 Difference Between AFLOW and Workflow Predicted Convex Hulls . . 93
4.13 Convex Hull of Mo-Ta-W Ternary System: AFLOW-CHULL Analysis . 95
4.14 Convex Hull of Mo-Ta-W Ternary System: DFT-Calculated Energies . 96
4.15 Mo-Ta-W Ternary System Predictions: 1-1-1 and 1-1-2 Compositions . 97
4.16 Crystal Structure of $Mo_1Ta_1W_1$: Workflow vs. AFLOW 98
4.17 Mo-Ta-W Ternary System Predictions: 1-2-3 and 3-1-1 Compositions . 101
4.18 Ternary Phase Diagram of MoTaW System: Workflow Prediction . . . 102
4.19 Difference Between AFLOW and Workflow-Predicted Convex Hulls: Mo-Ta-W Ternary System 103
4.20 Convex Hull for Mo-Ta-W Ternary System: Stable Phases 103

5.1 Convex Hull Prediction Workflow with M3gnet 109
5.2 Water Molecule: Molecular and Graph Representation 110
5.3 MEGNet Architecture 113
5.4 Local Chemical Environment: Bonds and Angle 114
5.5 M3GNet Architecture 115

5.6 M3GW Workflow Overview: Binary Diagrams to DFT Calculations . . 118
5.7 Task Farming Workflow: Parallel Processing of Ternary Candidates . . 119
5.8 Speedup vs. Number of Processors 120
5.9 Comparison of SNAP-based Workflow and M3GW Workflow 122
5.10 Difference Between AFLOW and M3GW Predicted Convex Hulls: Ternary Phase Diagram 123
5.11 Difference Between Workflow and M3GW Predicted Convex Hulls . . . 124
5.12 Complete Mo-Ta-W Ternary Phase Diagram 125
5.13 Convex Hull Values and Enthalpy of Formation Comparison 126
5.14 Two-Dimensional Cubic Lattice: Different Magnetic Configurations . . 128
5.15 Parity Plot for Fe-Co-Ni Ternary System: Model Training and Testing . 128
5.16 Calculated Convex Hull for Al-Fe-Ni Phase Diagram: AFLOW Predictions 130
5.17 Crystal Structures of $Al_9Fe_1Ni_1$ (τ_2) and $Al_10Fe_3Ni_1$ (τ_1) 131
5.18 Al-Fe-Ni Ternary Convex Hull with Experimental Data: Phases τ_1 and τ_2 132
5.19 Al-Fe-Ni Ternary Convex Hull: Stable Intermetallics from M3gnet-based Workflow 133
5.20 Difference Between AFLOW and M3GW Predicted Ternary Convex Hulls 134
5.21 Complete Ternary Phase Diagram for Al-Fe-Ni System 135
5.22 Comparison with Complete when Experiments are added 135
5.23 Convex hull Distance 136
5.24 Distance (δ) from AFLOW-Calculated Convex Hull for Bi-Fe-Zr 138
5.25 Distance (δ) from AFLOW-Calculated Convex Hull for Bi-Fe-Ta 139

6.1 Conventional and Primitive Cells for Heusler Compounds 144
6.2 Periodic Table of the Elements: Elements Used in Heusler Alloys 145
6.3 Histogram of δ_{AFLOW} Distances from Convex Hull for Magnetic Heusler Alloys 146
6.4 Tetragonal Distorted Structure of $Au2Ag1Mn_1$ 148
6.5 AF1 and AF2 Configurations in FCC Cell: Magnetic Moments 149

6.6 Workflow 1 152

6.7 Workflow 2 153

6.8 Distance from Convex Hull (δ_{AFLOW}) for Heusler Alloys: Experimental Synthesis Marked 154

6.9 Corrected distance from the convex hull histogram 163

6.10 Electronic Band Structure for $Pt2Mn1Zn_1$ Full Heusler 167

6.11 Electronic Band Structure for $Fe2Ge1Mn_1$ Full Heusler 168

6.12 Electronic Band Structure for $Rh2Cr1Zn_1$ Full Heusler 169

6.13 Electronic Band Structure and Density of States for $Co2Mn1Si_1$ Full Heusler 169

A.1 PCA Plot: Au and Cu Local Environments 183

B.1 The Ag-Au Binary Convex Hull Analysis 184

C.1 Binary Systems Mo-Ta-W Convex Hull Analysis 186

List of Tables

2.1 Cayley table of Z_4. 38

2.2 Hash table of the complete decoration of a lattice with four sites. Incomplete decorations are enclosed withing black rectangles. 38

2.3 Hash table of a lattice decoration with four sites. Incomplete decorations are depicted in red, and the starting decoration is shown in blue. Redundant decorations are enclosed within black rectangles. 39

3.1 Optimal Hyperparameters for SNAP Models in Binary Systems: Weight Parameters 56

3.2 Average Errors for 10 SNAP Models in Three Binary Systems 57

3.3 Hyperparameters, a summary for Cu-Ag-Au ternary 59

4.1 Parent structures pool, the case of Cu-Ag-Au system. 75

4.2 SNAP Model Predictions: Prototype A vs. Prototype B with Varied Elemental Weights 80

4.3 Model Training and Cross-Validation Errors: 5-Model Ensemble with Varied Atomic Weights 82

4.4 Cu-Ag-Au Ternary System Predictions: 2-2-1 and 3-1-1 Compositions . 91

4.5 Structural Parameters for $Mo_1Ta_1W_1$ Compound: AFLOW vs. Workflow Predictions 99

4.6 Mo-Ta-W Ternary System Predictions: 1-2-2 and 1-1-4 Compositions . 100

5.1 Stoichiometries, Max Atoms per Supercell, and Total Structures Created and Screened 132

5.2 Distance from Convex Hull (δ) for Metastable Al-Fe-Ni Compounds . . 137

5.3 Distance from Convex Hull for Bi-Fe-Zr Ternary System 140

5.4 Distance from Convex Hull for Bi-Fe-Ta Ternary System 140

6.1 Heusler Compounds experimentally synthesized and predicted Thermodynamically stable 159

6.2 Energy difference Ferromagnetic-Antiferromagnetic 160

6.3 Unstable Heusler Compounds Experimentally Synthesized 162

6.4 Heusler Compounds with Highest Distance Below the Convex Hull . . . 164

6.5 Tetragonal Distorted Predicted Heusler Compounds: Magnetic Moment, ΔE_{C-T}, and δ_{corr} 165

D.1 Stable synthesized Heusler Compounds cubic vs tetragonally distorted energies 189

D.2 Stable non-synthesized Heusler Compounds Catalog 196

D.3 Stable non-synthesized Heusler Compounds Catalog 203

Chapter 1

Introduction

1.1 Materials Science has shaped the World

No one can deny that materials have played an important role in the existence and advancement of humankind [1]. History is intertwined with the pursuit of materials that exhibit the best mix of required properties. A visit to a national history museum will be capable of persuading any individual. A variety of artifacts from different historical eras are presented.

In the first museum section usually, stone, wood, shells and clay are the materials predominantly used. These materials were primarily employed in crafting tools, weapons, and shelters. They held such significance in the daily lives of people that they were buried alongside them to accompany them in the afterlife. Historians even named the corresponding historical eras based on the predominant materials of the time, designating this historic area as the Stone age.

Following that section, one can observe the introduction of a more sophisticated material—an alloy of copper (Cu) with tin (Sn), named bronze. Bronze dominated ancient civilizations for nearly 2100 years. This was due to its remarkable mechanical properties and relatively low melting temperature, which makes it easier to manipulate than its predecessor, stone.

A variety of materials continued to shape the world in the following centuries, and they all shared a common characteristic: they were more advanced than the materials

previously used. These innovations often sparked revolutions in the industries and economies of nations fortunate enough to harness their potential.

If the reader has not yet been persuaded of the importance of materials in everyday life, this last example will surely convince them. Consider that you are reading these lines from the screen of their computer. One has to reflect on how many different classes of materials are working in concert to enable you to read these sentences.

The pursuit of more advanced materials lies at the heart of human advancement. Traditionally, this endeavor relied heavily on experimental methods. However, this approach is not only time-consuming, significantly reducing throughput and making it impossible to explore vast chemical spaces, but it is also expensive in terms of both workforce and resources. Fortunately, advances in computational materials science and artificial intelligence have made the theoretical discovery of materials with enhanced properties faster and increasingly accessible.

1.2 Magnetic Materials

The workflows developed in this thesis will ultimately be employed to navigate the expansive chemical space—a space formed through the combinatorial arrangements of various elements and stoichiometries—in the quest for materials exhibiting magnetic properties. It would be beneficial to introduce briefly this class of materials.

Magnets [2] are a class of materials in which the atomic spins allign between themselves, creating a macroscopic order. The interactions between two neighbouring atoms with atomic spin, $\mathbf{S}_i$, are of electrostatic nature. Heisenberg formulated the exchange Hamiltonian as follows,

$$H = -\sum_{i,j} J_{ij} \mathbf{S}_i \mathbf{S}_j, \tag{1.1}$$

where the coupling constant between neighboring atoms, i and j, denoted as J_{ij}, governs the strength of the interaction. The values of the coupling constant, J_{ij}, change with the type of magnetic ordering. For instance, negative values imply that spins

have an energy minimum when antiparallelly aligned, resulting in antiferromagnetic materials. In contrast, positive values lead to the formation of ferromagnetic order, where the spins are aligned parallel to each other, as presented in Figure 1.1.

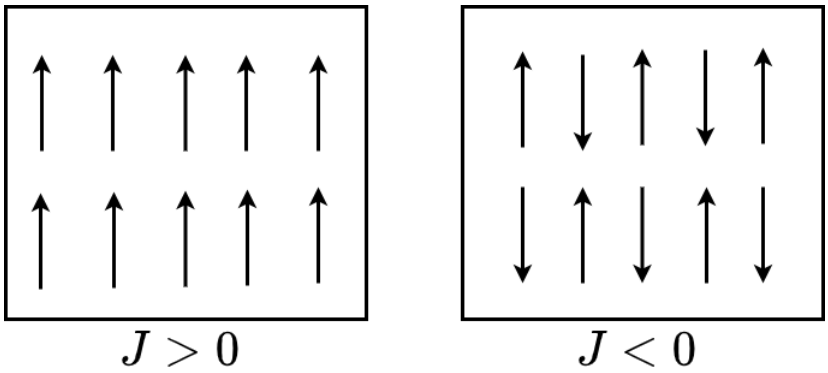

Figure 1.1: The two most common types of magnetic ordering, ferromagnetic (left) and antiferromagnetic (right).

Both these magnetic orderings cease to exist above a critical temperature, giving rise to a different magnetic structure, where the spins have no specific alignment (paramagnetism). This critical temperature for ferromagnetic materials is known as the Curie temperature, denoted as T_{C}, while for antiferromagnetic materials, it is referred to as the Néel temperature, denoted as T_{N}.

In the present work, we mainly focus on ferromagnetic materials. For a ferromagnetic material to be useful in a given technology, its critical temperature should exceed significantly the room temperature. Unfortunately, not many materials exhibit such property, making the vast majority of magnets known so far to be paramagnetic at room temperature. Interestingly, there is no material with higher Curie temperature than Cobalt (Co), $T_{\mathrm{C}} = 1400K$. However, it is worth noting, as indicated in [3], that magnets can be crafted by including practically any element from the periodic table excluding the noble gases and the highly radioactive ones. This fact provides us with immense flexibility when it comes to choosing compatible materials and specific stoichiometries, thereby greatly expanding the pool of potential candidates.

The vastness of this chemical space defies exploration through experiments. In order to tackle this challenge, an inverse design approach that leverages machine-learning models for property prediction and high-throughput calculations to narrow down our

search to specific areas within the vast material space is the strategy of choice.

1.3 High-throughput and Machine-Learning Techniques

High-throughput computational material design is a rapidly evolving field within materials science [4]. It combines advanced ab-initio methods for assessing thermodynamic stability and calculating electronic properties, with data science. This powerful synergy provides new capabilities for storing, managing and analyzing vast databases to extract intriguing relationships and fundamental patterns among families of materials, offering fresh insights into the design of exciting novel materials.

The steps that high-throughput frameworks usually follow imitate the experimental procedure, where a material is virtually grown and studied. Subsequently, the data are stored in databases and an analysis is performed. These techniques have been used in a variety of problems in different areas of materials science.

There are various approaches to use high-throughput techniques in materials research. One strategy involves starting from experimental insights about a class of materials and then expanding the search combinatorially by introducing a variety of different elements into a crystal structure of interest. For example, in Ref. [5] researchers explored the chemical space of ABO_3 structures in their search for high-performance piezoelectrics. In another study [6], the Heusler alloy family was investigated for high-performance magnets by decorating the crystal structure with all the possible combinations of a specific pool of elements.

An alternative approach is to use theoretical criteria to search a specific materials database for materials of interest. An example of this approach is found in Ref. [7], where researchers used criteria based on Bardeen–Cooper–Schrieffer (BCS) superconductivity [8] to screen the JarvisDFT [9] database for superconducting materials.

Most of these studies rely on ab-initio methods, such as density functional theory (DFT), which are known to be computationally intensive. This complexity makes exploring vast chemical spaces a challenging task. However, recent advances in machine-learning and applied statistics have greatly expanded the toolkit available to computational

materials scientists, significantly increasing the screening throughput.

Machine-learning has found a wide range of applications in the field of computational materials science. From serving as surrogates for DFT to predicting material properties, both approaches significantly enhance the throughput of the materials discovery workflow. Various Machine-Learning Inter-Atomic Potentials (MLIAPs) [10–14] are currently in use, accurately mapping the potential energy surface of compounds and enabling the study of systems on larger time and size scales without compromising accuracy. Models trained on properties extracted from ab-initio calculations are capable of predicting crucial parameters, including Curie temperature (T_C) [3], the critical superconducting temperature [15], and even crystal structure information [16].

Machine-learning methods, when combined with high-throughput calculations in inverse design workflows, have the capability to pinpoint the most promising regions within the chemical space for a specific application. This synergy enables the discovery of the next generation of high-performance materials.

1.4 Inverse Design

Utilizing high-throughput methods to explore a significant portion of the chemical space and subsequently employing data analytics tools to assess the properties and stability of compounds remains computationally demanding. This challenge arises from the use of ab-initio methods, which are known for their computational cost. However, in recent years, a novel paradigm has emerged, where the property of interest defines the chemical space to be explored, followed by methods of increasing accuracy to screen and identify the most promising candidates. This approach is known as inverse design [17].

The main components of most inverse-design workflows typically are a property predictor, a prototype structure generator, and a series of high-throughput calculations. In the final stages, high-accuracy ab-initio calculations are employed to examine the properties of the most promising candidates, alongside experimental synthesis, if appropriate. Starting from a vast number of created prototypes, different tools are used to characterize the potential candidates. In the first stage, machine-learning models able to predict

the property of interest, for example, the Curie temperature in our case, are used to screen the structures. For the promising candidates, high-throughput calculations are performed, and their thermodynamic stability is assessed. Moving onto the next step, high-fidelity DFT is used to study the materials of interest more accurately and determine whether they are of interest for potential experimental synthesis. As we move towards the last layers, the number of prototypes are reduced significantly and only the most promising and the most exciting survive up to the last layers of the screening. A schematic representation is shown in Figure 1.2.

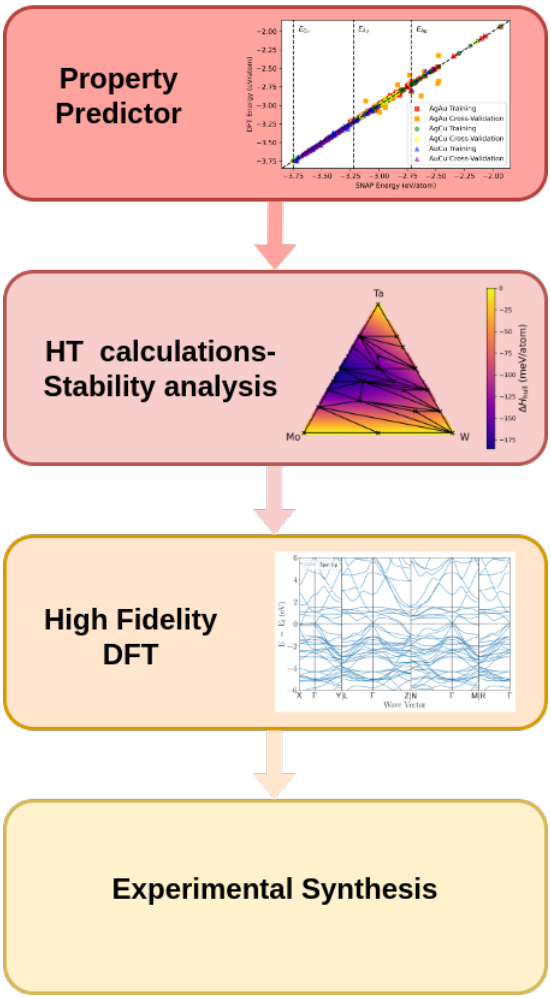

Figure 1.2: A schematic representation of an inverse design workflow is presented. Its main components are highlighted. Initially, a property predictor based on machine-learning tools is employed to explore the materials space. Subsequently, high-throughput (HT) calculations are used to evaluate the stability of the structures. This is followed by high-fidelity DFT calculations, which provide further insights into the properties of the materials, and ultimately, the experimental synthesis

As can be observed in Figure 1.2 a variety of different techniques need to work in concert to tackle such a complicated task. In the final section of this Introduction, we

will provide a brief statement outlining our contribution to this complex problem.

1.5 Our contribution

Here, we present the outline of the thesis and how the following chapters are connected to the inverse-design workflow that was discussed previously.

In Chapter 3, we explore the initial steps of implementing an inverse design workflow. This involves benchmarking the boundaries and gaining insights into training machine-learning force fields to serve as energy predictors using readily available data. The models discussed are valuable for such kinds of workflows as they function as rough energy screening tools during the initial stages of a prototype-selection workflow.

In Chapters 4 and 5, we build upon the knowledge obtained in the first step. We establish a prototype-design workflow for predicting ternary phase diagrams, comparing it to state-of-the-art workflows, and employing it to discover novel intermetallics within various ternary transition-metal systems. Subsequently, we extend this workflow to systems containing magnetic elements, where we assess its strengths and weaknesses.

In Chapter 6 a high-throughput study is presented aimed at uncovering interesting materials belonging to the Heusler alloy class. We build different workflows in order to assess possible lattice distortions from the ideal cubic cell as well as different magnetic ordering.

Overall, the work presented illustrates in a natural way the progression of ideas and research contributions within the context of materials science and inverse design methodologies.

Chapter 2

Theoretical Background

This chapter serves as an introduction to the computational tools utilized throughout the thesis. Multiple methods have been employed collectively to produce the results presented in the following chapters. The goal of this thesis is ultimately to present a data-driven workflow for predicting ternary phase diagrams. In order to achieve this, various methods, including ab-initio calculations and different types of machine-learning and data analytics tools, as well as computational thermodynamics concepts have worked in concert. Therefore, it is crucial to introduce the reader to the fundamentals of these methods.

In the following sections, we present the fundamentals of Density Functional Theory (DFT) [18]. Additionally, we provide an overview of the most widely used functionals. Special emphasis will be placed on the approximations implemented in the Vienna ab-initio Software Package, commercially known as VASP, as this software was extensively utilized for the majority of the ab-initio calculations reported in this work.

Following that, we will introduce the general concepts of machine-learning (ML) and machine-learning force fields (MLFF). These tools were employed as surrogate models to replace computationally expensive DFT in the creation of the ternary phase-diagram workflow.

An introduction to the construction of phase diagrams and the fundamental concepts of materials thermodynamics will also be provided. Additionally, we will introduce other tools employed in this work, such as the Automatic FLOW for Materials Discovery

(AFLOW). AFLOW is a data informatics package that integrates data analytics, data handling, and data sharing tools into a comprehensive platform.

2.1 Density Functional Theory

The birth certificate of DFT is considered the famous paper by Hohenberg and Kohn (HK) in 1964 [19]. In this paper, the foundational ideas that underpin DFT were laid out. The special role of the density of particles in the ground-state of a quantum many-body system was discussed. The idea is that *all ground-state* properties of a system can be considered as unique *functional* of the ground-state charge density.

Shortly after the paper by Hohenberg and Kohn in 1964, a seminal work from Kohn and Sham in 1965 [20] laid the foundation upon which modern methods have been built. These methods have enabled us to calculate properties of molecules and solids that would otherwise have been impossible to predict.

2.1.1 Hohenberg and Kohn Theorems

For any system of interacting particles in an external potential, $V_{\text{ext}}(\mathbf{r})$, supposing that the nuclei are fixed, one can write the total energy operator of the system, known as Hamiltonian, as the sum of the operators for the kinetic, $\hat{T}$, and the potential energy, $\hat{V}$, of the system as shown in Equation (2.1) (here we neglect the repulsive nucleus-nucleus contribution).

$$\begin{aligned} \hat{H} &= \hat{T} + \hat{V} = \\ &= -\frac{\hbar}{2\mu_e}\sum_i \nabla_i^2 + \sum_i V_{ext}(\mathbf{r}_i) + \frac{1}{4\pi\epsilon_0}\sum_{i\neq j}\frac{e^2}{|\mathbf{r}_i - \mathbf{r}_j|}. \end{aligned} \tag{2.1}$$

Knowing the Hamiltonian operator, defined by the external potential, one can solve the Schrödinger equation to determine all the states of the system, $\Psi_i(\{\mathbf{r}\})$ these indeed the ground-state wave-fucntion, $\Psi_0(\{\mathbf{r}\})$, and ultimately the ground-state density, $n_0(\mathbf{r})$.

$$n_0(\mathbf{r}) = \frac{\langle \Psi_0 | \, \hat{n}(\mathbf{r}) \, | \Psi_0 \rangle}{\langle \Psi_0 | \Psi_0 \rangle}, \tag{2.2}$$

where the density operator is $n(\mathbf{r}) = \sum_{i=1,N} \delta(\mathbf{r} - \mathbf{r}_i)$. The intuition of Hohenberg and Kohn allows us to determine the external potential directly from the ground-state density, $n_0(\mathbf{r})$. DFT is based on two theorems introduced by Hohenberg and Kohn in the first sections of the paper [19].

In the first theorem, it is proven that for any interacting many-body system subjected to an external potential $V_{\text{ext}}(\mathbf{r})$, the potential can be uniquely determined by the ground-state density $n_0(\mathbf{r})$ up to a constant. This leads to a fully determined Hamiltonian and enables the determination of all states within the studied system. The theorem implies that all properties of the system can be determined solely from the ground-state density.

In order to prove the theorem, we assume two different external potentials, $V_{\text{ext}}^{(1)}(\mathbf{r})$ and $V_{\text{ext}}^{(2)}(\mathbf{r})$ that differ only by a constant and lead to the same ground-state $n(\mathbf{r})$. These two external potential are thus associated to two different Hamiltonians, $\hat{H}^{(1)}$ and $\hat{H}^{(2)}$, which have different ground-state wavefunctions $\hat{\Psi}^{(1)}$ and $\hat{\Psi}^{(2)}$. However, from the hypothesis we assumed that these two wavefunctions correspond to the same ground-state energy $n_0(\mathbf{r})$.

Furthermore, we know that the $\Psi^{(1)}$ is not the ground-state of the $\hat{H}^{(2)}$ and vice-verse, $\Psi^{(2)}$ is not the ground-state of the $\hat{H}^{(1)}$. Then we can write for that the energy of the given system is:

$$E^{(1)} = \left\langle \Psi^{(1)} \right| \hat{H^{(1)}} \left| \Psi^{(1)} \right\rangle < \left\langle \Psi^{(2)} \right| \hat{H^{(1)}} \left| \Psi^{(2)} \right\rangle \tag{2.3}$$

The inequality in Eq. (2.3) means that the ground-state is not degenerate. Then one can write,

$$\begin{aligned} \left\langle \Psi^{(2)} \right| \hat{H^{(1)}} \left| \Psi^{(2)} \right\rangle &= \left\langle \Psi^{(2)} \right| \hat{H^{(2)}} \left| \Psi^{(2)} \right\rangle - \left\langle \Psi^{(2)} \right| \hat{H^{(1)}} - \hat{H^{(2)}} \left| \Psi^{(2)} \right\rangle \\ &= E^{(2)} + \int d^3r \, \left[V_{ext}^{(1)}(\mathbf{r}) - V_{ext}^{(2)}(\mathbf{r}) \right] \, n_0(\mathbf{r}) \end{aligned} \tag{2.4}$$

which results in

$$E^{(2)} < E^{(1)} + \int d^3r \ \left[V_{ext}^{(2)}(\mathbf{r}) - V_{ext}^{(1)}(\mathbf{r})\right] \ n_0(\mathbf{r}) \tag{2.5}$$

Starting from the $E^{(2)}$ of the system and following the same approach, we end up in symmetrical equations, where only the superscripts are exchanged as follows,

$$E^{(1)} < E^{(2)} + \int d^3r \ \left[V_{ext}^{(1)}(\mathbf{r}) - V_{ext}^{(2)}(\mathbf{r})\right] \ n_0(\mathbf{r}) \tag{2.6}$$

If we sum Equations (2.6) and (2.5) together, we will obtain the inequality $E^{(1)} + E^{(2)} < E^{(1)} + E^{(2)}$. Clearly, such an inequality cannot exist. This establishes the desired property that there cannot be two different external potentials that differ by more than a constant and correspond to the same non-degenerate ground-state density.

Since the Hamiltonian of the system is now well defined, one can solve the Schrödinger equation to uniquely determine the wavefunction corresponding to the ground-state, which is the one with the lowest energy. In other words, this theorem asserts that, in the case of electrons in a material, the electron density uniquely determines both the positions and types of nuclei.

In the second theorem, Hohenberg and Kohn discuss that a universal energy functional, $E[n]$, can be defined, and that the ground-state energy of the system corresponds to the global minimum of this functional. This functional $E[n]$ is minimized only for the ground-state density $n_0(\mathbf{r})$, meaning that the functional is sufficient to determine the exact ground-state energy and density.

Since all the properties of a system can be expressed as a functional of the density $n(\mathbf{r})$, then the total energy functional is given as follows,

$$\begin{aligned} E_{\mathrm{HK}}[n] &= T[n] + E_{\mathrm{int}}[n] + \int d^3\mathbf{r} \ V_{ext}(\mathbf{r})n(\mathbf{r}) + E_{II} = \\ &= F_{\mathrm{HK}}[n] + \int d^3\mathbf{r} \ V_{ext}(\mathbf{r})n(\mathbf{r}) + E_{II}, \end{aligned} \tag{2.7}$$

where E_{II} is the Coulomb repulsion energy of the nuclei. The functional $F_{\mathrm{HK}}[n]$ contains all the contributions in the energy from the kinetic, potential and internal

energies. If we now consider a system with ground-state density of $n^{(1)}(\mathbf{r})$ that determines an external potential $V_{\text{ext}}^{(1)}(\mathbf{r})$ then from the Equation (2.7) we can find,

$$E^{(1)} = E_{\text{HK}}[n^1] = \left\langle \Psi^{(1)} \right| \hat{H}^{(1)} \left| \Psi^{(1)} \right\rangle, \tag{2.8}$$

and for a different density, $n^{(2)}(\mathbf{r})$, which determines a different wavefunction $\Psi^{(2)}$ we have that,

$$E^{(1)} = \left\langle \Psi^1 \right| \hat{H}^{(1)} \left| \Psi^{(1)} \right\rangle < \left\langle \Psi^{(2)} \right| \hat{H}^{(1)} \left| \Psi^{(2)} \right\rangle = E^{(2)}. \tag{2.9}$$

This means that if the functional $F_{\text{HK}}[n]$ in Equation (2.7) holds, one can minimize the total energy of the system by varying the corresponding density functional and ultimately determine the exact density and energy of the ground-state.

The HK functional is defined only for densities that can be represented by an external potential [21], which are called "V-representability". Subsequently, Levy-Lieb [22–25] gave an alternative definition of functional that extends the previous definition to densities that are derivable from a wavefunction of N electrons, Ψ_N, which are called "N-representabily".

So far, it has been demonstrated that a functional can be formulated for any density, provided certain conditions are met. By minimizing this functional, one can obtain the density and energy of the actual interacting many-body system. However, no specific method has been introduced to determine this functional beyond the various definitions established thus far.

2.1.2 Kohn-Sham DFT

Adopting the approach proposed by Kohn and Sham (KS) in 1965 [20] made DFT one of the most widely used methods for electronic structure calculations. Their approach consists in replacing the difficult problem of an interacting many-body system, for which we can write its Hamiltonian as follows,

$$\begin{aligned}\hat{H} = &-\frac{\hbar^2}{2\mu_e}\sum_i \nabla_i^2 - \sum_{i,I}\frac{Z_I e^2}{|\mathbf{r}_i - \mathbf{R}_\mathrm{I}|} + \frac{1}{4\pi\epsilon_0}\sum_{i\neq j}\frac{e^2}{|\mathbf{r}_i - \mathbf{r}_j|} \\ &- \sum_I \frac{\hbar^2}{2M_\mathrm{I}}\nabla_I^2 + \frac{1}{4\pi\epsilon_0}\sum_{I\neq J}\frac{Z_I Z_J e^2}{|\mathbf{R}_\mathrm{I} - \mathbf{R}_\mathrm{J}|}\end{aligned} \tag{2.10}$$

where electrons are denoted as lowercase subscripts and nuclei as uppercase subscripts. In Eq. (2.10) M_I is the mass of the nucleus, I, and Z_I is the charge of the nucleus, I. Then if we set the mass of the nuclei to infinity, the kinetic energy of the nuclei can be ignored. This is known as the Born-Oppenheimer approximation [26].

One can then substitute this problem with an alternative auxiliary system that is easier to solve. The underlying idea is to correlate the ground-state density of the original interacting system with that of a non-interacting one. This approximation leads to a set of independent-particle equations for the non-interacting system, which can be exactly solved using numerical methods. At the same time, all the complexities arising from the interacting many-body part of the problem are transferred to the exchange and correlation potential, which is a functional of the density. Subsequently, one can solve these equations to determine the ground-state density, although with an approximation applied to the exchange and correlation functional.

Two criteria need to be taken into account in order to construct the auxiliary single-particle system. In the first one, the ground-state density of the interacting system must be identical to the ground-state density of a system of non-interacting particles. Secondly, the Hamiltonian of the auxiliary system is created by the sum of the operators of the usual kinetic and an effective local potential $V_{\mathrm{ext}}^{\sigma}(\mathbf{r})$ that acts on an electron of spin σ at point $\mathbf{r}$. All the calculations are then performed on the auxiliary independent-particle system defined by the auxiliary Hamiltonian (which can be defined in Hartree units) as follows,

$$\hat{H}_{aux} = -\frac{1}{2}\nabla^2 + V^{\sigma}(\mathbf{r}) \tag{2.11}$$

Then the density of this non-interacting system is given by Equation (2.12),

$$n(\mathbf{r}) = \sum_{\sigma} \sum_{i=1}^{N^{\sigma}} |\psi_i^{\sigma}(\mathbf{r})|^2 \tag{2.12}$$

where ψ_i^{σ} are all orbitals that correspond to electrons with spin σ. The independent kinetic energy can then be expressed as follows,

$$T_S = -\frac{1}{2} \sum_{\sigma} \sum_{i=1}^{N^{\sigma}} \langle \psi_i^{\sigma} | \nabla^2 | \psi_i^{\sigma} \rangle . \tag{2.13}$$

The classical Coulomb repulsion, E_{Hartree} of the electron density can be defined as well,

$$E_{\text{Hartree}} = \frac{1}{2} \int d^3r d^3r' \frac{n(\mathbf{r}) n(\mathbf{r}')}{|\mathbf{r} - \mathbf{r}'|}. \tag{2.14}$$

This led us to rewrite the expression (2.7) for the energy functional as follows.

$$E_{KS} = T_S[n] + \int d\mathbf{r} V_{ext}(\mathbf{r}) n(\mathbf{r}) + E_{\text{Hartree}}[n] + E_{\text{II}} + E_{\text{XC}}[n] \tag{2.15}$$

For Equation (2.15) to be equal to Equation (2.7) all the many body effects are grouped into the exchange and correlation energy $E_{\text{XC}}[n]$. The exchange and correlation functional then can be written in terms of HK functionals,

$$E_{\text{XC}}[n] = F_{\text{HK}}[n] - (T_S[n] + E_{\text{Hartree}}[n]). \tag{2.16}$$

If the exchange and correlation functional is known, then one can proceed and calculate the ground-state energy of the many-body problem by solving the KS equations.

2.1.3 Kohn-Sham Variational Equations

Up to this point, we have introduced the concept of replacing the challenging many-body interacting problem with that of non-interacting particles, which is easier to be solved using numerical methods. For the solution to be found, the minimization of the KS energy functional needs to be performed with respect to either the density or the external potential. We can see from Eqs. (2.15) and (2.13) that the kinetic energy is a functional of the orbitals but the other terms are functionals of the density. Then one

can use the chain rule to derive the variational equation,

$$\frac{\delta E_{KS}}{\delta \psi_i^{\sigma *}} = \frac{\delta T_S}{\delta \psi_i^{\sigma *}} + \left[\frac{\delta E_{ext}}{\delta n(\mathbf{r}, \sigma)} + \frac{\delta E_{Hartree}}{\delta n(\mathbf{r}, \sigma)} + \frac{\delta E_{XC}}{\delta n(\mathbf{r}, \sigma)} \right] \frac{\delta n(\mathbf{r}, \sigma)}{\delta \psi_i^{\sigma *}} = 0 \tag{2.17}$$

By using the Lagrange multipliers to enforce particle conservation, this equation leads to the Kohn-Sham Schrödinger-like equation,

$$\left(H_{\mathrm{KS}}^{\sigma} - \epsilon_i^{\sigma}\right) \psi_i^{\sigma} = 0, \tag{2.18}$$

where ϵ_i^{σ} are the eigenvalues and the H_{KS} is the Kohn-Sham hamiltonian.

$$H_{\mathrm{KS}}^{\sigma}(\mathbf{r}) = -\frac{1}{2}\nabla^2 + V_{\mathrm{KS}}^{\sigma}(\mathbf{r}) \tag{2.19}$$

and:

$$V_{\mathrm{KS}}^{\sigma}(\mathbf{r}) = V_{\mathrm{ext}}(\mathbf{r}) + V_{\mathrm{Hartree}}(\mathbf{r}) + V_{\mathrm{XC}}^{\sigma}(\mathbf{r}) \tag{2.20}$$

The Equations (2.18), (2.19), and (2.20) are known as the Kohn-Sham equations. The solution of these equations typically follows a self-consistent procedure. Furthermore, it should be noted that these equations are independent from any approximation and would lead to the exact ground-state density and energy should the exact exchange and correlation functional be known.

2.1.4 Solution to the Kohn-Sham Equations

An iterative approach is adopted to solve the Kohn-Sham equations. These equations are solved using a self-consistent manner, meaning that the input is adjusted until convergence. The key idea is that an initial guess for the electron density is used to compute the effective potential, which is then used to solve the Schrödinger equation. From this solution, a new electron density is obtained.

The process is repeated iteratively: the new electron density is used to update the effective potential, which is then used to solve the Schrödinger equation again. This

cycle continues until the electron density and effective potential converge to a self-consistent solution, meaning that further iterations do not significantly change these quantities. The accuracy of a given calculation is determined by a threshold value, which specifies the difference in a given property (e.g., energy) between consecutive steps.

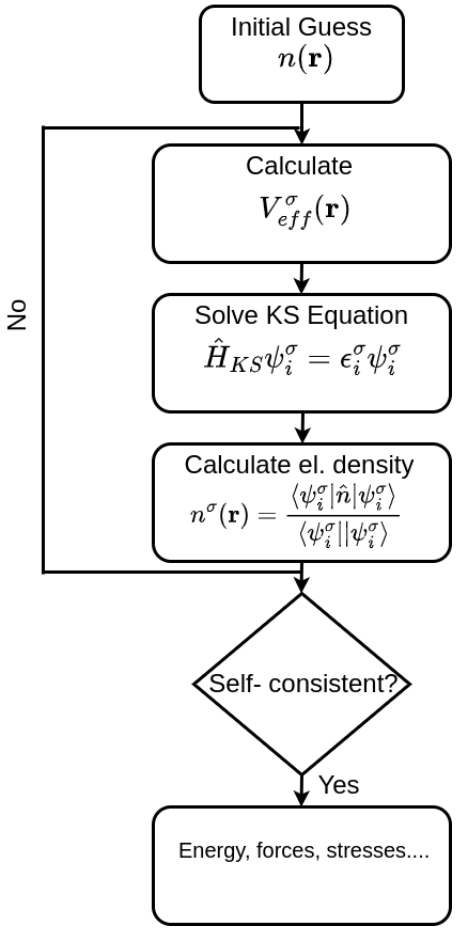

Figure 2.1: A schematic representation of the self-consistent cycle used for the solution of the Kohn-Sham equations. From an initial guess for the electron density the effective potential is calculated. Then, the Schrodinger-like Kohn-Sham equation is solved and the new electronic density is calculated. If the difference is above a threshold, then the electron density will be used to calculate the new value and the loop starts again. Otherwise the energies, forces and any additional ground-state properties are calculated.

2.1.5 Exchange and Correlation Functionals

Density functional theory is the lead method in ab-initio calculations of the ground-state properties of a quantum many-body system. However, a range of approximations must be considered. The total energy, E_{total} of the system can be expressed as,

$$E_{total} = T + E_{\text{estat}} + E_{\text{XC}} \tag{2.21}$$

where the T is the kinetic energy of the Kohn-Sham non-interacting system of electrons, the electrostatic contribution is E_{estat} and the exchange and correlation effects are included in E_{XC}. This subsection is dedicated to this important last term of Eq. (2.21), as it is the one to correct for the missing electronic energy. So far no closed form for the exchange and correlation functional has been found. However, there is a variety of different approximated ones that are used. We will rapidly review the Local Density Approximation (LDA) and Generalised Gradient Approximation (GGA), which are two of the most frequently utilised approaches in literature. The latter has been used throughout this work.

In the first approximation, considering a point of space $\mathbf{r}$ where the electron density takes a value of n($\mathbf{r}$), then the exchange and correlation energy is the energy of a uniformly distributed electron gas [20] computed at that density. This approximation assumes that there are no rapid changes in the electron charge density. The value is given by Equation (2.22).

$$E_{\text{XC}}[n(\mathbf{r})] = \int d^3\mathbf{r}\; n(\mathbf{r})\; \epsilon(n) \tag{2.22}$$

For materials where the charge density is closer to the homogeneous electron gas, for example metals, this approximation is expected to work well.

In the Generalised Gradient Approximation (GGA) [27], which is considered to be an improved version of LDA, one not only considers the value of the electron density at a point, $\mathbf{r}$, but also the gradient of the density, $\nabla\, n(\mathbf{r})$, which gives information about the slope of the charge density at that point. In this work, the GGA Perdew, Burke, and Ernzerhof functional will be employed for our calculations. The general expression is given by the following equation,

$$E_{\text{XC}}^{\text{PBE}} = \int d^3\mathbf{r}\; n(\mathbf{r})\; \epsilon_{\text{XC}}^{\text{PBE}}(r_s(\mathbf{r}), s(\mathbf{r}), \zeta(\mathbf{r})), \tag{2.23}$$

where the r_s is the Wigner-Seitz radius , given by $r_s = (\frac{4\pi\, n}{3})^{\frac{-1}{3}}$, ζ is the relative spin polarisation and s is the reduced density gradient. The exact expression for $\epsilon_{\mathrm{XC}}^{\mathrm{PBE}}$ is constructed to satisfy a range of criteria explored in detail in Ref. [27].

In the present work, we have performed DFT calculations, as introduced in the preceding sections, using the Vienna ab-initio Software Package (VASP) [28–31].

2.2 Machine Learning Interatomic Potentials

Calculating the ground-state energy using ab-initio methods, such as DFT, can be computationally expensive, especially when performing thousands of calculations for a specific system. Machine-learning provides tools to overcome this challenge. In this study, we train machine-learning models to serve as surrogates for DFT in predicting the ground-state energy of the systems under investigation. Therefore, it is essential to provide the reader with the foundational knowledge regarding the machine-learning techniques applied in this work.

2.2.1 Machine-Learning and Types of Learning

The machine-learning (ML) term refers to the variety of techniques used to address problems for which exact algorithm development may be inefficient. These problems are tackled by enabling machines to "discover" their " own" algorithms [32], eliminating the need for explicit programming or guidance from human-developed algorithms.

In other words, provided that the necessary data sufficiently sample the space of the studied problem, one can algorithmically build a statistical model based on that dataset. This means that in the end, the trained model learns a mathematical function that connects the input with the output. In order to enable the machine to construct such relationships, one needs to provide the model with a vector of numbers representing the important characteristics of the problem, called the feature vector. Then, an optimization process begins, adjusting the parameters of the model to reproduce the output in the most accurate way possible and to predict the output

for unseen cases more effectively. A schematic representation of a generic ML model is shown in Figure 2.2.

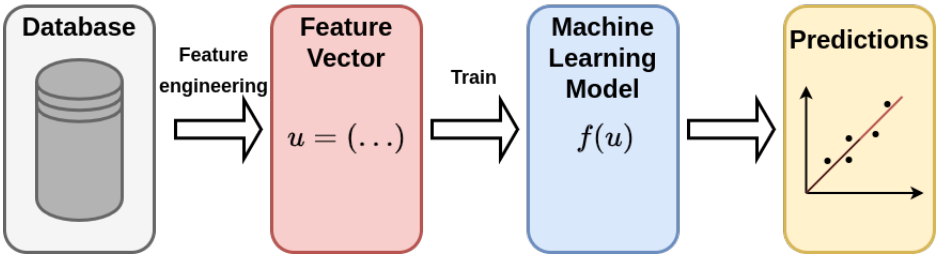

Figure 2.2: Schematic representation of the main steps of a machine-learning workflow.

Furthermore, there are various types of learning, including supervised [33], unsupervised [34], and reinforcement learning [35]. The differences between these types of learning results from how the model interacts with the dataset and the type of data used for training. In the first case, the model is trained on labeled data $\{(\mathbf{x}_i, y_i)\}_{i=1}^{N}$, where each data point is represented as a feature vector $\mathbf{x}_i$ corresponding to a label y_i. The goal of supervised learning is to construct a model that takes a feature vector $\mathbf{x}_i$ as input and returns the label y_i. In unsupervised learning, the dataset consists of a collection of unlabeled examples, $\{\mathbf{x}_i\}_{i=1}^{N}$, and the model's objective is to extract insights from the provided data. In the last category, the model interacts with the user based on a reward system, allowing the model to learn through examples. In this work, we primarily focus on the first category of learning as we train machine-learning models to replace computationally intensive DFT calculations.

2.2.2 Ridge Regression and Model Training

In the present work, we focus on training linear models, namely linear ridge regression. The main reason behind that choice is the lack of available data points, as the goal of this project is to explore how well models perform, when trained on readily available data. Then, it is proved that linear models [36, 37], when combined with highly nonlinear descriptors (in our case, bispectrum components) are able to fit complex relationships [38–42].

Let us assume to have a database ($\{(\mathbf{x}_i, y_i)\}_{i=1}^{N}$) consisting of N different pairs of data points corresponding to the vectors $\mathbf{x}_i$ and the output label y_i. A typical

linear model assumes a function that maps the inputs to the outputs through a linear relationship. To predict the values y_i corresponding to the example $\mathbf{x}_i$, one can use Equation (2.24),

$$y_i = f^{Ridge}(\mathbf{x}) = \mathbf{a} \cdot \mathbf{x}_i \tag{2.24}$$

Here, $\mathbf{a} = (a_1, a_2, \ldots, a_p)$ represents the vector containing the learned coefficients, where p is the number of features in the vector $\mathbf{x}_i$. In order to determine the coefficients $\mathbf{a}$ one has to optimise a specific loss function, which measures how well the model performs with respect to known data. A famous example is the least squares $L^{LS}(\hat{y}_i, y_i) = \sum_{i=1}^{N}(\hat{y}_i - y_i)^2$, where $\hat{y}_i$ is the known label corresponding to $\mathbf{x}_i$ and y_i is the output of the linear model. The coefficients $\mathbf{a}$ correspond to the ones that minimize the value of a specific loss function. The ridge regression case can be considered as an extension to least-squares, as it adds a regularization term to the least-squares loss function. The loss function can then be written as follows,

$$L^{Ridge}(\mathbf{a}) = \sum_{i=1}^{N}(y_i - \mathbf{a}x_i)^2 + \lambda|\mathbf{a}|^2. \tag{2.25}$$

The second term in Eq. (2.25) is called the regularization term and corresponds to a L_2 regularization [43]. The constant λ corresponds to a hyperparameter of the model, so it has to be minimised in order to provide the most optimal model. The aim of the regulatisation is to prevent overfitting by imposing a penalty on large model parameters (outliers), helping to create a more generalized model that performs well on unseen data.

An overfitted model [44] is one that exhibits excessive complexity for the dataset it is intended to fit. While the loss function typically attains low values, these models tend to capture not only the underlying patterns, but also the noise within the data. Consequently, they become less useful for making predictions on data that was not part of the training set.

An underfitted model [44] is the opposite, characterized by being a mathematical

model that is overly simple for the dataset it is meant to fit. These models typically exhibit higher loss functions and perform poorly on unseen data. For instance, a linear fit applied to non-linear data is a classic example of underfitting. In Figure 2.3, a visual representation of an underfitted, overfitted, and correctly fitted model is presented.

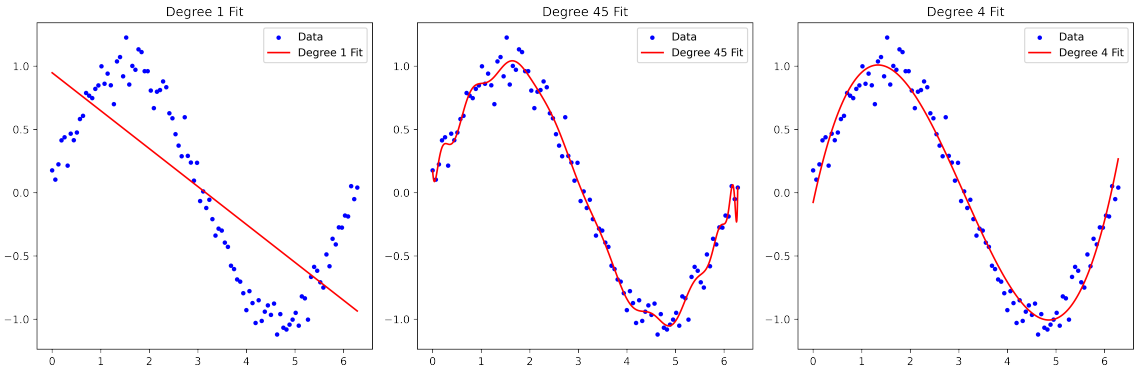

Figure 2.3: Illustration of Underfitting (left), Overfitting (middle), and Proper Fitting (right). In this figure, different polynomial orders were used to fit the same sine function. It is demonstrated that as the degree increases, the models transition from a significant underfitting, which is too simple to represent the data, to a highly complex model that learns the noise introduced to the dataset (overfitting). The last panel show a well balanced fit.

2.2.3 Matrix Notation and Gradient Descent

The same equations can be expressed in matrix notation, which simplifies their implementation through vectorization. Vectorization is a technique in which the implementation of a mathematical equation is transformed from a scalar approach, where pairs of operands are processed one at a time, into vectorized operations that handle multiple pairs of operands simultaneously. In thi way the calculations are made faster by orders of magnitude.

Consider a system where we have N vectors represented by $\mathbf{x}$, with each of these vectors corresponding to p distinct features. Then, we can define as the matrix $\mathbf{X}$ the $N \times p$ matrix, where the row k corresponds to the $\mathbf{x}_k$, namely,

$$\mathbf{X} = \begin{bmatrix} x_{11} & \cdots & x_{1p} \\ \vdots & \ddots & \vdots \\ x_{k1} & \cdots & x_{kp} \\ x_{N1} & \cdots & x_{Np} \end{bmatrix}. \tag{2.26}$$

In contrast, $\mathbf{Y}$ corresponds to the vector of all the outputs y_i and the vector $\mathbf{a}$ is the vector of coefficients. Then, one can write the Equation (2.24) in vector form as

$$\mathbf{Y} = \mathbf{X}\mathbf{a} \Leftrightarrow \begin{bmatrix} y_1 \\ \vdots \\ y_N \end{bmatrix} = \begin{bmatrix} x_{11} & \cdots & x_{1p} \\ \vdots & \ddots & \vdots \\ x_{k1} & \cdots & x_{kp} \\ x_{N1} & \cdots & x_{Np} \end{bmatrix} \begin{bmatrix} a_1 \\ \vdots \\ a_p \end{bmatrix}. \tag{2.27}$$

The loss function, defined in Equation (2.25), can be writen as follows,

$$L^{Ridge} = (\mathbf{Y} - \mathbf{X}\mathbf{a})^\intercal(\mathbf{Y} - \mathbf{X}\mathbf{a}) + \lambda \mathbf{a}^\intercal \mathbf{a}. \tag{2.28}$$

After defining the loss function, it is important to discuss the algorithm used to optimize the values of the coefficients $\mathbf{a}$. Although there are a variety of different optimisation algorithms such as probabilistic methods like Bayesian optimisation [45] or brute force methods like grid-search, by far one of the most popular is gradient descent.

Gradient descent [46] is an iterative optimization algorithm for finding the local minimum of a differentiable function. The core idea of this method is to start from a random guess and move in the opposite direction of the gradient of the function at the current point until one reaches the minimum. We start by calculating the partial derivative of Equation (2.25) with respect to the optimisation parameter,

$$\frac{\partial L^{Ridge}}{\partial \mathbf{a}} = -2\sum_{i=1}^{N} x_i(y_i - \mathbf{a}x_i) + 2\lambda\mathbf{a}, \tag{2.29}$$

and in matrix notation

$$\frac{\partial L^{Ridge}}{\partial \mathbf{a}} = -2\mathbf{X}^{\intercal}(\mathbf{Y} - \mathbf{X}\mathbf{a}) + 2\lambda\mathbf{a}. \tag{2.30}$$

Then, by starting from a random choice of the vector $\mathbf{a}$, one can optimize it iteratively by updating the values in the following way

$$\mathbf{a}_{i+1} = \mathbf{a}_i - \eta\frac{\partial L^{Ridge}}{\partial \mathbf{a}}. \tag{2.31}$$

Here, the subscript i refers to the updated vector $\mathbf{a}$, and η represents the learning rate. The optimization algorithm continues to iterate until convergence, which occurs when the change in the loss function falls below a certain predefined threshold.

2.2.4 Interatomic Potentials

Interatomic potentials [47] are functions that correlate the structure of a given system of atoms with its potential energy. By taking the derivative of this interatomic potential with respect to the atomic coordinates, one can calculate the forces acting on the system. Interatomic potentials are commonly used in molecular dynamics simulations to explain and predict material properties [48, 49].

Interatomic potentials can be written as a summation of contributions that correspond to one, two, three, etc., atoms at a time. The total potential can be expressed as follows,

$$V_{\text{total}} = \sum_{i=1}^{N} V_1(\vec{r}_i) + \sum_{i,j=1}^{N} V_2(\vec{r}_i, \vec{r}_j) + \sum_{i,j,k=1}^{N} V_3(\vec{r}_i, \vec{r}_j, \vec{r}_k) + \cdots \tag{2.32}$$

where V_1, V_2, V_3, etc. are the one-, two-, three-body terms correspondingly. A variety of different interatomic potentials have been proposed with arguably the most famous being the Lennard-Jonnes potential [50]. The function of this potential is a sum of a repulsive term ($\propto r^{-12}$) that dominates at very short distances and an attractive term $\propto r^{-6}$, which dominates at intermediate distances. The complete function then is

$$V_{\text{LJ}}(r) = 4\varepsilon\left[\left(\frac{\sigma}{r}\right)^{12} - \left(\frac{\sigma}{r}\right)^{6}\right], \tag{2.33}$$

where ε is the depth of the potential, σ is the distance at which the potential is takes the zero value and r is the distance between the centers of the two particles. In applications these values are fitted with to experiments or theoretical calculations. Combining these two terms in the Lennard-Jones potential, the model captures both the strong repulsion at very short distances (to prevent particles overlap) and the attractive forces that become significant at intermediate distances. Other types of parametric potentials are the Morse potential [51], the Ziegler-Biersack-Littmark (ZBL) potential [52] and others.

2.2.5 Machine Learning Interatomic Potentials, the Case of SNAP

Machine Learning Interatomic Potentials (MLIAPs) employ machine-learning methods to map the potential energy surface (PES), including the total energy and interatomic forces, as functions of the atomic positions. In a concept similar to empirically fitted force fields, the parameters of ML interatomic potentials are optimized using provided data, typically computationally expensive DFT calculations. However, MLIAPs do not make any assumptions about the shape of the interatomic potential. Instead, they directly learn all information from the input data. Once the potential has been fitted, it can be used to predict the energies, forces, and stress tensors of larger ensembles of atoms without the need for additional reference data, and it does so in a fraction of the time. This approach provides access to ab-initio accuracy in molecular dynamics simulations for extended length and time scales.

In this study, the Spectral Neighbor Analysis Potential (SNAP) serves as a DFT surrogate. SNAP operates under the assumption of a linear relationship between the local environment, expressed in bispectrum components, and the atom energy. SNAP has been employed to train robust models [37, 39, 40] with a limited amount of data. As SNAP is extensively utilized throughout this work, it is crucial to introduce the key concepts related to this type of interatomic potential.

The fact that the PES is a smooth function of the nuclear coordinates [10], is a property that makes interatomic potentials useful. Then, the property of nearsightedness [53]

states that the electron density at a point is only weakly affected by atoms that are not near. This results to the main assumption that the energy of a configuration of atoms can be expressed as a sum of contributions of different clusters of atoms as expressed in Equation (2.34),

$$E_{\text{tot}} = \sum_{i=1}^{N_{\text{atom}}} \varepsilon^{\text{Local}}(\{\mathbf{r}_{ij}\}), \tag{2.34}$$

where $\mathbf{r}_{ij}$ is the relative position between the atoms i and j. Therefore, it is reasonable to create a class of descriptors that represents the local chemical environment of each atom, or the relative positions and bonds of the neighborhood. In general, this is done by identifying geometrical structures composed of the pair distances and angles. One of the descriptors studied by Bartók et al. [10, 54, 55], namely the bispectrum of the neighbor density mapped on to the 3-sphere, forms the basis for their Gaussian Approximation Potential (GAP) [10]. SNAP interatomic potential also uses the same basis.

The derivation starts by expressing the density of neighbor atoms around a central atom i at a location $\mathbf{r}$. This can be considered as a sum of δ-functions in the three dimensional space,

$$\rho_i(\mathbf{r}) = \delta(\mathbf{r}) + \sum_{r_{ii'}<R_{\text{cut}}} f_c(\mathbf{r}_{ii'}) w_{i'} \delta(\mathbf{r} - \mathbf{r}_{ii'}). \tag{2.35}$$

Here, $\mathbf{r}_{ii'}$ is the vector connecting atom i to atom i', $w_{i'}$ represents the elemental weights, used to distinguish different species, and R_{cut} denotes the cut-off radius that defines the local neighborhood. The last two types of parameters are hyperparameters of the problem, which means that, in order to obtain an optimized SNAP potential, they must be optimized. The function $f_c(r)$ [56] is a smooth function defined to ensure that the contribution of the atoms goes smoothly to zero as the distance from the central atom increases above R_{cut}. In SNAP this is defined as follows,

$$f_c\left(R_{ij}\right)\begin{cases}0.5\left[cos(\frac{\pi r}{R_{\text{cut}}})+1\right] & \text{for } r \leq R_{\text{cut}}\\ 0 & \text{for } r > R_{\text{cut}}\end{cases}. \tag{2.36}$$

In order to expand the angular part of the neighbor density one can use the basis of the spherical harmonics [57], $Y_m^l(\theta,\phi)$ where $l = 0, 1, 2, \ldots$ and $m = -l, \ldots, l$. The radial part of the neighbor density is expanded onto a radial basis and multiplied by the spherical harmonics. In the work of Bartók et al. the radial distance is mapped onto an angle $\theta_0 = \theta_0^{max}\frac{r}{R_{\text{cut}}}$. This projection is similar to a Riemann projection, and the choice of it allows for a more sensitive representation for the entire range.

The 4D hyperspherical harmonics $U^j_{m,m'}(\theta_0,\theta,\phi)$ are used as a basis for the 3-sphere [57]. Then the neighbor density can be expanded as follows,

$$\rho(\mathbf{r}) = \sum_{j=0,\frac{1}{2},\ldots}^{\infty}\sum_{m=-j}^{j}\sum_{m'=-j}^{j} u^j_{m,m'}U^j_{m,m'}(\theta_0,\theta,\phi), \tag{2.37}$$

where the coefficients of expansion, $u^j_{m,m'}$ are given by,

$$u^j_{m,m'} = \left\langle U^j_{m,m'}\middle|\rho(\mathbf{r})\right\rangle, \tag{2.38}$$

and the $U^j_{m,m'}$ are the Wigner matrices [57]. Since the neighbor density is represented as a sum of δ-functions, each term in the expansion can be expressed as a sum over discrete values of the corresponding basis function as follows,

$$u^j_{m,m'} = U^j_{m,m'}(0,0,0) + \sum_{r_{ii'}<R_{\text{cut}}} f_c(r_{ii'})w_i U^j_{m,m'}(\theta_0,\theta,\phi) \tag{2.39}$$

However, although we have expanded the neighbor density into coefficients, $u^j_{m,m'}$ is it known [57] that these coefficients are complex valued, so they are not suitable to be used as descriptors of the local chemical environment. Furthermore, they do not contain the symmetries that we would like them, such as invariant under rotation. However, it was shown that the scalar triple product of the expansion coefficients are real-valued and are invariant under rotation [55]. Then, the bispectrum components

can be written as follows,

$$\mathbf{B}_{j_1,j_2,j} = \sum_{m_1,m_1'=-j_1}^{j_1} \sum_{m_2,m_2'=-j_2}^{j_2} \sum_{m,m'=-j}^{j} (u^{j}_{m,m'})^* H^{jmm'}_{\substack{j_1 m_1 m_1' \\ j_2 m_2 m_2'}} u^{j_1}_{m_1,m_1'} u^{j_2}_{m_2,m_2'}. \tag{2.40}$$

Here, $H^{jmm'}_{\substack{j_1 m_1 m_1' \\ j_2 m_2 m_2'}}$ represents the Clebsch-Gordan coefficients of the SO(4) group. The advantage of the bispectrum components lies in their ability to capture both radial and angular information, while inherently preserving the necessary symmetries. The number of these components is determined by the value of j in Equation (2.37), which is now denoted as $j_{\max}$. In most implementations, it is multiplied by two, $2j_{\max}$, so to take integer values [37].

The different hyperparameters in this descriptor are the cut-off radius R_{cut}, the $2j_{\max}$, and the elemental weights $w_{i'}$. The first one, controls the amount of interactions that are taken into account when building the feature vector, so it controls the amount of information that is encoded in the feature vector. The second hyperparameter, $2j_{max}$, controls the complexity of the feature vector. For example, as we increase it, the more complex the models produced are. The last ones, the elemental weights $w_{i'}$, add information regarding the different atomic species.

The model can then be trained to correlate the descriptor calculated by Equation (2.40) with the energy produced by quantum mechanical calculations. In order to do that, we assume that the local energy can be decomposed into separate atomic energy contributions, as from Equation (2.34), but now the atomic energy ε is a function of the descriptors. In this case, it is the vector containing the bispectrum components $\mathbf{B}^i = (B^i_1 \dots B^i_K)$, where K is controlled by $2J_{\max}$. Then, for a system of N_{atoms} atoms we can write,

$$E_{tot} = \sum_{i=1}^{N_{\text{atoms}}} E^i_{\text{SNAP}}(\mathbf{B}^i). \tag{2.41}$$

It is assumed that the SNAP atomic energy, $E^i_{\text{SNAP}}(\mathbf{B}^i)$, is a linear function of the descriptors. Then the linear equation can be written as

$$E^i_{SNAP}(\mathbf{B}^i) = a_0^{\beta_i} + \mathbf{a}^{\beta_i}\mathbf{B}^i, \tag{2.42}$$

where β_i is the chemical identity of atom i and $a_K^{\beta_i}$ are the coefficients for the atoms of type β. The excercise is then reduced to an optimisation problem of a linear function, meaning that one has to find the values of the coefficients $\mathbf{a}^{\beta_i}$ that reproduce the accuracy of the ab-initio simulations. In the case of a structure consisted of N_{atoms} of a single type one can write,

$$\begin{aligned} E_{tot} = \sum_{i=1}^{N_{atoms}} E^i_{SNAP}(\mathbf{B}^i) = \sum_{i=1}^{N_atoms} (a_0 + \mathbf{a} = \mathbf{B}^i) = \\ = N_{atoms}a_0 + \mathbf{a}\sum_{i=1}^{N_{atoms}} \mathbf{B}^i. \end{aligned} \tag{2.43}$$

By calculating the derivative of the total energy with respect to the position of the atoms are then calculate the forces that act on the atoms of the structure,

$$\mathbf{F}^j_{SNAP} = -\nabla_j E_{tot} = -\mathbf{a}\sum_{i=1}^{N_{atoms}} \frac{\partial \mathbf{B}^i}{\partial \mathbf{r}_j}, \tag{2.44}$$

and the stress tensor,

$$\mathbf{W}_{SNAP} = \sum_{j=1}^{N_{atoms}} \mathbf{r}_j \otimes \mathbf{F}^j_{SNAP} = -\sum_{j=1}^{N_{atoms}} \mathbf{r}_j \otimes \sum_{i=1}^{N_{atoms}} \frac{\partial \mathbf{B}^i}{\partial \mathbf{r}_j}. \tag{2.45}$$

From a single quantum mechanical calculation for a system of N_{atoms} atoms, in general, we have access to $3N_{\text{atoms}} + 7$ data points, namely the energy, the six values of stress tensor and the $3N_{\text{atoms}}$ forces. In general, an interatomic potential should be trained on all the available data. In the next few equations we formulate the excercise in a matrix notation form. In order to find the optimal values for the coefficients of the vector $\mathbf{a}$, one has to follow the methodology presented in Sections 2.2.2 and 2.2.3,

$$\begin{bmatrix} \vdots & \vdots \\ N_{atoms} & \sum_{i=1}^{N_{atoms}} \mathbf{B}^i \\ \vdots & \vdots \\ 0 & -\sum_{i=1}^{N_{atoms}} \frac{\partial \mathbf{B}^i}{\partial r_j^\beta} \\ \vdots & \vdots \\ 0 & -\sum_{j=1}^{N_{atoms}} r_j^\beta \sum_{i=1}^{N_{atoms}} \frac{\mathbf{B}^i}{\partial r_j^\beta} \\ \vdots & \vdots \end{bmatrix} \begin{bmatrix} a_0 \\ \mathbf{a} \end{bmatrix} = \begin{bmatrix} \vdots \\ E_s^{DFT} \\ \vdots \\ \mathbf{F}_{j,\beta}^{DFT} \\ \vdots \\ \mathbf{W}^{DFT} \\ \vdots \end{bmatrix}. \tag{2.46}$$

The objective now is to determine the coefficients of the vector **a** in such a way that the predictions for these quantities can accurately reproduce the data points provided to the model. Thompson et al. [37] achieved this by employing least-squares optimisation. In our case, as discussed earlier, we are utilizing ridge regression.

Lastly, a mention should be made about the variety of different fingerprints that have been successfully implemented and used in a variety of studies. A necessary condition is that they present the same symmetries as the property one has to predict. In our case, we are interested in energy predictions. Hence, the relevant fingerprints should be invariant under translation and atomic permutation, while they are usually constructed to be locally rotational invariant. Just to name a few of the most used MLIAPs: Behler-Parinello symmetry functions, combined with Neural Networks in Neural Network Potentials (NNP) [56] which successfully employed to perform molecular dynamics simulation for bulk silicon with ab-initio accuracy. The Smooth Overlap of Atomic Position (SOAP) descriptors with Gaussian process regression in Gaussian Approximation Potentials (GAP) [10], used to accurately describe bulk semiconductors and iron at high temperature. Furthermore, invariant polynomials with linear regression in Moment Tensor Potentials (MTP) [12] and N-bond basis functions with linear regression in Atomic Cluster Expansion (ACE) [58]. The models employing the feature vectors highlighted before utilize a DFT dataset to fit the model parameters and are capable of predicting energies and forces at ab-initio accuracy, provided these are made for structures for which the model interpolates.

2.2.6 Applications

Machine Learning Interatomic Potentials (MLIAPs), trained on data extracted from ab-initio calculations, present a compelling alternative to computationally expensive DFT. While still a relatively young field in materials science, MLIAPs find applications in a range of different fields. In the following paragraphs, we will present a selection of studies in which the versatility and effectiveness of incorporating such tools into material prediction workflows is demonstrated.

MLIAPs based on SNAP and neural networks, have previously been employed to map the potential energy surface of multiple phases and reconstruct the $T = 0$ K phase diagram, thereby determining the lowest energy structures for metallic alloys. A notable example is the case of the Ni-Mo binary system as demonstrated in reference [38]. In that study, a SNAP model tailored for the Ni-Mo binary system achieved excellent agreement with experimental data in predicting the Ni-Mo phase diagram. Furthermore, it exhibits near-DFT accuracy in predicting various key properties, including elastic constants, formation energies, melting points, and more, across the entire range of binary composition. This surpasses the accuracy of the embedded-atom method potentials previously used for the same purpose.

In the case of reference [59] a neural network based interatomic potential was trained for the Au-Li binary system. They used the trained interatomic potential to explore the miscibillity in that binary phase diagram, discovering a variety of structures near the convex hull. Furthermore, they were able to find three structures at the convex hull, which means that they are thermodynamically stable. Another case where a NN-based interatomic potential was used is that of the Mg-Ca binary alloy [60] where a trained model was used to find two different stable phases.

Another example of an interatomic potential being employed to explore a ternary phase diagram can be found in reference [61]. In this study, an interatomic potential was trained to reproduce the energies, phonon dispersions, and formation enthalpies of Cu, Pd, Ag, Cu-Pd, Cu-Ag, Pd-Ag, and Cu-Pd-Ag systems. Attempts have been made to predict the stability of a given material [62, 63] directly by measuring its distance

from the convex hull. These models leverage available databases, combining data from various stoichiometric compositions, chemical species, and crystal structures to provide the necessary information.

However, when it comes to SNAP interatomic potentials, their applicability has been somewhat limited to explore a wide range of different structures and stoichiometries, and they have not been extensively utilized to discover new stable alloys. In contrast, Neural Network Potentials (NNPs) have been trained on very large datasets, typically containing thousands to tens of thousands of structures. This enables NNPs to capture a comprehensive set of structures, similar to what is required for constructing a fully ab-initio convex hull.

One of the few cases where a MLIAPs trained on a limited number of structures, was used to predict materials' stability in an accelerated manner is illustrated in the work of Gubaev et al. [64]. In their research, they performed ab-initio calculations on a range of structures, between 383 and 2,393, to train a MLIAP capable of reproducing binary and ternary convex hulls. The selection of these structures was facilitated by an efficient active learning algorithm [64], which explored approximately $10^4 - 10^5$ configurations for each phase diagram. This approach demonstrated that MLIAPs have the potential to aid high-throughput computational searches of novel alloys.

2.3 Prototype Creation Strategies

The crystal structure is undoubtedly one of the most significant attributes of a material, as it exhibits a strong correlation with its properties. Knowing the arrangement of atoms is important for studying their properties as well as to estimate their stability. It is significant in many different areas of science in which someone wants to know the structure of a given material. Since it is a global optimization problem, finding a solution is not always possible. The primary focus is on thermodynamically stable structures, as those are more probable for experimental synthesis in ambient conditions. However, metastable structures also offer valuable insight into a specific compound under particular conditions, such as temperature or pressure. However, determining

the atomic arrangement in a material solely on the basis of its stoichiometry remains an ongoing scientific challenge. Various strategies have thus far been employed to tackle this problem. In the following subsection, I will provide a concise overview of some well-known approaches. In addition, we will introduce the methodologies employed in this work.

One of the most commonly used approaches to predict crystal structures is the ab initio random structure search (AIRSS) [65]. The underlying idea behind this strategy is that, when no prior knowledge of the atomic arrangements of a material is available, it is reasonable to begin by relaxing random structures. However, as outlined in the foundational paper of this method [65], several criteria must be followed. For instance, the volume of a specific material can be estimated based on the volume of its components, and the distances between atoms should be appropriate, avoiding both overly close and overly distant configurations. This ensures that the optimisation algorithm to refine the structures can operate effectively. This approach has been applied to a wide range of problems. It has been used to study the phases of silane (SiH_4) [66], to predict its crystal structure, to confirm the expected metallic behaviour, and demonstrate that silane can exhibit high temperature superconductivity. This phenomenon arises from the pre-compression of hydrogen induced by the presence of the group IV element. In another interesting study, the same author, utilised a random structure search to study the phase diagram of hydrogen sulphide at high pressures [67].They employed this method to predict the crystal structures of different compositions throughout the phase diagram. Another application that combines the advantages of AIRSS with machine-learning potentials [68] is presented. In this work, the same author, used this methodology to uncover a large unit cell structure in the high-pressure phase diagram of silane, as well as to identify the correct crystal structure for the 12-atom icosahedral alpha-boron and the 28-atom gamma-boron.

Another well-known method employs an evolutionary algorithm [69] to search for structures that lie at the minimum of the potential energy surface. In the evolutionary crystal structure algorithm SPEX [70] starting from a variety of different inputs such as

stoichiometry, pressure-temperature conditions, and the number of atoms, just to name a few. It creates the parent structures (the first generation step) then, by imitating the Darwinian evolution idea, the structures created before are combined and a relaxation step will bring them to the minimum. New structures are produced by slicing the parent over during an heredity phase, and the new generation of structures is created by mutation, change of the cell, by permutation or by switching elemental identities of the atoms in the crystal. This strategy has been used in a variety of works and has yielded results, especially for crystal structures under extreme conditions [71]. Furthermore, they proposed and studied a super-hard phase of monoclinic carbon [72], in agreement with the experiments. Also, they studied and proposed that under pressure sodium becomes transparent [73], which is due to the fact that under pressure it transforms into an insulating phase.

Although these strategies yield truly remarkable results, they are computationally intensive because of the need for an exhaustive number of ab-initio calculations. Furthermore, due to their probabilistic nature, they do not guarantee to always find the absolute minimum. However, they are ideal for those who want to find novel compounds and focus on a specific system. This makes them challenging to employ within a high-throughput framework.

2.3.1 AFLOW Dictionary Method

Starting with the main idea of the task we aim to address—creating an inverse design workflow that combines high-throughput and machine-learning techniques—the challenge of efficiently generating candidate structures. In particular, the objective of this study was to combine elements from the transition metal region of the periodic table to create ternary alloys. This implies that the chemical environments of the anticipated structures would be variations of the binary constituents. Here, our prototype generation workflow draws inspiration from the dictionary method utilized by AFLOW [74, 75] and the derivative structure creator developed by Hart et al. [76–78]. Both of these methods are known for their speed. Furthermore, the structural diversity of the structures

created is sufficient for the problem we want to tackle. In the following paragraphs, we will introduce these two methods, which played a crucial role in the present work.

We start from the dictionary method, which is a more high-throughput-oriented method for generating crystal structure prototypes, particularly for constructing binary and ternary phase diagrams. The concept behind this strategy is rather straightforward. By having an encyclopedia [79–81] containing all available atomic positions and cells of known materials, one can utilise the prototypes and decorate them with the desired elements. Such approach has been used in a variety of high-throughput studies, where the crystal structure of an interesting family of compounds was used as a prototype and decorated accordingly. In references [6, 82], the crystal structure of the Heusler family of alloys is explored using high-throughput calculations. In the first work, the Heusler alloy structure was decorated accordingly to search for novel magnetic materials. They assessed the stability of a quarter of a million different compounds and predicted and synthesised three novel magnets. In the second work, an experimental criterion was employed, namely the electron count to be equal to 19, in order to search for semiconductors. Here, Figure 2.4 shows the procedure used when considering the dictionary method.

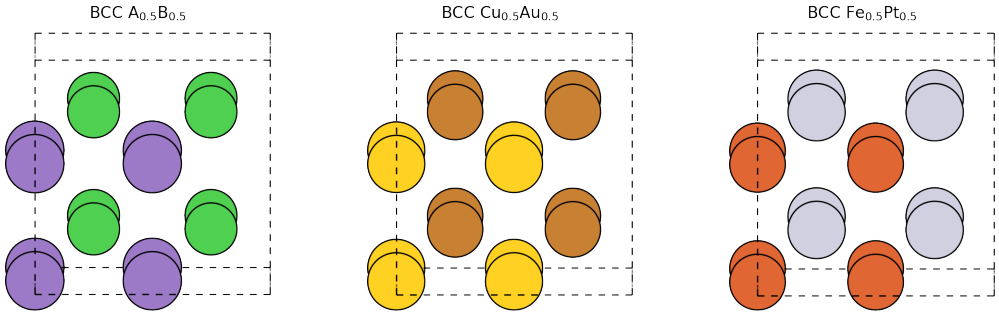

(a) $A_{0.5}B_{0.5}$ (b) $Cu_{0.5}Au_{0.5}$ (c) $Fe_{0.5}Pt_{0.5}$

Figure 2.4: The figure shows the body-centered cubic 2x2x2 supercell. In the leftmost panel, the general $A_{0.5}B_{0.5}$ binary alloy is depicted, where A atoms are shown in green and B atoms are shown in purple. In the central figure the $Cu_{0.5}Au_{0.5}$, where Cu atoms are shown in bronze and Au atoms are show in yellow. In the rightmost figure the $Fe_{0.5}Pt_{0.5}$, where Fe atoms are shown in red and Pt atoms are show in grey.

In general, apart from decorating already known crystal structures, there is a scaling process that ensures the volume of the created structure to be in accordance with the

volume of the constituent elements, known as Vegard's law [83]. This ensures that the relaxation step is more efficient and corrects for abnormal structures. The disadvantage of the dictionary method is that this approach is less likely to predict crystal structures that have not been explored before. AFLOWLIB employs this strategy to create the structures used for a given convex hull with success, as it is able to find a variety of different stable intermetallics in the space of binary and ternary alloys.

2.3.2 Enumlib

The idea of populating a known crystal structure with a specific stoichiometric decoration is a fundamental aspect of this work. However, decorating the lattice sites with various motifs can be a challenging task, especially when creating supercells based on a specific unit cell, as the number of decorations scales with the available sites. Several tools have been developed for this purpose [76, 84]. We have determined that the algorithm best suited to address the challenges of our proposed solution is the enumeration algorithm developed by Hart et al. [76], as it provides the required throughput for our purposes. The following section will introduce the key concepts of this method.

The algorithm, as described in references [76–78], is designed to generate all the different *derivative superstructures* from a given parent structure. This category of structures consists of those, whose lattice vectors are multiples of a *parent lattice*, and their atomic basis vectors correspond to lattice points of the parent lattice. Furthermore, it is capable of generating all unique rotationally and translationally decorations or *colorings*.

The definition of a lattice, A, is presented. If there is a set $E = \{\epsilon_1, \epsilon_2, \ldots, \epsilon_k\}$ of linearly independent vectors in n-dimensional Euclidean space in $\mathbb{R}^n$ then we can write

$$A(E) = \{\sum_{i=1}^{k} \lambda_i \epsilon_i \mid \lambda_i \in \mathbb{Z}\} \tag{2.47}$$

is called a lattice with basis E and k is the dimension of A(E). Then, the basis can compactly be represented as a square $n \times k$-matrix with vectors $\epsilon_1, \epsilon_2, \ldots, \epsilon_n$ as columns.

At the heart of the algorithm lies the concept of *superlattice* of size n. Let us consider

the transformation $B = AH$, where A is the basis of the lattice defined in Equation (2.47) (in general, this can be any lattice), H is a matrix of integer elements, and B is the transformed lattice. The determinant of the transformation matrix gives the size of the supperlattice B. For instance, if $det(H) = -1, +1$ then the transformation is just a change in basis. If $det(H) = 2$ then the lattice B is a superlattice of size n =2. Different H matrices with the same determinant correspond to different bases for the same lattice. These matrices are in the lower-triangular Hermite normal form (HNF) that is given by the equation

$$\begin{bmatrix} a & 0 & 0 \\ b & c & 0 \\ d & e & f \end{bmatrix}. \tag{2.48}$$

In cases where $0 \leq b < c$ and $0 \leq d, e < f$, the determinant is defined by the multiplication of the diagonal elements. Finding all the Hermite Normal Form (HNF) matrices for a specific size n is the initial step of this algorithm. For a given size n, one would start by identifying all the different diagonal elements and then determining the rest of the elements in an algorithmic way (for the complete procedure, see page 3 of the reference [76]).

Calculating all Hermite Normal Form (HNF) matrices defines all the derivative lattices that can be created using a parent lattice. However, not all of these lattices are unique. Following the first step, the lattice symmetry of the parent lattice is leveraged to remove redundant structures that are related to others already in the list by rotation, reflection, or change in basis. In order to do that for each new superlattice $B_i = AH_i$ the algorithm checks that it is not a rotated duplicate of a previous superlattice, B_j. The problem can be reduced to ensuring that the matrix $B_j^{-1}R^{-1}B_i$ contains only integer elements, where R is the rotation matrix.

Subsequently, the algorithm calculates all possible element decorations for each distinct superlattice. For a superlattice of size n corresponding to a specific HNF, there are n sites available for decoration. If there are k different elements to choose from, the

total number of possible decorations is k^n. However, there may still be redundancy in the decorated structures, so further steps are taken to eliminate duplicate structures from the list.

In order to remove the redundancy of the created decorations, arguments based on group theory are utilised, rather than comparing the structures geometrically as was done in other algorithms [84]. This helps to maintain the linear scaling of the algorithm, making it suitable for high-throughput applications. In the first step of the algorithm, the elimination of the translation duplicates takes place.

Let us assume a system of four sites $n = 4$ that we want to decorate with 2 elements (e.g. Ag and Au). Then, the Cayley table is calculated for the $Z_4 = (0, 1, 2, 3)$, this corresponds to the sum modulo 4. The matrix is presented in Table 2.1.

X	0	1	2	3
0	0	1	2	3
1	1	2	3	0
2	2	3	0	1
3	3	0	1	2

Table 2.1: Cayley table of Z_4.

This provides all the different unique permutations, namely $(0, 1, 2, 3)$, $(1, 2, 3, 0)$, $(2, 3, 0, 1)$, $(3, 0, 1, 2)$ corresponding to the rows of the table. All the different $4^2 = 16$ decorations can be calculated, Table 2.2.

AgAgAgAg	AgAgAgAu	AgAgAuAg	AgAgAuAu
AgAuAgAg	AgAuAgAu	AgAuAuAg	AgAuAuAu
AuAgAgAg	AuAgAgAu	AuAgAuAg	AuAgAuAu
AuAuAgAg	AuAuAgAu	AuAuAuAg	AuAuAuAu

Table 2.2: Hash table of the complete decoration of a lattice with four sites. Incomplete decorations are enclosed withing black rectangles.

It can be observed that the decorations inside the rectangle are incomplete as they consist of only one element. However, redundancy exists for the rest of the decorations. In order to identify redundant structures, the Cayley table can be used. For example, we know that the unique decorations are $(0, 1, 2, 3), (1, 2, 3, 0), (2, 3, 0, 1), (3, 0, 1, 2)$.

Starting from the string in the second column, AgAgAgAu, we can create pairs like (0,Ag), (1,Ag), (2,Ag), and (3,Au). By comparing these pairs with the list of decorations, we can identify the redundant ones, namely AgAgAuAg, AgAuAgAg, and AuAgAgAg, as shown in Table 2.3.

AgAgAgAg	AgAgAgAu	AgAgAuAg	AgAgAuAu
AgAuAgAg	AgAuAgAu	AgAuAuAg	AgAuAuAu
AuAgAgAg	AuAgAgAu	AuAgAuAg	AuAgAuAu
AuAuAgAg	AuAuAgAu	AuAuAuAg	AuAuAuAu

Table 2.3: Hash table of a lattice decoration with four sites. Incomplete decorations are depicted in red, and the starting decoration is shown in blue. Redundant decorations are enclosed within black rectangles.

Finishing this procedure, the superstructures of AgAgAgAu, AgAgAuAu, AgAuAgAu, and AuAuAuAg remain. In the next step, the decorations that are equivalent under the exchange of labels are removed. This is done because the composition can be recovered by making all possible label exchanges. For example, here the superstructure corresponding to AgAgAgAu and AuAuAuAg is the same, so one of them can be removed. Next, the structures that correspond to non-primitive structures are removed. This results from the fact that structures of smaller sizes have already been enumerated.

In the last step, the structures that correspond to label-rotation duplicates are removed. The label-rotation duplicates are identified using the properties of the quotient group and the Smith Normal Form (SNF) transformation. The row and column operations required to transform the HNF matrix of a superlattice into its SNF can be represented by two integer transform matrices, L and R, so that $LHR = S$, where S is the SNF matrix. The present algorithm was implemented with the use of the left transformation matrix L. The n members of the quotient group are represented with three components and together form the $3 \times n$ matrix G. These are transformed under a rotation to give new labelings G' as,

$$G' = LA^{-1}R(LA^{-1})^{-1}G. \tag{2.49}$$

As these checks are performed within the quotient group, duplicate labelings are

eliminated in a time proportional to the number of labelings in the list.

The main details of the method are explained in reference [76]. However, this methodology was initially constrained to Bravais lattices. In a second paper [77], the algorithm was extended to nonprimitive parent lattices, providing the freedom to create derivative structures using any parent structure. In a third paper [78], the creation of derivative structures for cases with fixed concentrations was discussed. This extension to the algorithm allows us to increase the number of atoms used for decoration in a given structure.

2.4 Thermodynamic Stability

A crucial component of an inverse design workflow is a methodology to assess the potential for the laboratory synthesis of a predicted material. The main objective of this thesis is to implement a workflow with the necessary throughput to explore the vast materials space. In computational materials science, one arbitrarily can study any imaginary material as long as it obeys some general physical laws (e.g. no overlapping of atoms, etc.) and come up with a variety of materials that hold several interesting properties. However, only a small fraction of the predicted compounds can be experimentally synthesized. Each unsuccessful attempt to do so results in a waste of resources. In order to accurately assess the likelihood of successful synthesizing of a predicted material, we utilized materials thermodynamics.

Let us consider a crystalline solid material denoted as A_xB_y. This compound is characterized by two key parameters: its composition, which determines the proportions of its constituent elements, A and B, as well as their types; and the crystal structure, which describes how these elements arrange themselves in space. To be considered stable under a predefined set of conditions, the energy of this material cannot be reduced by rearranging the atomic positions.

The decrease in energy can occur with two distinct mechanisms in which phase separation or phase transition must take place. Phase separation is observed when the material undergoes decomposition, resulting in the formation of a mixture with

the same average composition. Phase transition occurs when there is an alternative crystal structure that reduces its energy in a fixed composition. For a material to be thermodynamically stable, all possible phase separation and phase-transition reactions must be thermodynamically unfavorable. The Gibbs free energy [85] of the binary A_xB_y, is defined as follows,

$$G(T, p, x, y) = H - TS, \tag{2.50}$$

where x and y are the atomic concentrations. The same process can be easily generalized to higher-order materials. In Eq. 2.50, T is the temperature and p is the pressure. One can observe an entropy term S and an enthalpy term H. Due to the constraints of our high-throughput workflow, we limit our calculations to the determination of zero-temperature ground-state energies using density functional theory. We can determine the enthalpy of formation as follows,

$$H = H_{A_xB_y} - (xH_A + yH_B), \tag{2.51}$$

where $H_{A_xB_y}$, H_A and H_B are the calculated enthalpies of formation for the binary and the corresponding unaries. In other words, a material is considered stable relative to its components, when the decomposition of the material requires overcoming an energy barrier, as shown by the following equation,

$$\mathrm{A}_x\mathrm{B}_y \longrightarrow x\mathrm{A} + y\mathrm{B} + \Delta G > 0. \tag{2.52}$$

For the decomposition of the binary material into its components, an amount of energy should be added to the system. By neglecting the entropy contribution to the Gibbs free energy, this energy is equal to the enthalpy of formation. The thermodynamically stable phases correspond to the outermost points on the plot of the enthalpy of formation as a function of composition for the binary and ternary systems. This is mathematically expressed by calculating the convex hull of the system. Schematically, is presented in Figure 2.5. For these plots we are going to use the Cu-

Ag-Au ternary system, which is one of the materials systems employed as a test bed for the algorithms discussed in this thesis:

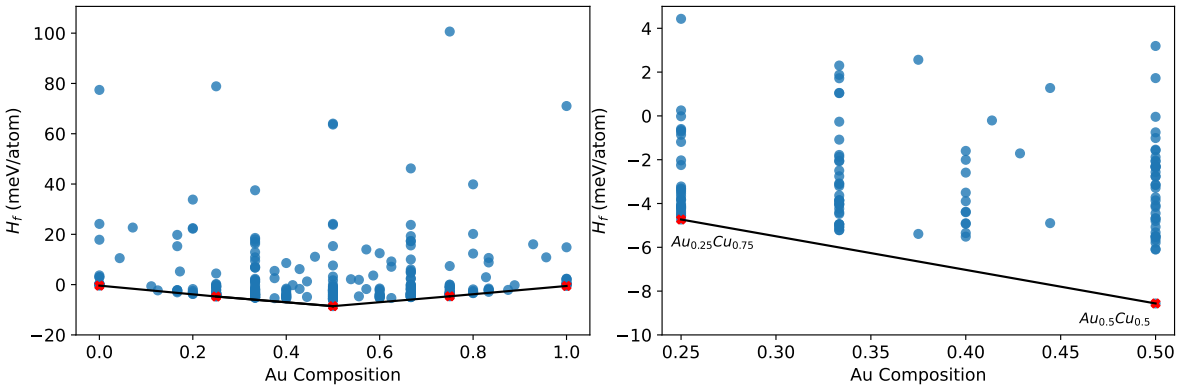

(a) Phase Diagram for AuCu (b) Zoomed version

Figure 2.5: Phase diagram of the AuCu binary system. On the left panel, the complete phase diagram is presented. The stable structures (convex hull structures) are marked with red "x", the calculated convex hull with the black line, and the calculated structures with blue circles. In the right panel, a zoomed version of the same phase diagram is presented.

The convex hull analysis visually demonstrates the stability against phase separation for all ground-state polymorphs within the relevant chemical space of interest. It assesses whether a given material can lower its energy by decomposing into a linear combination of materials with the same average composition. However, constructing a phase diagram is not a trivial task.

In order to create an accurate phase diagram a large number of ab-initio calculations have to be performed. For instance, for the phase diagrams presented in Figure 2.5 around 300 DFT calculations were performed. To construct the convex hull, which is the mathematical object created by connecting the outermost structures with straight lines as seen in the right panel of the Figure 2.5, Quick-Hull [86] algorithm was employed.

In this case, five thermodynamically stable structures are identified, and denoted with red "x". The distance of a given structure from the convex hull is considered a metric of its stability. Should a material below the calculated convex hull be found, the convex hull landscape changes, and the stability of the remaining compounds is reassessed. However, if a material is discovered above the convex hull, its distance from

the convex hull serves as a metric of stability. Neglecting the entropy contribution means that there is always the chance that an entropic contribution could potentially stabilize the studied material. This introduces an energy cut-off in which the predicted materials might be synthesized. In this work [87], the ideal entropic contribution to the Gibbs free energy is assessed for systems with different numbers of distinct elements, showing that as the number of elements increases the entropy contribution dominates the Gibbs free energy, making the convex hull analysis unsuitable for stability analysis. Nevertheless there are studies [88, 89] that assume this cut-off to be as high as 100 meV/atom. In this work, stable structures are identified as those calculated to be on the convex hull.

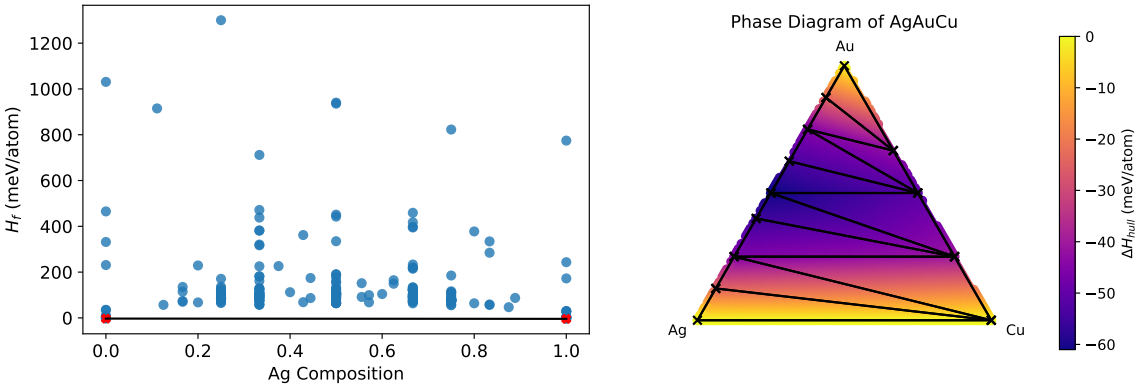

(a) Phase Diagram for AgCu (b) Ternary Phase Diagram AgAuCu

Figure 2.6: In the left panel the phase diagram of the AgCu is presented. The stable structures are denoted with red "x", and the convex hull with the black line. In the right panel, the Cu-Ag-Au ternary phase diagram is shown, and the enthalpy of formation of the convex hull at this point is presented as color-coded. The black lines define the corresponding convex hull planes.

As an example, the convex hull for the AgCu binary system is presented in Figure 2.6, when no stable structures are identified. The experimentally observed [90] miscibility gap between these two elements is recovered. The same analysis can be extended for systems containing more elements. On the right hand side of Fig. 2.6 the ternary phase diagram of the Cu-Ag-Au system is presented. In the same manner, the 3-dimensional convex hull is created.

As the number of elements increases, the compositional entropy contribution to the Gibbs free energy also increases, making the approximations employed so far

unreliable. However, for ternary systems, as demonstrated by Toher et al. [87], enthalpy continues to play a significant role in determining the Gibbs free energy, making the existing approximations a reliable stability criterion. Moreover, from a combinatorial perspective, numerous unexplored ternary systems remain within the space of transition metal elements, a fact that holds potential for exciting physics. With 38 transition metals, there are $C_3^{38} = 8436$ possible ternary systems. In essence, there is still "plenty of room" (to paraphrase the famous quote by R.P. Feynman [91]) within the space of ternary compounds to uncover exciting new physics.

2.5 AFLOW and AFLOWLIB

Recent advances in software and hardware have drawn attention to the high-throughput way of exploration. Such types of workflow take advantage of massively parallelized systems to explore vast materials spaces by performing thousands of calculations simultaneously. This kind of calculations aims to remove the human factor as much as possible. After the study of interest is initialized, then suitable software is handling most of the simulations. Human involvement occurs at a later time, when insights need to be drawn out of these studies. Then the amount of data created has to be stored for further analysis in the future.

Various different software are used in such types of studies, Automated Interactive Infrastructure and DAtabase [92] (Aiida), Python Materials Genomics [93] (pymatgen) and the Automatic FLOW [74] (AFLOW) just to name a few. The calculated properties are stored in databases and can be accessed with the use of appropriate application program interfaces (API). Such types of databases are AFLOWlib [75], materials project [94] and the Open Quantum Materials Database [95] (OQMD) to highlight a few.

In the present work, many of these tools will be employed, meaning that a brief introduction to them is necessary. We have mostly used AFLOWlib and the tools that come with the AFLOWsoftware. The main reason is the vast amount of data stored in that database, mainly about ternary phase diagrams, with more than 3 million

calculated enthalpies of formation by the time this thesis was completed.

2.5.1 RESTful API and AFLOW-CHULL

Being able to communicate with such types of database is crucial for high-throughput studies. In order to access the data stored in AFLOWlib, the RESTful API will be employed throughout this work. This offers an accessible way to communicate with the database in a query-based approach. The API is organized in a project-oriented way, with respect to the type of the compound (e.g. unary, binary, ternary etc.). For example, if someone wants to access the calculated enthalpy of formation of a corresponding entry, characterized by its label (i.e. 278), of a binary phase (i.e. AgAu), one has to write a query with the following format,

```
http://{Database name}/{stored project}/{AgAu}/{278}/ ?enthalpy_cell
```

Different keywords (e.g. the last part of the query) can be used to access a variety of properties such as the magnetic moment, the distance from the convex hull, and the band gap value, just to mention a few. Keywords that give information about the parameters of the calculation performed are also available, making it easier for someone to reproduce the corresponding calculations.

Another important aspect that AFLOW offers is the convex hull creation tool, AFLOW-CHULL [96]. This algorithm retrieves the data stored in the database, it can create the convex hull and it can calculate the distance from it for the structures available into the database.

However, it is important to note that AFLOWCHULL cannot be used to assess the distance of a newly calculated structure, as the convex hull is only calculated for structures already stored in the AFLOWlib database. Nevertheless, it remains a valuable tool that offers a starting point for understanding the shape and depth of the convex hull for a given ternary system. Furthermore, it is important to highlight that AFLOWlib offers one of the most comprehensive ternary phase diagram databases. It includes phase diagrams for 30,307 ternary systems, with an average assessment of

approximately 90 candidates for each ternary system across 10 different stoichiometries. This combination of features makes AFLOWlib an ideal benchmark for our ternary phase diagram prediction workflow.

2.5.2 AFLOW standards

To ensure the quality of the calculations submitted in the AFLOW repository, specific convergence criteria must be followed. These criteria are described by Calderon et al. [97] and are called the AFLOW standards. In this subsection, we will quickly present the criteria used in the calculations stored in the AFLOWLIB database. The k-mesh is constructed using the Monkhorst-Pack scheme [98]. For the hexagonal (hP) and rhombohedral (hR) Bravais lattices, it ensures that the mesh is Γ-centered to preserve the hexagonal symmetry. The number of sampling points, N_i, is proportional to the norm of each corresponding reciprocal Bravais lattice vector, $\vec{b_i}$, and are minimized ensuring the following condition,

$$N_{\mathrm{KPPRA}} \leq \min \left[\prod_{i=1}^{3} N_i \right] \times N, \tag{2.53}$$

where N_{KPPRA} is the number of k-points per reciprocal atom and N the number of atoms in the cell. In particular, N_{KPPRA} is chosen at 10,000 for all static calculations and at 6,000 for all geometry relaxations. For bandstructure calculations the number is increased to 15,000 in order to ensure a well-converged charge density. For the energy cut-off, a kinetic energy of 1.4 times the one provided by the VASP pseudopotentials is generally used, whereas in our case we used a flat energy of 600 eV, which is always greater than the standard used and ensures optimisation of 10^{-3} eV. Geometry relaxations are considered to be convergent when the atomic forces are smaller than 10^{-3} eV/Å.

The structure optimisation calculations are performed in two steps. First, an optimisation with a KPPRA of 6,000 points is performed, followed by a self-consistent static calculation to determine the ground-state energy. For bandstructure calculations,

an SCF calculation is first performed in order to produce a well-converged electron density; then a non-SCF calculation is performed taking into account a high-symmetry KPOINT path as specified by Setyawan et al. [99]. For the calculations throughout this thesis, we went a step further and enforced tighter convergence criteria in most of the cases, which we will review in greater detail in the following chapters.

2.5.3 Thesis overview

Having introduced the computational tools employed, we now move onto the central part of this dissertation, where the main results will be presented. The results are presented in three chapters, corresponding to the three projects that I have worked on during the past few years.

In the third chapter, a machine learning interatomic potential will be constructed as a surrogate to DFT. There, we benchmark whether a specific training procedure can be utilized to train models that extrapolate into unseen data, using training sets made specific from structures that are byproducts of previous phase diagram constructions.

In the fourth chapter, a material discovery workflow will be implemented, benchmarked, and employed to search for stable intermetallic ternary structures. By exploiting insights from the first project, this method can find novel ternary compounds by leveraging the byproducts of the binary phase diagram construction. This model is then used to study the ternary phase diagrams for a variety of systems and is compared with state-of-the-art methods.

In the fifth chapter, the previously implemented workflow will be used to predict novel ternary intermetallics for systems that contain magnetic elements. This methodology is compared to known phase diagrams and the strengths and drawbacks are discussed.

The sixth chapter of this work focuses mostly on the family of Heusler alloys. Here, we use high-throughput density functional theory calculations to investigate tetragonal distortions and antiferromagnetic ordering and assess their stability in the search for novel antiferromagnetic or tetragonally distorted materials.

Chapter 3

ML Surrogate Model for Accelerating the Search of Stable Ternary Alloys

This work is published at [100]. The research was conducted as a collaboration between the author of this thesis and H. Rossignol. All parts of the above paper are equally contributed by the first two authors.

3.1 Introduction

Discovering stable alloy phases is a complex and computationally intensive task, involving numerous ab-initio calculations to evaluate the ground-state energies of a plethora of stoichiometries and crystal structure decorations. In fact, for a given system, one must study structures varying both in stoichiometries and crystal structures. Creating a plot of the enthalpy of formation as a function of the stoichiometry provides a criterion for determining whether an alloy is metastable or thermodynamically stable. This tool is called a phase diagram. Generating an accurate ternary phase diagram for a given system often requires more than a thousand calculations. This comes from the fact that the corresponding binary phase diagrams need to be studied before attempting to proceed to the ternary one.

Calculating an accurate phase diagram, even when knowing the crystal structures for the studied stoichiometries, remains an intimidating task. However, most of the time, this knowledge is unavailable, necessitating the sampling of a plethora of crystal structures using computationally demanding ab-initio calculations (relaxations and SCF) for each given stoichiometry. This leads to a pool of potential candidates in the equilibrium state. Out of these materials, the one exhibiting the lowest ground-state energy is selected as a single stable point in the phase diagram. By calculating the convex hull, the straight line that envelopes all the points demonstrating the lowest ground-state energy, as displayed in Figure 3.1 one can obtain information regarding the stable and metastable structures present in the system of interest.

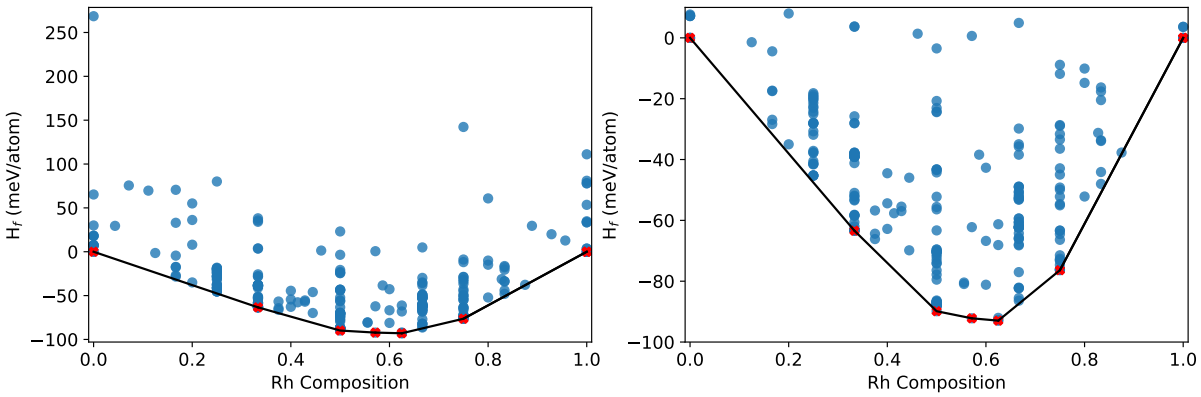

Figure 3.1: The convex hull diagrams of the HfRh binary phase diagram is presented. In the left panel the complete graph is shown whereas in the right panel a zoomed version of the convex hull for $H_f < 0$ meV/atom. The stable phases are denoted with red crosses and the convex hull bounds with black solid lines. Then, rest calculations are depicted with blue circles. Seven stable intermetallics are found in that phase diagram.

For the phase diagram presented in Figure 3.1, 267 SCF calculations are needed, as well as structural relaxations for unit cells that went up to 30 atoms. As we can see, the vast majority of the phases lie above the convex hull. To determine the crystal structures of the required stoichiometries, the go-to method for calculating the ground-state energy is density functional theory (DFT). However, density functional theory can quickly become expensive as the number of atoms increases, and the level of accuracy it provides is not always necessary when the goal is to screen a large materials space.

Advances in machine-learning tools and the combination of them with materials

science make it possible to train machine-learning force fields, which provide accuracy compared to ab-initio simulations. Once trained, these force fields offer a much quicker alternative to ab-initio simulations. In many cases, these force fields are trained on curated datasets, aiming to sample the materials space as extensively as possible. This process often becomes time-consuming, and the time taken to create the database is comparable to performing the calculations firsthand.

In this study, we explore the possibility of integrating machine-learning models into the construction of ternary convex hull diagram workflows, using a highly restricted dataset consisting only of by-products of the binary phase construction. Specifically, we train a set of spectral neighbour analysis potentials (SNAPs) over readily available binary phases and establish whether this is sufficient to predict the energies of novel ternaries.

The studied approach does not require any new calculations specific for the construction of the model, but just avails of data stored in binary-phase-diagram repositories. The goal of this work is to assess whether such trained models offer the precision required to *order* the energy of a given pool of materials efficiently. If this criterion is satisfied, then perhaps such trained potentials can be employed in materials discovery workflows. By combining it with structure creation algorithms such as the AFLOW dictionary method [79–81] to generate a pool of structures, the trained force-field would serve as a preliminary screening tool.

In this work, we use the Spectral Neighbour Atomic Potential (SNAP) to describe the local chemical environment (feature vector) as discussed in Section 2.2.5. By using the assumption that the energy of our system can be decomposed in the sum of the atomic energies, E_i, corresponding to the elements, Z_i and provided that we have a data set that contains the atomic coordinates and the total energies, E_{tot}^{DFT}, we use ridge regression to train our SNAP models as defined in Equation (3.1).

$$\min \left[\left| E_{\text{tot}}^{DFT} - E^{SNAP}(B_i, \boldsymbol{\alpha}) \right|^2 + \lambda |\boldsymbol{\alpha}|^2 \right] \tag{3.1}$$

where $E^{SNAP}(B_i, \boldsymbol{\alpha})$, is the energy of the fitted SNAP model compared to the DFT-

calculated value, E_{tot}^{DFT}. The constant λ is used as a hyperparameter during the training process in order to minimise the error on the validation set while the training set is used for the fitting.

The Vienna Ab-initio Software Package [28] (VASP) was used to perform the DFT total energy calculations presented in this chapter, namely to create the dataset of the model. VASP makes use of periodic boundary conditions, a plane wave basis set, and the Projected-Augmented-Wave (PAW) method with pseudopotentials. All calculations are performed with a plane wave cutoff of 600 eV and an energy convergence criterion of 10^{-4} eV. The standard generalised gradient approximation as parameterised by Perdew, Burke, and Ernzerhof [27] is used throughout, together with the corresponding VASP pseudopotential library. The convergence criteria set by the AFLOW standard [97] are employed throughout this chapter. Regarding the k-mesh, it is constructed using the Monkhorst-Pack scheme and ensuring that the mesh is Gamma-centered for the hexagonal (hP) and rhombohedral (hR) Bravais lattices. The number of sampling points, N_i, is proportional to the norm of each corresponding reciprocal Bravais lattice vector, $\vec{b_i}$, and are minimised ensuring the following condition.

$$N_{\text{KPPRA}} \leq \min \left[\prod_{i=1}^{3} N_i \right] \times N. \tag{3.2}$$

Here, N_{KPPRA} is the number of k-points per reciprocal atom and N the numb er of atoms in the cell. In particular, N_{KPPRA} is chosen to be 10,000 for all static calculations, which results in a finely sampled k-space and at 6,000 for all geometry relaxations. The structural relaxations are considered to converge when the atomic forces are less than 10^{-3} eV/Å.

The calculation of the bispectrum coefficients necessary for SNAP, is performed with the LAMMPS software [101], while the energy fitting is performed with an internal Python library that makes use of the SCIKIT-LEARN package [102]. The hyperparameters of the model are $J_{\max}$, R_c and the set of elemental weights, $w_{i'}$, are optimised with the Tree-Parzen estimator (TPE) algorithm [103–105], which is a Bayesian Optimisation algorithm, as implemented in OPTUNA [106].

3.2 Results

The goal of this work is to assess whether a SNAP model trained on data extracted from the binary-phase construction can be used in a material-discovery workflow. This means that such a trained model should have an extrapolatory ability accurate enough to screen structures and order them energetically. As a first step, it is sensible to start with the easiest of the cases; for this reason, the Cu-Ag-Au ternary system was considered. The Cu-Ag-Au system has been extensively studied both experimentally [107] and theoretically [108], and it provides a simple first benchmark for our methodology because it does not present complex chemical environments (noble metals). This arises from the fact that the chosen elements are metals which belong to the same column in the periodic table. They share a filled d-band and crystallize in the same crystal structure (face-centered cubic).

An ensemble of SNAP models are trained individually over each of the three binary systems, namely Ag-Au, Cu-Ag, and Cu-Au, for which AFLOWlib contains 261, 190 and 260 structures, respectively. The associated unary systems are included as well.

In order to ensure consistency, eliminating all the errors that unconverged calculations would introduce into our models and make sure that we have a robust database, we preferred to rerun static DFT calculations according to the standards presented in Section 2.5.2, for all unary and binary structures. However, it was later proved that using the AFLOWlib energies directly provides us with the necessary accuracy for the use these models are intended.

3.2.1 Learning Curve

In order to determine the amount of data to be used as a training set during the training process, one has to plot the learning curve. The learning curve graphically depicts how a model becomes more proficient in a certain task as a function of the amount of data that is trained on. For this task, we trained one model for each of the binary phases by splitting the data into a training and a cross-validation set over a range of different proportions as shown in Fig. 3.2.

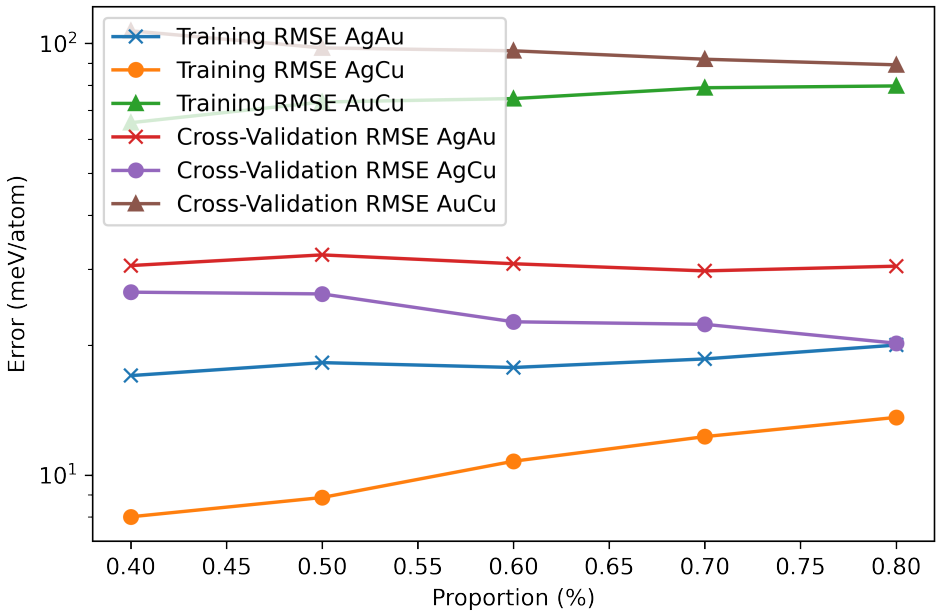

Figure 3.2: Learning curve of the models trained on the data from each binary phase diagram, namely Ag-Au, Cu-Au, Cu-Ag. The optimum amount of data necessary for the training set is 80% and 20% for the cross-validation.

It can be seen from Fig. 3.2 that a split of 80% for training and 20% for the cross-validation set is ideal for training the models presented. Following the process to determine the amount of data needed for the training process, we then move onto the hyperparameters optimisation for the ensemble of the models.

The data set is now divided into a training set and a cross-validation set, while the ternary phases present in AFLOWlib are used as a test set. This strategy aims to train a ternary-agnostic model and assess its ability to predict the energy of ternary structures. By doing that, we aim to quantitatively measure the extrapolation power of the trained models to predict the energy of a given ternary.

3.2.2 Hyperparameter Optimisation

The hyperparameter optimisation step is of great importance during the model training process. It is the process with which one determines the values for all the different parameters that are used in a model. Poorly optimised models often result in inadequate insights regarding the task trained to perform on. Additionally, during this stage, the behaviour of the model under different conditions can be examined. In our case, the hyperparameters that need to be optimised are $J_{\max}$, which regulates the degree of

expansion used to represent the chemical environment as stated in Equation (2.37), R_{cut}, which represents the radius cutoff defining the neighbourhood of a given atom used in the representation, and the elemental weights , w_i, used to create the representation of the neighbour density.

To perform the optimisation, we employed OPTUNA [106] and especially the Tree-structured Parzen Estimator [103–105] (TPE) algorithm. This is a Bayesian algorithm that, following a rapid screening of the defined hyperparameters space, is able to identify the areas of interest and focus in fine-tuning the parameters in this relatively small range of values. The significant advantage of this algorithm is that it spends the majority of the time in searching in the relevant optimization area. This gives us the freedom to explore wider areas compared to using a grid-based algorithm, which would spend most of the search time in non-interesting hyperparameter areas.

The parameters R_{cut} and $w_{i'}$ are optimized simultaneously. For the cutoff radius we searched an interval between 3 Å and 10 Å which corresponds to a distance greater than that of the first neighbors for the systems of interest. For the elemental weights $w_{i'}$, positive values between 0 and 5 are selected. The same ensemble strategy discussed previously was followed to reduce any bias resulting from the small number of available data points.

For each optimization step, an ensemble of 10 different SNAP models was trained, corresponding to a different random split (80% for training and 20% for the cross-validation set) of the available data. The Root Mean Squared Error (RMSE) of the ensemble defined as the average value of the RMSE on the cross-validation set for each trained model was used as the value for optimization. The hyperparameter tuning is carried out 50 times for 400 steps for each of the systems explored, and the hyperparameters that minimize the RMSE are then selected. The values corresponding to each of the models trained on binary systems are presented in Table 3.1.

Regarding J_{max} throughout the optimization of the hyperparameters, we employed J_{max} equal to 3, which corresponds to 30 (chemical neighborhood) + 1 (intercept of the fit) parameters. Following that step, we used J_{max} equal to 4, which corresponds to

Hyperparameter	Ag-Au	Cu-Ag	Cu-Au
$J_{\max}$	3	3	3
R_c	4.144006	4.358127	4.452703
w_X	0.526867	0.174029	0.193797
w_Y	0.701251	0.225576	0.341620

Table 3.1: Summary of the optimal hyperparameters for the SNAP models individually trained over the binary systems. Here w_X and w_Y refer to the weights of the X and Y species of the X-Y binary system.

a more complex feature vector of 56 descriptors. In fact, using a less complex feature vector allows one to save computational time during the optimization process, letting you explore a more complex hyperparameter space.

3.2.3 Binary Phases Trained Models

In this first step, the models presented are trained only on data extracted from a single binary phase, namely Ag-Au, Cu-Ag, and Au-Cu. This benchmarks our idea of training a machine-learning interatomic potential to predict the energy of structures that are structurally similar to those it has been trained on. The split is 80% training and 20% cross-validation. To divide the data sets, we employ the Monte Carlo cross-validation strategy, which involves generating multiple random splits of the total data.

To mitigate the bias introduced by a small subset of structures in the training set, an ensemble strategy was implemented due to the structural diversity of available data. For each model, we trained 10 different models using random splits of the training data. Then the mean average of the prediction made by each of the SNAP models of the ensemble is considered as the final output. Throughout this work, the SNAP ensemble will be called *SNAPs*. The averages of the mean absolute error (MAE) and the root mean square error (RMSE) are presented, over 10 SNAP models, for the three binary systems for the training set (T) and the cross-validation (CV) set are presented in the Table 3.2

The accuracy of the trained models is found to be on the order of ∼10 mev/atom,

Error (meV/atom)	Ag-Au	Cu-Ag	Cu-Au
MAE (T)	2.63	2.82	4.30
RMSE (T)	4.37	4.01	6.25
MAE (CV)	6.85	7.27	8.57
RMSE (CV)	13.83	15.15	15.73

Table 3.2: Summary of the average errors over 10 SNAP models for the three binary systems. T = training, CV = cross-validation

which is enough to be used as a screening tool. To visually display the results, a parity plot for one model randomly chosen from the trained ones is presented in Figure 3.3.

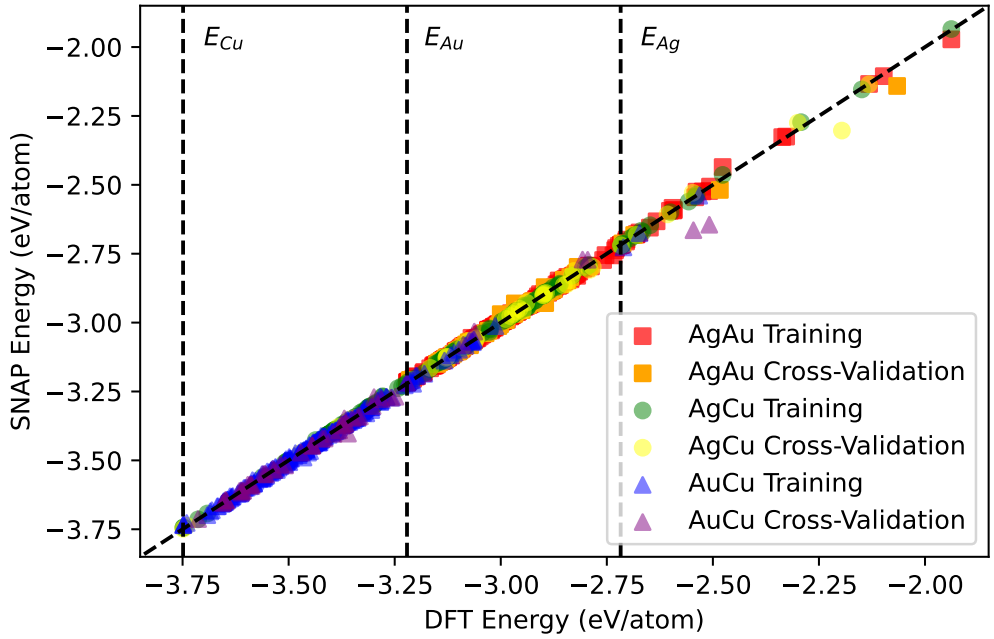

Figure 3.3: Parity plot presenting the SNAP predicted energies compared to the DFT calculated for the Ag-Au,Cu-Ag,Cu-Au binary systems. The DFT calculated energies of the elemental Cu, Ag and Au are shown with the vertical dashed lines.

It can be observed that all three binary systems are fitted to a similar standard. The cross-validation errors are of the order of 10^{-2} eV/atom. This error is due to the fact that there are high-enthalpy structures present in the database for all the systems. These data points have proved to be more challenging to fit, even when present in the training data set. This can be seen by their distance with respect to the parity line as seen in Figure 3.3. Furthermore, from Table 3.1 one can see that the optimal value for

R_c of the Ag-Au binary system is lower than that of the other two binaries. Also, it is optimal to have a larger weight for Au, while having a lower weight on Cu compared to the other two elements helps to reduce the error.

3.2.4 Testing over the ternary phases

The models trained in the previous subsection are those trained over each binary system individually. They contain information on a couple of species at a time. Hence, they cannot predict the energy of a ternary structure. The next step in this study will be to use all available data extracted from the three binary phases, namely, Ag-Au, Au-Cu, and Ag-Cu. Here, we have employed the same strategy as before, we train another ensemble of SNAPs. However, we use the entire library of unique unary and binary compounds available (677 data points). We use a 80% / 20% split between the training data set and the cross-validation data set to create these sets, we used Monte-Carlo cross-validation.

For the hyperparameters optimization, we followed the same strategy as before. We use the Tree-Parzen-Estimator algorithm, which is a Bayesian method as implemented in OPTUNA to scan the hyperparameter space. Then, we used an ensemble of models trained with a different random split of the available data. Finally, we employed the mean average of the predictions made by each SNAP model of the ensemble as the output taken by the optimization algorithm. The hyperparameter tuning is carried out 50 times for 400 steps for each of the systems explored, and the hyperparameters that minimize the RMSE are selected. The values corresponding to each of the models trained all the binary systems are presented in Table 3.3.

Following the optimization of the hyperparameters, we trained an ensemble of SNAPs. To perform the testing we used the 78 ternary structures contained in AFLOWlib for the Cu-Ag-Au ternary phase diagram, for which we first recalculated their ground-state energies with DFT. The parity plot for this model is presented in Figure 3.4. As before, the data presented belong to a SNAP prediction of a model randomly chosen from the 10 of the ensemble.

Hyperparameter	Cu-Ag-Au
$J_{\max}$	4
R_c	4.647073
w_{Ag}	0.305086
w_{Au}	0.418890
w_{Cu}	0.245647

Table 3.3: Summary of the hyperparameters used for the Cu-Ag-Au SNAP models trained over the combined binary phases.

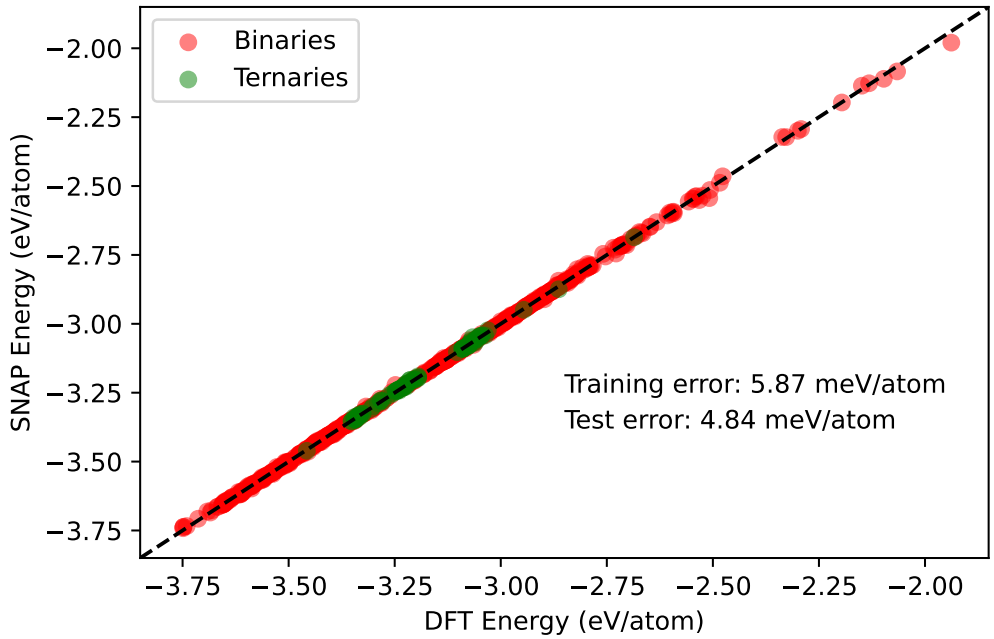

Figure 3.4: Parity plot, showing the SNAP-predicted energies against the DFT ones, for both the binary (training and cross-validation set) and ternary (test set) compounds contained in AFLOWlib for the Cu-Ag-Au system. Here the SNAP models forming the ensemble have been trained on the entire pool of binary phases. The RMSE is reported in the legend.

From Figure 3.4 we can see that our ensemble of SNAP models have the same accuracy in predicting the ground-state energy for both the binaries and the ternary phases. This strengthens our hypothesis that a machine-learning model, which has knowledge of enough binary structures is capable of accurately predicting the ground-state of the ternary structures. Note that the interactions found in the ternary structures, namely the three-body interactions of Cu-Ag-Au species, are not present in the binary

structures. However, this first result implies that, despite the lack of such interactions in the description of the local chemical environment, an accurate prediction of the total energy is still possible. This gives insight into the similarities of the chemical environments when studying such types of alloys. Furthermore, it is established that by training on data extracted from the binary phase diagrams. The SNAP models are able to predict the ground-state energy of fully relaxed ternary structures.

More quantitatively, the RMSE of the model is 5.87 meV/atom for the training set, and it actually decreases marginally to 4.84 meV/atom for the test one. Interestingly, this is even lower than the cross-validation error found for individual binary SNAPs (see Table 3.2), a result that we attribute to the more extended diversity of the chemical environments that the model now has to fit to.

3.2.5 Testing on Novel Ternaries

We have now established that an MLIAP trained on data used to create the binary phase diagrams is capable of predicting the energy of the ternary structures that are available in the AFLOWlib. To put our models against a more severe task, we are now investigating whether the models can predict the energy for structures not present in the AFLOWlib database. The dictionary method, as implemented in the AFLOW encyclopedia [79–81], was employed to create 42 structures that are not available in the database.

In order to create structures with the dictionary method, one has to decide on the structure that will be used during the decorating process. Subsequently, this unit cell undergoes a decoration with the designated chemical species. To obtain a more accurate estimate of the volume of the unit cell, the algorithm considers the volumes of the elements that are used for decoration. Consequently, an appropriate volume optimization procedure is performed to ensure that the volume per atom in the resulting structure is aligned with the weighted average of the constituents, as specified by Vegard's law [83].

Then, DFT relaxation is performed for the newly created ternaries until the forces

are below 10^{-3} eV/$\mathring{A}$. We finally assess the extrapolation ability of the SNAP models to predicting the ground-state energy of both the relaxed (R) and the initial non-relaxed (NR) ternary prototypes. The SNAP ensemble used here is the same as the one introduced in Section 3.2.4. The results are presented in Figure 3.5.

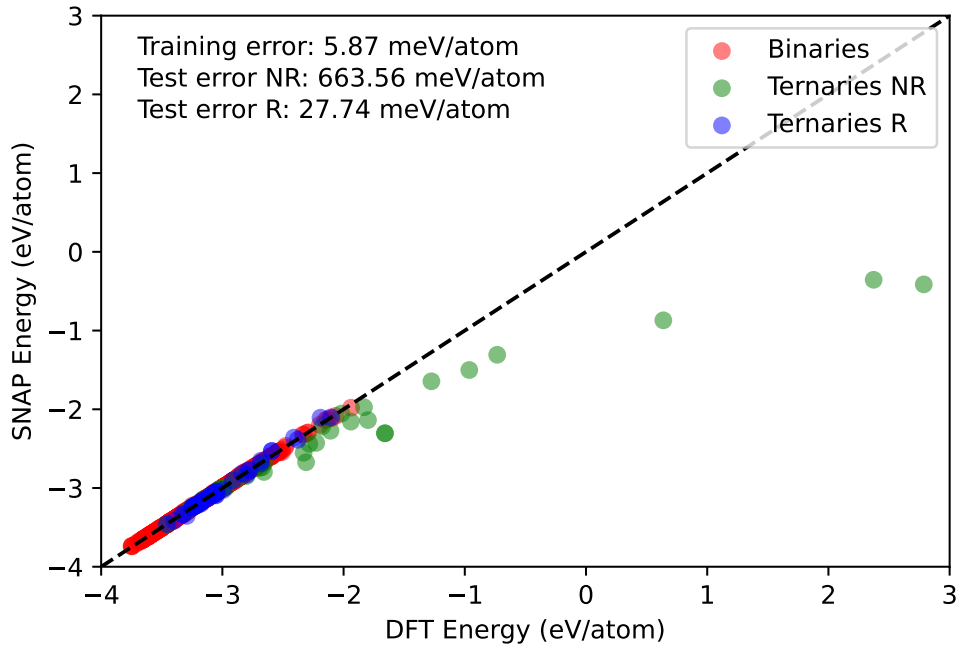

Figure 3.5: Parity plot, showing the SNAP-predicted energies against the DFT ones, for both the binary compounds contained in AFLOWlib (training set) and for a new set of ternary phases either in their prototypes, non-relaxed (NR), geometry or after full DFT relaxation (R). Here, the SNAP models forming the ensemble have been trained on the entire pool of binary phases as described in Section 3.2.4. All data are for the Cu-Ag-Au system.

We need to recall that the goal of this work is to create a force field capable of screening a large pool of structurally different ternary candidates. This does not imply high accuracy, but rather the ability of the force field to screen the low energy from the high energy structures. Furthermore, this task becomes more difficult when the database is fixed and one cannot curate it by sampling the structural space widely enough. From the figure displayed, we can observe that once the structures are fully relaxed by DFT, the error is satisfactory, which confirms that the good energy estimate for ternary compounds does not remain limited to the data available from the AFLOWlib. In this case, the RMSE grows from 4.84 meV/atom for the original ternaries included in AFLOWlib to about 27.74 meV/atom for the new relaxed prototypes,

reflecting the more diverse set of structures generated for this test.

However, when one tries to predict the energy of the prototypes as constructed by the dictionary method, the error is significantly ;arger. We now report a RMSE of 663.56 meV/atom, with SNAP systematically underestimating the DFT energy. Surprisingly, there is still a fraction of the created structures on which the SNAP model performs well; these structures appear to be structurally closer to the equilibrium ones. Furthermore, we can see that the energy per atom of these structures is in the same range as the ones sampled in the training set, giving a first hint regarding the similarity of the local chemical environments of the binary and ternary structures. It should be emphasized that SNAP can correctly identify the DFT energy trend, suggesting that such a trained model can be employed as an effective screening tool in materials discovery workflows. The keypoint of this analysis proves that an ensemble of SNAP models, trained on relevant data extracted from the binary phase diagram, can extrapolate to associated generic ternary structures when these are near or at their equilibrium geometry and can accurately estimate the energy ordering for the non-equilibrium ones, characteristics that make such-trained models valuable components in materials discovery workflow.

Generally, the dictionary method and all the materials discovery workflows start with a non-relaxed crystal structure, and they gradually optimize it to reach the relaxed candidate. Being able to relax these structures is of great importance when we want to reduce the ab-initio simulations, normally used for the relaxation, to zero. Therefore, it is important to benchmark whether such constructed SNAP models are able to drive the atomic relaxation.

For this task, we employed the LAMMPS package [101] for geometry optimization, where the energy and force convergence criteria are set at 10^{-4} eV and 10^{-3} eV/Å respectively. The relaxation then is performed in two consecutive steps; in the first step, the atomic positions are optimized; in the second step, we relax both the cell parameters and the atomic positions. This procedure is repeated five times for each structure to ensure convergence. We find that although the resulting SNAP-optimized structures generally

have a lower DFT-computed total energy than the unrelaxed ones, they are still far from the optimal DFT-computed geometries. This means that although the ensemble SNAP is capable of some relaxation, in general it is not able to find the equilibrium structure. In Figure 3.6 we provide the difference in energies of the unrelaxed and SNAP relaxed structures with respect to the energy of the fully ab-initio relaxed structure.

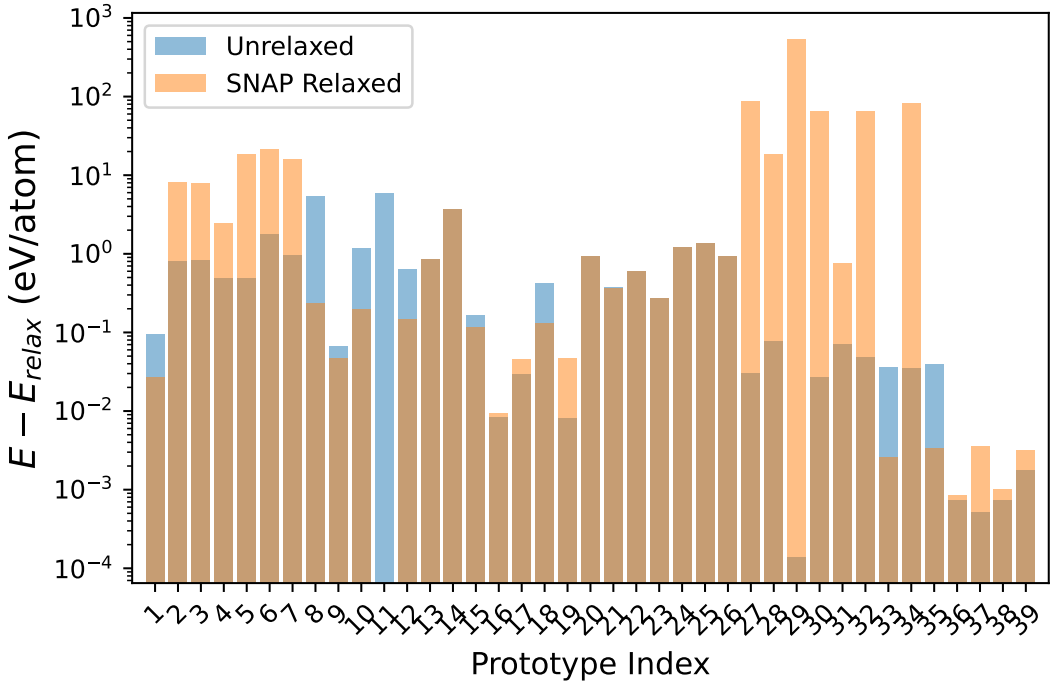

Figure 3.6: The energy difference between the SNAP relaxed (Orange) or Unrelaxed (Blue) with the DFT relaxed structure. An arbitrary label is assigned for each relaxed structure, as shown in the x-axis. For some cases SNAP-relaxed structure is lower in energy than the unrelaxed (e.g. 1,8,9), in one case, 11, is able to fully relax the structure, for the rest the SNAP relaxed structure is more distorted from the created unrelaxed.

Still, there are structures in which snap relaxation results in unrealistic geometries, such as overlapping between atoms. For these the DFT calculation was not even possible. As we observe, the energy difference in most cases remains the same or increases as a result of the poor relaxation performance. However, there is a structure for which SNAP is able to fully relax it, see label 11 in 3.6.

In order to obtain further insights regarding this result, we performed a principal component analysis (PCA) using the sklearn library. This technique projects the feature space into lower dimensions; in this case, we used two dimensions, so that one can visually perform a comparison between the training set and the test structures. We

compare the training set and the structure encountered along the DFT relaxation path of a given prototype. This analysis was performed for each of the three species, namely Cu, Ag and Au, separately. The PCA plot for the first two principal components of Ag is presented in Figure 3.7.

The graphs for Cu and Au are presented in the Appendix A. In the PCA plot the local chemical environments of Ag sampled in the training set are coloured blue. These are included in the binary phases. The coloured points are then obtained through the DFT relaxation trajectory starting from the black one. This initial configuration is found to be in a region of poorly sampled feature space and the relaxed structure ends up in a high density one (yellow). This plot visually explains the good performance of the SNAP, model when the structure is near or at equilibrium, as such structures result in a well-sampled part of the feature space. However, in order to reach this structure, the system has to move across poorly represented areas of the parameter space.

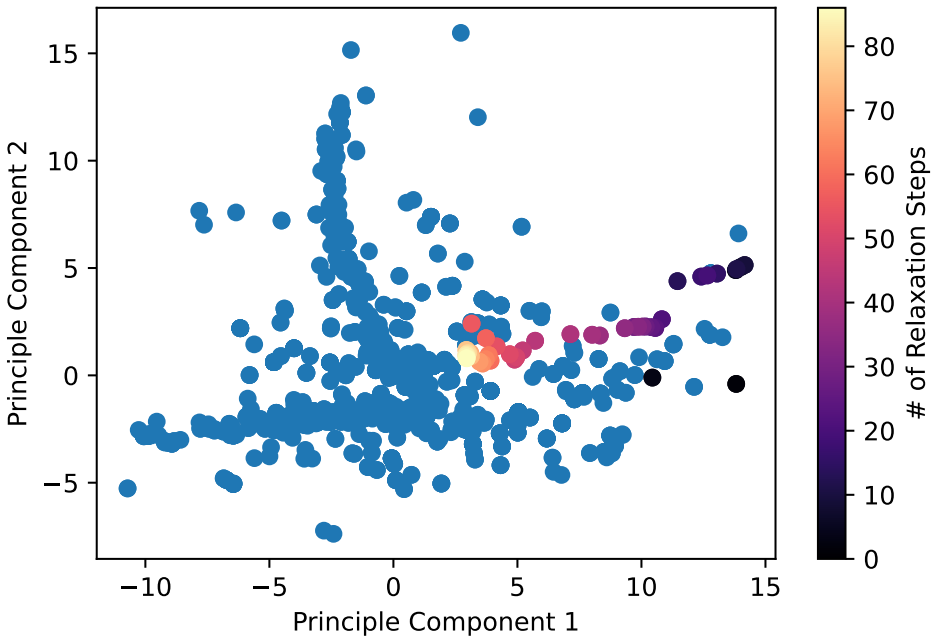

Figure 3.7: Principal Components Analysis plot for the first two components of the local chemical environments of Ag sampled in the training set (blue circles). The coloured circles denote the local chemical environments of Ag encountered through the relaxation path. Interestingly, DFT relaxation begins in a region of the feature space that is poorly covered by the training set. However, it ends up in a region of high density.

An interesting fact is that the binary feature space is inhomogeneously distributed

with many high- and low-density areas. Furthermore, there are many uncharted regions, which can lead to poor performance of the machine-learning model when predicting atomic energy for environments belonging to these spaces. Initially, it is evident that the relaxation trajectory starts from an area unknown to the SNAP model, which explains the initial poor performance. As the relaxation progresses, the structure travels over areas that were not sampled in the training set and eventually reaches a densely populated area, leading to more accurate energy predictions.

Poor energy estimation in the initial steps of the relaxation process translates into inaccurate force predictions, meaning that the SNAP relaxation process is not driven towards structural equilibrium. This explains the fact that such trained force fields are not able to perform relaxation. However, there are approaches by which one can face such a type of problem. In this context, one can attempt to curate a given training set to fill the voids in the feature space. An approach involves using a more sophisticated way of selecting the structures that create the training set, through the use of relevant metric. For example, in this Ref. [40] a Gaussian metric was used to identify unknown structures from the training set. Then, by including these structures to the training set, resulted in a robust force field capable of performing molecular dynamics and relaxation.

Another stratety is to tailor [109] a force field, especially for a specific application, by starting from a handful of initial structures. However, such types of strategy require a considerable amount of DFT calculations. This seems to fail the scope of the present work, which is to generate a force field by taking advantage of only the available data extracted as byproducts of the binary phase diagram workflows. Furthermore, by adding DFT calculations to a materials discovery workflow, results in lowering the throughput by a considerable amount, making the exploration of large materials space impossible. Moreover, in the case of a ternary phase diagram, adopting the above strategies could lead to the number of DFT calculations needed becoming comparable to the ab-initio calculations needs for the creation of the entire phase diagram.

As one can observe from Fig. 3.7 the relaxation ends up in a densely populated area

of the feature space. Perhaps selecting a better initial candidate structure could result in improved performance of the MLIAP, without requiring data curation by introducing new calculations. This approach may lead to enhanced relaxation performance without specifically altering the available database.

3.2.6 Model Benchmark: Cd-Hf-Rh and Ti-Mo-Pt

In this subsection, to expose our models to a more rigorous benchmark, we selected phase diagrams that offer a more complex landscape of chemical environments. The rationale behind the choice of elements for the ternary systems is to select early (Ti and Hf), mid- (Mo and Rh), and late (Pt and Cd) transition metals. Furthermore, the selection of these particular elements was guided by the fact that the data available from the binary phase diagrams of AFLOWlib, were deemed sufficient to train a machine-learning model.

It should be emphasised that each of the ternary phase diagrams offered more than 800 crystal binary structure-energy pairs, and they contain the same number of ternary prototypes (90 structures) that will be used as test set. However, emphasis should be given to the fact that one of the three binaries is always over-represented in these two datasets, namely Ti-Mo for Ti-Mo-Pt and Cd-Hf for Cd-Hf-Rh, in contrast to the balanced dataset of the Cu-Ag-Au phase diagram.

The selection of these phase diagrams offers a more challenging task, providing us with a larger chemical variety than that provided by the noble metal systems. In order to simulate the exact procedure of a materials discovery workflow that starts from already available data, we did not recalculate any DFT energies. This is an important difference from the approach followed before. On the one hand, the advantage of this tactic is that by reducing the DFT calculations to zero, we save valuable computational time. On the other hand, errors in convergence propagate to the MLIAPs produced. However, since the trained models are used for the screening of a large pool of candidates, high accuracy is not essential as long as it is capable of predicting the energy ordering satisfactorily.

The training process that followed is the same as before. The training and cross-validation set is constructed from the 80% and 20% of the available data (unary and binary compounds), respectively. The ternary structures are used for the test set. Then, an ensemble of SNAP models was used throughout the optimization of the hyperparameters, namely R_c, $J_{\max}$ and $w_{i'}$. The parity lines for the energy predictions of the ternary Cd-Hf-Rh and Ti-Mo-Pt systems are presented in Figure 3.8.

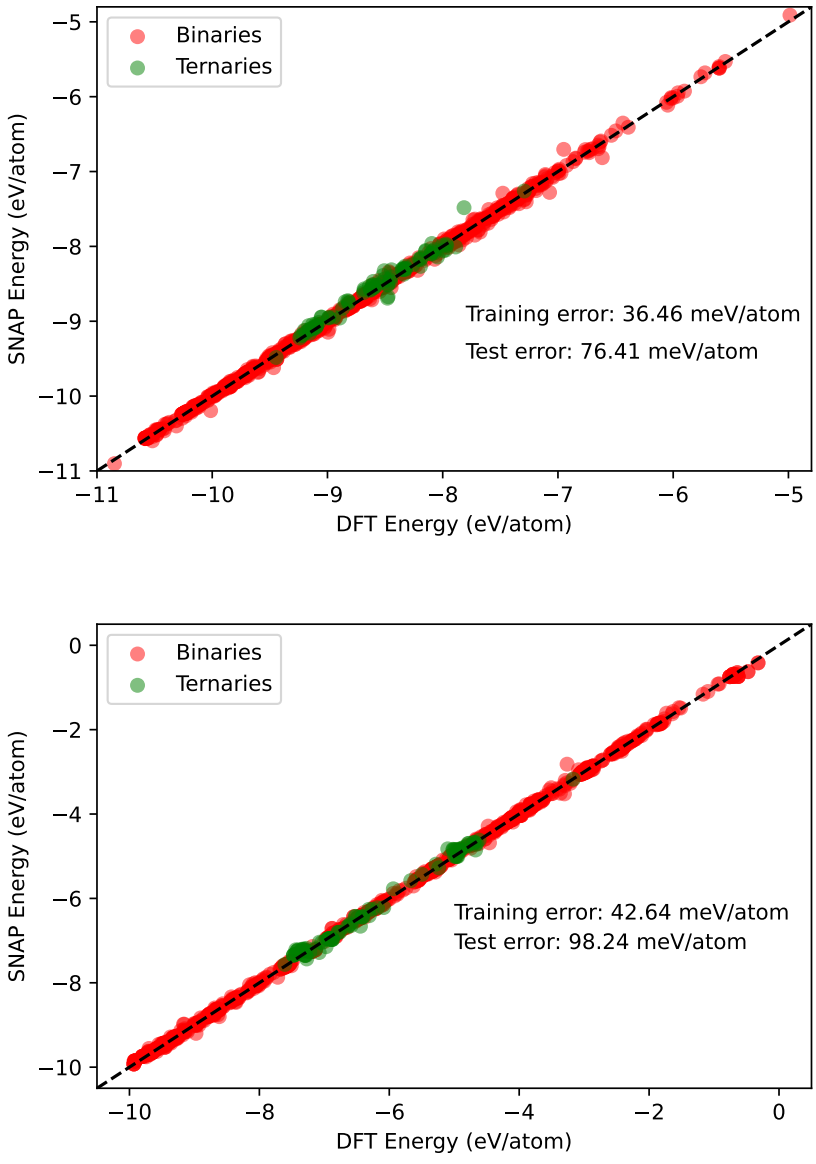

Figure 3.8: Parity plot of the comparison between SNAP-predicted and DFT calculates energies for the binary (training and cross-validation set) and ternary (test set) compounds contained in AFLOWlib. The Ti-Mo-Pt (upper graph) and Cd-Hf-Rh (lower graph). The ensemble models have been trained on the entire database of binary phases, and the legend provides the Root Mean Square Error (RMSE) for each case.

.

The main outlook from the parity plots presented in Figure 3.8 is that both systems closely follow the parity line; hence, they succeed in predicting the energy of the ternaries satisfactorily. In both cases, the values of the test errors are increased as compared to those of the noble metal system. It should be noted that in this case the energy range is much larger than that of the Cu-Ag-Au system. A better metric to compare the errors would be the percentage ratio with respect to the average energy per atom. The Cu-Ag-Au system was calculated to be 0.19% for the training set and 0.15% for the test set. These must be compared with 0.40% and 0.86% for Ti-Mo-Pt and to 0.74% and 1.57% for Cd-Hf-Rh. Such values reflect the increasingly complex chemical environments in which the SNAP models have to fit. Furthermore, errors become less significant when compared to the depth of the convex hull for these systems. For Ti-Mo-Pt for Ti-Mo-Pt and Cd-Hf-Rh the convex hull minimum is located at an enthalpy of formation of 951 meV/atom and 921 meV/atom respectively, compared to 61 meV/atom for Cu-Ag-Au.

3.3 Discussion and Conclusion

It would be beneficial to discuss how the work presented differentiates from the traditional way of building Machine Learning Interatomic Potentials, such as the approach that we have followed, the database we use, and the way we treat our data. Furthermore, it should be reminded that the aim of this potential is to be used as a screening tool in a materials discovery workflow and not to perform ab-initio accurate molecular dynamics simulations. The average error expected to be adequate to perform this task efficiently should lie around 50 meV/atom as stated in the relevant bibliography [62, 110, 111], where machine-learning screening tools were employed alongside with DFT calculations in high-throughput materials discovery workflows.

In this particular case, the greatest challenge that we are facing arises from the fact that the number of data is limited. Perhaps we would be able to create additional data; however, this approach is not suitable for this kind of use case, it only lowers the throughput of the method. The only choice with regard to the dataset available

is to remove data points that exhibit unphysical crystal structures and, as a result, a high enthalpy of formation. Furthermore, in our case we choose to use readily available data that are byproducts of the phase diagram construction process, rather than using a sophisticated process to create the used database. This research aims to investigate the quality, value and limitations of creating models using these databases, in our case AFLOWlib. Such types of databases offer structures that are relevant for the construction of the convex hull. They are made from a variety of compositions and space groups. The diversity that such databases offer is critical for the robustness in phase diagram construction workflows.

To better understand the differences between a tailor-made database and one that is already available I will present a couple of different studies of force fields trained to perform screening for a ternary phase diagram prediction workflow. The most relevant example is the work of Gubaev *et al* [64], which trains a Moment Tensor Potential (MTP) to accelerate the search for novel stable alloys for the Cu-Pd, Co-Nb-V and Al-Ni-Ti systems. The force field that they trained is capable of screening and performing relaxation. To train this model, they constructed a database using an active learning method. They created 10^4-10^5 structures from hexagonal-closed-packed (hcp), body-centered-cubic (bcc), and face-centered-cubic (fcc) supercells that are decorated with different stoichiometries. Then, the model is trained on the fly as the structures are relaxed. This resulted in a training set of 523 and 383 structures for Cu-Pd and Co-Nb-V. Interestingly, except from the numbers of the data available, a fundamental difference when comparing the two works is that the database they used to train the MTPs contains a lot of non-equilibrium structures. In our case, all included structures are at equilibrium, do not need to be generated, and are directly relevant for binary convex hull construction. Furthermore, forces and stress tensors were used for the training, in contrast to our study, since these data are not available from AFLOWlib.

Another example highlighting the differences between the work presented and the traditional way of training machine learning interatomic potentials (MLIAP) is the research conducted by Chen *et al.* [39]. This study discusses the conventional method

for deploying a SNAP model as a general force field. In their research, they trained and tested a general force field for molybdenum using a database containing approximately 10^3 training points. The diversity of the training set was high, encompassing ground-state phases from the Materials Project Database [112], surface slabs, and distorted large cells with up to 54 atoms. The variety of chemical environments sampled during the training process provided SNAP with sufficient information to act as a robust general force field capable of accurately performing Molecular Dynamics (MD) simulations over large length and timescales. Creating these curated databases is computationally intensive. It needs to be noted that only the materials project ground-state structures are readily available data and are not ideal when screening a large materials space.

In conclusion, we have benchmarked the accuracy and extrapolation ability of SNAP models, trained on readily available data extracted from binary phase diagrams, to predict the energy and estimate the thermodynamical stability of novel created ternary candidates. This analysis was presented for a noble-metal ternary system, namely, Cu-Ag-Au and a couple of mixed systems, namely, Ti-Mo-Pt and Cd-Hf-Rh, chosen to replicate the chemical variety that transition metal systems display.

We have established that SNAP models that exploit binary phase data are able to accurately predict the energy of novel ternaries, when those are close or near the equilibrium structure. However, the quality of the predictions starts to decrease as we move away from the relaxed structure as a result of the poor sampling of the chemical environments of the database used. Surprisingly, such trained models are able to predict the energy ordering of such compounds, indicating their effectiveness as screening tools in a high-throughput materials discovery workflow. Such kinds of MLIAPs can be used as a layer-1 screening solution to a phase diagram prediction algorithm that explores large materials spaces where high-throughput are more needed than high-accuracy.

Based on the results presented in this chapter, we can conclude that such trained force fields and freely available databases are useful and can be integrated in the construction of ternary-phase diagrams. This approach will improve once a more sophisticated strategy of generation of the prototypes is found.

Chapter 4

Machine-Learning-Assisted Construction of Ternary Convex Hull Diagrams

This work is published at [113]. The research was conducted as a collaboration between the author of this thesis and H. Rossignol. All parts of the above paper are equally contributed by the first two authors.

4.1 Introduction

The search for novel intermetallic ternary alloys is an intimidating task, as one has to perform a wide range of ab-initio calculations sampling various stoichiometries and exploring different crystal structures. While density functional theory (DFT) is the go-to method that provides the necessary accuracy, it is also highly expensive, especially when one wants to perform numerous calculations. As a result, using DFT in a high-throughput manner for exploring a combinatorially vast number of ternary systems becomes impractical. Therefore, it is crucial that alternatives to DFT be implemented in materials discovery workflows to make this search viable.

In this work, our aim is to tackle this problem by demonstrating how a machine learning interatomic potential (MLIAP) that is trained on data readily available and

relevant, extracted from one of the open databases, namely AFLOWlib [75], can be employed to screen a pool of ternary alloy prototypes. We have established [100] that an ensemble of SNAP [37] models trained on the crystal structure and energy pairs extracted from associated binary systems are capable of providing accurate predictions with a mean absolute error (MAE) of ~ 30 meV/atom for the energies of the corresponding ternary compounds, as long as they are close to or at equilibrium. Furthermore, such trained models are able to order energetically the candidates away from the equilibrium, a property that is much needed in materials discovery workflows.

Using an MLIAP as a DFT surrogate provides us with the required efficiency to screen large materials spaces once trained. The core of the workflow presented, lies on the fact that the chemical environments between the binary and ternary transition-metal alloys are similar [100]. In this work, the crystal structures of the binary compounds closer to the convex hull were employed for the decorating process, similar to the encyclopedia method seen in Chapter 2.3.1. This assumption is based on the idea that crystal structures close to the convex hull would potentially serve as better initial guesses for the structures chosen to be decorated, as opposed to randomly selecting them. This pool of decorated structures is then screened in a high-throughput manner using an ensemble of SNAP models. The lowest-enthalpy compounds are then chosen as the most promising candidates, and their energies are calculated using high-accuracy DFT. Subsequently, the ternary convex hull is calculated and updated.

The critical difference between the models employed in the workflow and the tailor-made MLIAPs employed for the convex hull construction is that all the data used, from the prototype generation stage to the models' training process, are readily available and extracted from the AFLOWlib database, resulting in an almost DFT-less workflow. In contrast to the strategy generally adopted of training models with databases tailor-made for a specific application [39, 64]. We have demonstrated that such trained force fields exhibit low enough error to predict the energy and accommodate a high-throughput search algorithm for novel ternaries. Through this workflow, we leverage the byproducts of the binary phase diagram construction already available in AFLOWlib

to predict the ternary convex hulls and identify stable configurations.

4.2 Ternary Phase Diagram Workflow

The main stages of the ternary convex hull prediction workflow, shown schematically in Figure 4.1, are explained here. The algorithm begins with the binary compounds from the AFLOWlib database and their associated DFT-calculated energies, the stable, metastable and unstable compounds provide the necessary structural diversity required by our approach. These databases are utilized to train an ensemble of SNAP models, as described in Chapter 3.

Following that, the convex hull of each binary phase diagram is constructed, and the distance of each structure from the convex hull is assessed. A crucial assumption is made here: the crystal structures of the binaries that are closer to the convex hull are more likely to form stable ternary intermetallics. This selection is preferred over a brute-force method that would suggest decorating all available crystal structures in the structure encyclopedia [79–81], something that would generate an enormous amount of candidate structures. The structures selected using these criteria form the *parent* prototypes.

Then, ternary candidates are generated by decorating the parent prototypes, creating all possible and unique derivative structures using the enumlib algorithm [76–78] explained in Chapter 2.3.2. These structures are subsequently relaxed using the ensemble of SNAP models. The energies and their standard deviation are predicted by the SNAP models, enabling the detection and removal of geometries for which relaxation has failed.

The structures exhibiting the lowest energy and standard deviation, indicating higher certainty in the predictions, are chosen as the most promising candidates. To ensure proper convergence, a full ab-initio relaxation is conducted, followed by a single-point self-consistent field (SCF) calculation with tighter convergence parameters. The energies of those structures are then used to update the convex hull. The ternary system Cu-Ag-Au is used to develop this methodology, serving as a first example of

the functionality of the algorithm.

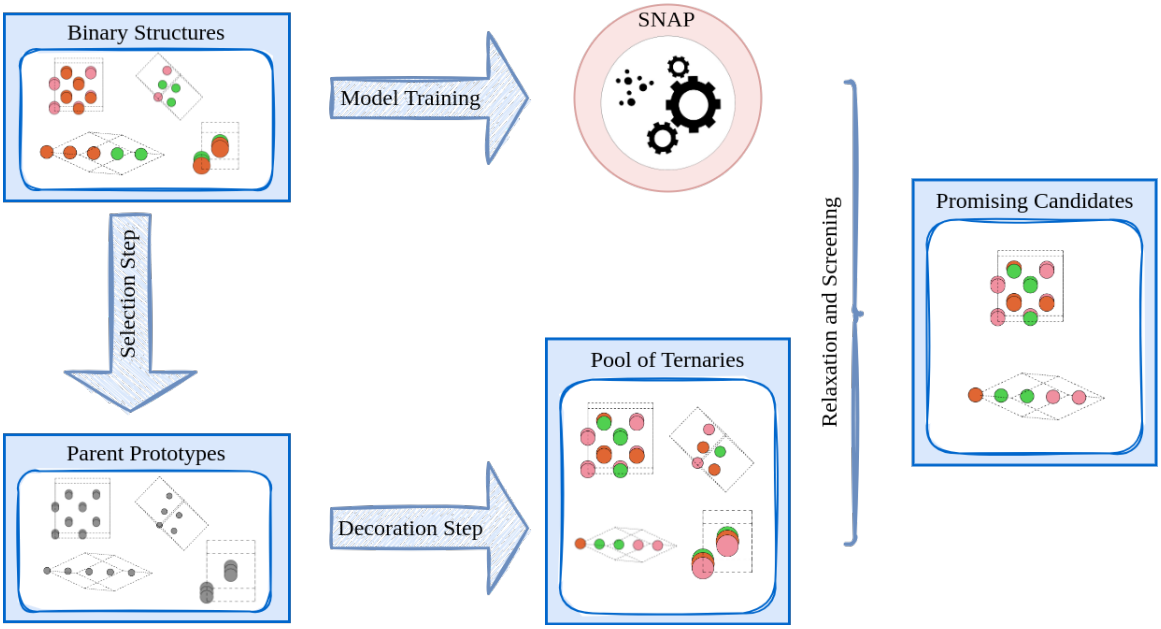

Figure 4.1: The convex hull prediction workflow implemented in this work begins with initializing the algorithm using the binary structures available (upper left corner). These structures are used for two purposes: i)Training the ensemble of SNAP models, and ii)Constructing the pool of parent prototype structures. Next, by decorating the parent structures with a specific stoichiometry all the possible derivative structures are created. Subsequently, the SNAP relaxation of these structures is performed, followed by screening of the lowest enthalpy structures. Then, a DFT relaxation and an SCF step are conducted, and finally, the phase diagram is updated.

In the following subsections, we will present the different stages of the workflow using the Cu-Ag-Au ternary phase diagram as an example. Following that, the Mo-Ta-W ternary system will be used as a benchmark against the state-of-the-art AFLOW-CHULL method of generating ternary phase diagrams.

4.2.1 The Prototype Generation stage

In the beginning of the workflow, a suitable library of binary prototype materials needed to be created. We have established in Chapter 3 that the local chemical environments of the prototypes constituting the binary convex hull are similar to the ternary ones, especially those that are near or at the equilibrium. This comes from the fact that a MLIAP trained on data extracted from the binary phase diagram is capable of accurately predicting the energy of novel ternaries, as shown in Figure 3.5. This guides the selection algorithm implemented to select the most promising candidates

for decoration.

The lowest-enthalpy criterion was implemented to select the most promising candidates for the decorating step. The rationale behind selecting this approach is based on the assumption that crystal structures of binary compounds, which are closer to their calculated convex hulls and thus more thermodynamically stable, are more likely to form stable ternary alloys when decorated. It is generally known that stable binary alloys can be made with substitutions of elements in the lattice of the elemental structures, for example, the Ag_3Au_1 is a face-centered cubic (*fcc*) variant of the parent crystal structure.

More specifically, for the Cu-Ag-Au ternary system, we scanned the binary convex hull of the binary constituents, namely Cu-Ag, Cu-Au, and Ag-Au and selected the compounds closer to the convex hull. All the data considered here are extracted from the AFLOWlib database. To avoid oversampling a specific binary phase diagram, we defined an energy window, which dictates the number of the structures sampled from each binary. This energy distance works as a hyperparameter to ensure homogeneous sampling of the binary data. The number of structures, N_{struct}, chosen from each binary phase diagram, as well as the energy window, ΔE, used, is presented in Table 4.1.

$X-Y$	N_{struct}	ΔE (meV/atom)
Ag - Au	24	1.7
Cu - Ag	25	65.4
Cu - Au	25	6.2

Table 4.1: Number of structures, N_{struct}, and the maximum distance, ΔE, from the convex hull (defined energy window) of the selected structures from each binary system. These constitute the parent structures pool.

It can be observed from Table 4.1 that in order to keep the selection of the three different binaries balanced, one has to use a higher energy window for the Cu-Ag binary phase diagram. As for the rest of the binaries, namely Ag-Au and Cu-Au a distance of the order of 10 of meV/atom is plenty for this reason. This reflects the fact that Ag and Cu are immiscible [114], meaning that no stable intermetallics are formed between these two elements. This can also been observed from the fact that all the

binaries formed with a combination of these two elements exhibit positive enthaply of formation, resulting in a distance far from the convex hull (i.e. tie line that connects the two elementary phases). The visual representation of the observations discussed above for the Cu-Au and Cu-Ag binaries is presented in Figure 4.2, the figure for the Ag-Au system is presented in the Appendix B.

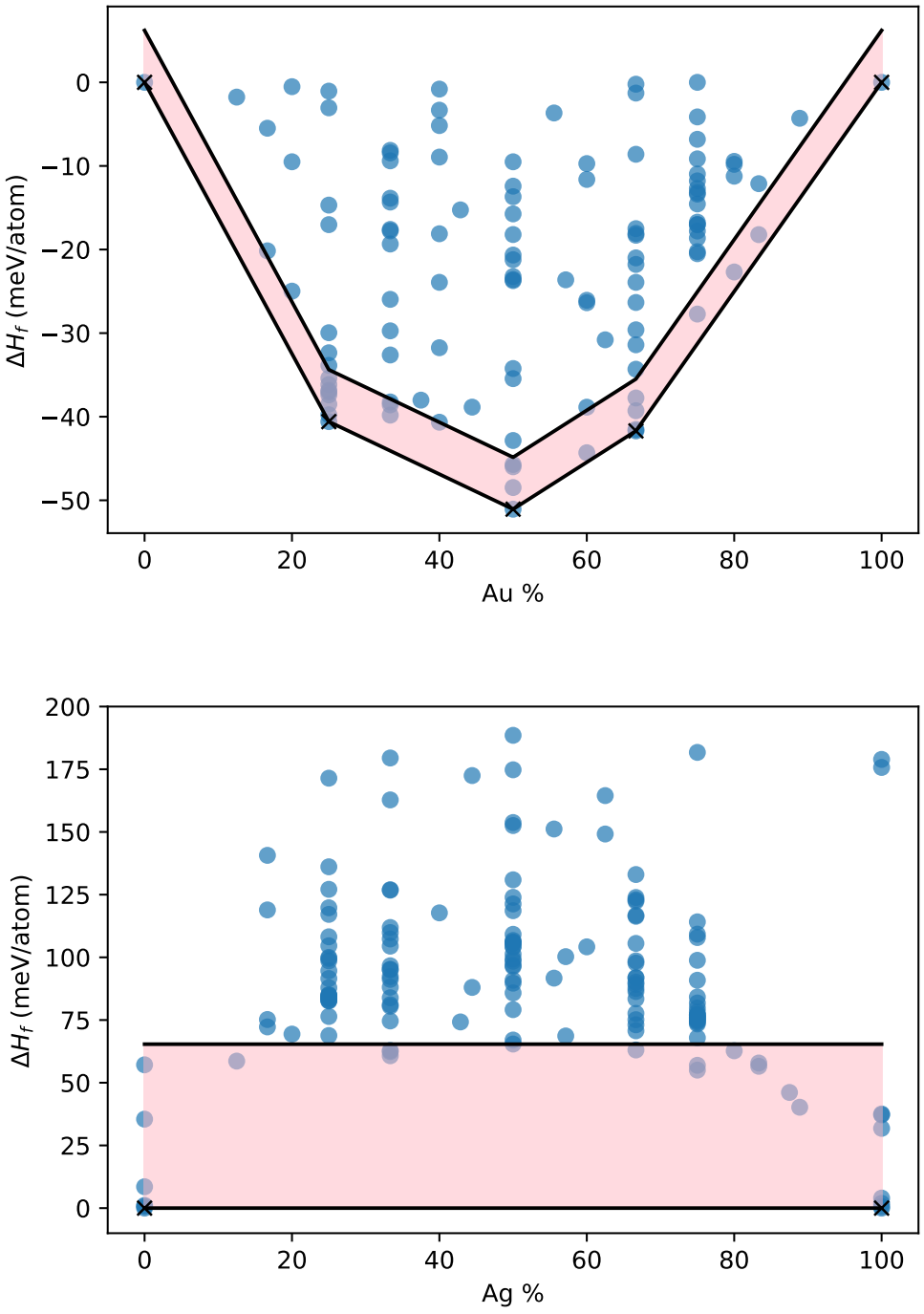

Figure 4.2: The energy window employed for the selection of the necessary number of crystal structures for the Cu-Au and Cu-Ag binaries. The structures selected as parent structures lie inside the pink area.

We observe an inverse relationship between the convex hull depth and the energy interval used for sampling. This is due to the fact that deeper convex hulls exhibit a higher number of metastable structures close to the stable ones. However, the number of candidates chosen to create the pool of parent structures is a function of the computational resources and is used as a hyperparameter of the workflow.

Following the selection of the prototypes, the structures are then stripped of their chemical identity, which is done to make the comparison between the structures more efficient. To avoid redundancy, the AFLOW symmetry tool (AFLOW-SYM) [115] is employed. AFLOW-SYM is a tool that let us identify the symmetry properties of a given material based on different representations that include the spacegroup, the point-group, the Wyckoff positions, etc. Then, by comparing them, a database of given crystal structures is grouped into sets that exhibit the same structural characteristics. This is done to ensure that the parent crystal structures are unique. Furthermore, all structures are reduced to their primitive cells at this step of the workflow. This leads to a library of unique, undecorated prototypes, extracted from the binary convex hulls. Following this analysis, for the case of Cu-Ag-Au ternary, 40 unique structures proceed to the stoichiometry decoration selected from the initial 74. A sample of the structures that were chosen to be decorated is presented in Figure 4.3.

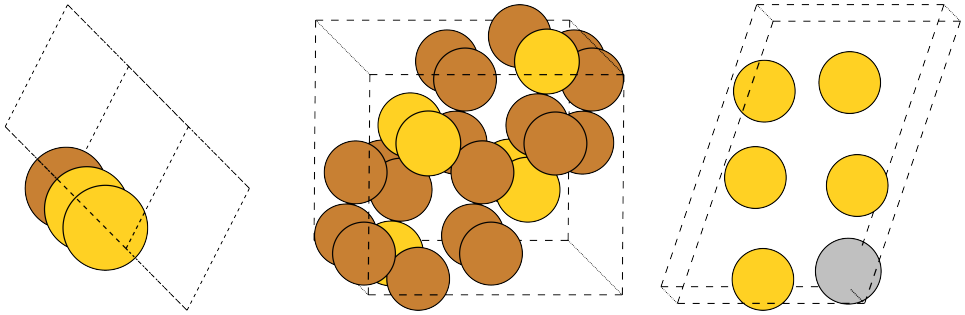

Figure 4.3: A sample of the structures chosen for decoration is presented. Here, gold color denotes the Au element, silver represents Ag, and bronze is used for Cu.

The structural diversity of the candidates used for decoration can be observed in Figure 4.3. Following that step, the library of the 40 unique structures is decorated accordingly. A fixed stoichiometry is used each time for the decoration of the parent structures; furthermore, the number of atoms for the created ternaries will be fixed

as well up to a certain number N_{max}. The prototypes with the number of atoms compatible with the fixed stoichiometry, a set of all the unique derivative structures is created by using the procedure explained in more details in the Section 2.3.2. In general, enumlib [76–78] is an algorithm that by analyzing the symmetries of a specific cell can determine all the unique atomic configurations and decorations.

This concludes the first part of the workflow and results in a set of unique ternary compounds of a specific stoichiometry, inspired by the binary structures. An MLIAP is then employed to relax and screen the created ternary compounds.

4.2.2 Ensemble of Models

The creation of possible candidates follows an energy screening with the use of SNAP. The approximation that most MLIAPs work under is that the total energy, E, of a crystal structure consisted of N number of atoms can be expressed as the sum of all contributions of atomic energy, E_i as expressed in Equation (4.1).

$$E = \sum_{i=1}^{N} E_i \, . \tag{4.1}$$

Here, a linear function is trained to create a relationship between the local chemical environment expressed by bispectrum components $\mathbf{B}_i^{\alpha_i}$ for the atom, i, of element, α_i. The summation of the SNAP-predicted atomic energies defined as defines the total energy predicted by SNAP defined as follows.

$$E_{\mathrm{SNAP}}\left(\mathbf{r}^N\right) = \sum_{i=1}^{N} \beta_0^{\alpha_i} + \beta^{\alpha_i} \cdot \mathbf{B}_i^{\alpha_i} \, , \tag{4.2}$$

where $\beta_0^{\alpha_i}$ and β^{α_i} are the species dependent linear coefficients of the machine-learning (ML) model, fitted in the training process. Further details on the potential used can be found in Section 2.2.5.

In Chapter 3 was discussed that a SNAP model taking advantage of the linear form of the function trained and the highly non-linearity of the feature vector once trained exhibits good accuracy with a small number of features, 55 bispectrum coefficients +1

intercept used here, and a small dataset, typically of $\sim 10^3$ structures.

In order to increase the robustness of our predictions, an ensemble of SNAP models trained and optimized using a different random subset of the available data is employed for the screening of the available structures. The advantages behind this strategy lie in the fact that using an ensemble of models provides you with information regarding the uncertainty of the prediction, by calculating the mean and standard deviation of the predicted values.

The ensemble is defined as a set of K different trained models, $\left\{E^k_{\mathrm{SNAP}}\right\}^K_{k=1}$, in our case $K = 5$ models were trained. Each model is trained in a different random set of data and has seen a different variety of chemical environments. Having an ensemble of SNAPs also helps address biases resulting from small training sets. The energy prediction for a given structure is given as the average of the energy predictions, μ, and the standard deviation, $\hat{\sigma}$, of the predictions is defined as follows.

$$\mu = \hat{E}\left(\mathbf{r}^N\right) = \frac{\sum_{k=1}^{K} E^k_{\mathrm{SNAP}}\left(\mathbf{r}^N\right)}{K}\,, \tag{4.3}$$

$$\hat{\sigma}\left(\mathbf{r}^N\right) = \sqrt{\frac{\sum_{k=1}^{K}\left(E^k_{\mathrm{SNAP}}\left(\mathbf{r}^N\right) - \mu\right)^2}{K}} = \sqrt{\frac{\sum_{k=1}^{K}\left(E^k_{\mathrm{SNAP}}\left(\mathbf{r}^N\right) - \hat{E}\left(\mathbf{r}^N\right)\right)^2}{K}}\,. \tag{4.4}$$

where $\mathbf{r}^N$ are the positions for a given system of N atoms, $\hat{E}$ or μ is the average value of the predictions from the ensemble of K models and the standard deviation $\hat{\sigma}$, is defined as in Equation (4.4). Following, the same model-training approach, discussed in Chapter 3, the training set is consisted of all the available binary alloys and unaries obtained from the AFLOWlib database. Their energies have been re-calculated for consistency. All the SCF single-point DFT calculations are performed with VASP [28] software and the convergence parameters are in close alignment to the AFLOW-standards [97]. The same approach was adopted during the training for the Mo-Ta-W ternary system, the key difference compared to the Cu-Ag-Au system lies in the fact that the data used for the prediction of the Mo-Ta-W phase diagram are

precalculated and stored in the AFLOWlib database. Furthermore, we demonstrate that models trained on data extracted from AFLOWlib offer enough accuracy to be used in a convex hull construction algorithm.

The ensemble of models employed in this workflow is consisted of five models trained with the complete database, each trained model utilizes a different set of elemental weights, $w_{\mathrm{Cu}}, w_{\mathrm{Ag}}, w_{\mathrm{Au}}$ for Ag, Au and Cu to calculate the bispectrum components. This difference in the training process is adapted in order to distinguish effectively compounds with identical positions in their structures (i.e. structures created from the same parent) but with different atomic site decoration.

Let us consider two different compounds that originate from different decorations of the same parent structure. If the SNAP model employs identical atomic weights to calculate the bispectrum components, it will predict equal energies for these compounds, even though they are decorated differently. This is because the local geometries that translate into the feature vector are the same, as stated in Equation (2.37).

We need to remind ourselves that candidate structures, at this stage, are created by decorating a parent structure accordingly. This is presented graphically in Figure 4.4, where two candidates were created with different decorations of the same parent structure, here the composition $\mathrm{Cu_1Ag_1Au_2}$ of a *bcc* cell. The only difference between these two structures lies in the permutation of the Ag and Cu atoms. In Table 4.2, the SNAP predictions are shown for a variety of different elemental weights.

w_{Cu},	w_{Ag},	w_{Au}	E^{Top}(eV)	E^{Bottom}(eV)
1	1	1	-25.640	-25.640
1	1	2	-25.879	-25.879
1	2	1	-25.717	-25.676
2	1	1	-26.162	-26.047
3	1	2	-25.640	-25.742

Table 4.2: Total energies predicted by a SNAP model for prototypes A (Top) and B (Bottom), different weights were employed to calculate the bispectrum components for each case. In other words, for each case, the models trained on different feature vectors taking into account different elemental weights. All values are given in meV/atom.

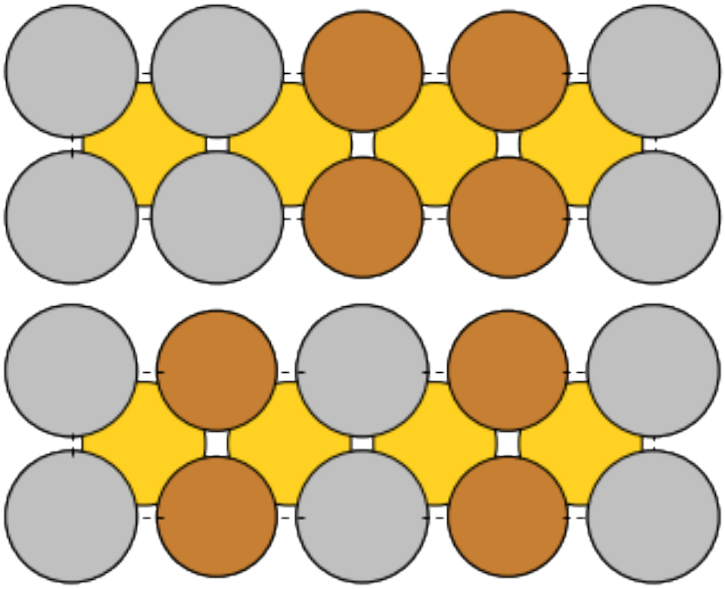

Figure 4.4: Different decorations of the same parent structure for the creation of two different compounds, here gold color corresponds to Au, silver to Ag, bronze to Cu and z-axis is with yellow. Prototype A (upper figure), Prototype B (lower figure).

From Table 4.2 we observe that when identical weights are used to calculate the bispectrum component, SNAP models trained on these data are unable to distinguish the diversity introduced by different decoration of the same parent structure. The ensemble of the trained models in this work employ different values for the elemental weights for each of the species available in the training set.

The optimization of R_{cut} and J_{max} of the MLIAPs used in this work was carried out before the choice of the values for the elemental weights. These values were optimized manually and independently using 10-fold Monte Carlo cross-validation, the elemental weights in that step were assumed as $1-1-1$ for Cu-Ag-Au correspondingly. The optimized values used are : R_{cut}=3.5 Å and J_{max}=4. To optimize the atomic weights we performed a grid search taking integer step of 1 for values spanning from -5 to 5. Then the five sets of weights that minimize the cross-validation (CV) root mean squared error (RMSE) are chosen for the ensemble of the SNAP models. Training and cross-validation errors for each model of the ensemble are given in Table 4.3. The ensemble of these models was then used to screen the prototype structures that exhibit the lowest values of enthalpy of formation.

From Table 4.3 can be observed that the RMSE for the cross-validation set are of the order of $\sim 80\ meV/atom$, below the values used so far in the literature [62], which

w_{Cu}, w_{Ag}, w_{Au}			Training MAE	Training RMSE	CV MAE	CV RMSE
1	1	2	8.0	13.4	27.1	83.5
1	2	2	8.7	13.5	24.8	64.7
-1	-2	-1	9.7	16.4	30.6	86.4
-1	-2	-2	8.5	13.2	23.5	64.3
-1	-1	-2	7.7	13.1	25.6	75.0

Table 4.3: The training and the cross-validation errors for the ensemble of 5 models used for screening. Errors are presented as a function of the different set of atomic weights w_i'. All values are given in meV/atom.

is enough to perform the selection of the most promising candidates.

4.2.3 Screening of the Prototypes

After completing the first steps of the algorithm, we obtain an ensemble of SNAP force fields, each trained by considering a different set of atomic weights, along with a pool of potential candidates. The objective of the proposed workflow is to screen structures that demonstrate low energy, hence resulting in a low enthalpy of formation for a specific stoichiometry.

The pool of created structures exhibits a wide SNAP-predicted energy distribution, E^{SNAP}, as shown in Figure 4.5 and the parity plot in Figure 3.5. In order to be able to accurately screen the created candidates, the force field must be accurate at the low end of the energy distribution and capable of predicting the energy ordering at the higher end, as we established in Chapter 3. We have shown that even though such-trained MLIAPs accurately predict the energy of structures close or near at the equilibrium, their reliability decreases as we move away from the relaxed structure or for crystal structures that are not sampled during the training process, as seen in the Principal Component Analysis (PCA) plot in Figure 3.7. As a result, an informed decision regarding the candidate geometry can increase the robustness of the final decision. This is at the heart of the method used in this work and has already been introduced by the fact that binary compounds are sampled to be used as parent structures during the decoration step.

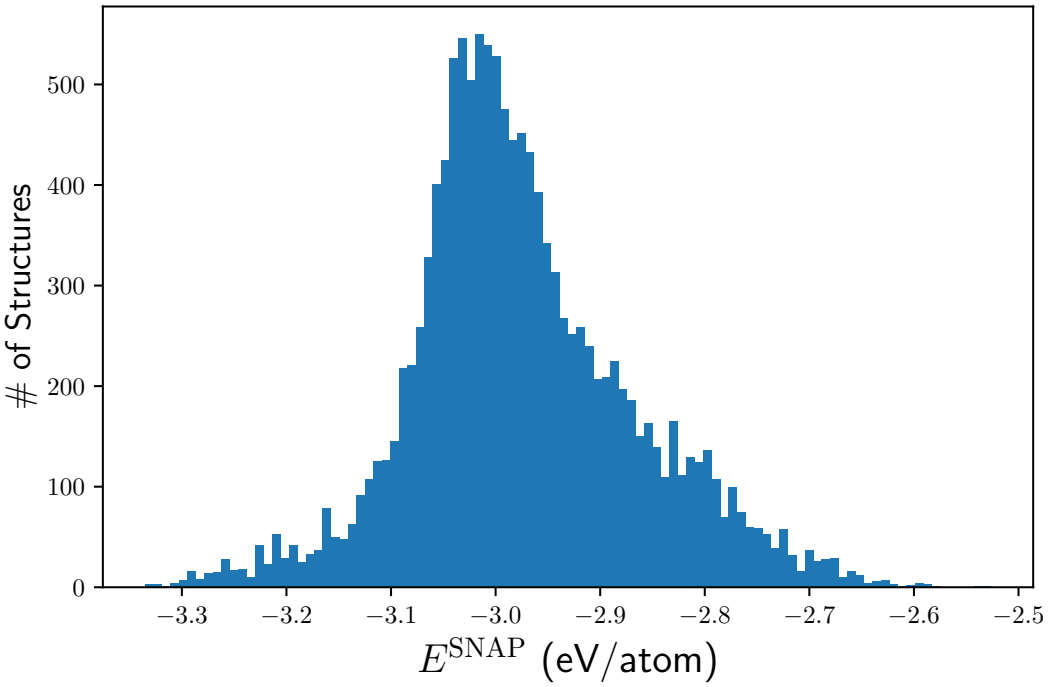

Figure 4.5: Here, the SNAP-predicted Energy distribution,E^{SNAP}, for the structures with stoichiometry $Cu_1Ag_1Au_1$ as predicted with a SNAP force field randomly chosen from the ensemble.

By definition, the created candidate structures exhibit the same volume as the parent crystals from which they were created. However, one can adjust the volume to obtain a more accurate estimate and, consequently, a structure that closely approaches the equilibrium volume. To achieve this, a Vegard's law-like [83] approach was implemented to estimate the volume of the crystal structure. The volume of the created crystal is approximated by taking the weighted average of the elemental volumes of the constituent atoms and multiplying it by the number of atoms in the corresponding cell. Subsequently, it is adjusted accordingly through homogeneous expansion or contraction. This approximation satisfactorily reproduces the result for DFT-relaxed compounds, as can be observed from the Figure 4.6.

Having established a way to cleverly estimate the volume of a given material, we can use a SNAP-driven relaxation trying to approach equilibrium. For this step, the volume and lattice parameters are kept fixed. This choice stems from the fact that, while the database used for training the model includes structures with structural diversity, all of them are in equilibrium. This implies that, in the absence of distorted configurations in the training set, SNAP models exhibit poor performance when applied to perform

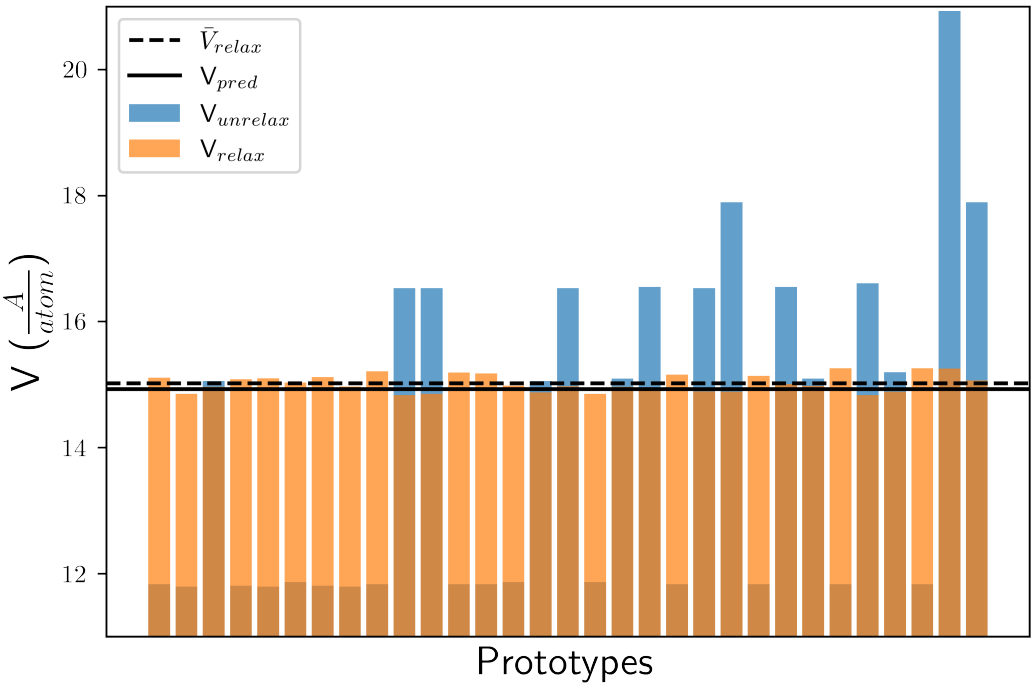

Figure 4.6: Plot showing the initial unrelaxed volumes and relaxed equilibrium volumes of a set of ternary prototypes at the stoichiometry $Cu_2Ag_1Au_1$. The dashed line indicates the mean equilibrium volumes for these compounds, while the solid line shows the volume predicted by the weighted average of the elemental volumes.

full structural relaxation. To be able to select the structures that exhibit the lower enthalpy, we are using a "cross-validated" energy prediction for each relaxed structure. The rationale behind this approach is to choose the energy and crystal structure that we are most certain has the lowest energy based on the standard deviation of the predictions.

In more detail, we used the ensemble of the trained SNAP models to drive the ionic relaxation. During this procedure each of the K SNAP models, trained in the entire database, is used to drive the relaxation of the internal degrees of freedom , with a maximum of N_s steps, for all the prototypes created. This leads to K relaxed structures which one would expect to relax in a different way. Furthermore, for each "relaxed" structure, we have $K-1$ predicted energies from the force fields that did not drive the relaxation. This is used as a form of cross-validation for the energy prediction for a given candidate. Then the mean and standard deviation of the energy predictions of the K-1 models are saved. Then for each prototype, we select the K relaxed structures with lowest "cross-validated" standard deviation, this corresponds to the structure for

which the relaxation is most probable to have been converged. Therefore, we end up with one relaxed structure per prototype. This procedure is presented graphically in the Figure 4.7.

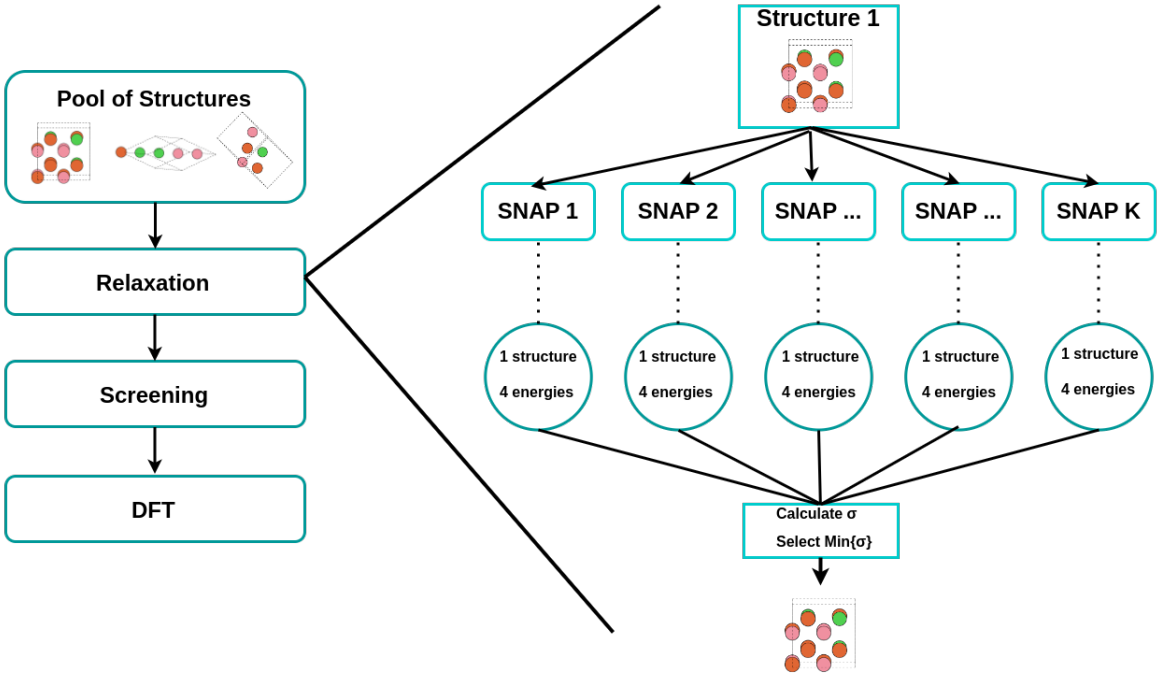

Figure 4.7: The relaxation procedure employed in the workflow for a single prototype is presented schematically. In the first step, the selected prototype relaxes its internal degrees of freedom using each of the K SNAP models. Then, an energy prediction is performed for the relaxed structure using the remaining K-1 SNAP models from the ensemble. Subsequently, the standard deviation is calculated and the structure and energy with the minimum standard deviation are selected.

The rationale behind this process is to take advantage of the robustness regarding the predictions that a cross-validation algorithm offers. Furthemore, we chose a fixed number of steps, N_s, for the relaxation in order to avoid leading to structures trapped in non-physical local minima of the potential energy surface (PES) of the driving SNAP model. Introducing this algorithm helps to avoid that from happening and offers a more accurate prediction for the relaxed structure at the same time. In general, SNAP performs relaxations with the largest change in energy occurring during the first few steps, similar to DFT-driven relaxation. By limiting the relaxation procedure to a fixed number of steps, we obtain structures that are lower in energy than the initial non-relaxed structure. This approach reduces the risk of obtaining high-energy structures, making the workflow more robust.

Furthermore, in a manner similar to the work discussed in Chapter 3, a cross-validation algorithm helps to remove the bias introduced by a specific SNAP model. During a typical SNAP relaxation, the structure is driven towards a geometric configuration that corresponds to the local minima of the potential energy surface (PES) fitted by the given model. In the case of an inaccurate relaxation, the standard deviation, $\hat{\sigma}$, of the energy calculated from the predictions of the rest of the SNAP force fields will be high enough for the workflow to avoid selecting the corresponding structure. It needs to be noted that since the training set is the same for all the MLIAPs in the ensemble, this could lead to a bias towards the same structure. This problem is addressed by using the standard deviation as the criterion for the selection of a specific structure out of the relaxed ones. More precisely, if several of the SNAP models are biased towards a falsely relaxed structure and they predict it to have low energy, this will lead to different predictions for each model, increasing the value of the standard deviation, and thus the uncertainty.

The "cross-validated" standard deviation prediction for all the structures must be less than a cutoff value, σ_{cut}, to be considered for the final energy screening. The value we used in this workflow is 10^{-3} eV/atom. Resulting in the last stage of the screening algorithm with a pool of candidate structures for which we are more confident about their predicted energies. Then, the ones with the lowest mean energy are chosen and relaxed with high-fidelity DFT. Here, we chose to fully relax ten structures per stoichiometry. The idea behind this choice is that there are energy errors in the workflow introduced by the MLIAPs used, and selecting a wider sampling window we manage to successfully sample almost always the lowest-energy structure without reducing the throughput of the workflow drastically.

The proposed workflow takes advantage of the binary materials space and the robustness of the cross-validation-based approaches in order to screen for the lowest-energy prototypes. This is done for a given fixed stoichiometry. Then, the energy of the proposed ternaries is calculated with full DFT relaxation and the convex hull is updated. The advantage of this workflow in comparison to other state-of-the-art

methods like AFLOW-CHULL [96] is that it focuses all the computationally demanding DFT calculations on the most promising candidates. The next step is to employ this workflow for the reconstruction of the ternary-alloy convex hulls of Cu-Ag-Au and Mo-Ta-W.

4.3 Results

Having defined a workflow that leverages the binary materials space to suggest possible ternary compounds and an ensemble of MLIAPs to screen for the low-energy ones, we are now required to benchmark this method against well-established state-of-the-art methods used for constructing ternary phase diagrams, namely AFLOW-CHULL. To do that, we first examine the performance of our workflow against the noble element Cu-Ag-Au ternary system, which has been extensively studied experimentally [116]. Then, we compared the predictions of our algorithm with one of the better-characterized phase diagrams extracted from AFLOWlib, specifically that of Mo-Ta-W, which presents four stable intermetallic phases. Using ab-initio calculated ternary phase diagrams as benchmarks of our workflow, we gain valuable insights regarding the effectiveness of the followed approach.

The Qhull [117] algorithm was used to calculate the convex hull for a given ternary. The same method was also used in AFLOW-CHULL, ensuring consistency in the comparison between the different approaches. For a given ternary system, the available data in AFLOWlib were downloaded to calculate the reference convex hull. Then to ensure consistency, we recalculated the energies of these compounds with the Vienna Ab-Initio Package (VASP) [28] (version 5.4.4). Throughout the entire process, we have strictly followed the AFLOWlib standards as outlined in reference [97]. The same Projector augmented wave (PAW) pseudopotentials that were employed from AFLOW are used for each element together with the Perdew-Burke-Ernzenhof (PBE) functional. For the plane wave cutoff, we used a value of 600 eV for all calculations, which is slightly above the 1.4 $\times$ ENMAX (default ENCUT (energy cut off) value provided by the pseudopotential) as proposed by the VASP team. The energy convergence

criterion for self-consistent field (SCF) calculations was defined as 10^{-4} eV. The ab-initio relaxations were considered converged when the forces were below 10^{-3} eV/Å . A Fermi-Dirac smearing of 0.2 eV was chosen for all the calculations. Regarding the $k-$point, a Γ-centered mesh was used with number of $k-$points per reciprocal atom (KPPRA) of more than 6×10^3 for the relaxations and 10^4 for the SCF calculations. The number of sampling points along each direction is proportional to the norm of the corresponding reciprocal lattice vector as defined by the Equation (3.2).

4.3.1 Cu-Ag-Au ternary convex hull

To measure the performance of our workflow, the first step would be to study a ternary system that has already been thoroughly investigated in this thesis. This system is the Cu-Ag-Au ternary phase diagram, which was extensively discussed in Chapter 3. Another reason for the selection of this ternary is that it provides ample data to train a robust MLIAP. Furthermore, we have already recalculated, using DFT, all the energies of the available structures extracted from AFLOWlib in Chapter 3. This makes it even more appealing, as the errors introduced by DFT convergence would be minimized. This advantage allows us to identify and correct any errors in the workflow implementation.

During the first attempt, we focused on the equiatomic $Cu_1Ag_1Au_1$ ternary and compounds with stoichiometric ratios of 2-1-1 and 2-2-1 (and the corresponding permutations). Furthermore, we ensured that the number of atoms in the unit cell remained less than 10 for all the systems studied. This was done to keep the number of derivative structures low. The reason behind the selection of these stoichiometries is that they have already been explored by AFLOW-CHULL, serving as benchmarks for our study. To assess the stability of a given structure, we calculate the energy distance from the convex hull, δ, for a given structure. The enthalpy of formation corresponding to the convex hull plane in this composition, denoted ΔH_f^{CH}, is subtracted from the formation enthalpy

of the compound studied, denoted ΔH_f^{Comp}. This distance is defined in Equation (4.5).

$$\delta = \Delta H_f^{Comp} - \Delta H_f^{CH} \tag{4.5}$$

The distance from the convex hull, δ, generally takes positive, negative, or zero values. Its value is used as a criterion to assess the thermodynamic stability of a studied compound. Positive values mean that the enthalpy of formation of the structure lies above the convex hull plane, resulting in a metastable or unstable structure. A zero or negative value means that the studied structure is considered thermodynamically stable, as it lies on or below the previously calculated convex hull. For the negative values, the convex hull is recalculated and the point that corresponds to the stoichiometry is added in the phase diagram, resulting in change of the shape of the convex hull. Furthermore, to highlight the potential of our workflow in exploring novel regions of a given phase diagram, we have also predicted the stability for structures in the 3-1-1 (and the permutations 1-3-1 and 1-1-3) compositions. The results of the workflow are presented in Figure 4.8. It can be observed that the workflow manages to identify one stable intermetallic phases namely $Cu_1Ag_1Au_2$. Interestingly, the $Cu_1Ag_1Au_2$ was already close to the convex hull, as calculated by AFLOW, without being able to touch it. This paradigm shows the versatility of our workflow to identify possible stable intermetallics.

The scalability and speed of the proposed algorithm allow us to investigate more regions of the phase diagram that would be computationally expensive with a DFT-based phase-diagram construction scheme. It should be noted that for these four stoichiometries we performed 40 relaxations and 4 SCF DFT calculations, whereas AFLOW performed 87 relaxations and 87 SCF DFT calculations, which comprises the vast majority of all the ternary calculations. The AFLOW strategy of constructing ternary phase diagrams is based on decorating the same amount of parent structures over all the studied systems; these crystal structures are extracted from known materials and stored in the AFLOW encyclopedia.

The workflow will then be employed to predict structures for the 2-2-1 and 3-1-1

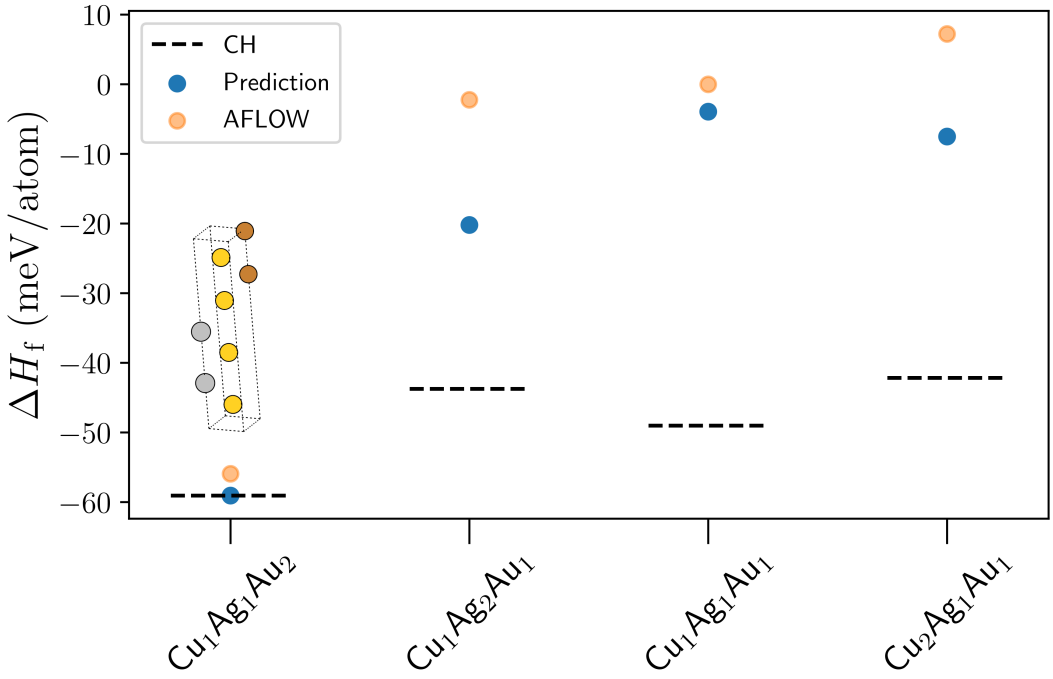

Figure 4.8: Workflow predictions for the Cu-Ag-Au ternary system across different stoichiometries. The graph presents the different compositions (x-axis) and their corresponding enthalpies of formation, ΔH_f. The blue dots denote the calculated enthalpy of formation of the prediction of the proposed workflow, whereas the orange ones represent the enthalpy of the best AFLOWlib prediction. The dashed line corresponds to marks the tie-plane positions of the convex hull. Here, the Au atoms are in gold, the Ag atom in silver, and the Cu atom in bronze. The proposed workflow manages to identify one stable intermetallic phase, namely $Cu_1Ag_1Au_2$. Furthermore, the workflow manages to outperform the AFLOW dictionary method during all cases presented.

stoichiometries (and their permutations). It should be noted that the latter compositions do not correspond to studied compounds. Instead, they serve as a showcase of the flexibility of the workflow. The results are presented in Table 4.4.

In Table 4.4, it is observed that the gold-heavy $Cu_1Ag_1Au_3$ compound exhibits a negative distance from the AFLOW-calculated convex hull, indicating that it is thermodynamically stable. Therefore, it is necessary to update the convex hull by incorporating this compound into the algorithm. Furthermore, it is observed that the proposed workflow outperforms the dictionary method during all the cases studied. Interestingly, the predicted structures are consistently closer to the convex hull compared to the ones proposed with the dictionary method. This means two things a) that the workflow effectively selects the relevant structures for creating the pool of ternary candidates and b) that the crystal structure of the binary compounds can be effectively

Stoichiometry	δ^{AFLOW} (meV/atom)	δ^{WP} (meV/atom)
$Cu_2Ag_2Au_1$	208.95	25.99
$Cu_2Ag_1Au_2$	205.69	37.45
$Cu_1Ag_2Au_2$	90.27	17.21
$Cu_3Ag_1Au_1$	–	20.35
$Cu_1Ag_3Au_1$	–	31.05
$Cu_1Ag_1Au_3$	–	-0.02

Table 4.4: Workflow predictions for the Cu-Ag-Au ternary system with 2-2-1 and 3-1-1 compositions. The stoichiometries and their corresponding distance from the convex hull, δ^{WP}, are presented. For the 2-2-1 compounds, the distance from the convex hull of the phases available in the AFLOWlib database, δ^{AFLOW}, are also given. Note that for all materials, the distance from the AFLOWlib convex hull tie plane is used as reference. A new gold-heavy intermetallic, namely $Cu_1Ag_1Au_3$ is predicted as stable (its crystal structure is displayed in Fig. 4.9).

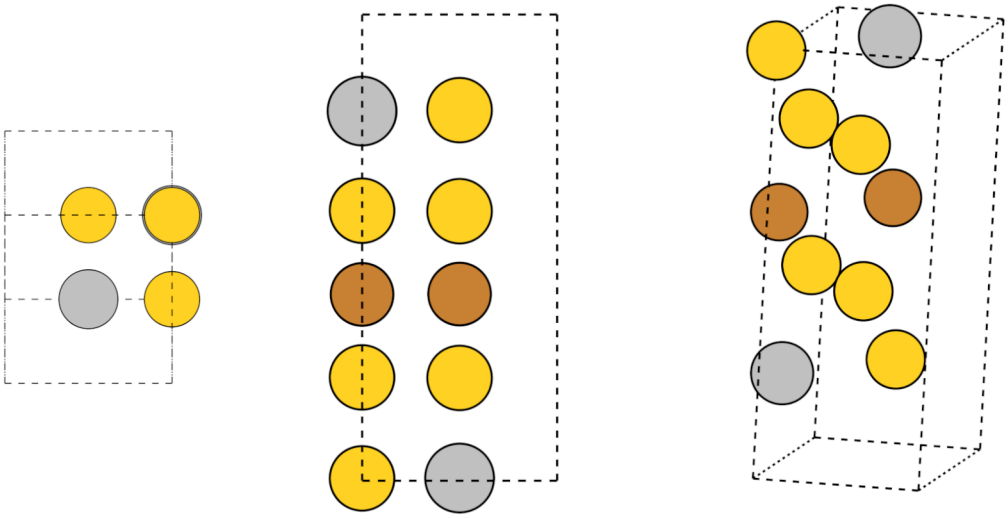

Figure 4.9: The unit cell of the crystal structure on the convex hull, namely $Cu_1Ag_1Au_3$, is presented in both a top-view with respect to the z-axis (left), a side-view along the x-axis (middle) and a tilted view (right). In this structure, gold (Au) atoms are represented in gold color, silver (Ag) atoms in silver color, and copper (Cu) atoms in bronze color.

used to create ternaries. Overall, these results highlight the success and potential of the proposed workflow for predicting stable ternary compounds.

Consistently predicting structures with a negative formation enthalpy gives us confidence in the reliability of the workflow. Interestingly, we have been able to

identify a couple of gold-heavy stable phases, namely $Cu_1Ag_1Au_2$ and $Cu_1Ag_1Au_3$. This indicates that a possibility of stable intermetallic phases exists on the gold side of the studied phase diagram. We have confidence in our prediction, given the fact that the dictionary method structure for $Cu_1Ag_1Au_2$ was within 3 meV/atom from the convex hull, suggesting the possibility of the existence of a stable phase. This is consistent with the formation of solid solutions in the gold-rich region of the experimentally studied phase diagram [116]. The rest of the structures are considered metastable, with an average distance from the convex hull of ∼30 meV/atom.

To visually interpret the differences between the phase diagrams, in Figures 4.10, 4.11 and 4.12 we present the phase diagram calculated by AFLOW and predicted from our workflow. Furthermore, the difference between these two phase diagrams is presented. For the AFLOW phase diagram, we recalculated the database consisting of the three binaries namely Cu-Ag, Ag-Au and Cu-Au, the unaries and the corresponding ternaries, then we used Qhull to calculate the convex hull. For our prediction, we added the newly predicted ternaries to the entire database, then we recalculated the convex hull.

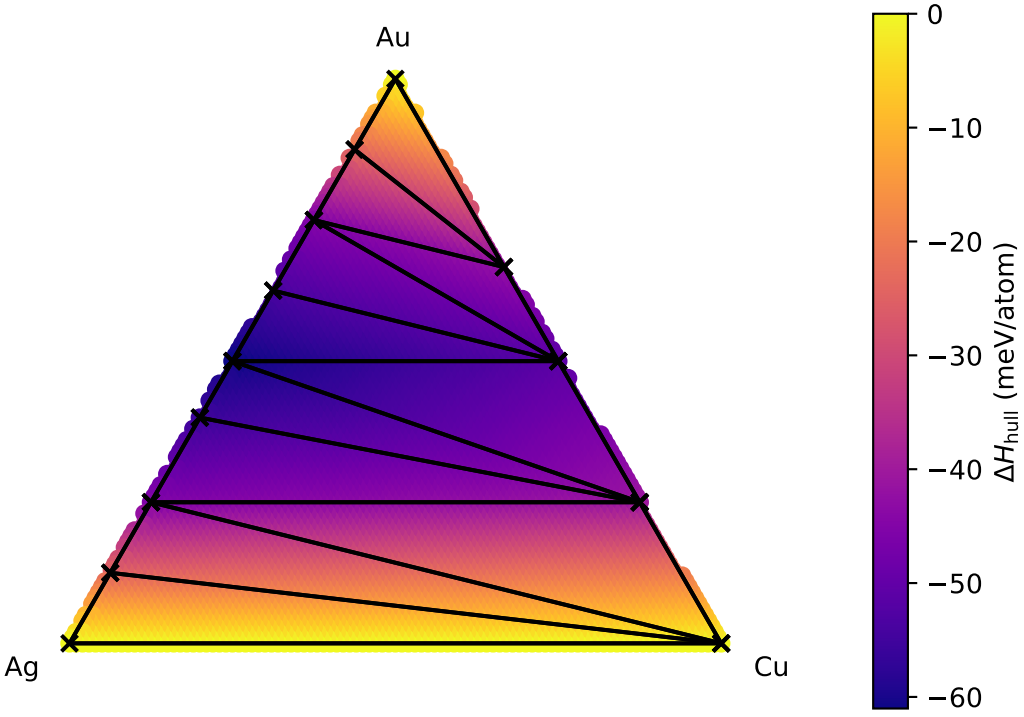

Figure 4.10: Convex hull of the ternary system Cu-Ag-Au as calculated using AFLOW-CHULL. The stable binary phases are denoted with black crosses and are located within the Ag-Au and Cu-Au binary systems. No stable ternary phases are predicted.

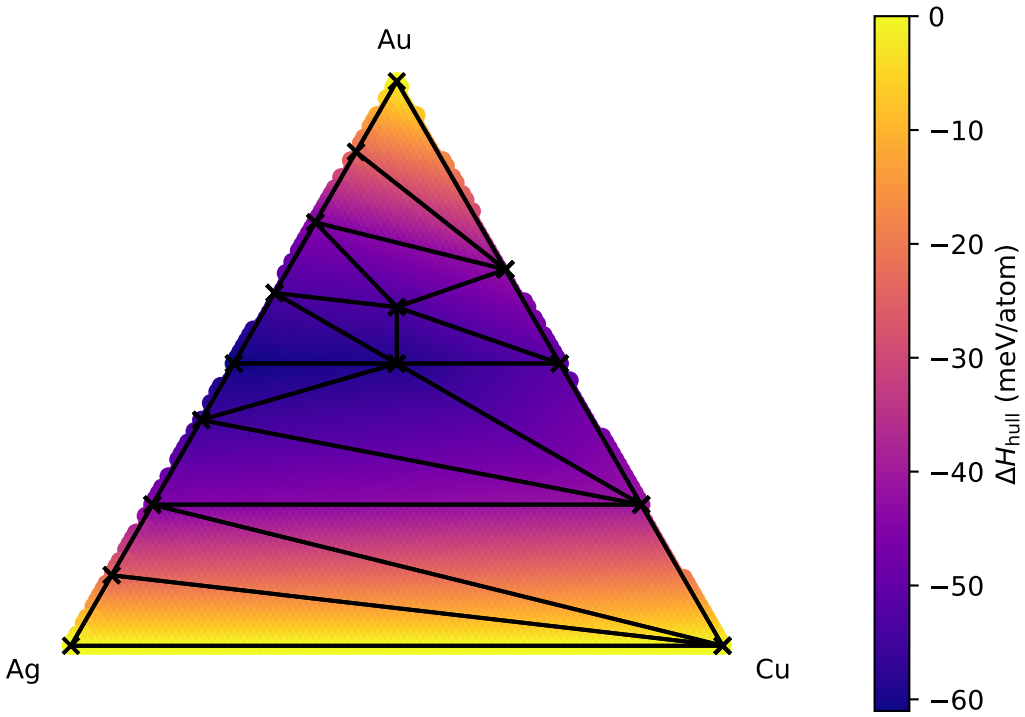

Figure 4.11: Convex hull of the ternary system Cu-Ag-Au as predicted from out workflow. The stable binary phases are denoted with black crosses and are located within the Ag-Au and Cu-Au binary systems. Two stable ternary intermetallics were found in the gold-heavy area, namely $Cu_1Ag_1Au_2$ and $Cu_1Ag_1Au_3$.

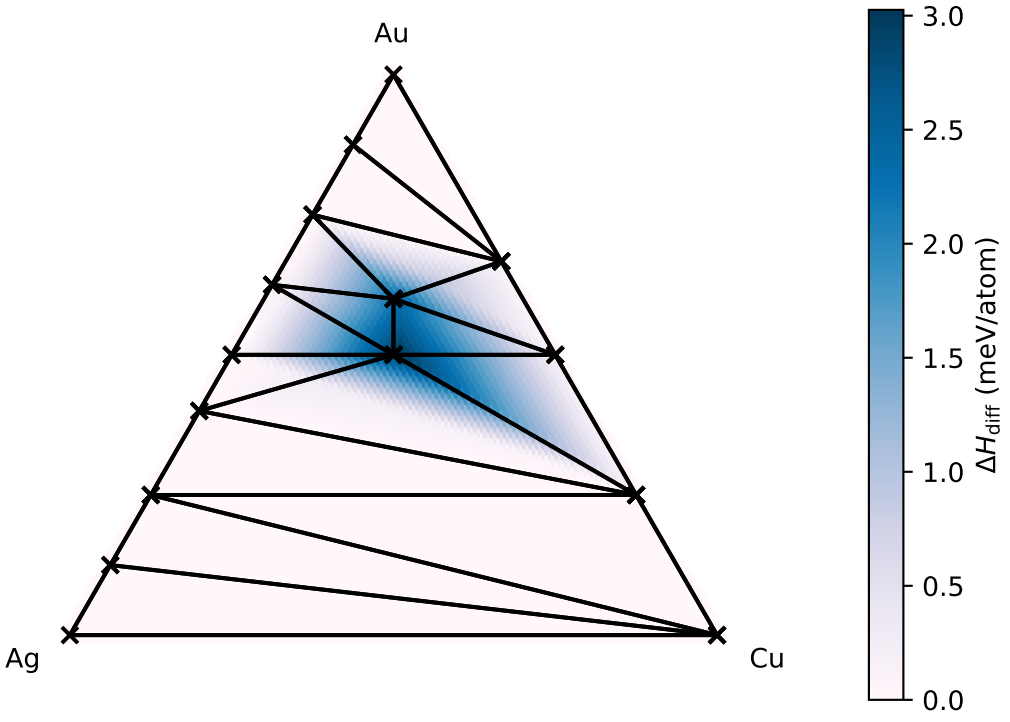

Figure 4.12: Difference between the AFLOW-predicted and the workflow-predicted convex hulls. A decrease in the depth of the convex hull calculated by AFLOW is observed in the gold-heavy area.

The ternary phases proposed with our workflow are consistent with the formation of solid solutions in the gold-rich region of the experimental phase diagram as reported in [116]. Furthermore, several ternary metastable structures were proposed with an average distance of the convex hull of ~ 30 meV/atom. Our analysis demonstrates the ability of the discussed workflow to predict and identify structures closer to the convex hull than those from the state-of-the-art dictionary method and uncover novel ternary phases, should they exist.

4.3.2 Mo-Ta-W ternary convex hull

To put our workflow to a more severe test, we chose to predict the phase diagram of a system that exhibits a plethora of stable intermetallics. Most of the ternary phase diagrams in the AFLOWlib database exhibit only a couple of stable ternary phases, and finding a ternary system that has more than two ternary intermetallics is quite rare. The criteria we used to identify the benchmark system is selecting a phase diagram created from transition metal elements where the highest number of intermetallic phases exist.

Using the AFLOW REST-API [118] to search the database, the Mo-Ta-W ternary system emerged as a good candidate. In fact, it exhibits the highest number of stable ternary phases in the entire database of transition-metal alloys. To reproduce the phase diagram predicted from AFLOW we extracted the stoichiometry and energy pairs from the database. The ternary phase diagram calculated from AFLOW is presented in Figure 4.13.

To be consistent with the analysis and the comparison between energy distances, we recalculated the energies of the structures used in the phase diagram shown in Figure 4.13. To do that, we used high-fidelity DFT consistent with the standards described in [97]. Then, we calculate the convex hull and reassess the stability for the ternary phases. The recalculated phase diagram is shown in Figure 4.14.

By recalculating the energy of the compounds used for the construction of the convex hull, the depth of it increased marginally. This increased the distance from the

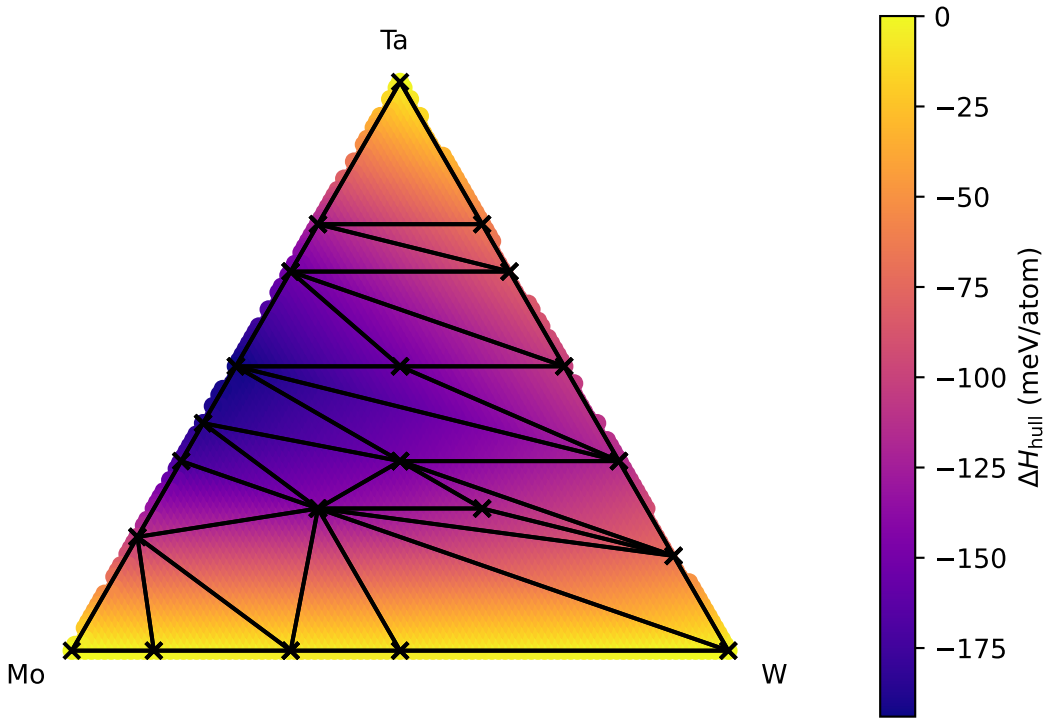

Figure 4.13: Convex hull of the ternary system Mo-Ta-W as calculated using AFLOW-CHULL. The stoichiometry-energy pairs extracted from the AFLOWlib database were used to reproduce the calculated phase diagram. There are four intermetallic phases predicted to be stable, depicted with black crosses, namely $Mo_1Ta_1W_1$, $Mo_2Ta_1W_1$, $Mo_1Ta_2W_1$, $Mo_1Ta_1W_2$.

convex hull for two of the four ternary phases. The distance from the convex hull for $Mo_1Ta_2W_1$ is 2×10^{-3} meV/atom and 6×10^{-4} meV/atom for the $Mo_1Ta_1W_2$. The distance from the convex hull for these "unstable" compounds is on the order of the DFT error, and practically they are considered stable compounds. The comparison will use the recalculated version of the convex hull. The comparison between the proposed workflow and the dictionary method will follow the same path as previously. We have made predictions corresponding to the same compositions as those presented in the previous section. Furthermore, we have used our method to explore areas of the phase diagram that are poorly covered by AFLOWlib.

The structure prototypes used for the element decoration are extracted based on their distance to the convex hull. More information on convex hull analysis can be found in the Appendix C. An ensemble of machine-learning models is trained using the entire available database. This ensemble of models is employed to refine and screen the pool of generated prototypes. Subsequently, the 15 structures with the lowest predicted energy

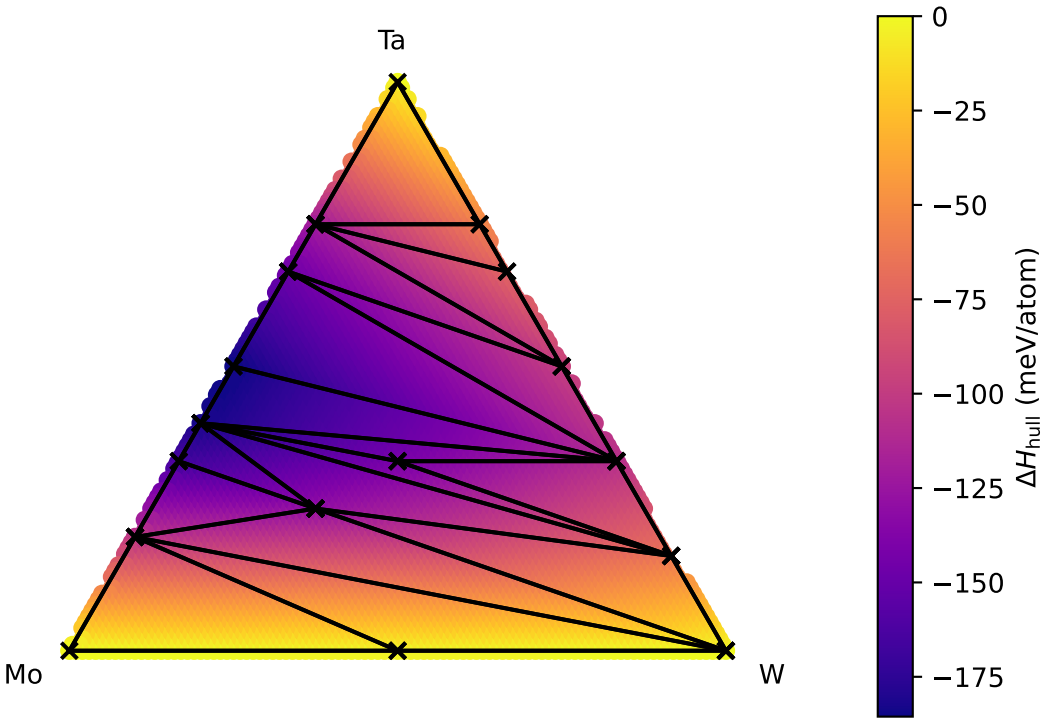

Figure 4.14: Convex hull of the ternary system Mo-Ta-W as calculated using AFLOW-CHULL. The DFT-calculated energies were employed to create the convex hull. The number of ternary structures reduced to two, depicted with black crosses , namely $Mo_1Ta_1W_1$, $Mo_2Ta_1W_1$.

are selected for sampling and subjected to DFT relaxation and stability assessment.

The significant difference compared to the workflow used for the Cu-Ag-Au ternary lies on the fact that now we use AFLOWlib's database to train the MLIAPs that drives the relaxations and the screening, without any further recalculation. As we discussed in Chapter 3 the accuracy of a force trained solely with the energies provided from AFLOWlib is enough to separate low- from high-energy structures. This increases the throughput of the workflow and gives us an option to increase the number of the structures selected for relaxation. The AFLOW REST-API is employed to download the energies and the crystal structures for the three binary convex hulls (Mo-W, W-Ta, and Mo-Ta), the data points used to train the MLIAPs consisted of binaries and unaries that were calculated for each system, namely 307, 306, and 941 for Mo-W, Ta-W, and Mo-Ta accordingly. It should be noted that one of the binaries, namely Mo-Ta is sampled more thoroughly compared to the rest. Following this approach, we managed to avoid about 1500 DFT calculations, some of them for cells up to 46 atoms,

which would greatly reduce the throughput of our workflow.

The workflow was employed to predict the stability for the 1-1-1 and 1-1-2 compositions. We then corrected the convex hull by adding the newly predicted compounds. In Figure 4.15 we present the comparison of the distance from the recalculated convex hull for the stoichiometries 1-1-1 and 2-1-1 (and the permutations).

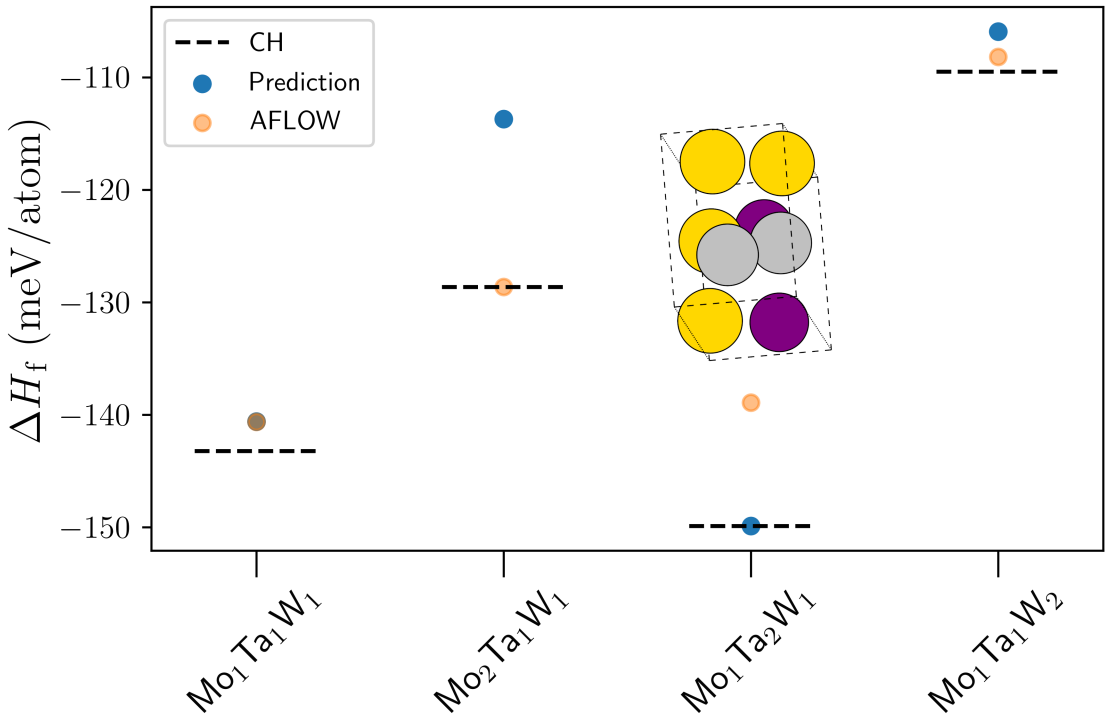

Figure 4.15: Workflow predictions for the Mo-Ta-W ternary system across different stoichiometries, 1-1-1 and 1-1-2. The graph presents the different compositions and their formation enthalpy ΔH_f. The blue points are associated to the predictions from the proposed workflow, whereas the orange ones represent the lowest-energy AFLOWlib's data. The dashed line marks the tie plane position of the convex hull. The unit cell of the crystal structure on the convex hull is presented as well. Here, Ta atoms are in gold, W in silver, and Mo in purple. The proposed workflow managed to identify one intermetallic phase, namely $Mo_1Ta_2W_1$.

In this case, we still predict one new stable intermetallic phase, namely $Mo_1Ta_2W_1$, which increases the depth of the convex hull, as can be observed in Figure 4.15. This time, our workflow consistently outperforms the best cases of the dictionary method. In fact, for two of the four stoichiometries investigated, we obtain compounds with energies similar to the ones present in AFLOWlib, while for one, $Mo_2Ta_1W_1$, our search yields a compound with higher energy.

As observed in Figure 4.15, the compound $Mo_1Ta_1W_1$ exhibits the same distance

from the convex hull for both the workflow and the AFLOW prediction. It is of interest to determine whether these two compounds share the same crystal structure or exhibit structural similarities. To conduct this analysis, the AFLOW-SYM tool is employed to calculate the space-group and lattice constants of each crystal. The two crystals display distinct symmetry groups and crystal systems. The one predicted by the workflow belongs to space group 8 and is categorized under the monoclinic crystal system, whereas the AFLOW-predicted crystal belongs to space group 107 and is classified as tetragonal. In Figure 4.16 a visual representation of the two crystals is shown and in Table 4.5 the lattice parameters are summarised.

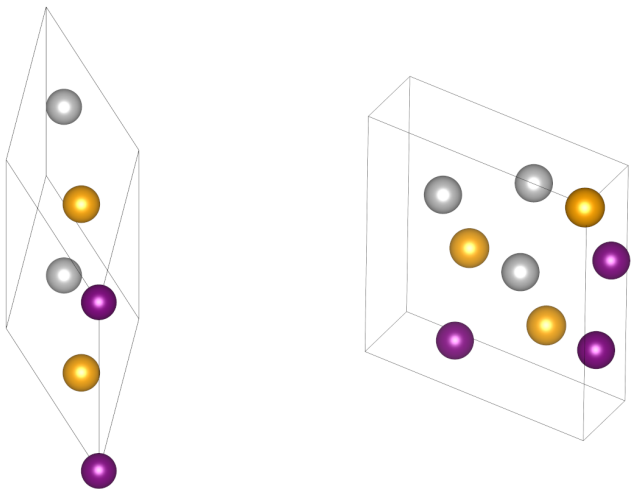

Figure 4.16: Workflow and AFLOW crystal structure predictions for the $Mo_1Ta_1W_1$ compound.The unit cell of the structures predicted by the two methods is visually presented. Here, the Ta atoms are in gold, W in silver, and Mo in purple.

Utilizing an approach that is heavily based on the quality of the trained force field means that the workflow improves as the quality of the MLIAP increases. However, in this instance we are exploring the case of an end-to-end workflow based solely on calculations already performed for the construction of the binary phase diagrams. In this context, the data used to train the MLFF are extracted from the AFLOWlib repository. As we saw in Chapter 3 there is a trade-off between accuracy and throughput by following this path. We anticipate that the trained force field will not be as accurate as the one used for the Cu-Ag-Au ternary system. It should be noted that minor

	Workflow	AFLOW
a (Å)	3.2045	5.3488
b (Å)	7.1661	5.3488
c (Å)	7.0234	5.3488
c/a	2.1916	1
α (°)	107.9623	145.0910
β (°)	103.1872	145.0910
γ (°)	90.0	50.1988

Table 4.5: Structural parameters regarding the AFLOW and the workflow prediction for the $Mo_1Ta_1W_1$ compound predicted from AFLOW and the workflow.

inconsistencies in the energy values translate to large errors in the force field [119]. Given this understanding, we have nevertheless demonstrated that novel phases can be predicted through an almost DFT-free workflow, due to the accessibility of our data within a database. Being able to avoid calculating the compounds already present in the binary phase diagrams saves us more than a thousand DFT calculations.

Having said that, perhaps a more accurate force field would also be able to find the AFLOWlib minimum for $Mo_2Ta_1W_1$ (see Fig. 4.15). However, it is demonstrated that the current workflow is already capable of creating and identifying the majority of the structures of interest and predicting candidates close to the convex hull. Emphasis should be given in the fact that this is the phase diagram for which the AFLOWlib's dictionary method works the best, as it is capable of detect 4 intermetallic phases, more than any other transition metal alloy phase diagram.

We proceed our analysis by comparing the predictions of our method with AFLOWlib for structures predicted as metastable. This provides us with insight into the behavior of our method in areas of the phase diagram susceptible to metastable structures. For this analysis, we compared the workflow predictions for the rest of the stoichiometries for which AFLOW fails in predicting stable structures. Furthermore, the enthalpy of formation for these structures takes positive values, and, as a result, the distances from the convex hull are large. More quantitatively, the best prediction is for $Mo_4Ta_1W_1$ with a distance of 320.95 meV/atom and the worst prediction is for $Mo_2Ta_1W_2$ with

1032.50 meV/atom. In Table 4.6 we provide a comparison of the distance from the convex hull for the structures predicted with our method, δ^{WP}, and those of AFLOWlib, δ^{AFLOW}.

Stoichiometry	$\delta^{AFLOW}(meV/atom)$	$\delta^{WP}(meV/atom)$
$Mo_2Ta_2W_1$	880.90	0.00
$Mo_1Ta_2W_2$	962.84	0.00
$Mo_2Ta_1W_2$	1032.50	8.50
$Mo_4Ta_1W_1$	320.95	46.56
$Mo_1Ta_4W_1$	516.30	3.25
$Mo_1Ta_1W_4$	334.16	0.33

Table 4.6: Workflow predictions for the Mo-Ta-W ternary system with 1-2-2 and 1-1-4 compositions. The stoichiometries and their corresponding distances from the convex hull, δ, are presented. Three intermetallics are predicted to be stable and two others to be metastable. Surprisingly, our algorithm is able to identify structures 3 orders of magnitude closer to the convex hull than those predicted from AFLOWlib.

Here, Table 4.6 illustrates the ability of our workflow to consistently predict structures that satisfy two key criteria: (i) proximity to the convex hull and (ii) negative formation enthalpies. The former indicates that the proposed workflow possesses the capacity to generate and identify stable intermetallic compounds if they do exist. This property makes it a powerful tool for materials exploration. The latter validates the physical intuition behind the approximation that crystal structures extracted from the closer-to-the-convex hull prototypes, once decorated, can be used as a viable option for the structure of the ternary phases. This indicates that such a workflow spends most of the time searching for a specific compound, with structures that are relevant.

More quantitatively, we were able to identify three novel intermetallic phases presented in Table 4.6, namely $Mo_2Ta_2W_1$, $Mo_1Ta_2W_2$, and $Mo_1Ta_1W_4$. Furthermore, we find two metastable phases with distances below 50 meV/atom. The advantages of the presented algorithm compared to the dictionary method are clearly displayed. The freedom for the structure search of the proposed algorithm is highlighted, proving that previously explored areas hide difficult-to-find stable intermetallics that a more versatile method will be able to unhide.

In the last part of the work and in accordance with the analysis of the Cu-Ag-Au ternary, we use the workflow to predict structures that belong to previously unexplored regions of the phase diagram. This gives us insight regarding the extrapolation ability of the workflow in predicting and identifying stable structures. The results are shown in Figure 4.17.

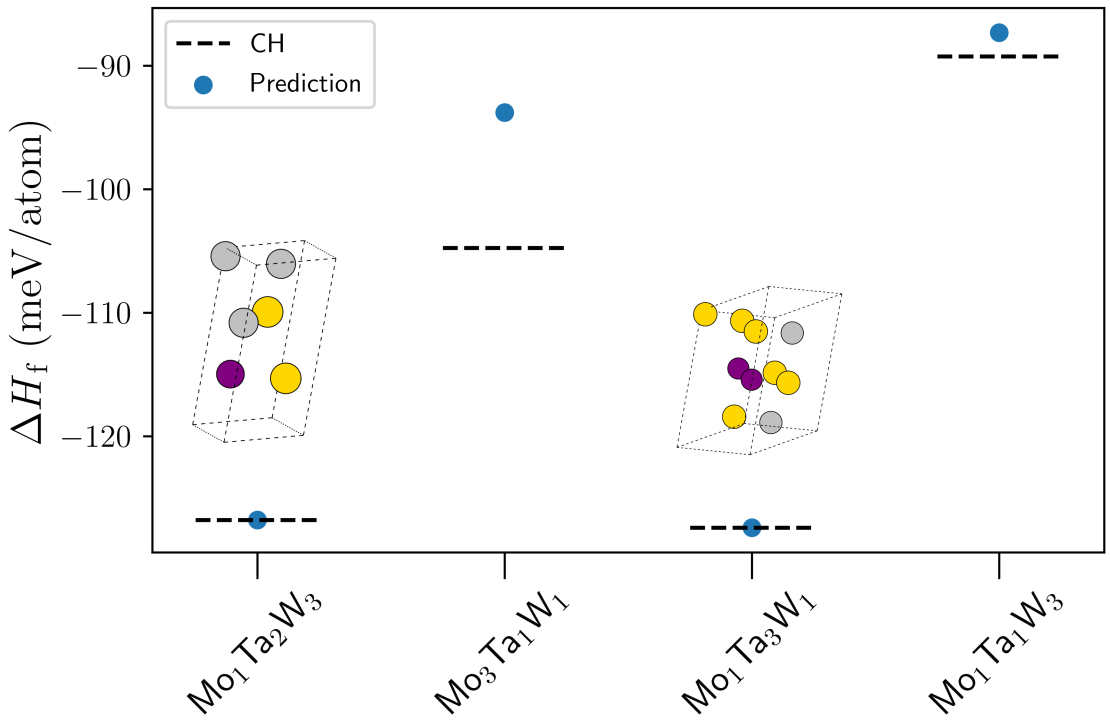

Figure 4.17: Workflow predictions (blue) for the Mo-Ta-W ternary system across different stoichiometries 1-2-3 and 3-1-1. The enthalpy of formation that corresponds to the minima of the convex hull is shown with the dashed line. The unit cell of the crystal structure on the convex hull is presented as well. Here, Ta atoms are in gold, W in silver, and Mo in purple. Two new intermetallics were identified namely $Mo_1Ta_2W_3$ and $Mo_1Ta_3W_1$.

The workflow successfully identifies two new intermetallics: $Mo_1Ta_2W_3$ and $Mo_1Ta_3W_1$. Furthermore, both predicted metastable phases are within 15 meV/atom distance from the convex hull. To be more quantitative, the distance from the convex hull for $Mo_3Ta_1W_1$ is 10.94 meV/atom, and for $Mo_1Ta_1W_3$ is 1.91 meV/atom. This solidifies the effectiveness of the proposed workflow as a tool suitable for materials discovery.

The introduction of stable phases in the Mo-Ta-W phase diagram translates into changes in the depth of the convex hull with respect to the newly predicted stable ternaries. The newly calculated convex hull is presented in Figure 4.18.

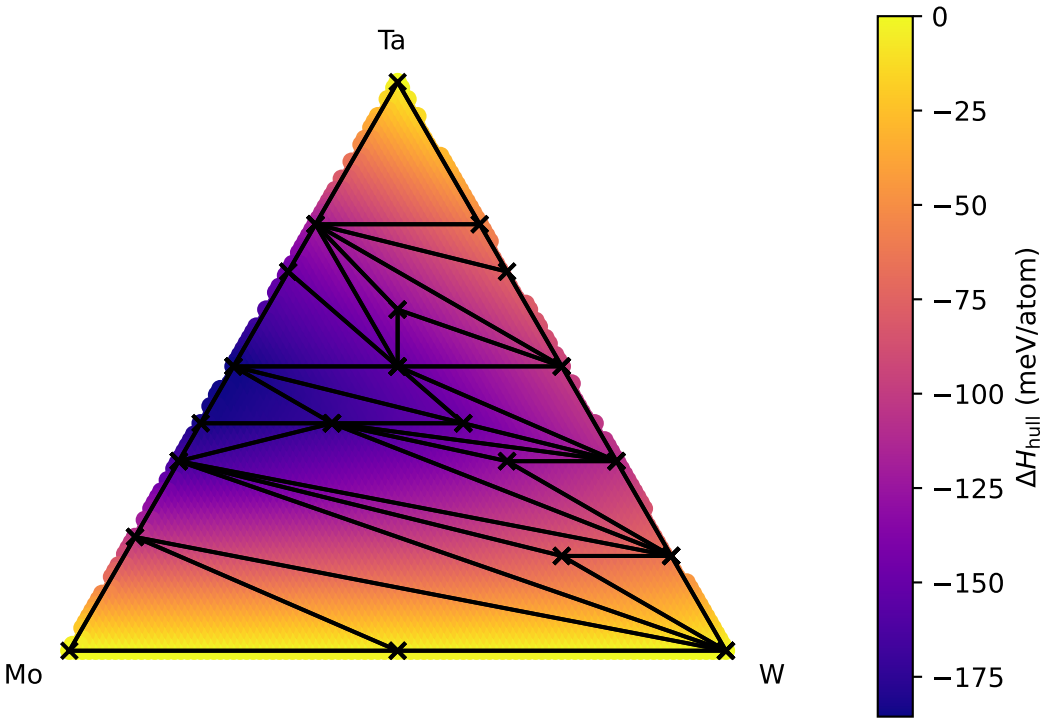

Figure 4.18: The ternary phase diagram of the MoTaW system. The color map suggests the calculated enthalpy of formation corresponding to each of these stoichiometries. The crosses represent the intermetallic phases that we discovered.

To better illustrate how the stable-predicted structures influence the landscape of the convex hull, we present a comparison between the two phase diagrams discussed (AFLOW- and workflow-predicted), in Figure 4.19. The complete phase diagram of the Mo-Ta-W ternary system that presents all the stable intermetallic phases predicted for this ternary system to date is presented in Figure 4.20.

At first glance, it is evident that the majority of identified ternary structures belong to the Ta-W region of the phase diagram. In the molybdenum-rich region, we encounter challenges in identifying any new intermetallic compounds, and we are unable to confirm the stability of $Mo_2Ta_1W_1$. The Mo-Ta-W ternary system is well-documented [120] for forming a ternary solid solution at finite temperatures across the entire phase diagram.

In the case of $Mo_2Ta_1W_1$, a closer examination of the crystal structure provides insights into our inability to identify it. This compound belongs to the family of Heusler compounds, and its unit cell corresponds to symmetry group 225 and face-centered cubic (*fcc*) crystal structure. A more thorough analysis of the parent structures sheds

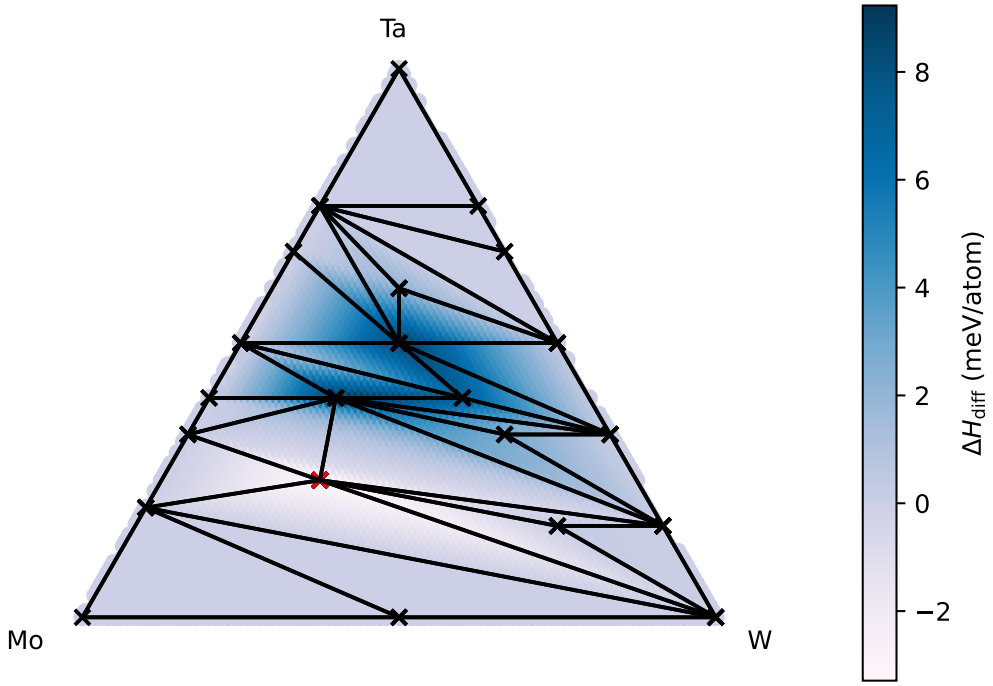

Figure 4.19: Difference between the AFLOW-predicted and the workflow-predicted convex hulls. A decrease in the depth of the AFLOW calculated convex hull in the Mo-Ta-W central area. However, there is an increase in the depth around the $Mo_2Ta_1W_1$ region and this comes from the lack of stability confirmation for this compound. Black crosses denote the structures predicted from the worfklow, and red crosses presents the structures predicted from AFLOW.

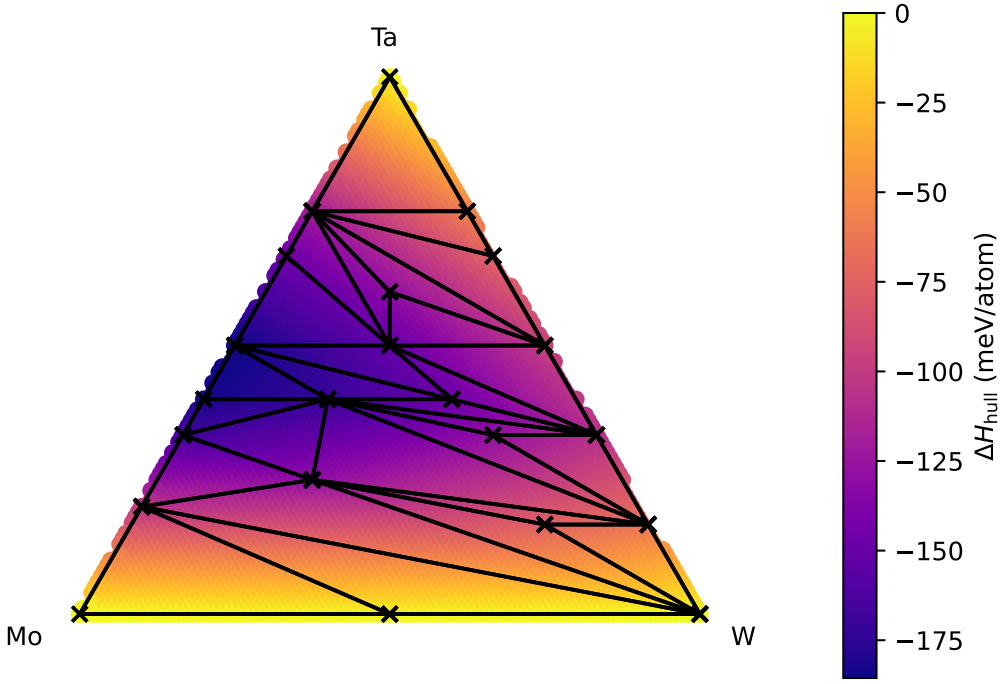

Figure 4.20: Complete convex hull construction for the Mo-Ta-W ternary system. The stable intermetallic phases predicted are presented with black crosses.

light on the result that we did not sample any structure from this specific space group or those closely related to it. This scarcity of similar structures in the binary phases could explain why the workflow was unable to identify this particular material.

Furthermore, it is important to note that the Mo-Ta binary system is significantly better sampled in AFLOWlib compared to the Ta-W and Mo-W systems. This could suggest that it is more challenging to approach the convex hull region near this facet. Additionally, the depth of the binary convex hull between Mo and W is considerably smaller than in the other binary systems. This implies that both Mo and W form more stable phases with Ta than with each other. These two factors may explain the greater difficulty in discovering stable intermetallic phases within the Mo-rich portion of the phase diagram.

4.4 Conclusion

In summary, this chapter outlines the development of a workflow capable of predicting crystal structures for compounds with specific stoichiometry and effectively screening them based on their energy prediction. The workflow relies on an ensemble of SNAP force fields to identify and select the most stable structures. Additionally, the underlying assumption of employing binary structures as prototypes for creating potential ternary compounds seems to be a good alternative to the state-of-the-art encyclopedia method.

Using a MLIAP as a DFT surrogate and reducing the amount of DFT calculations to minimum, offers the needed throughput and scales the ability of the workflow to perform well even when vast materials spaces need to be scanned. Then the proposed workflow is employed to map the ternary convex hull for two different transition metal alloy systems. Another crucial aspect of the proposed scheme is that relevant information is leveraged throughout the workflow. Both the force fields and the creation of the prototype ternary structures are based on the knowledge of the binary phases only. The availability of the data used in open databases such as AFLOWlib minimizes the need for DFT. This means that a phase diagram for a ternary system can be explored thoroughly with a few hundreds of DFT calculations. More importantly, these

DFT calculations are performed only for the ternary phases that have a high possibility of lying near or at the convex hull minimum. The versatility of the proposed scheme allows us to map previously unexplored ternary regions and help drive the search for novel material compounds with interesting properties.

The demonstrated workflow is generally capable of predicting crystal structures with negative formation enthalpy, which means that the parent prototypes used to create the candidate ternaries are relevant choices. Furthermore, it is able to identify novel intermetallics should they exist. To showcase the abilities of the models, we used two different ternary systems, namely Cu-Ag-Au and Mo-Ta-W. In both cases, we managed to predict stable phases that altered the convex hull landscape, resulting in a reduction of the convex hull by a few meV/atom.

Additionally, we identified a few metastable phases with an energy difference of less than 20 meV/atom that could potentially also be experimentally synthesized. In the Cu-Ag-Au ternary system, we pinpointed Au-rich compositions as the most promising region for stable intermetallics. Furthermore, for the Mo-Ta-W ternary system, which is one of the most studied and best-performing ternary phase diagrams in AFLOWlib, our method identified a variety of novel phases. This led to the correction of the phase diagram calculated by AFLOW-CHULL.

In summary, we have proposed an end-to-end phase diagram prediction algorithm which leverages the strengths of machine learning interatomic potentials as surrogates to DFT in order to scan large numbers of candidate structures. The presented workflow harnesses existing DFT calculations, enhancing its throughput and rendering it well-suited for scanning extensive materials spaces. This study serves as an illustration of how machine-learning tools can be seamlessly integrated with prototype generation techniques to build a pipeline, eliminating the need to generate extensive training sets. Instead, it achieves this by re-purposing data already present in large-scale databases.

Chapter 5

Machine-Learning-Assisted Construction of Magnetic Ternary Convex Hull Diagrams

The research was conducted as a collaboration between the author of this thesis and H. Rossignol. All parts of this chapter are contributed equally by the two authors.

5.1 Introduction

It has been demonstrated in Chapter 4 that a workflow integrating machine-learning tools with prototype creation algorithms enables the effective creation and screening of a wide range of different prototypes. This approach, using a minimal amount of DFT calculations, can generate an efficient and accurate ternary phase diagram prediction algorithm with the same quality as fully DFT-created ones. Interestingly, the predictions generated by these workflows are capable of altering the landscape of the AFLOW convex hull and suggesting areas of interest for forming stable intermetallics.

However, the lack of data or minor inconsistencies in the calculated energies translate into significant errors [119] resulting in a decrease in the quality of the screening abilities of the MLIAPs employed. For example, in the Mo-Ta-W ternary system discussed in Chapter 4.3.2, we are able to predict a variety of novel phases for the W-Ta side of the

phase diagram, but the workflow is not efficient in the Mo-rich area. Furthermore, to establish a robust SNAP-based workflow, an increase in the number of DFT relaxations was introduced, resulting in a decrease in throughput. However, it is established that such workflows are able to discover thermodynamically stable structures accurately and perform better than DFT-based methods.

The rise of universal Graph Neural Networks (GNN) [13, 121] offers an alternative to the linear models used in the previous work. Here, we investigate whether such pre-trained models are robust enough to completely bypass the MLIAPs ensemble. If that is the case, such ability would be a great advantage resulting in an increased throughput.

It is demonstrated in Ref. [13] that universal GraphNN is capable of effectively driving the relaxation of the atomic coordinates towards the right path, so that the relaxed structures are most of the time closer to the equilibrium than the initial structures. As a result, prototype structures generated by workflows employing these models, in the relaxation and energy ordering stage, are typically closer to equilibrium, reducing the number of DFT relaxation steps and decreasing computational time.

In this chapter, we investigate whether these models are capable of relaxing and screening ternary compounds that contain magnetic elements. Such an ability would provide them with an advantage over linear models. Although models that incorporate information about magnetic moments exist [122, 123], creating the database with which they are trained is not trivial, as it involves computationally expensive calculations, such as spin-spiral calculations in the case of reference [122]. This makes them less than ideal candidates for integration into relaxation and screening workflows.

Here, we explore the possibility of replacing the linear model (namely SNAP) with a universal GNN (in this case, M3gnet [13]) within the context of the previous workflow. This transition results in a more scalable and simplified workflow scheme. A visual representation of the workflow is presented in Figure 5.1.

After providing a concise overview of the workflow, we introduce the employed Graph Neural Network (GNN) in more detail. Then, we use this workflow to replicate

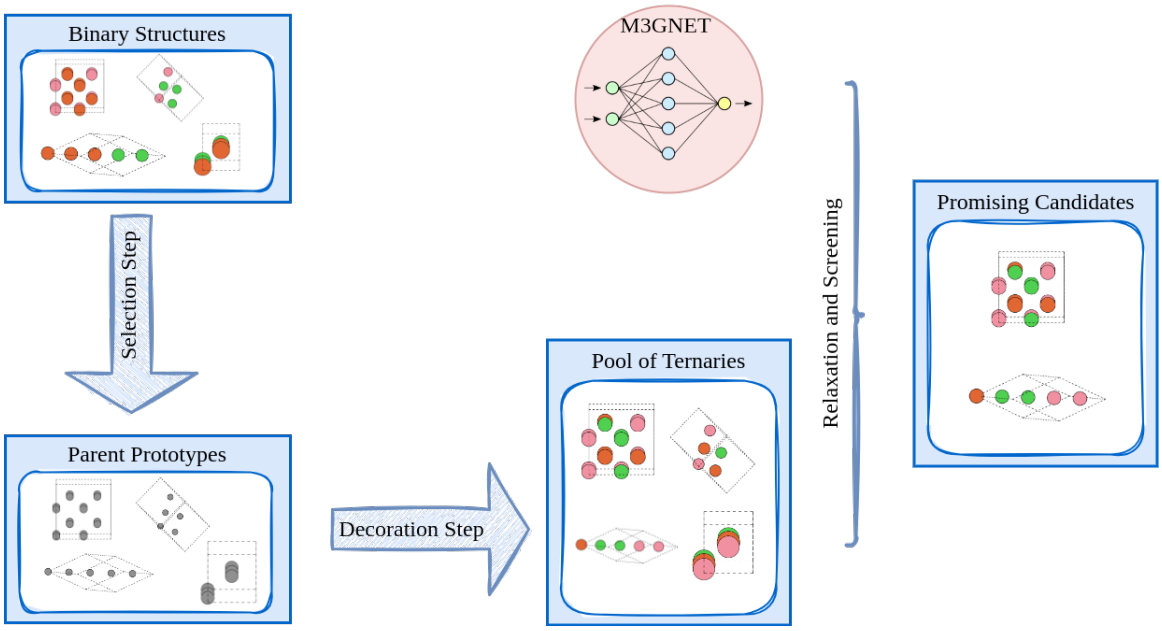

Figure 5.1: The convex hull prediction algorithm, implemented by replacing SNAP with M3gnet. The workflow makes use of the binary structures available to initialise a pool of parent structures. Then, the derivative structures are created from the parent prototypes with the corresponding ternary decoration. Subsequently, the relaxation of these structures is performed followed by the screening of the lowest enthalpy structures. Finally, a DFT relaxation and an single-point SCF calculation are conducted. The phase diagram is updated incorporating the new information.

the results for the Mo-Ta-W ternary system as a benchmark. Following that, we present the results for the Al-Fe-Ni and Bi-Fe-X (with X representing Zr or Ta) ternary systems.

5.2 Graph Neural Networks: MEGNet and M3gnet

Given the significant use of graph neural networks in this chapter of the thesis, it is crucial to provide a more comprehensive introduction to this kind of interatomic potential, in particular of the Megnet and M3gnet architectures. It should be noted that no training was performed for the GNN utilized here. We trace the historical development of how MEGNet [121] initially used as property predictor evolved into M3gnet [13], which is used as a universal force-field.

The discussion starts by introducing the MatErials Graph Network (MEGNet) [121]. Graphs are considered as a natural representation of molecules and crystals, where the nodes/vertex (V) represent the atoms and the edges (E) correspond to the bonds.

The visual representation of the water molecule (H_2O) and the corresponding graph is presented in Figure 5.2.

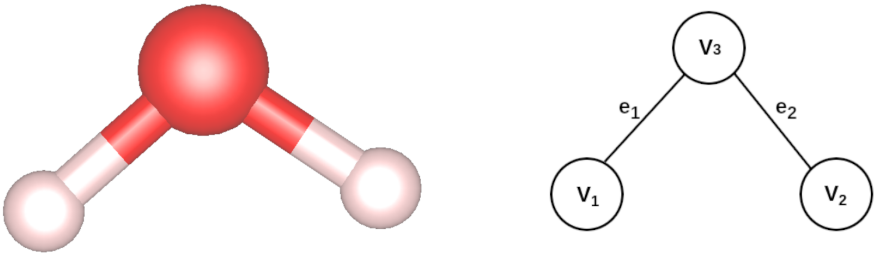

Figure 5.2: On the left hand side of the figure, the water (H_2O) molecule is depicted, with red representing Oxygen and pink representing Hydrogen. On the right hand side, one can see the corresponding graph representation. This graph consists of three vertices,v_1, v_2, and v_3, and two edges, e_1 and e_2.

Although MEGNet is applicable to both molecules and crystals, our focus in this discussion is primarily on the latter, because of the greater relevance to our work. The key distinction between the description of a crystal and a molecule lies in the way the bonds are defined. In the case of crystals, bonds are defined through a radius cutoff, in a way similar to that used in linear potentials, defining the local chemical environment.

The graphs used in the MEGNet model are represented as G = (E, V, $\mathbf{u}$), where E encompasses bond information E = $\{ (e_k, r_k, s_k) \}_{k=1:N}$ for a given system of N atoms. Here, e_k denotes the bond attribute vector, while r_k and s_k refer to the indices of the atoms forming this bond. For example, in Figure 5.2, for $k = 1$, e_1 corresponds to the bond between the atoms indexed by r_1 and s_1 that correspond to node 1 and node 3. Here, the nodes, V, is a set of v_i corresponding to an atomic attribute vector for the atom i in a system that contains N^v atoms. Lastly, the global state vector $\mathbf{u}$ is a vector that contains state attributes.

For the atom attributes, v_i, the atomic number Z of the corresponding element is used. The bond attributes e_k, are then expanded over a Gaussian basis. The state

vector **u**, a vector of two zeros, is initialised and works as a placeholder for any global-state attributes of the system. This initial graph, G, is then fed into an ensemble of MEGNet blocks, which return an updated graph representation, G′ = (E′, V′, **u**′). This update of the representation could perhaps lead the model to "learn" information regarding the magnetic property of the materials without explicitly adding information about the magnetic moment. Subsequent to these blocks enters into the output layer that makes the prediction.

In order to calculate the updated version of the graph, a series of updates needs to take place. The first update acts on the bond attributes e_k, where it leverages information of itself, and the attributes of the connecting atoms v_{r_k} and v_{s_k}, in addition to the global state vector **u**. The updated e'_k is calculated as expressed in Equation (5.1),

$$\mathrm{e}'_k = \phi_{\mathbf{e}}(v_{s_k} \oplus \mathbf{v}_{r_k} \oplus \mathbf{e}_k \oplus \mathbf{u}), \tag{5.1}$$

where $\phi_{\mathbf{e}}$ represents the update function, learned during the training procedure. In this case, a two-layer neural network is chosen for improved model accuracy, and $\oplus$ symbolizes the concatenation operator. The atom attributes v_i are then updated using information from the atom itself, the bonds connected to it, and the global state. In order to calculate the number of bonds and the updated version of the atom attributes, the updated version of the bond attributese'_k from the Equations (5.1) are used,

$$\bar{\mathbf{v}}_i^e = \frac{1}{N_i^e} \sum_{k=1}^{N_i^e} \{e'_k\}_{r_k=i}. \tag{5.2}$$

Then, the update is performed in a similar way to Equation (5.1), namely

$$\mathrm{v}'_i = \phi_{\mathbf{v}}(\bar{\mathbf{v}}_i^e \oplus \mathbf{v}_i \oplus \mathbf{u}). \tag{5.3}$$

Here, Equation (5.2) corresponds to average pooling and Equation (5.3) involves updating atomic details using all the available information up to that stage. The update function $\phi_{\mathbf{v}}$ follows the same learning approach as before, employing a dense two-layer neural network trained to approximate it. Finally, the global attribute **u** is updated taking

advantage of the global information of the atoms, the bonds and itself as follows,

$$\bar{\mathbf{u}}_i^e = \frac{1}{N^e} \sum_{k=1}^{N_i^e} \{e'_k\}. \tag{5.4}$$

$$\bar{\mathbf{u}}_i^v = \frac{1}{N^v} \sum_{i=1}^{N_i^v} \{v'_i\}, \tag{5.5}$$

$$\mathbf{u}' = \phi_{\mathbf{u}}(\bar{\mathbf{u}}_i^e \oplus \bar{\mathbf{u}}_i^v \oplus \mathbf{u}), \tag{5.6}$$

where N^e and N^v are the total number of bonds and atoms in the system, respectively. Regarding the update function ϕ, the choice is made solely to enhance the performance of the model and it is treated as a hyperparameter of the model. For all the cases, a dense deep neural network with two hidden layers was used. Then, the updated function can be approximated with Equation (5.7), based on the weights, W_i and biases, b_i, of each layer,

$$\phi = W_3(\zeta(W_2)(\zeta(W_1\dot{x} + b_1)) + b_2) + b_3, \tag{5.7}$$

where W_3 corresponds to the weights of the output layer and W_2 and W_1 are the weights of the second and first hidden layer, respectively. A graphical representation of the MEGNet architecture is presented in Figure 5.3.

MEGNet was mostly used as a property predictor, mainly for energy, of molecules and crystals. In contrast, M3gnet is used as an interatomic potential. M3gnet trained on a subset of Materials Project database [94] that contains more than 187,000 ionic relaxation steps that offer more than 187,000 energies, 16,000,000 forces and 1,600,000 stress tensors, is a universal potential for 89 elements. In the next few paragraphs we are going to discuss it in greater detail.

The key difference between MEGnet and M3gnet that allows the latter to be used as an interatomic potential is the addition of a many-body interaction component in the representation. In this case, the input graph is referred to as $G = (V, E, X, [\mathbf{M}, \mathbf{u}])$ where, in a similar way as previously, V contains information regarding atoms, E

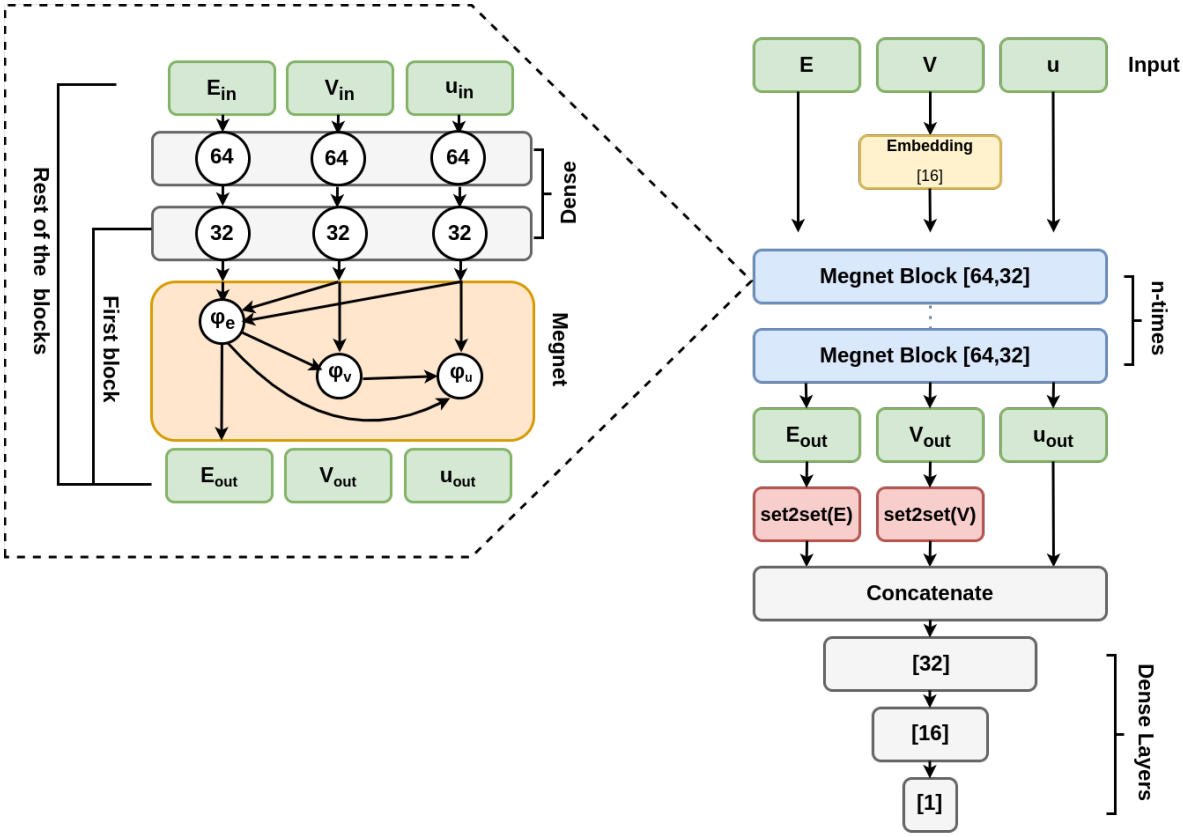

Figure 5.3: A graphical representation of the MEGNet architecture. Initially the graph representation $G = (E, V, \mathbf{u})$ is fed to the model. In the case of crystals the representation regarding atoms, V, is expanding into 16-element vector, with the use of an embedding layer. Following that, the representation is fed in a series of MEGNet blocks, the components of which are two fully connected hidden layers and the updating functions that are approximated with two fully connected hidden layers as well. Also, for training purposes the input representation is added in the output of the block, in a similar way to the Residual Network [124]. Consequently, a set2set layer reduces the atom and bonds representation, that so far was a set of components for each atom, to a single vector, following by a concatenation step. Then, a number of fully connected layers results to an output layer.

corresponds to bond information, $\mathbf{u}$ is the global state information, X is the information regarding the atomic coordinates, and M is a 3×3 crystal matrix necessary in order to obtain predictions for the stresses and forces, using backpropagation.

Suppose a chemical environment with atoms i, j and k as shown in Figure 5.4 then the angle between the bonds e_{ij} and e_{ik} is denoted as θ_{jik}. In order to calculate the updated bond equations, the three-body angular interactions are expanded with the use of Bessel and spherical harmonics as in the Ref. [125]. The bond update function is rewritten as,

$$\tilde{\mathrm{e}}_{ij} = \sum_k j_l(z_{ln}\frac{r_{ik}}{r_c})\, Y_l^0(\theta_{jik}) \odot (\mathbf{W}_u u_k + \mathbf{b}_u) f_c(r_{ij}) f_c(r_{ik}), \tag{5.8}$$

$$e'_{ij} = e_{ij} + g(_2\tilde{e}_{ij} + _2) \odot \sigma(_2\tilde{e}_{ij} + _1), \tag{5.9}$$

$$f_c(r) = 1 - 6(\frac{r}{r_c})^5 + 15(\frac{r}{r_c})^4 - 106(\frac{r}{r_c})^3 \tag{5.10}$$

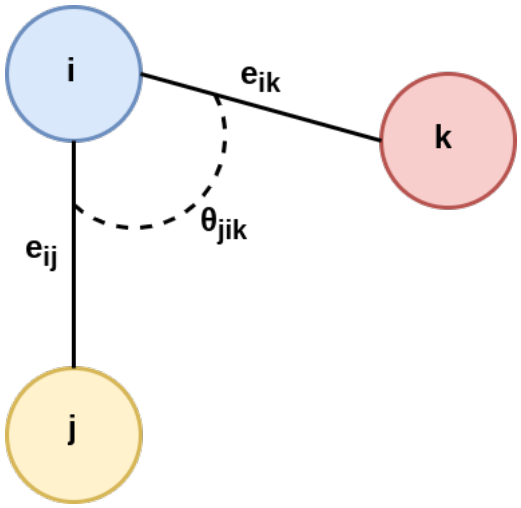

Figure 5.4: Local chemical environment between the atoms i, j and k. The corresponding bonds are denoted with e_{ij} and e_{ik} and the angle between these bonds is represented by θ_{ijk}.

where $\mathbf{W}$ and $\mathbf{b}$ are the weights and biases of the neural network. The spherical Bessel function is j_l and the spherical harmonic with $m = 0$ are Y_l^0, the $\odot$ operator corresponds to the element-wise product, σ corresponds to the sigmoid function and the $f_c(r)$ is given by Equation (5.10). Furthermore, $g(x) = x\sigma(x)$ is the nonlinear activation function. Following that, similarly to MEGNet, the bond, atom, and global state information are updated. The only difference lies in the updating function used in this new model. Here, it is represented by a gated multilayer neural network. The gated multi-layer NN is an architecture that combines traditional NN with a gating mechanism that controls the flow of information. This enhances the learning of complex patterns. The equations in which the updating mechanism takes place are presented as follows

$$\mathbf{e}'_{ij} = e_{ij} + \phi_e(u_i \odot u_j \odot e_{ij} \odot u)\mathbf{W}_e^0 \mathbf{e}_{ij}, \tag{5.11}$$

$$v'_i = v_i + \sum \phi'_e(v_i \odot v_j \odot e'_{ij} \odot u)\mathbf{W}_e^{0\prime} \mathbf{e}_{ij}, \tag{5.12}$$

$$u' = g[\mathbf{W}_2^u g\{\mathbf{W}_1^u(\frac{1}{N_v}\sum_i^{N_u} \mathbf{v}_i \odot \mathbf{u}) + b_1^u\} + \mathbf{b}_2^u], \tag{5.13}$$

where N_v is the number of atoms of the system. The updating functions ϕ_e and ϕ'_e are approximated in a similar way as previously. A graphical representation of the architecture of the model used in this work is presented in Figure 5.5.

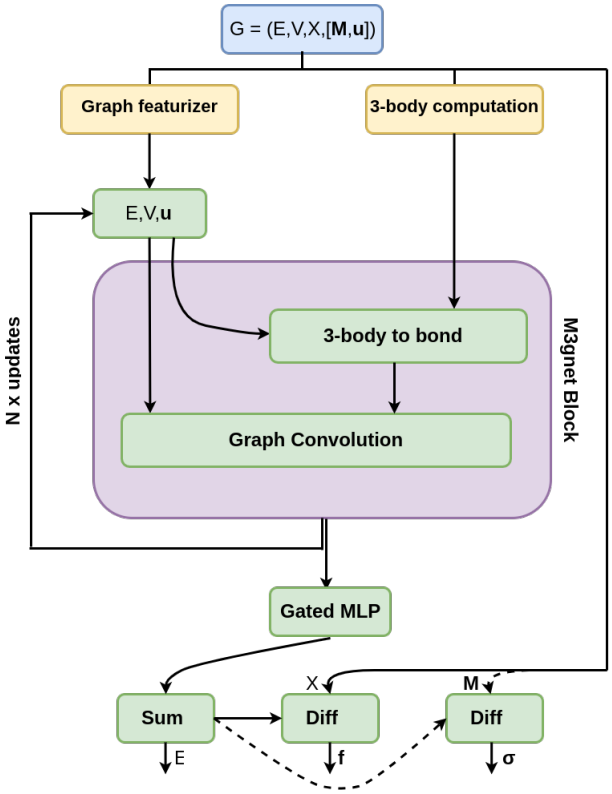

Figure 5.5: In this figure a graphical representation of the M3gnet architecture is presented. Initially the graph representation $G = (E, V, X, [\mathbf{M}, \mathbf{u}])$ is introduced to the model. Then, based on this information a graph featurizer and a 3-body calculation step are introduced. Following that, the M3gnet block in which we have the 3-body to bond step which uses bond information regarding the description to calculate the 3-body interactions. Then in the graph convolution step, the update of the bond, atom, and global state information takes place. Exiting the stacked M3gnet blocks there is a gated Multilayer Perceptron (MLP) resulting in the output layer.

As observed in Figures 5.5 and 5.3 the differences between these two models are limited to the architecture. The key difference of M3gnet is related to how the

information regarding the local chemical environment is implemented in the descriptor. This upgrade is crucial, so that M3gnet can be employed as an interatomic potential, in contrast to its predecessor, which was mainly used as a property predictor.

5.3 M3gnet-based workflow : M3GW

Here, we explain the different parts of the M3gnet-based workflow (M3GW) with respect to the previously implemented SNAP-based one. These both share the same underlying idea and core steps. For a given ternary system, say A-B-C, energy and crystal structure information for compounds involved in the convex hull construction of the three binary phases, namely A-B, A-C, and B-C, is extracted. Subsequently, a preliminary pool of parent structures is chosen based on their convex hull energies. The energy window, which determines the maximum distance from the convex hull for structure selection, is then individually calibrated for each binary phase diagram. This ensures a balanced pool of parent prototypes, where each binary convex hull contributes an equal number of structures. Next, the AFLOW-SYM tool [115] is utilized to identify structures with unique crystal lattices and the fewest number of atoms.

The pool of structures established in the previous step serves as the *parent* prototypes, used in the decorating process. Enumlib [76] is, then, utilized to generate all possible derivative structures for a given stoichiometry up to a specific number of atoms, $N_{\max}$, creating the candidate compounds. The key difference in M3GW lies in the fact that there is no potential training or optimization process. Furthermore, there is no need for multiple relaxations per candidate structure.

The procedure is then rather straightforward, where the MLIAP relaxes the structure (in this case we relaxed each of the structures for 50 steps). Then the energy of the relaxed structure is assessed and stored. Upon completion of the relaxation process, the workflow arranges the predicted structures based on their energies. The 15 structures associated with the lowest energies are then selected for DFT relaxation.

Here, DFT calculations performed during this workflow with the Vienna Ab-initio Simulation Package (VASP) [28]. Projector augmented wave (PAW) pseudopotentials

are used for each element together with the Perdew-Burke-Ernzerhof (PBE) functional [27]. A 600 eV plane-wave cutoff is used for all calculations. The energy convergence criterion for each self-consistent cycle is 10^{-4} eV. Full atomic relaxations are performed (update of the atomic positions, cell volume and lattice parameters) with a stopping criterion on the forces of 10^{-3} eV/Å. A Fermi-Dirac smearing of 0.2 eV is chosen and a Γ-centered k-point mesh is used for all calculations. The density of the mesh and the spacing between the k-points are chosen according to the convergence criteria of AFLOW [97]. The mesh is system specific and determined from the N_{KPPRA} (number of k-points per reciprocal atom) as defined in Equation (3.2). The total number of sampling points per reciprocal atom is then minimized, and N_{KPPRA} is used as a lower bound. Values of 10^4 and 6×10^3 are used for static calculations and relaxations, respectively.

In cases where magnetic elements are present in the system studied, collinear spin-polarized calculations are performed. Initialization of magnetic moments aligns with the AFLOW standards [97]. Specifically, a magnetic moment of 5 μ_b/atom is initialized for Fe, while for the remaining elements we employ 1 μ_b/atom. It is important to note that this workflow does not include spin-orbit coupling due to its high computational cost, which makes it unsuitable for high-throughput applications. A graphical representation of the workflow discussed is presented in Figure 5.6.

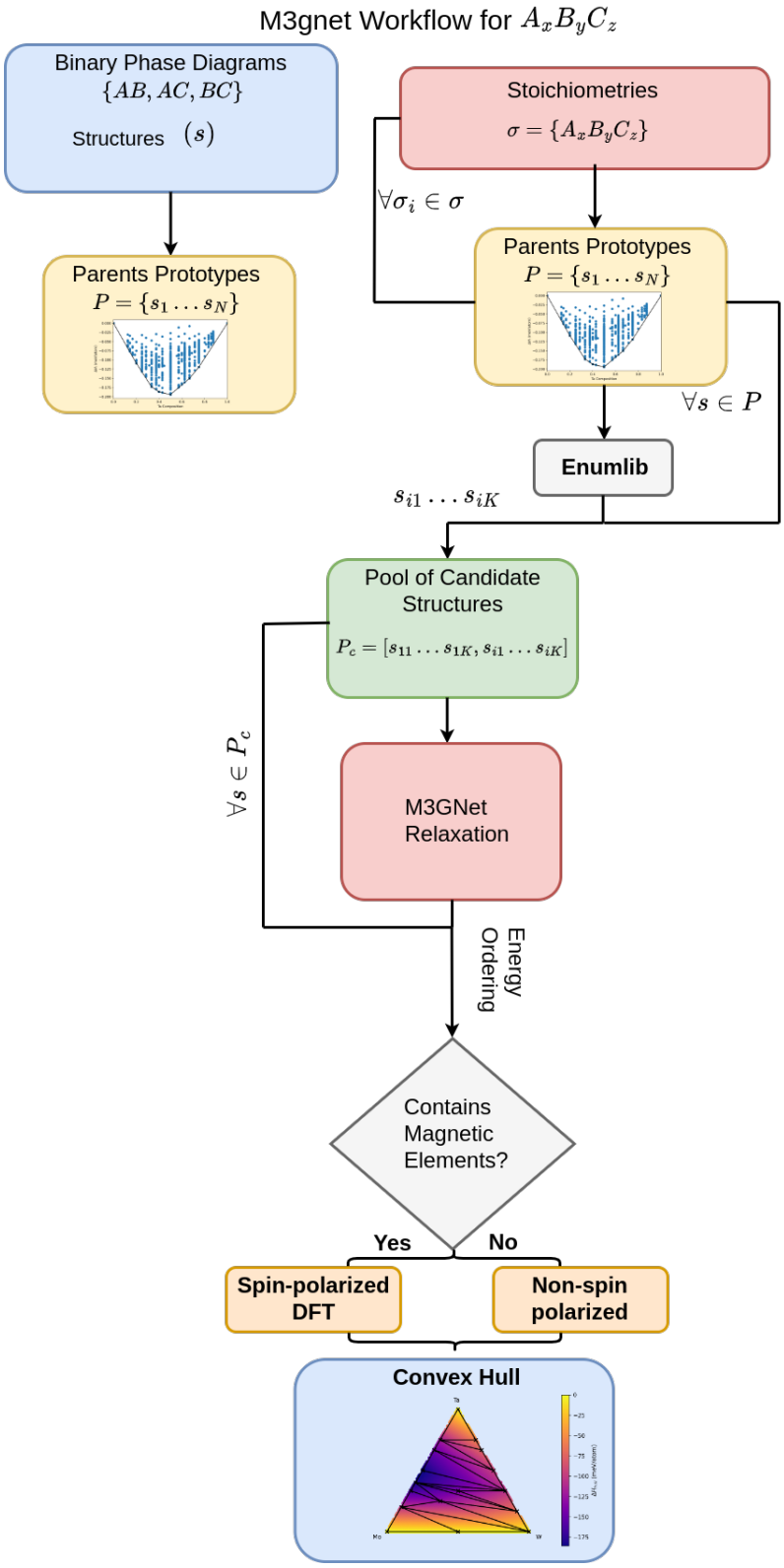

Figure 5.6: The main steps of the M3GW are illustrated in a flowchart. The process begins by extracting the binary phase diagrams of the system's constituents. Next, a parent prototype set is formed by selecting structures that closely align with the convex hull of each binary phase. For each stoichiometry under investigation and for every parent structure, derivative structures are generated using enumlib [76–78], provided that the parent structure is appropriate. Then, M3gnet is employed to perform a relaxation for each structure produced in the previous step, sorting them based on energy. In the final step, for the 15 structures that correspond to those with the lowest predicted energy, DFT calculations are initiated.

It is of great interest to discuss the throughput of this workflow. The most expensive part of this algorithm is the relaxation and the energy prediction part. To be able to run the workflow in parallel in a high-performance computing (HPC) system, we take advantage of the task farming system that almost all HPC systems provide. This helps us to run one calculation per CPU, meaning that we can run multiple parallel calculations on a single node. To take advantage of this option, after creating the pool of ternary prototypes, we split them into batches and perform the relaxation of a corresponding batch per CPU in a node. Then, the results are collected and ordered based on their energy. A graphical representation of this procedure is presented in Figure 5.7.

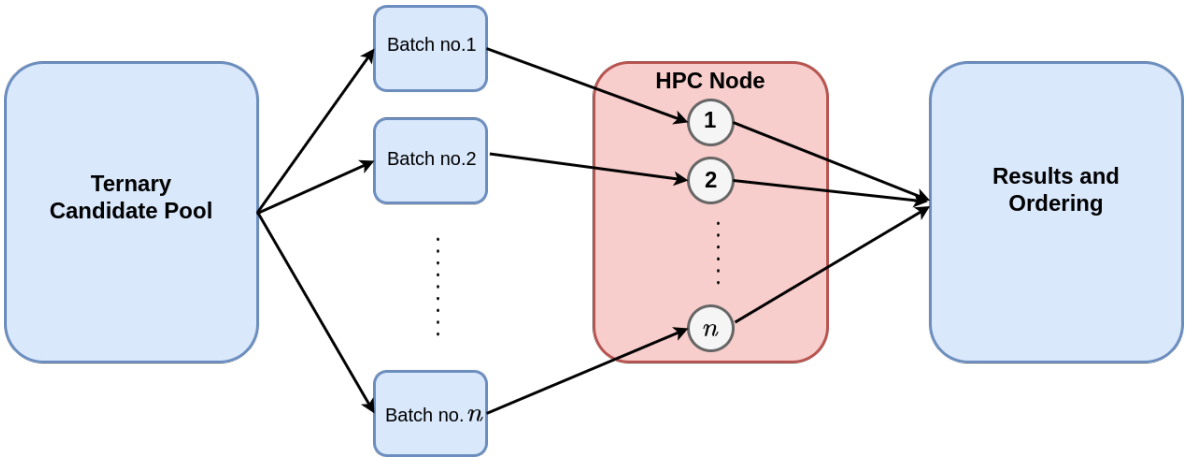

Figure 5.7: A graphical representation of the task-farming approach used in this workflow. Firstly, the created amount of ternary candidates is splitted into batches. Then, each of the CPUs in a given node is allocated with the relaxation and the prediction of energy for each structure in the batch. Then the energies are collected and ordered.

In order to measure how this split affects the running time, we performed a parallel efficiency test. For this test, 70,000 candidate structures created with M3GW were used. Following that, we split them into batches according to the number of processors. Then we initialized a 50-step relaxation and an energy prediction for each one of them. To quantitatively measure the effect in the CPU-hours of the split of the data, we calculated the parallel efficiency ϵ as defined

$$\epsilon = \frac{1}{P}\frac{T_1}{T_P}, \tag{5.14}$$

where P is the number of processors used. Here, T_1 is the time it takes for the calculation to run in one processor and T_P is the time for the number of P processors. Then the speedup is defined as $S = \epsilon P$. The results are presented in Figure 5.8.

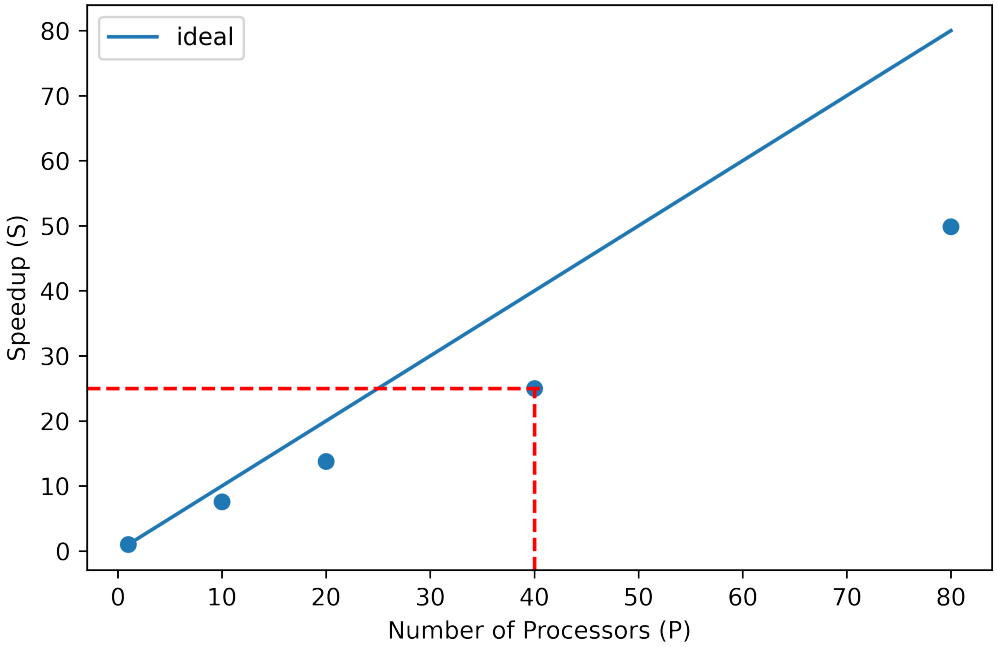

Figure 5.8: Speedup as a function of the number of processors. It is observed that there is a decline from the ideal linear case. For our case we selected to split the calculations in 40 batches as it is the maximum number of cores per node in the cluster that we are using.

By selecting 40 CPUs to run our calculations, we take advantage of the entire cluster node available. The clock time that takes for the system to relax 70,000 structures in 40 processors is 74 minutes, which provides us enough freedom to increase the maximum number of atoms used to create the derivative structures.

5.4 Results

This section is divided into three subsections, each aimed at presenting the main outcomes of our methodology. Firstly, we evaluate the efficacy of our newly developed workflow by comparing its performance against the well-studied Mo-Ta-W ternary phase diagram (see Chapter 4). Secondly, we employ our workflow to study ternary systems containing magnetic elements. In particular, we use the extensively researched Al-Fe-Ni phase diagram as a benchmark [126, 127] to assess the reliability of our

workflow when it comes to exploring systems containing magnetic elements. Lastly, we use the workflow to predict the convex hulls of different Bi-Fe-X systems, where X can be either Ta or Zr, in the search of novel magnetic materials with interesting properties.

Regarding evaluating the stability of the predicted prototypes and ensuring consistency in the analysis, the same procedure as in Chapter 4 is followed. The QHull algorithm [117] is used to calculate the convex hulls presented in this chapter. The data used to construct the reference convex hull correspond to the thermodynamically stable ground-state compounds calculated and stored in the AFLOWlib repository. In order to ensure consistency among calculations, the energies of these compounds were recalculated with the Vienna Ab-Initio Simulation Package (VASP) [28]. Throughout the entire process, we have adherently followed the AFLOW standards defined by Calderon et al. [97].

5.4.1 Mo-Ta-W ternary system

We used M3GW to predict the ternary convex hull of the Mo-Ta-W system as a benchmark. This ternary system was chosen because it was extensively studied with the first version of the workflow, presented in Chapter 4, and was also thoroughly investigated with the AFLOW encyclopedia method. The usefulness of the present methodology is associated to the performance with this system as compared to the previous workflow. Furthermore, this comparison serves to demonstrate the capabilities and limitations of the workflow. M3GW demonstrates several differences compared to the SNAP-based workflow, particularly in the selection of the candidate compounds, as discussed in Section 5.3.

The parent structures used for the prototype creation are the same as those used in Chapter 4.3.2, for more details, see Appendix C. As before, the maximum number of atoms, $N_{\max}$, was chosen to be equal to nine. As expected, the universal potential might be less accurate in the energy predictions compared to an MLIAP created specifically for a studied system. In order to balance this decrease in accuracy, we increase the number of structures selected for DFT relaxation to 30, needs to be noted that with

SNAP-based worfklow we sampled 15 compounds per stoichiometry. Phase diagrams for the Mo-Ta-W ternary systems predicted with the SNAP-based workflow and M3GW are presented in Figure 5.9.

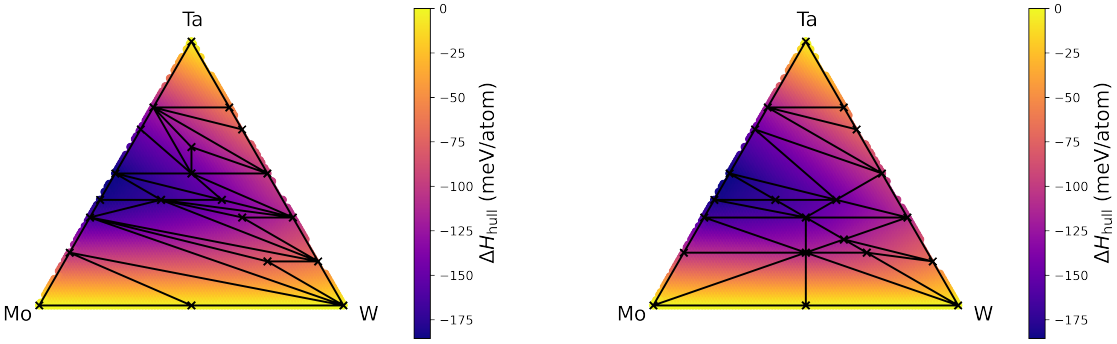

(a) (b)

Figure 5.9: The SNAP-based workflow predictions (a) and the M3GW ones (b) are presented. It can be observed, that while the SNAP-based workflow offers better results in the Ta-W heavy region, the M3GW one excels in predicting structures in the Mo-W rich region. Both workflows demonstrate sufficient accuracy in the central area of the phase diagram.

We observe that both phase diagram predictors have sufficient accuracy in the central region of the phase diagram. Interestingly, this area is where the AFLOW encyclopedia method also excels. On the one hand, the SNAP-based workflow [see Figure 5.9(a)] performs better than M3GW in the Ta-W region, as it is able to identify five stable intermetallics. Interestingly, the Ta-W binary system exhibits the larger number of thermodynamically stable binary compounds compared to the rest of the binary phase diagrams, namely 5. On the other hand, the M3gnet-based workflow [see Figure 5.9(b)] performs slightly better in the Mo-W region of the phase diagram as it is able to predict three novel ternary intermetallics. Furthermore, both methods are able to identify one W-rich thermodynamically stable ternary alloy. The training set of M3gnet contains a higher volume of data for Mo and W as compared to Ta [13], a fact that could potentially explain the higher accuracy towards this area of the phase diagram. The distribution, in fact, could potentially explain why M3gnet is capable of selecting the lowest energy structures in that specific area more efficiently. The difference between the M3GW and the AFLOW-predicted convex hull is presented in Figure 5.10, which shows schematically how the phase diagram changes with the use

of each of the different workflows.

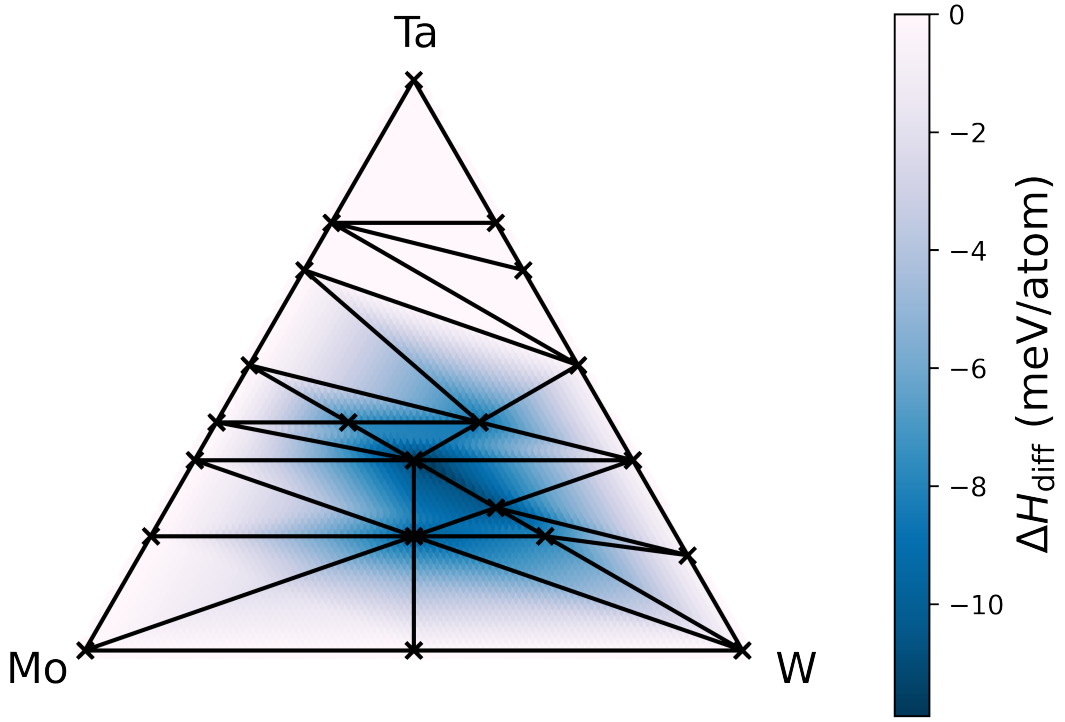

Figure 5.10: The difference between the AFLOW- and the M3GW-predicted is graphically presented. We can see that the M3gnet-based workflow is performing better compared to the AFLOW-predicted ternary phase diagram. The maximum difference between these two convex hulls is of 11.90 meV/atom.

The shape of the convex hull changes when compared to the one calculated with AFLOW (shown in Figure 4.13) which leads to the prediction of novel intermetallics. The newly calculated stable intermetallics are $Mo_2Ta_2W_1$, $Mo_1Ta_2W_2$, $Mo_2Ta_1W_2$, $Mo_1Ta_1W_3$, and $Mo_1Ta_1W_2$, while the compound predicted by both methods is $Mo_1Ta_1W_1$. Interestingly, the $Mo_2Ta_1W_1$ compound predicted as stable by the AFLOW-CHULL is now predicted to be metastable on the newly calculated convex hull. Overall, we see that using M3GW the predicted convex hull changes shape in the central and Mo-W-rich area, leading to a decrease of around 10 meV/atom.

Following that step, it is crucial to compare the results obtained from M3GW with those predicted from the SNAP-based workflow. In order to do this we calculated the difference between the convex hulls constructed with SNAP and M3GW. This is presented schematically in Figure 5.11. Two distinct regions, blue and red, are observed. In the blue one, the M3GW is able to predict structures with lower energy

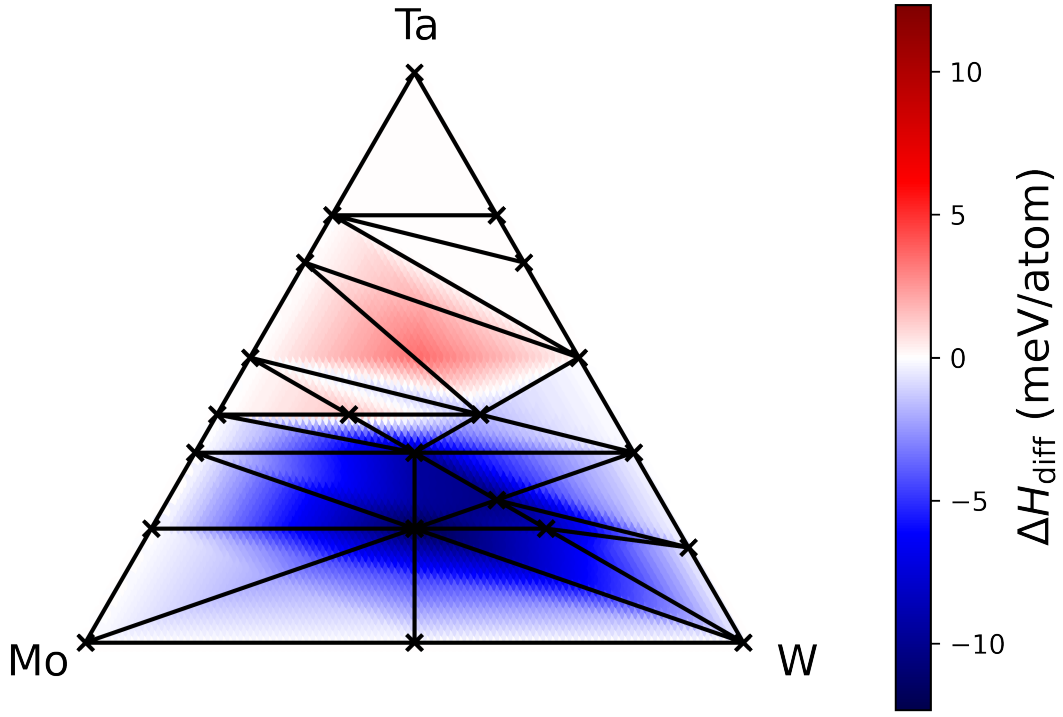

Figure 5.11: The difference between the SNAP-based and the M3GW-predicted convex hull is graphically presented. It can be seen that two regions exist. The red region is where the SNAP-based workflow identifies low-energy structures, with a convex hull depth increase of 3 meV/atom at the lowest point. In contrast, the blue region is where the M3GW performs better in identifying low energy structures, reducing the convex hull depth by 12.33 meV/atom at the lowest point.

than those predicted with the SNAP-based workflow, this results to decrease in the depth of the convex hull up to 12.33 meV/atom. This region corresponds to where the M3GW finds the majority of the thermodynamically stable ternary intermetallics. In contrast, in the red one, the M3GW-predicted convex hull is 3 meV/atom higher than that computed with the SNAP-based workflow. A combination between these two methods would be beneficial for a thorough investigation of that particular phase diagram. Combining the predictions from these two workflows results in a phase diagram showing phases in the largest area of it, according to the experimental literature [120], which states that a solid solution is expected across all the ternary phases.

By combining the predictions of these two workflows, one can construct a "complete" phase diagram of the Mo-Ta-W ternary system. In the next step of the analysis, we combine all the ternary structures predicted from the SNAP-based and M3GW and we

compute the convex hull. We refer to this phase diagram as " complete ". This phase diagram is presented in Figure 5.12.

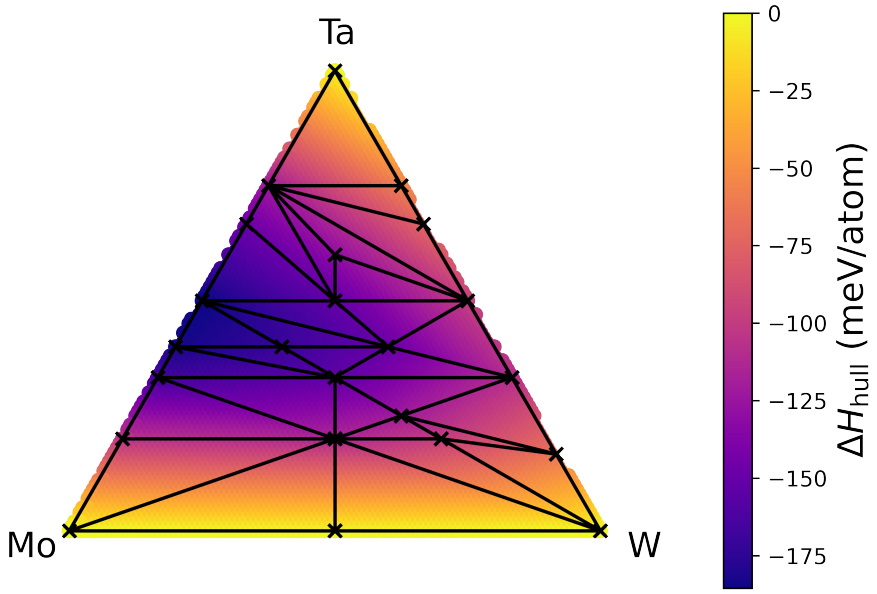

Figure 5.12: The "complete" Mo-Ta-W phase diagram is displayed. In this diagram, we can discern eight distinct intermetallics with Mo-Ta-W stoichiometries of 1-1-1, 1-1-2, 1-2-1, 2-2-1, 2-1-2, 1-2-2, 1-3-1, and 1-1-3. When SNAP-based and M3GW are combined, stable intermetallics can be identified throughout the entire ternary phase diagram.

In the final part of our analysis, we focus on the compounds predicted to be thermodynamically stable using either the SNAP-based or M3GW workflows. To gain a better understanding of the contribution of each workflow, namely SNAP-based and M3GW, to the 'complete' phase diagram, we present the formation enthalpy for the compounds predicted by M3GNET (depicted as blue pentagons), the SNAP-based workflow (represented by black crosses), and AFLOW (shown as orange circles). Additionally, we include the enthalpy of formation at the convex hull predicted by AFLOW, CH_{aflow}, and M3GW, CH_{M3gnet}, presented as red and green dashed lines correspondingly. This plot is presented in Figure 5.13.

The general result arising from Figure 5.13 is that there is a decrease in the depth of the convex hull for all the cases studied when the MLIAPs-based workflows are used. Furthermore, M3gnet is capable of identifying structures that lie close or at the convex hull. In cases where it is not capable to find a compound thermodynamically stable as for the Ta-rich compounds, the structures predicted are sufficiently close to

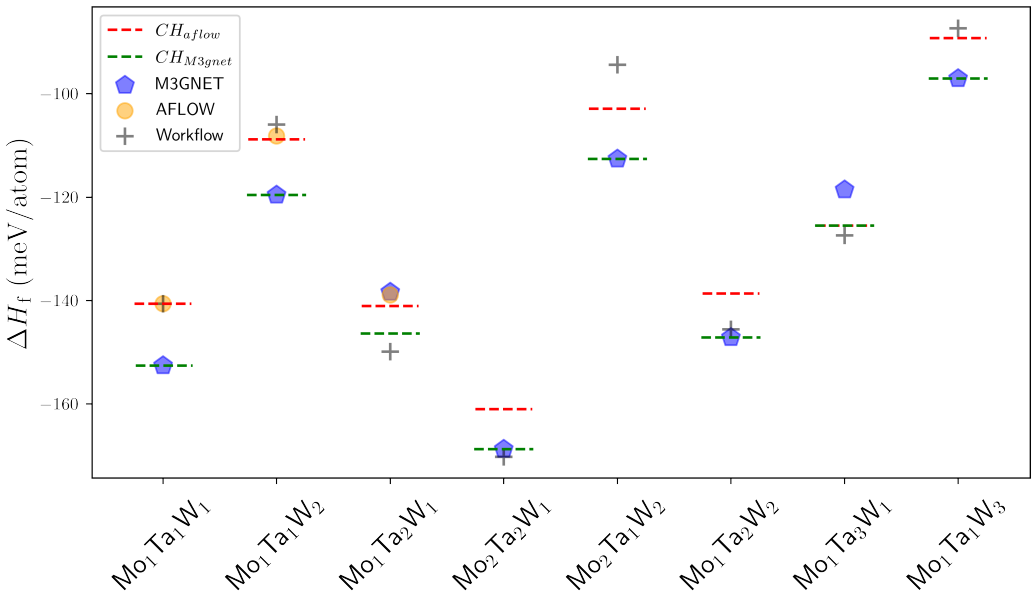

Figure 5.13: The convex hull values as predicted by AFLOW (red dashed line) and M3gnet (green dashed line) for each studied stoichiometry are presented. The lowest enthalpy of formation for the structures predicted with each methodology is presented, namely AFLOW (orange circles), SNAP workflow (black crosses), and M3gnet workflow (blue pentagons). In general a decrease in the depth of the convex hull with respect to the AFLOW predicted one is observed, apart the $Mo_1Ta_3W_1$, where both methods yield the same result. For the majority of the cases, the compounds predicted by the M3gnet workflow exhibit lower energy than those predicted by the AFLOW or SNAP-based workflow. Note that for $Mo_1Ta_2W_1$ and $Mo_1Ta_3W_1$, the compounds predicted from the SNAP-based workflow exhibit lower energy than those predicted from M3GW. Overall, the MLIAP based workflows perform consistently better than the AFLOW encyclopedia method. Note that AFLOW predicts negative enthalpy of formation for only the $Mo_1Ta_1W_1$, $Mo_1Ta_1W_2$, $Mo_1Ta_2W_1$.

the prediction of the SNAP-based workflow, with the difference being of the order of a few meV/atom. It is not surprising that the AFLOW encyclopedia method underperforms in almost all cases studied. The number of structures that can be scanned is on the order of 10^2, while machine-learning-based methods can screen approximately 10^5 to 10^6 compounds, which are based on a variety of parent structures, providing more versatility than fully ab-initio methods.

In conclusion, the advantages of the presented method stem from the fact that it employs a universal potential that does not require retraining for each new system under investigation. This approach can significantly increase throughput, as the focus shifts towards selecting a broader range of parent structures for decoration. Furthermore, the method robustly guides the relaxation of a compound along the correct path, reducing

the time needed for the DFT relaxation in the final stages of the workflow. However, it should be noted that such force fields may exhibit lower accuracy compared to force fields tailored specifically for a given system.

5.4.2 Al-Fe-Ni ternary system

In this subsection, the M3gnet-based workflow will be used to predict the phase diagram of ternary compounds that contain magnetic elements. Before moving to the main results, let us explain why a SNAP-based workflow would not be capable of predicting the energies of such structures.

The machine-learning model that we have used so far is able to learn the relationship between the local chemical environment and the total energy of the system. In order to do so it expands the neighbor density over a given basis thus creating the necessary feature vector. In the case of SNAP the local chemical environment is defined within the radius cut off, R_{cut}, and it is expanded on the basis of 4D hyperspherical harmonics. Subsequently, the use of the triple-scalar product of the coefficients of the expansion leads to the definition of the bispectrum components, as discussed in Section 2.2.5.

Consider now a magnetic material, for a two-dimensional cubic lattice presented in Figure 5.14. The SNAP force field does not contain any information regarding the magnetic state of a structure. In fact, for these two lattices, the trained model would predict the exact same energy, because no information on the magnetic state is introduced in the representation. Although, their total energy is different. Having no possibility to distinguish different magnetic orders makes SNAP a bad choice to integrate into a workflow that aims to discover materials that contain magnetic elements. Moreover, although force-fields that contain information regarding the magnetic moment of the system exist [122, 123] the data that such models need and the training process are not trivial.

In order to demonstrate this point, we have downloaded the crystal-structures and spin-polarized DFT energies from the AFLOWlib repository for the Fe-Co-Ni ternary system. Then, we fit a SNAP in the same way as discussed in Chapter 3. The results

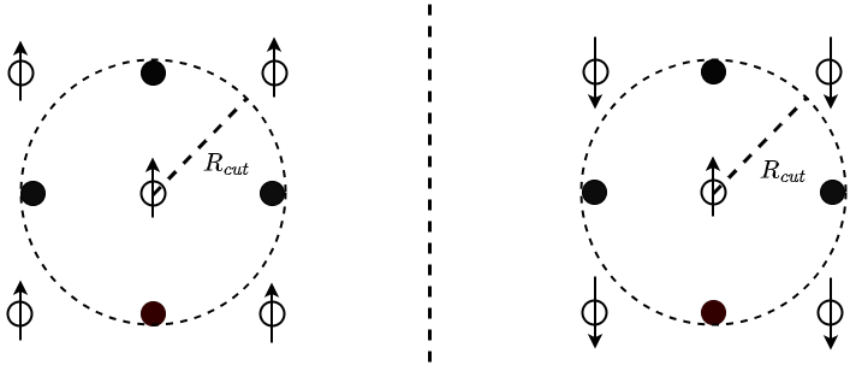

Figure 5.14: A two-dimensional cubic lattice for two different magnetic configurations.

are shown in Figure 5.15.

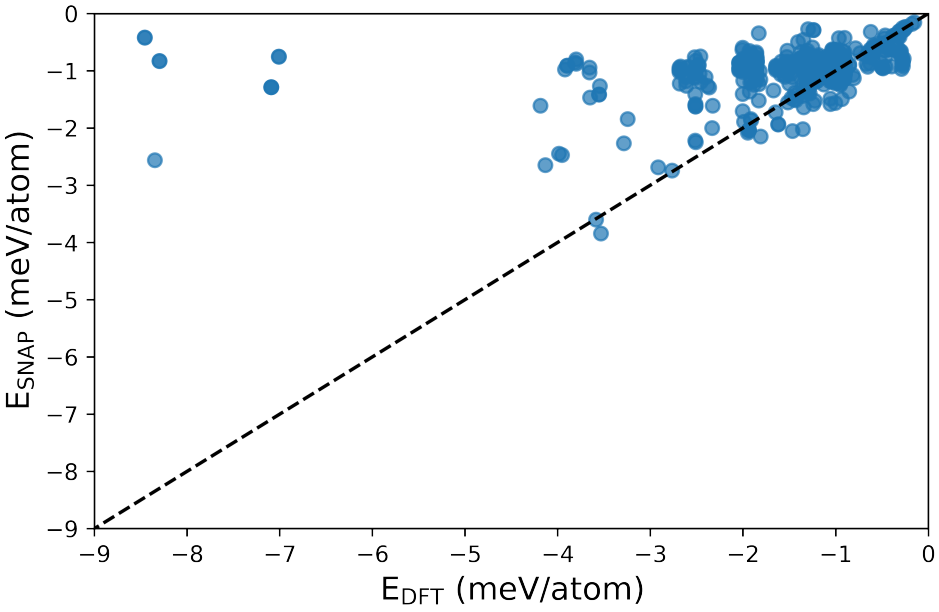

Figure 5.15: Parity plot for the Fe-Co-Ni binaries, namely Fe-Co, Fe-Ni, and Co-Fe. Here, the model is trained and optimized with the three binary systems. It can be observed that the trained model fails to predict the energies of the binaries that it was trained on. Also, no clear trend can be observed as the model predict high energy for structures that are known to exhibit low energy.

In the parity plot in Figure 5.15, one can observe that a SNAP model trained with the three binary constituents of the Fe-Co-Ni ternary system cannot predict the energies for the compounds with which it was trained. Furthermore, no clear energy trend is presented, as low-energy structures are predicted to exhibit high energy. This is due to the SNAP model lacking information regarding the magnetic state of the corresponding compounds.

There are works in the literature that incorporate information regarding the magnetic

moment in the description of the local chemical environment. For instance, the power-spectrum for vector fields in [123] introduces descriptors that take into account the magnetic structure of the compound. Another work is that contained in reference [122], where a spin Hamiltonian term was added to SNAP and deployed and deployed to correct the total energy with its magnetic component.

In contrast to the previously discussed methods that incorporate information about the magnetic state of the system into the feature vector, M3gnet, trained with DFT calculations of compounds containing magnetic elements (Fe, Co, Ni, etc.), has demonstrated robustness in guiding the relaxation towards the correct path and accuracy in sufficiently ordering the structures. Although this seems surprising, it can be attributed to the mechanism by which graph neural networks update the representation during the training process. Furthermore, the update of the global attribute that is incorporated in the descriptor might be able to learn information regarding the magnetic state of the system.

The first system containing magnetic elements employed to benchmark our method is the Al-Fe-Ni system. The rationale behind this choice lies in the fact that it is a well-studied ternary system, both experimentally and theoretically [126, 127]. Furthermore, all the elements form stable binary alloys with each other, for example the Al-Ni binary system exhibits the maximum convex hull depth and forms 6 stable binary alloys. This means that there is a high probability that ternary intermetallics are discovered.

In order to ensure consistency in the analysis performed in this chapter, we start by re-calculating the AFLOW-predicted phase diagram. The structures used from AFLOW to calculate the phase diagram are extracted with the use of AFLOW REST-API. Subsequently, VASP [28] was used to perform DFT calculations, with the energy cutoff and plane cutoff following the AFLOW standards defined by Calderon et al. [97] (for more information, see Chapter 5.3). The phase diagram predicted by AFLOW is presented in Figure 5.16.

Here, in Figure 5.16 we reproduce the shape of the convex hull as predicted with AFLOW. One stable ternary intermetallic phase is predicted for the $Al_2Fe_1Ni_1$ and the

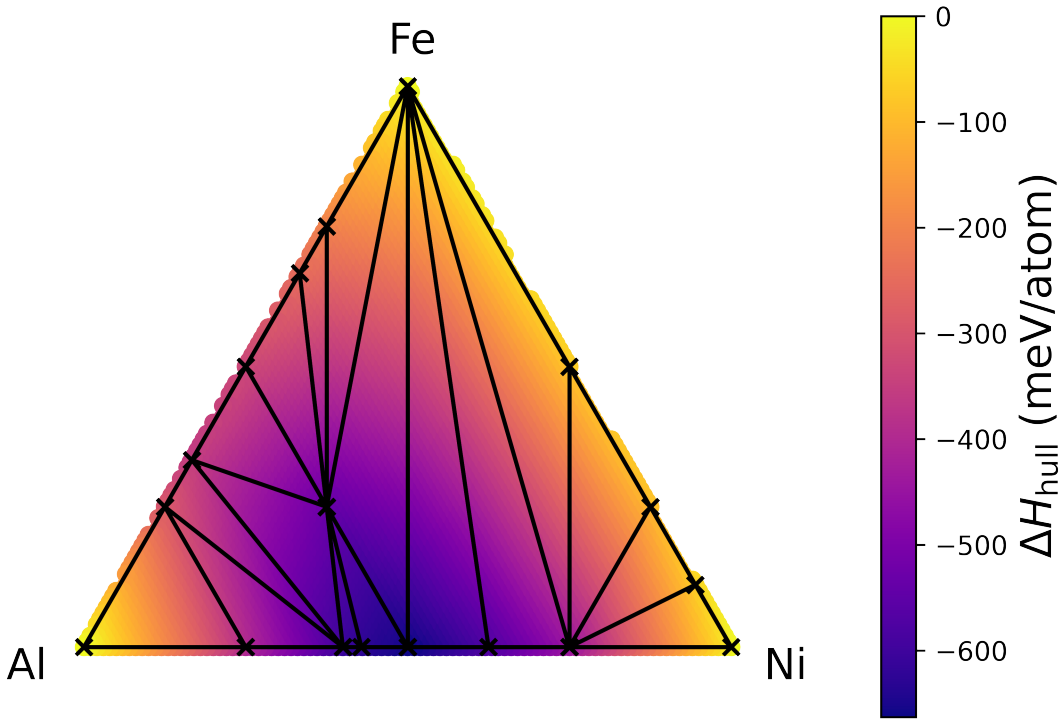

Figure 5.16: Calculated convex hull for the Al-Fe-Ni phase diagram as predicted with AFLOW. Here, a stable intermetallic was found in the Al-rich area, namely $Al_2Fe_1Ni_1$.

maximum depth of the convex hull is identified at the Al-Ni (Al_1Ni_1) side of the convex hull. Moreover, the number of stable binaries remained unchanged for each side of the convex hull.

It is experimentally [128] and theoretically known that there are two more intermetallic phases in the aluminum-rich area of the ternary phase diagram. These two phases correspond to the $Al_{10}Fe_3Ni_1$ (τ_1), which is of Co_2Al_5-structure type as was found in reference [129] and $Al_9Fe_1Ni_1$ (τ_2), which has been found to crystallize in a monoclinic lattice of Co_2Al_9-structure type as reported in reference [130]. Initially, these two compounds were not considered due to the fact that their unit cells contain a significantly large number of atoms (28 and 22 atoms respectively), making them impractical for examination using a high-throughput algorithm. In order to perform a more complete analysis, we have calculated the ground-state energy of these two intermetallic phases, added them to the phase diagram, and assessed their stability. The structures for the two phases are extracted from the reference [128]. The crystal structures of the phases τ_1 and τ_2 are presented in Figure 5.17.

Subsequently, the enthalpies of these two intermetallic compounds are incorporated

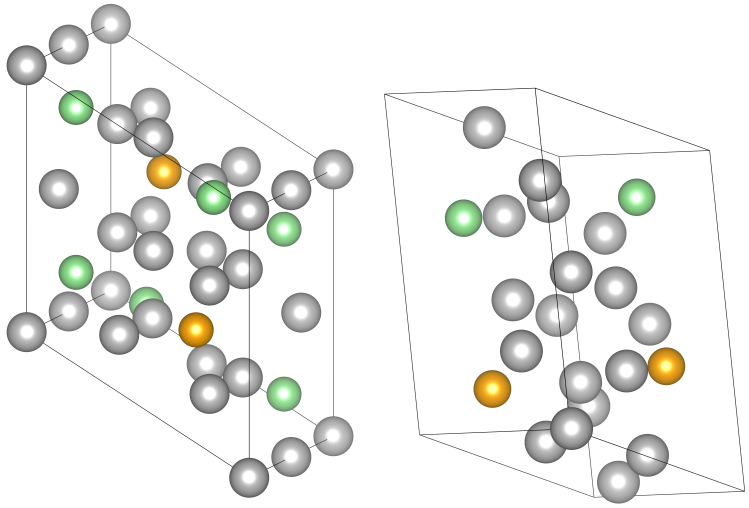

Figure 5.17: The crystal structures of $Al_{10}Fe_3Ni_1$ ($\tau 1$, left panel) and $Al_9Fe_1Ni_1$ (τ_2, right panel) are depicted. Here, Aluminum (Al) atoms are shown in gray, Iron (Fe) atoms are represented in orange, and Nickel (Ni) atoms are depicted in green. These compounds belong to the 194 and 14 space group correspondingly.

into the ternary database utilised to construct the AFLOW ternary convex hull, and their stability is evaluated. The ternary convex hull created using all available data (AFLOW and experimental) is presented in Figure 5.18. The newly calculated convex hull will be used as a benchmark for the rest of this subsection.

Subsequently, the M3gnet workflow, as introduced in Section 5.3 is used to predict the ternary convex hull of the system. The increased throughput now enables us to increase the maximum number of atoms in the cell when creating the pool of candidate structures. Furthermore, to compensate for the reduced accuracy that a universal force field provides, the number of structures sampled by DFT is increased to 30. The workflow was then used to create and screen structures that span 33 distinct stoichiometries. Table 5.1 provides information on the explored stoichiometries, the maximum number of atoms $N_{\max}$, and the total number of structures created for each different stoichiometry.

A total of 10,334,288 structures were generated and screened to create the phase diagram predicted with the M3gnet-based workflow. The predicted ternary phase of the Al-Fe-Ni diagram is presented in Figure 5.19.

We have identified four stable intermetallics as shown in Figure 5.19, namely $Al_2Fe_1Ni_1$, $Al_3Fe_2Ni_1$, $Al_4Fe_2Ni_1$ and $Al_2Fe_4Ni_1$. Surprisingly, all the predicted compounds

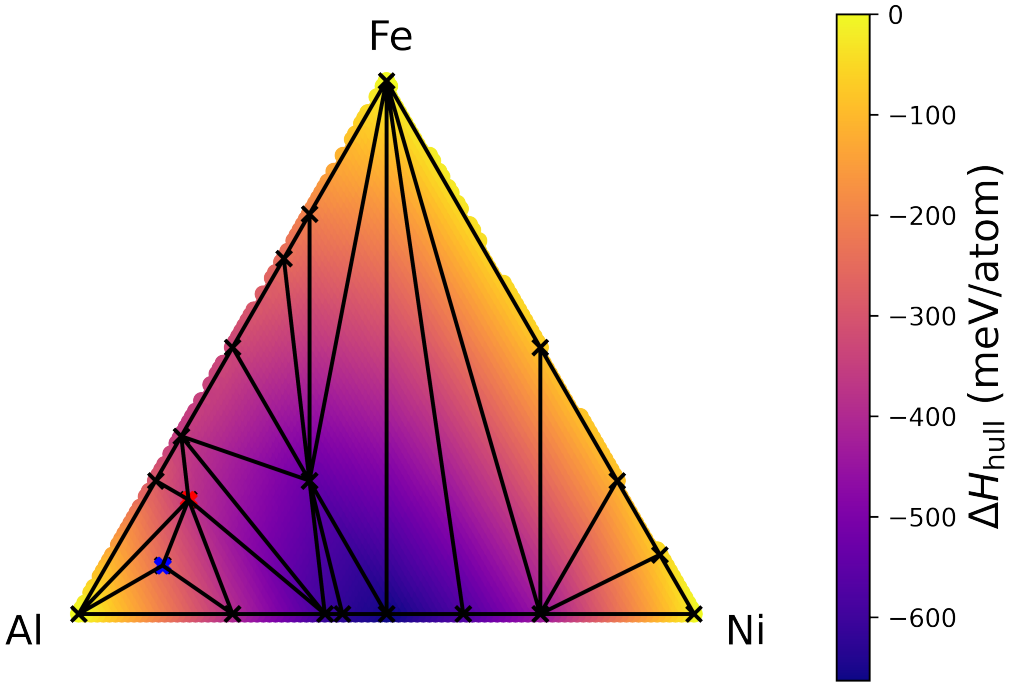

Figure 5.18: The Al-Fe-Ni ternary convex hull, computed through the incorporation of experimental data into the AFLOW dataset, is displayed. Phase τ_1 is indicated by a blue cross, while phase τ_2 is indicated by a red cross. The intermetallic phases shown in this phase diagram are three, namely $Al_2Fe_1Ni_1$, $Al_9Fe_1Ni_1$ and $Al_{10}Fe_3Ni_1$.

Stoichiometry (Al-Fe-Ni)	N_{max}	Structures Created
111	9	13358
112 (121,211)	12	1590192
113 (131,311)	10	42774
114 (141,411)	12	359208
115 (151,511)	14	215238
122 (212, 221)	10	101346
124 (142,214,241,421,412)	14	2527835
132 (213,231,312,321)	12	2674450
133 (313,331)	14	2806860
223 (232,322)	7	3027

Table 5.1: The table presents the information regarding the stoichiometries, maximum number of atoms per supercell and the total number of stuctures created and screened.

belong to the aluminum-iron rich region of the ternary phase diagram. Interestingly, the Al-Fe binary forms a variety of stable binary intermetallics. Also, the convex hull on this side is shallower than that on the aluminum-nickel side. Note that, $Al_2Fe_1Ni_1$

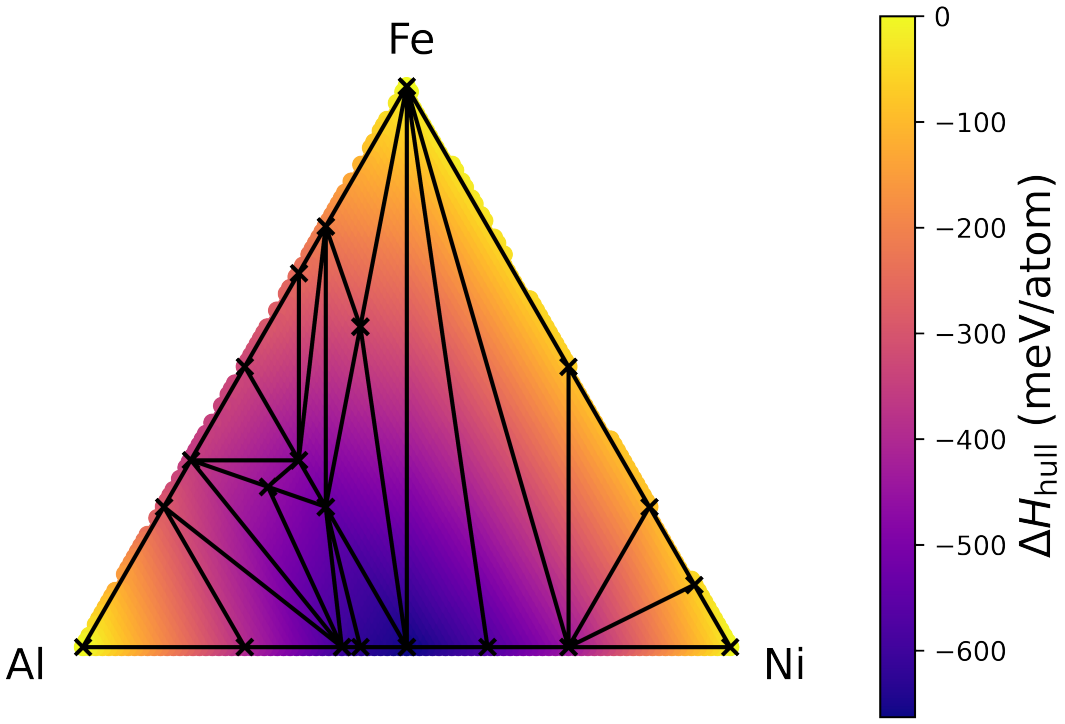

Figure 5.19: The Al-Fe-Ni ternary convex hull as predicted from the M3gnet-based workflow. Interestingly, we predict a total of four ternary stable intermetallics, namely $Al_2Fe_1Ni_1$, $Al_3Fe_2Ni_1$, $Al_4Fe_2Ni_1$ and $Al_2Fe_4Ni_1$. It should be noted that $Al_2Fe_1Ni_1$ is predicted to be stable in both the AFLOW and M3gnet-based workflows.

is predicted to be stable in both AFLOW and M3gnet-based workflows. From the experimental phase diagram presented in reference [128] it can be seen that a solid-state solution of $B2$-type (BCC structure) is found in the neighborhood of the predicted structures.

A comparison between the convex hull predicted by AFLOW and that from M3GW is presented next, in Figure 5.20. It can be seen that for most of the phase diagram the shape of the convex hull remains unchanged. However, for the red region, where M3GW returns lower-energy structures than AFLOW, it is capable of identifying a stable intermetallic structure and increasing the depth of the convex hull by 4.71 meV/atom. In contrast in the blue region, the AFLOW encyclopedia method outperforms the M3GW, predicting a convex hull that it is deeper. This results in increasing the distance of the convex hull for the $Al_4Fe_2Ni_1$ and $Al_2Fe_4Ni_1$, which are now considered metastable.

In the last part of this analysis we combine all the theoretically predicted ternaries,

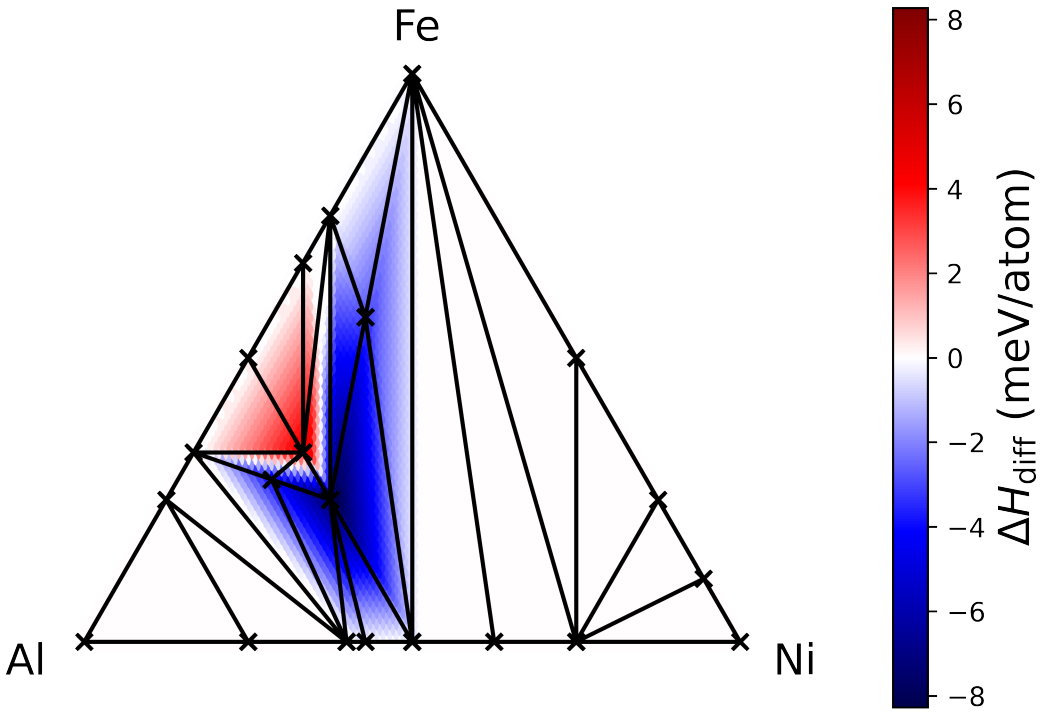

Figure 5.20: The difference between the ternary convex hulls predicted by AFLOW and M3GW. Interestingly, we observe that for most of the phase diagram, the shape of the convex hull does not change. However, in the region near to $Al_2Fe_1Ni_1$, the AFLOW encyclopedia method performs better (blue region), predicting a structure which is 8.27 meV/atom lower than those found by M3GW. It should be noted that $Al_2Fe_1Ni_1$ is predicted to be stable from both methods. This change in the depth of the convex hull results in $Al_2Fe_4Ni_1$ and $Al_4Fe_2Ni_1$, to become metastable. For the red region we see that M3GW outperforms dictionary method and is able to predict one new intermetallic, increasing the depth of the convex hull by 4.71 meV/atom.

namely AFLOW and M3GW and we assess their stability. The phase diagram that is created then is referred as the "complete". The complete theoretical phase diagram is presented in Figure 5.21. The M3GW is capable of identifying one additional ternary intermetallic, namely $Al_3Fe_2Ni_1$. Furthermore, M3GW is able to identify the $Al_2Fe_1Ni_1$ as stable intermetallic. A more thorough comparison between the two phase diagrams (see Figure 5.20) proved that the predicted structure is metastable and that a different isomer is found stable at this stoichiometry, predicted from AFLOW.

Subsequently, a comparison is made between the convex hull shown in Figure 5.18, which corresponds to the ternary convex hull calculated once the experimental structures are added, and the one theoretically predicted shown in Figure 5.21, the complete one. This comparison is shown in Figure 5.22.

Two distinct regions can be observed in Figure 5.22. In the red region, where

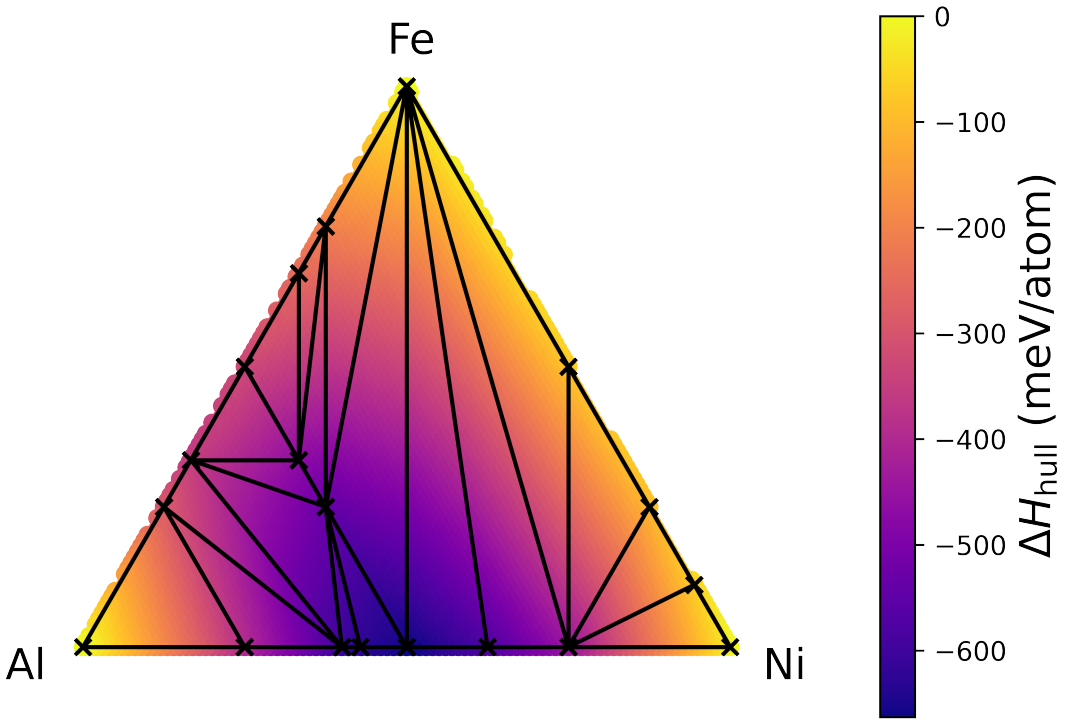

Figure 5.21: The complete theoretically predicted ternary phase diagram for the Al-Fe-Ni system. It can be seen that two different intermetallics predicted, namely $Al_2Fe_1Ni_1$ (predicted by both) and $Al_3Fe_2Ni_1$ (predicted from M3GW).

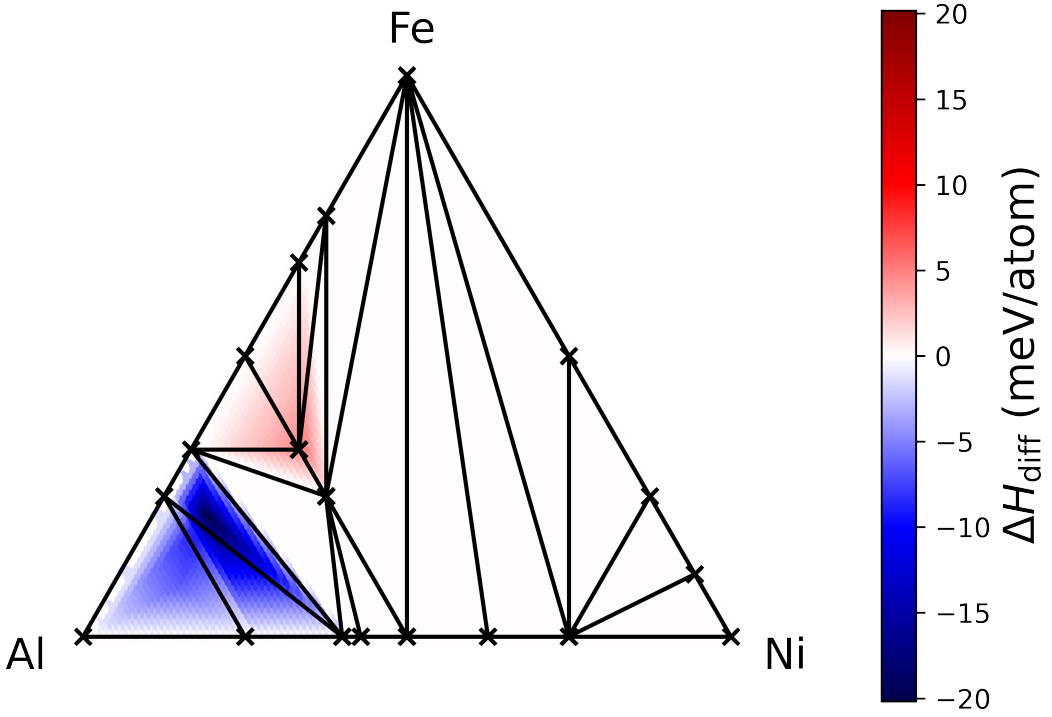

Figure 5.22: The complete theoretically predicted ternary phase diagram for the Al-Fe-Ni system. It can be seen two different intermetallics predicted, namely $Al_2Fe_1Ni_1$ (predicted by both) and $Al_3Fe_2Ni_1$ (predicted from M3GW).

$Al_3Fe_2Ni_1$ was identified by M3GW, the convex hull depth experiences a slight decrease. In contrast, in the blue region where experimentally synthesized compounds were included, the convex hull undergoes a significant change on the order of 20 meV/atom.

In the last part of the analysis, the distance from the AFLOW-predicted convex hull, δ, will be calculated for all different stoichiometries studied over the Al-Fe-Ni ternary system.This comparison is presented in Figure 5.23.

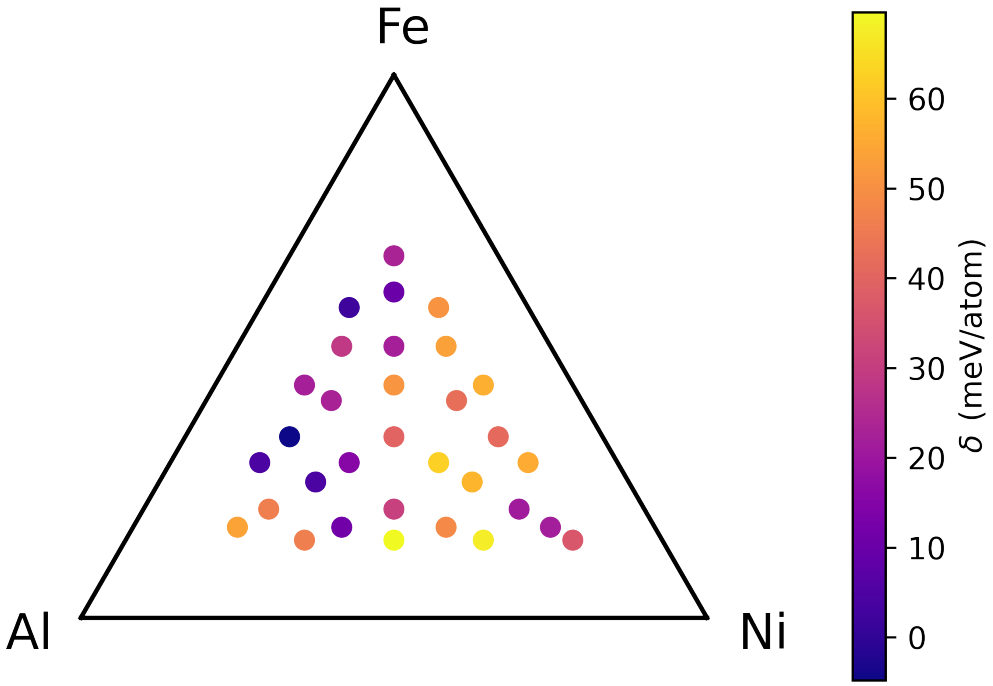

Figure 5.23: The distance, δ, with respect to the AFLOW-calculated convex hull, for each one of the searched stoichiometries for the Al-Fe-Ni ternary system.

The analysis identifies the Al-Fe side of the ternary phase diagram as the most promising for the discovery of stable or metastable structures. In addition to the structures identified as stable, namely $Al_2Fe_1Ni_1$ and $Al_3Fe_2Ni_1$, the workflow is capable of identifying a variety of structures closer than 15 meV/atom from the convex hull in the Al-Fe-heavy region, namely $Al_1Fe_3Ni_1$, $Al_2Fe_4Ni_1$ and $Al_4Fe_2Ni_1$. These compounds can be considered metastable. In the experimental literature, it is well-documented that the Al-Fe binary system forms a variety of stable alloys [131]. Regarding the ternary phase diagram, several studies have explored the Al-rich side, such as the

references [126, 128, 132]. In these works, the structures τ_1 and τ_2 were identified, along with $B2$ solid state solution that span over these stoichiometries. However, needs to be noted that these works do not report any structures with a percentage of Iron exceeding 30%, making it challenging for us to make direct comparisons. Their distances from the convex hull, δ, are calculated and presented in Table 5.2.

Stoichiometry	δ (meV/atom)
$Al_1Fe_3Ni_1$	10.06
$Al_2Fe_4Ni_1$	2.39
$Al_4Fe_2Ni_1$	4.48

Table 5.2: The distance from the convex, δ for the Al-Fe-Ni compounds considered as metastable. As it can be seen, all of them belong to the Al-Fe region of the phase diagram.

The versatility and capability of the proposed workflow regarding the search for stable and metastable ternary alloys that include magnetic elements is highlighted in this chapter.

5.4.3 Bi-Fe-X ternary system

In the final section of this chapter, we utilize the implemented workflow to search for potential ternary intermetallics within the Bi-Fe-X system, where X stands for Zr or Ta. The rationale of the project revolves around the combination of heavy metals with magnetic elements. The underlying concept is to merge bismuth (Bi), a heavy metal, with iron (Fe), a magnetic element. This could potentially lead to compounds with high magneto-crystalline anisotropy since the spin-orbit coupling increases with the atomic number. Despite the experimentally known immiscibility between Bi and Fe, as discussed in reference [133]. Perhaps studying a ternary system where the third element form alloys with Fe and Bi could lead to ternary intermetallics. This intermediary element could serve to bridge the gap and establish the ternary system.

The first system of interest is Bi-Fe-Zr. It can be seen both experimentally and theoretically that zirconium forms stable phases with the rest of the constituents,

namely iron [134] and bismuth [135]. The idea of using zirconium as an intermediary element, comes from the fact that it is able to form stable binary alloys with the rest of the elements in the ternary.

The second system of interest is Bi-Fe-Ta. For this system, we tried to explore a ternary consisting of a heavy metal, bismuth (Bi), a magnetic element, iron (Fe), and a refractory metal, tantalum (Ta). For the Bi-Ta binary system, complete immiscibility is reported [136], while the Fe-Ta binary system forms a range of binary alloys that are known experimentally [137].

To perform this analysis, we employed the developed workflow to search for 34 unique stoichiometries on both phase diagrams. We used the same elemental compositions as those employed to search for ternaries in the Al-Fe-Ni system. These consisted of 1-1-1, 2-1-1, 3-1-1, 4-1-1, 5-1-1, 3-2-1, 3-3-1 and 4-2-1, considering also their elemental permutations. We then calculated the distance from the AFLOW-predicted convex hull. To ensure consistency in the analysis, we extracted the compounds calculated as stable from AFLOW and recalculated their energy with single-point DFT as described in Section 5.3. The results are shown in Figure 5.24 and 5.25.

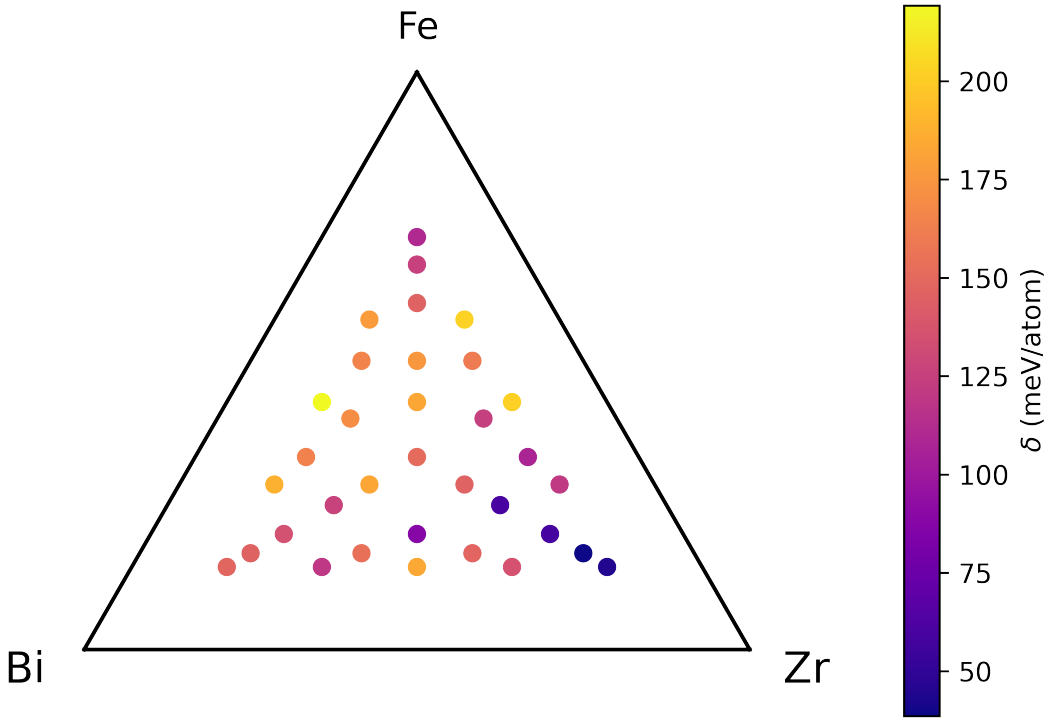

Figure 5.24: The distance, δ, with respect to the AFLOW-calculated convex hull, for each one of the stoichiometries investigated for the Bi-Fe-Zr ternary system.

It is observed that no stable structure is discovered in the Bi-Fe-Zr ternary system. The closest one to the convex hull structure predicted from the workflow is found at the Zirconium edge and its distance from the convex hull is of 38.56 meV/atom, a structure that would be characterized as unstable.

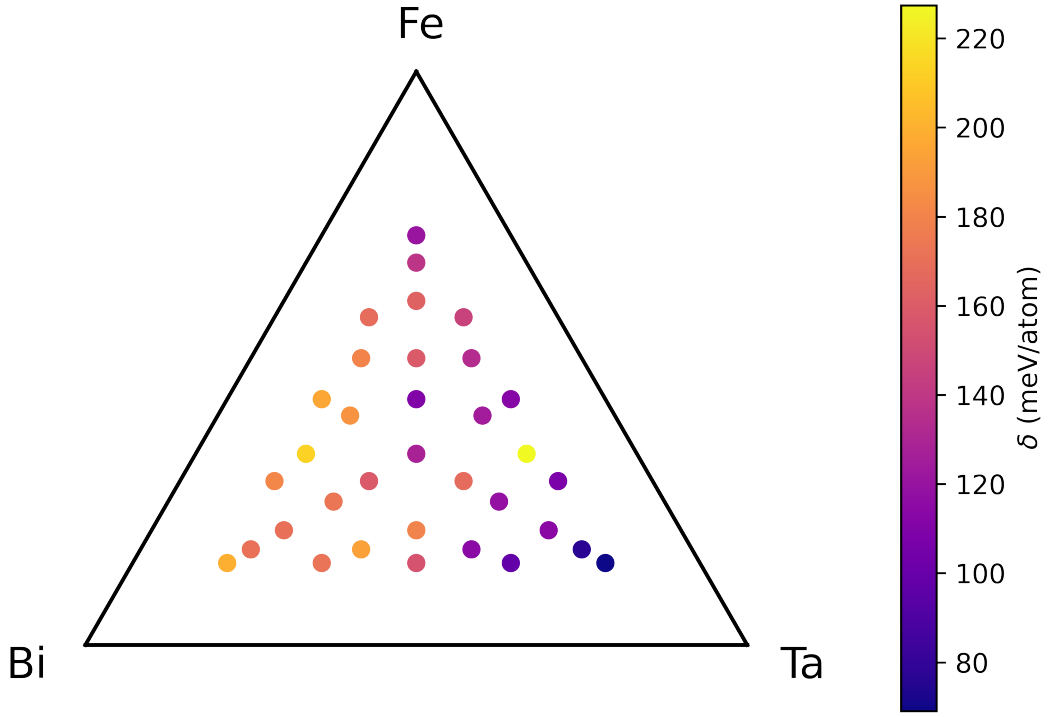

Figure 5.25: The distance, δ, with respect to the AFLOW-calculated convex hull, for each one of the stoichiometries investigated for the Bi-Fe-Ta ternary system.

No stable structure is discovered in the Bi-Fe-Ta ternary system. The closest to the convex hull structure predicted from the workflow is found at the Tantalum edge. Its distance from the convex hull is 69.05 meV/atom, a structure that would be characterised as unstable. Interestingly, for both systems, the structure closest to the convex hull is found at the edge of the binary system that creates the highest number of stable binaries.

For completeness reasons in Table 5.3 and 5.4, we present a comparison between the distance from the convex hull for the best-performing structures predicted by both AFLOW and M3GW.

Although the M3GW workflow is not able to identify any new intermetallics in the case of the Bi-Fe-X ternary phase diagrams, surprisingly, it is performing better than AFLOW in discovering structures closer to the convex hull. In general, the ternary

Stoichiometry	δ^{M3GW} meV/atom	δ^{AFLOW} meV/atom
$Bi_2Fe_1Zr_1$	126.17	165.95
$Bi_1Fe_1Zr_1$	150.97	200.09
$Bi_1Fe_1Zr_2$	60.093	218.12
$Bi_1Fe_4Zr_1$	124.98	142.90
$Bi_1Fe_2Zr_1$	175.28	337.38
$Bi_2Fe_2Zr_1$	170.22	430.60
$Bi_1Fe_2Zr_2$	124.35	446.05

Table 5.3: The distance from the convex hull for the M3GW predicted, δ^{M3GW}, and AFLOW predicted, δ^{AFLOW}, structures for the Bi-Fe-Zr ternary system.

Stoichiometry	δ^{M3GW} meV/atom	δ^{AFLOW} meV/atom
$Bi_1Fe_3Ta_1$	127.86	248.36
$Bi_2Fe_1Ta_1$	173.31	277.84
$Bi_1Fe_1Ta_2$	118.51	413.91
$Bi_1Fe_2Ta_1$	158.50	406.04
$Bi_1Fe_2Ta_2$	124.71	383.54
$Bi_2Fe_2Ta_1$	187.46	758.93

Table 5.4: The distance from the convex hull for the M3GW predicted, δ^{M3GW}, and AFLOW predicted ,δ^{AFLOW}, structures for the Bi-Fe-Ta ternary system.

systems selected for exploration in this chapter were not ideal because bismuth is known to be immiscible with magnetic elements such as iron or cobalt [138] and to form binary alloys with a handful of elements such as lead and tin [139]. Perhaps a system containing magnetic elements, where all the pairs of the elements form stable binaries would be a better alternative.

5.5 Conclusions

In conclusion, we have implemented and tested a phase diagram prediction workflow that creates and assesses structures containing magnetic elements. This workflow is based on a universal machine-learning interatomic potential trained with data extracted from the relaxation trajectories stored in the Materials Project Database [112]. The universal nature of the potential employed in this chapter allows us to increase the maximum number of atoms in the unit cell. To balance the decrease in accuracy of

the employed model, we also increased the structures selected for DFT calculations. This workflow is used to predict the phase diagram for four different ternary systems, namely Mo-W-Ta, Al-Fe-Ni, Bi-Fe-Zr, and Bi-Fe-Ta.

In the case of Mo-Ta-W. It is shown that this workflow has enhanced performance in the central and Mo-rich region, in contrast to the SNAP-based workflow. Furthermore, for the rest of the phase diagram, it is shown that they exhibit similar accuracy. Interestingly, we are able to discover a couple of novel intermetallics on the Mo-heavy side of the phase diagram, namely $Mo_2Ta_2W_1$, $Mo_1Ta_2W_2$, $Mo_2Ta_1W_2$, $Mo_1Ta_1W_3$, $Mo_1Ta_1W_2$, and $Mo_1Ta_1W_1$.

Following that, the same workflow was employed to study the Al-Fe-Ni ternary phase diagram. The challenge we faced came from the fact that we introduced magnetic elements into the systems of study. Interestingly, M3gnet, which is not trained specifically to describe magnetic structures, is able to identify one stable ternary on the Al-Fe side of the phase diagram, namely $Al_2Fe_1Ni_1$ and $Al_3Fe_2Ni_1$, as well as some metastable structures, namely $Al_1Fe_3Ni_1$, $Al_2Fe_4Ni_1$, and $Al_4Fe_2Ni_1$.

Lastly, we used the proposed workflow to explore the Bi-Fe-X phase diagrams, where X is either Zr or Ta. The interesting combination of elements, which could potentially enhance the magnetocrystalline anisotropy was the driving force of that selection. However, our workflow was not capable of identifying any novel ternaries within these systems. This result is supported by the fact that bismuth is an element that forms alloys with only a handful of other elements in the periodic table such as lead and tin [139].

Chapter 6

High-throughput study of Tetragonally Distorted and Antiferromagnetic Heusler Alloys

6.1 Introduction

In this chapter, our focus will be on presenting the results and methodologies used to conduct a high-throughput study across the family of Heusler alloys. The goal is to identify ternary Heusler alloys that exhibit tetragonal distortion, while also identifying their magnetic orders. We will reassess their thermodynamic stability and select the most promising candidates for experimental synthesis and further exploration.

The history of Heusler alloys began in 1903 when Fritz Heusler discovered that a ternary compound with the elemental composition of $Cu_2Mn_1Al_1$ behaved like a ferromagnet, even though the elements from which it is composed in their bulk form are not ferromagnetic by themselves [140]. This collection of materials includes compounds that exhibit a variety of interesting properties. For example, it includes ferromagnetic materials with high critical temperatures [6], T_C, antiferromagnets [89], low thermal conductivity semiconductors [141], and superconductors [142].

The crystal structure of Heusler alloys is formed by four interpenetrating face-centered-cubic crystal, fcc, lattices. Most commonly, it crystallizes in the $Fm\bar{3}m$ (225)

space group, and the general chemical formula is $X_2Y_1Z_1$. In these lattices, the two X atoms occupy the $(\frac{1}{4},\frac{1}{4},\frac{1}{4})$ and $(\frac{3}{4},\frac{3}{4},\frac{3}{4})$ positions, namely the 8c Wyckoff positions, Y atoms are at $(\frac{1}{2},\frac{1}{2},\frac{1}{2})$, 4b Wyckoff positions, and Z atoms occupy the positions (0,0,0), 4a Wyckoff positions. The Heusler alloy family is completed by inverse-Heusler and half-Heusler. Inverse-Heusler [143] crystallize in the F$\bar{4}$3m (216) space group, and the general chemical formula is $(XY)(XZ)$. Here, the X elements occupy the 4a, (0,0,0), and 4d Wyckoff lattice positions, $(\frac{3}{4},\frac{3}{4},\frac{3}{4})$, whereas Y and Z are at the 4b and 4c positions, $(\frac{1}{2},\frac{1}{2},\frac{1}{2})$ and $(\frac{1}{4},\frac{1}{4},\frac{1}{4})$, respectively. The half-Heusler [144] is of the general type XYZ and it crystallizes in the F$\bar{4}$3m (216) space group. The X atoms occupy the 4a Wyckoff positions, while Y and Z are at the 4b and 4c positions, respectively. In Figure 6.1, we present the conventional cells for full-, inverse-, and half-Heusler, as well as the primitive cell for full-Heusler.

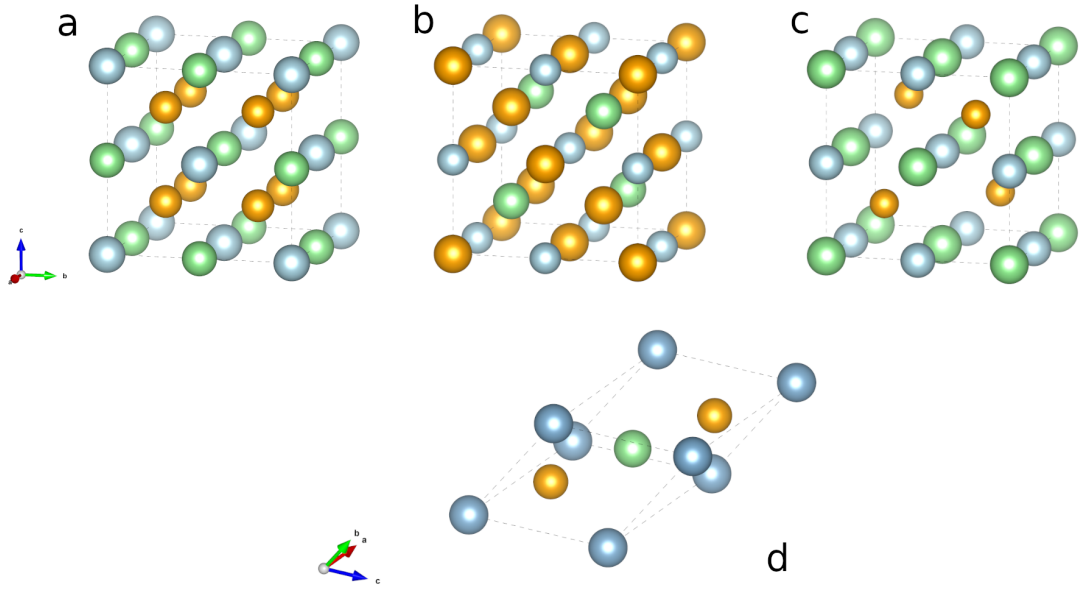

Figure 6.1: Atomic distribution for full-Heusler (a), inverse-Heusler (b) and half-Heusler alloys(c) are presented. The primitive cell for the full-Heusler (d) is presented as well. Here, X elements are denoted with gold color, the Y elements with green, and the Z elements with blue.

Given the established presence of several high-performance magnets within the Heusler alloy family as documented by reference [145], it becomes justifiable to conduct a high-throughput study aimed at identifying any remaining magnets within this family should they exist. In a previous study performed by Sanvito et al. [6], they

created a library of all the possible Heusler alloys by decorating the primitive cell [see Figure 6.1(d)] with all the permutations of elements that belong to the $3d$, $4d$, and $5d$ periods of the periodic table, as well as some elements from groups III to V in a combinatorial fashion. The full list of the elements used in this work is presented graphically in Figure 6.2.

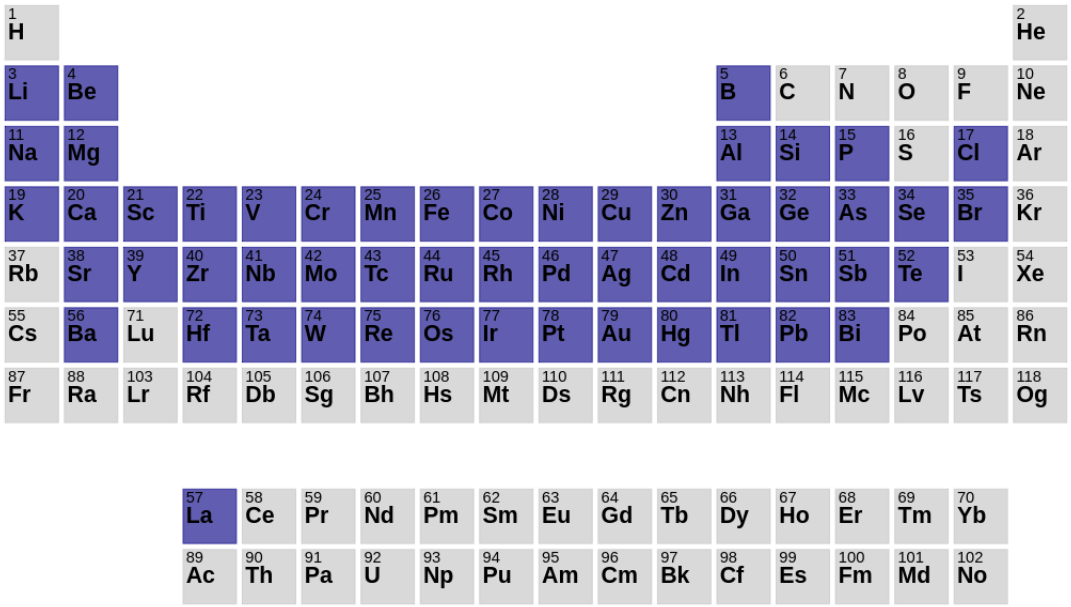

Figure 6.2: Periodic table of the elements. The elements used for the creation of the Heusler alloys studied by Sanvito et al. [6] are represented in blue.

Then, all the possible combinations of three elements were used to decorate the primitive cell for full-, inverse-, and half-Heusler, resulting in 236,115 prototypes, which are then relaxed with the use of spin-polarized density functional theory calculations. Subsequently, their energy was calculated using single-point DFT, and the distance from the convex hull for each ternary system was assessed to determine their stability. Finally, those who carry magnetic moment and those who have negative enthalpy of formation are considered for further investigation. Then, for the remaining candidates, they created the corresponding phase diagrams and assessed their thermodynamic stability by calculating the distance from the convex hull. In the last step, a small fraction of materials from the initial pool was considered for experimental synthesis.

For a compound to be thermodynamically stable, its distance from the convex hull should be zero. In order to calculate the convex hull and the distance from it, we

construct the phase diagram, which represents the Gibbs free energy as a function of composition. The structures with the lowest Gibbs free energy define the convex hull, and the distance of a compound from the hull determines its thermodynamic stability. Gibbs free energy consists of an entropic and an enthalpic term, as defined in Chapter 2. In our case, where DFT calculations are employed to calculate the ground-state energy of the system, we neglect the entropic contribution to the Gibbs free energy. This means that for a given system, the phase diagram is calculated as a function of the enthalpy of formation with respect to the composition. In our case, the enthalpy of a system is equal to the DFT total energy. It is reasonable to expect that as the AFLOW database continues to grow and more compounds are added to the corresponding phase diagrams, the distances from the convex hull for some compounds will eventually change. In Figure 6.3, we present the histogram of the Heusler alloys with an AFLOW-calculated distance of less than 100 meV/atom from the convex hull, δ_{AFLOW}, which exhibit a non-zero magnetic moment. Furthermore, the compounds that have been experimentally synthesized are indicated with red dashed lines.

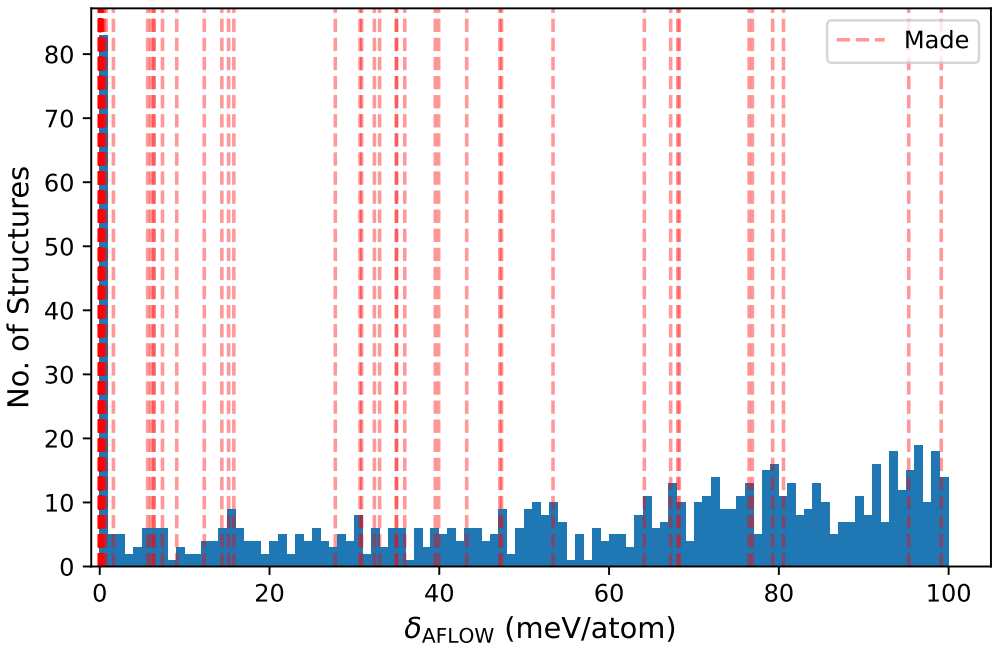

Figure 6.3: The histogram of the AFLOW-calculated distance from the convex hull, δ_{AFLOW}, is presented for the Heusler alloys that exhibit non-zero magnetic moment. The compounds known to have been experimentally synthesized are marked with red dashed lines.

Note that about 80 magnetic Heusler alloys are known to have been synthesized to

date, and in Figure 6.3 they are denoted by red dashed lines. Plotting their distances from the convex hull using vertical red dashed lines reveals a considerable concentration in the zero or near-zero region, as expected. However, a significant number of structures are found to be above that threshold, lying towards the metastable or unstable regions. The reason for this can be attributed to various factors, such as wrong magnetic configurations (e.g., antiferromagnetic instead of ferromagnetic) or lattice distortions not captured by the primitive cell representation (e.g. tetragonal distortion) in the ground-state, or disorder that was not accounted for when the analysis took place. Furthermore, when determining the energy threshold at which a structure is deemed stable or unstable, it is advisable to expand the criteria to incorporate possible entropic contributions.

The purpose of this study is to explore various conditions that could potentially bring the compounds closer to the convex hull. In order to achieve this, we investigate potential tetragonal distortions and explore the possibility of high-symmetry antiferromagnetic order. Then, we correct the distance from the convex hull and identify those that are thermodynamically stable. We aim to identify as thermodynamically stable the large majority of the Heusler compounds known to have been experimentally synthesized. This success rate defines the accuracy of the computational scheme. Then, we extend the methodology and assess the stability of the ones that have not yet been synthesized.

6.2 Computational details

6.2.1 Tetragonal Distortion and Antiferromagnetic configurations

The present work aims to investigate the corrections to the DFT energy associated to different cell and magnetic order. These distinctions have been documented in the literature [145] and will be explored here. It is stated in reference [6] that the ground-state of five Heusler compounds, namely $Co_2Nb_1Zn_1$, $Co_2Ta_1Zn_1$, $Pd_2Mn_1Au_1$,

$Pd_2Mn_1Zn_1$ and $Pt_2Mn_1Zn_1$, is tetragonally distorted. However, the rhombohedral primitive cell employed in the high-throughput study is unable to accommodate this tetragonal distortion. The reason for this is that the rhombohedral cell belongs to the trigonal system, while the tetragonal one belongs to the tetragonal system, and the fundamental symmetries of these two systems are incompatible. In order to accommodate a tetragonal distortion within the trigonal system, one must break the inherent symmetry constraints. In our case, to capture a possible tetragonal distortion, we will start from the conventional cubic cell to simulate the material (see Figure 6.1) and elongate it along one of the axes. In this work, the structures are created using the python materials genomics library, Pymatgen [93]. A graphical representation of the tetragonally distorted cell used in this work is presented in Figure 6.4.

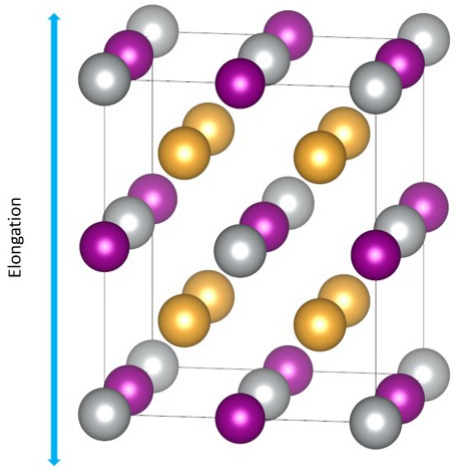

Figure 6.4: The tilted view of the tetragonal distorted structure of $Au_2Ag_1Mn_1$, where Au atoms are presented in gold, Ag atoms in silver and Mn atoms in purple. The elongation axis is shown in blue color.

In the original study of reference [6] only the ferromagnetic order was taken into account. However, there are several Heusler alloys that present antiferromagnetic order, such as $Ir_2Mn_1Al_1$ [146] and $Ir_2Mn_1Ga_1$ [147]. As such, the most common antiferromagnetic orders reported in the literature [145] will be explored. Here, in the antiferromagnetic 1 (AF1) state, the magnetic moment orientation is located in the [001] planes, whereas in the antiferromagnetic 2 (AF2) state, the magnetic moment is staggered in the [111] plane. In these planes, there is ferromagnetic order, and they are oriented in an antiferromagnetic manner with respect to each other. Due

to the presence of inversion symmetry, all the arrangements within the {001} and {111} planes are considered equivalent, respectively. The initial magnetic moments utilized in this study were obtained from AFLOWlib. A visual representation of the two antiferromagnetic orders investigated is depicted in Figure 6.5.

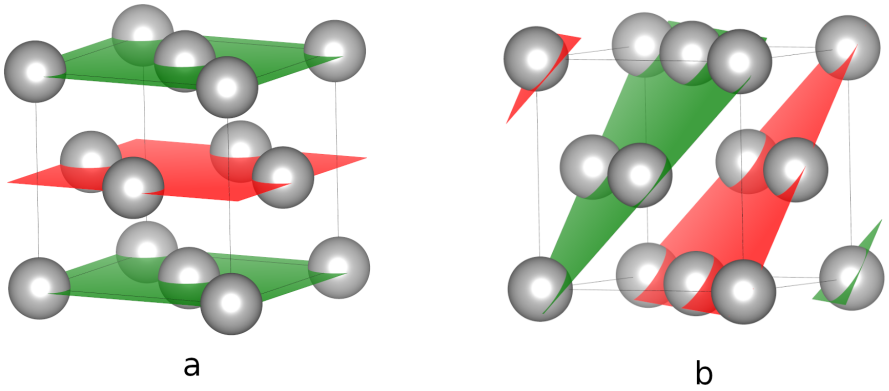

Figure 6.5: The AF1 (a) and AF2 (b) configurations accounted for in this study, are depicted within an fcc cell. The red planes correspond to atoms with negative magnetic moments (e.g. pointing down), while the green planes represent those with positive values (e.g. pointing up). Adopted from reference [89].

6.2.2 DFT details

All properties are calculated with DFT in the GGA as parametrized by Perdew, Burke and Ernzenhof [27], together with the corresponding VASP pseudopotential library. The software used for the calculations is the Vienna Ab-initio Simulation Package (VASP) [28]. Each structure is relaxed with spin-polarized collinear DFT. A convergence criterion on the energy of 10^{-4} eV is employed throughout this work. For all DFT calculations, the convergence criteria are closely aligned with the AFLOW standards as defined by Calderon et al. [97]. The Monkhorst-Pack scheme [98] is adopted to construct the k-mesh, and the number of sampling points, N_i, is proportional to the norm of each corresponding reciprocal Bravais lattice vector, $\vec{b_i}$, and is minimised ensuring the following condition.

$$N_{\mathrm{KPPRA}} \leq \min\left[\prod_{i=1}^{3} N_i\right] \times N \tag{6.1}$$

Here, N_{KPPRA} is the number of k-points per reciprocal atom and N is the number of atoms in the cell. In particular, N_{KPPRA} is chosen at 10,000 for all static calculations and at 6,000 for all the geometry relaxations following the AFLOW standard [97]. The geometry relaxations are considered to be converged when the atomic forces are smaller than 10^{-3} eV/Å.

6.2.3 Convex hull Distance Correction

In order to correct the AFLOW-calculated distance from the convex hull, δ_{AFLOW}, as calculated in reference [6], a specific procedure needs to be followed, which involves comparing the formation enthalpies. For each compound under study, we conducted a single-point DFT calculation using the same cell, pseudopotentials, and convergence parameters as employed in [6]. This calculation provided us with the reference energy, denoted as E_{ref}. This was performed in order to create a highly-converged reference energy, avoiding any software version and pseudopotentials incompatibility issues. Furthermore, we computed the value of the distance from the AFLOW convex hull, δ_{AFLOW}, using AFLOW-CHULL [96].

In order to calculate the correction on the distance from the convex hull, δ_{corr}, and ultimately determine the corrected distance from the convex hull, δ', for a compound of the form X_2YZ, we must compute the difference between the formation enthalpies for the reference calculation, $H_{\mathrm{f}}^{\mathrm{ref}}$, and the new calculation, H'_{f}. The formation enthalpies for each of these calculations are presented in Equations (6.2),

$$\begin{aligned} \Delta \mathrm{H}_{\mathrm{f}}^{ref} &= E_{\mathrm{ref}}(X_2YZ) - 2E(X) - E(Y) - E(Z), \\ \Delta \mathrm{H}_{\mathrm{f}}^{new} &= E_{\mathrm{n}}(X_2YZ) - 2E(X) - E(Y) - E(Z). \end{aligned} \tag{6.2}$$

In these equations, $\mathrm{E}(X_2YZ)$ represents the DFT-calculated energy of the ternary compound, while $E(X)$, $E(Y)$, and $E(Z)$ denote those of the ground-state of its constituent elements. The correction to the calculated convex hull, δ_{corr}, is defined

as the difference between the enthalpy of formation for the reference and the new calculation. The correction in the convex hull distance, denoted as δ_{corr}, is defined in Equation (6.3).

$$\begin{aligned} \delta_{\text{corr}} &= \Delta \text{H}_{\text{f}}^{new} - \Delta \text{H}_{\text{f}}^{ref} \\ &= E_{\text{n}}(X_2YZ) - E_{\text{ref}}(X_2YZ) \end{aligned} \tag{6.3}$$

Subsequently, the newly calculated distance from the convex hull, δ', is computed by adding δ_{corr} to δ_{AFLOW} as in Equation (6.4),

$$\delta' = \delta_{\text{AFLOW}} + \delta_{\text{corr}} \tag{6.4}$$

In the case, where the newly calculated structure exhibits a lower energy than the reference calculation, meaning that E_{n} is less than E_{ref}, the newly calculated structure is considered to be in the equilibrium state, meaning that the correction δ_{corr} takes negative values, thus reducing the distance from the convex hull. In the opposite case, δ' remains unchanged, indicating that the previously calculated state is the equilibrium one.

6.2.4 Workflow

The workflows employed to study the tetragonal distortion, as well as the different magnetic configurations, are presented in this subsection. The general workflow consists of two steps. In the first step, a reference calculation is performed using a ferromagnetic order for the relaxed structure obtained from AFLOW. In the second stage, the corresponding changes in the lattice or magnetic order are applied, followed by an atomic relaxation and a single-point DFT calculation. Subsequently, the correction of the distance from the convex hull is calculated, and the thermodynamic stability is assessed. A graphical representation of the workflow used for the tetragonal distortion is presented in Figure 6.6.

The workflow followed to calculate the antiferromagnetic configurations is presented in Figure 6.7. The rationale remains the same as before: we utilize reference calculations

conducted in the initial step. Subsequently, we generate the antiferromagnetic configurations depicted in Figure 6.5. After generating these configurations, we determine the lowest energy magnetic structure. This lowest-energy magnetic configuration is then used to adjust the convex hull distance obtained from AFLOW, allowing us to assess the stability of the configurations. Importantly, the cell employed for the various magnetic configurations can now accommodate tetragonal distortion as well, allowing us to accommodate changes in the lattice and magnetic order simultaneously. Before initiating the relaxation process, we also apply a tetragonal distortion. This step ensures that we account for the possibility of both tetragonally distorted and antiferromagnetic configurations.

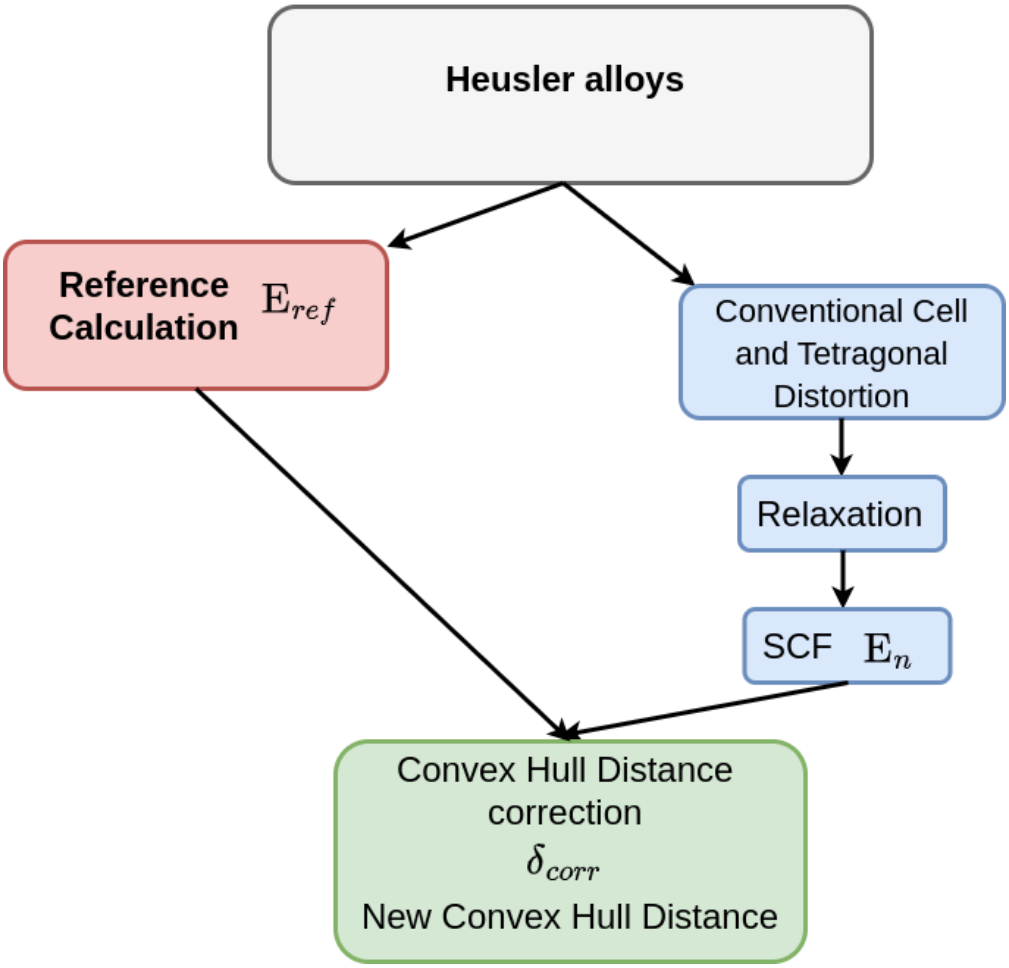

Figure 6.6: Workflow for the investigation of possible tetragonal distortions in the Heusler alloys. For all the Heusler alloys studied in this work a reference calculation is performed. Then the conventional cubic cell is created with the use of pymatgen [93] and a tetragonal distortion is applied. Then a relaxation and an single point DFT calculation is performed. The energy calculated is used to correct the AFLOW distance from the convex hull, δ'.

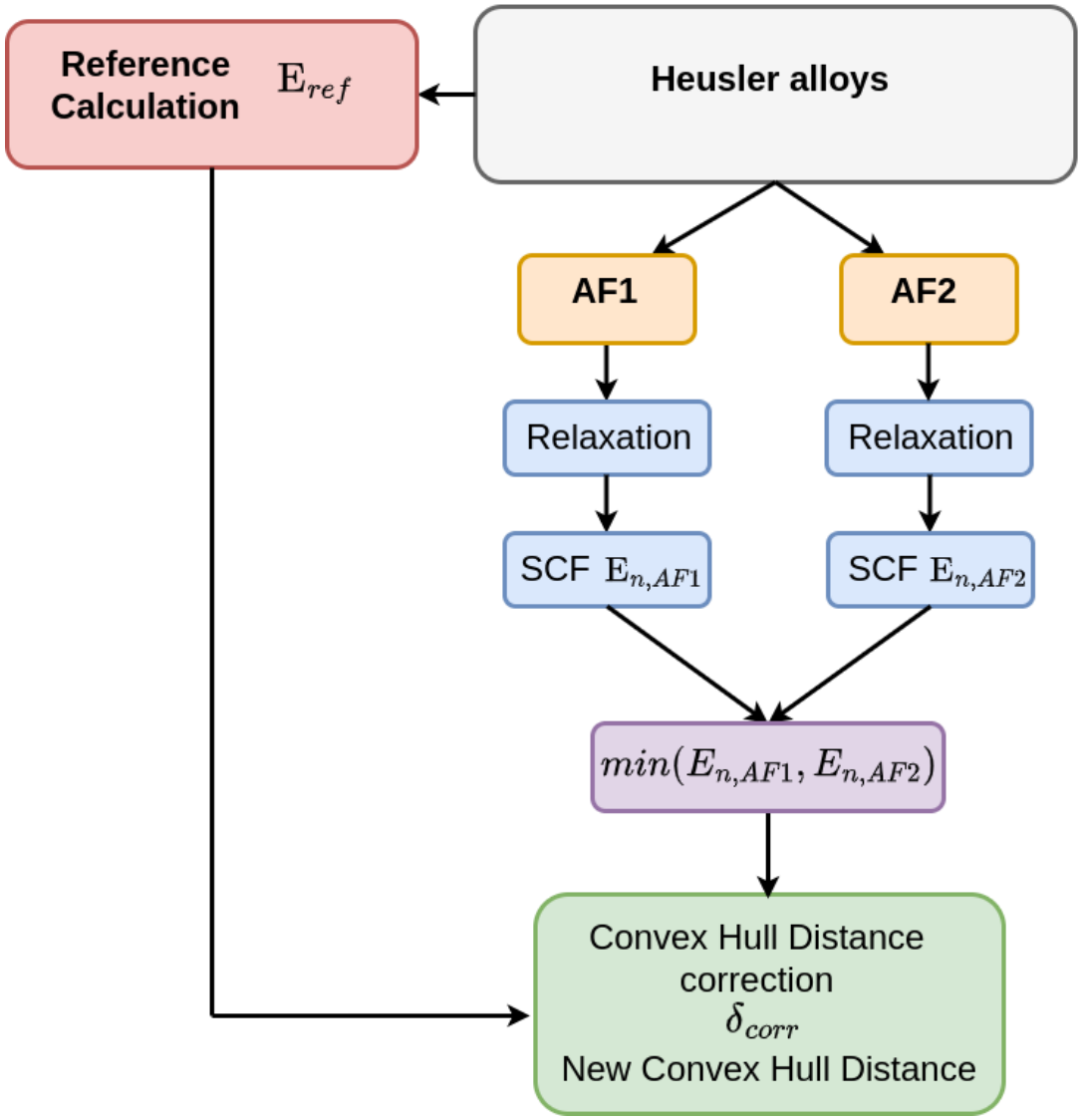

Figure 6.7: Workflow for determining the magnetic ground state of Heusler alloys. Two distinct antiferromagnetic configurations are initialised and relaxed, followed by a single-point DFT calculation. The reference energies previously calculated are used to calculate the correction to the distance from the convex hull.

6.3 Results

6.3.1 Correcting the Convex Hull Distance

As AFLOW continues to expand, more data are added to the existing database, a fact that has the potential to reshape the convex hulls once they are recalculated. The initial step of this work involved updating these distances and observing how the landscape depicted in Figure 6.3 evolves. We utilized AFLOW-CHULL [96] to construct ternary phase diagrams containing the compounds of interest and calculated the updated convex hull distances, δ_{AFLOW}. The new version of Figure 6.3 is presented

in Figure 6.8.

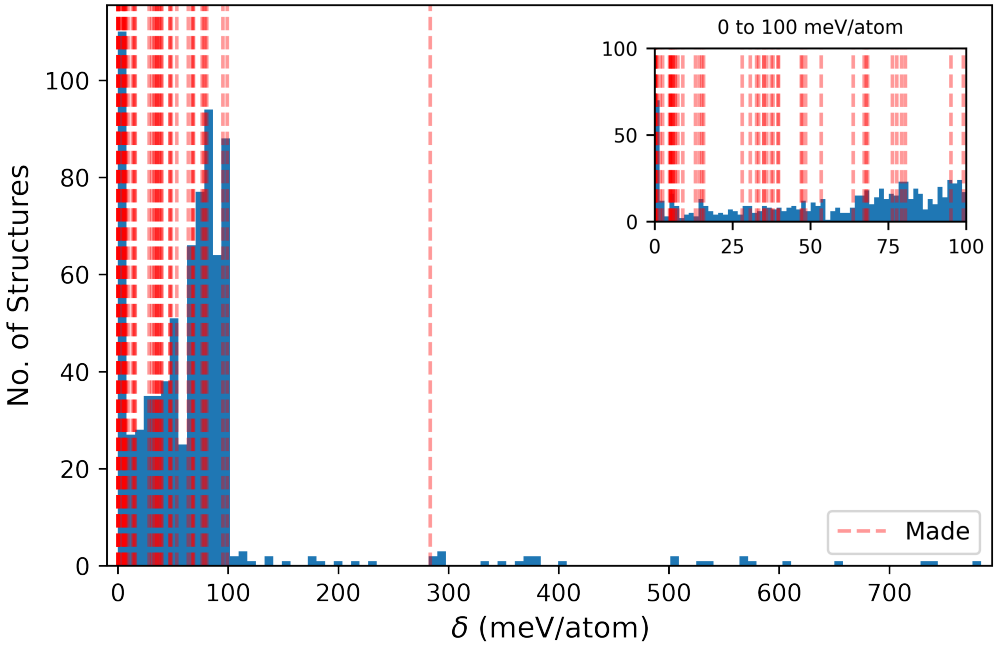

Figure 6.8: In the main histogram, we present the distance from the convex hull for the Heusler alloys of interest, denoted as δ_{AFLOW}. The compounds known to have been experimentally synthesized are indicated with red dashed lines. Additionally, in the upper-right corner, we provide a zoomed-in version of the plot, focusing on the range of 0 to 100 meV/atom distance.

We observe that the x-axis now spans a wider range of energies. This comes from the fact that new calculations are added to the database, resulting in the increase of the depth of the convex hull, and hence in the increase of the distance from the convex hull for some compounds. For instance $Ru_2Ge_1Mn_1$ which was considered stable at 0.086 meV/atom, now it is considered unstable with a distance of 283.338 meV/atom. Interestingly, this alloy is experimentally synthesised as reported in [148]. However, it is not clear from this reference whether the created sample had any type of disorder or if it was metastable, as not much of the studied material was synthesised in order to perform rigorous experiments. Interestingly, AFLOW predicts a stable intermetallic with stoichiometry 2-1-1 of the Ru-Ge-Mn ternary phase diagram. This compound is a tetragonal distorted structure related to the Heusler family, as they are created from the same prototype, with spacegroup 139. Another example is the $Mn_2Co_1Ga_1$; its distance from the convex hull increases from 81.26 meV/atom to 332.78 meV/atom, and it is considered unstable. This occurred due to the additional structures in the

ternary phase diagram, resulting in an increase in the depth of the ternary convex hull, thereby increasing the distance for the studied compound.

The majority of the experimentally synthesized compounds, are situated away from the convex hull, are found within the sub-100 meV/atom region. Consequently, our study primarily focuses on the region when the calculated δ_{AFLOW} is below 100 meV/atom. This choice is based on the likelihood that compounds in this range are more susceptible to move closer to the convex hull, via a potential correction of their distance, than those that are several hundreds of meV/atom away from it. When the magnetic configurations change, it is expected that the enthalpy gain will be on the order of tens of meV/atom, as it is influenced by the exchange interaction, as reported in reference [89]. In the case of lattice distortions, it is anticipated that the enthalpy gain will exceed that associated to the magnetic order, still not enough to move a compound a couple of hundreds of meV/atom closer to the convex hull. This choice also saves around 100 DFT calculations (both relaxations and single point). Furthermore, in this work, full and inverse Heusler alloys will be treated separately from the half-Heuslers.

Another important aspect of this analysis is related to the energy threshold up to which we are confident that a predicted compound is considered thermodynamically stable. Gibbs free energy is consisted from an enthalpic and an entropic term as defined in Equation (2.50). Although we are able to calculate the enthalpy of a system with DFT, calculating the entropy is not trivial, especially when needs to be done for a large number of compounds. In this work, we estimate the ideal entropy of mixing within the Heusler alloys lattice and utilize it as a threshold to determine stable structures. In our case, we will be employing two distinct approximations for this energy threshold. In the first one, we assume the regular structure of a Heusler alloy, while in the second case, we consider an ideal solid solution of the $B2$-type. The $B2$-type lattice, characterized by the prototypical compound CsCl [149], is an ordered body-centered cubic lattice with two distinct atomic sites (0,0,0), Wyckoff position 1a, and $(\frac{1}{2}, \frac{1}{2}, \frac{1}{2})$ corresponding to a Wyckoff position of 1b. We assume the second structure as it is reported in a

variety of studies [148, 150, 151] where there is structural disorder and corresponds to our upper limit.

Let us take a Heusler alloy, $A_2B_1C_1$. Its primitive cell is composed of 4 sites. If we take into account the symmetries of the crystal, we obtain two equivalent 8c Wyckoff positions, one 4a and one 4b. For the studied Heusler to be formed, we can have two different configurations, where the B-species and the C-species elements exchange positions, namely AABC and AACB. Then the entropy value, S, is determined by Equation (6.5).

$$S = k_B ln(\Omega), \tag{6.5}$$

where k_B is Boltzmann's constant and Ω is the number of different microscopic states available to the system. The entropic contribution is then defined as TS. At $T = 298$ K, the calculated value is 17.81 meV, representing the entropic contribution arising from structural disorder between positions Y and Z. This entropic contribution, when divided by the assumed number of atoms in the cell, serves as the first upper limit for the distance from the convex hull at which the compounds are considered thermodynamically stable. Therefore, the upper limit is defined at a distance of 4.45 meV/atom away from the convex hull.

When considering the $B2$ lattice type, we encounter two non-equivalent sites. If we expand the cell into a supercell to accommodate four elements for decoration, we end up with four sites. There exist four distinct ways to decorate a supercell of $B2$-type, namely AABC, ABAC, ACAB, and BCAA. The entropic contribution to the Gibbs free energy, as calculated using Equation (6.5), for the same temperature, amounts to 35.62 meV. This corresponds to the entropic contribution observed when a solid solution of $B2$-type is formed, and is the upper boundary for a compound to be considered stable. The entropic contribution value, divided by the number of atoms assumed in the studied cell (4), defines the furthest distance from the convex hull at which a compound is considered thermodynamically stable, namely 8.91 meV/atom.

For all the compounds presented, we employed a machine learning model to predict

their corresponding critical temperatures, denoted as $T_{\mathrm{C}}^{\mathrm{pred}}$. The pre-trained model used for this task is a random forest regressor [152] trained on experimental data. The experimental dataset used to train this model is the same as the one used by Nelson et al. [3], enriched with additional information from the database [153]. The model uses a 129-element feature vector containing chemical information, such as the atomic number, the number of valence electrons, group and the period corresponding to the elements constituting the compound, and a one hot encoding of the compound chemical formula, etc. More details can be found in Ref. [3]. It is important to note that in the case of an antiferromagnetic material, the predicted temperature corresponds to the Néel temperature. Moreover, in these cases, it is expected that the prediction may be less accurate due to the fact that the vast majority of the database consists of ferromagnetic materials. Nevertheless, the prediction still offers a useful estimate of the critical temperature.

After applying the workflow for the compounds that are known to have been experimentally synthesized, we have identified that 51.5% of those, fall below the energy threshold of 4.45 meV/atom. Specifically, of the 80 compounds, 41 meet this criterion. When the second boundary is used, namely 8.91 meV/atom, additionally ten compounds are considered thermodynamically stable, namely 51 out of 80 compounds, and the success rate increases to 63.75%. This defines the success rate that our workflow has in order to determine the compounds that could be potentially experimentally synthesized. In the analysis, we focus mostly on the first threshold. The compounds predicted to be stable are listed in Table 6.1. Additional information provided in the table includes the Heusler type [inverse (IH) or full Heusler (FH)], tetragonal distortion (Tet), antiferromagnetic order [Type 1 (AF1) or Type 2 (AF2)], the experimental Curie temperature when it is available, $T_{\mathrm{C}}^{\mathrm{exp}}$, the corresponding corrected distance from the convex hull, δ', and the relative references. Here, in Table 6.1 we present the 51 compounds, identified as thermodynamically stable by applying the threshold of 8.91 meV/atom.

Compound	IH/FH	Tet	AF1	AF2	T_C^{pred} (K)	T_C^{exp} (K)	δ' (meV/atom)	Ref.
$Rh_2Mn_1Sn_1$	FH	✗	✓	✗	381.62	431	-9.71	[154]
$Rh_2Ge_1Mn_1$	FH	✗	✓	✗	399.59	431	-8.15	[155]
$Ru_2Fe_1Ga_1$	FH	✗	✗	✓	466.34	✗	-2.11	[148]
$Co_2Al_1Zr_1$	FH	✓	✗	✗	212.91	185	-0.65	[156]
$Rh_2Ga_1Mn_1$	FH	✗	✗	✓	141.35	✗	-0.58	[148]
$Co_2Mn_1Ti_1$	FH	✓	✗	✗	714.91	1040	-0.50	[6]
$Co_2Al_1Ta_1$	FH	✓	✗	✗	293.78	260	-0.45	[157]
$Co_2Sc_1Sn_1$	FH	✓	✗	✗	226.47	268	-0.35	[158]
$Ru_2Ge_1V_1$	FH	✓	✗	✗	190.94	✗	-0.33	[159]
$Mn_2Ga_1V_1$	FH	✓	✗	✗	673.54	783	-0.23	[160]
$Ru_2Cr_1Ge_1$	FH	✓	✗	✗	197.88	✗	-0.22	[161]
$Rh_2In_1Mn_1$	FH	✓	✗	✗	225.53	✗	-0.14	[162]
$Ru_2Al_1Mn_1$	FH	✓	✗	✗	290.02	353	-0.08	[163]
$Fe_2Co_1Ge_1$	IF	✓	✗	✗	885.71	✗	-0.03	[164]
$Rh_2Al_1Fe_1$	FH	✗	✗	✗	463.99	✗	0.00	[148]
$Pd_2Mn_1Sn_1$	FH	✗	✗	✗	223.78	198	0.00	[165]
$Ir_2Ga_1Mn_1$	FH	✗	✗	✗	370.55	65	0.00	[147]
$Co_2Ge_1Ti_1$	FH	✗	✗	✗	354.42	386	0.00	[166]
$Fe_2Co_1Si_1$	IF	✗	✗	✗	982.50	723	0.00	[167]
$Ru_2Cr_1Si_1$	FH	✗	✗	✗	164.14	✗	0.00	[168]
$Mn_2Ge_1Ru_1$	IF	✗	✗	✗	304.62	✗	0.00	[169]
$Mn_2Pd_1Pt_1$	FH	✗	✗	✗	349.87	320	0.00	[6]
$Mn_2Fe_1Ge_1$	IF	✗	✗	✗	280.37	~ 200	0.00	[170]
$Rh_2Al_1Mn_1$	FH	✗	✗	✗	190.33	✗	0.00	[148]
$Co_2Al_1Nb_1$	FH	✗	✗	✗	364.51	383	0.00	[166]
$Co_2Al_1Fe_1$	FH	✗	✗	✗	950.79	~ 1150	0.02	[171]
$Ni_2Al_1Mn_1$	FH	✗	✗	✗	564.51	✗	0.03	[172]

$Co_2Al_1Mn_1$	FH	✓	✗	✗	711.37	[600, 1000]	0.04	[173]
$Co_2Mn_1Si_1$	FH	✓	✗	✗	845.75	1014	0.06	[174]
$Co_2Al_1V_1$	FH	✗	✗	✗	312.12	✗	0.06	[175]
$Co_2Fe_1Ge_1$	FH	✗	✗	✗	982.31	✗	0.07	[175]
$Co_2Al_1Ti_1$	FH	✗	✗	✗	193.20	✗	0.10	[175]
$Pd_2In_1Mn_1$	FH	✗	✗	✗	282.88	✗	0.16	[176]
$Co_2Fe_1Si_1$	FH	✗	✗	✗	1023.85	1100	0.17	[175]
$Co_2Ge_1Mn_1$	FH	✗	✗	✗	801.12	✗	0.23	[175]
$Ru_2Mn_1Si_1$	FH	✗	✗	✗	278.96	✗	0.29	[177]
$Co_2Mn_1Sn_1$	FH	✓	✗	✗	672.16	✗	0.37	[178]
$Mn_2Al_1V_1$	FH	✗	✗	✗	626.62	760	0.47	[179]
$Fe_2Mn_1Si_1$	FH	✗	✗	✓	300.07	220	0.52	[180]
$Ir_2Al_1Mn_1$	FH	✗	✗	✓	373.55	500	3.24	[181]
$Co_2Ga_1V_1$	FH	✗	✗	✗	364.61	✗	4.75	[182]
$Co_2Ga_1Nb_1$	FH	✗	✗	✗	375.08	✗	5.01	[183]
$Co_2Fe_1Ga_1$	FH	✗	✗	✗	1087.8	1093	5.06	[184]
$Mn_2Co_1Ga_1$	IF	✗	✗	✗	646.62	740	5.07	[185]
$Co_2Ga_1Mn_1$	FH	✗	✗	✗	664.53	650	5.08	[186]
$Co_2Ga_1Hf_1$	FH	✗	✗	✗	203.82	✗	5.19	[166]
$Co_2Mn_1Sb_1$	FH	✓	✗	✗	463.66	600	5.58	[187]
$Co_2Ga_1Ti_1$	FH	✗	✗	✗	200.66	✗	5.88	[166]
$Fe_2Ge_1Mn_1$	FH	✗	✗	✓	451.44	428	7.01	[180]
$Au_2Al_1Mn_1$	FH	✗	✗	✗	225.71	240	7.42	[188]

Table 6.1: The experimentally synthesized Heusler compounds that exhibit the lowest calculated distance from the convex hull. Their predicted lattice distortion is indicated, as well as the magnetic order. Additionally, both their predicted and experimentally measured Curie temperatures are presented as well as the relevant experimental reference.

For compounds where the antiferromagnetic order seems to be the ground-state,

we calculated the difference between the ferromagnetic and antiferromagnetic energies to quantitatively assess their magnetic energy $\Delta E_{\mathrm{F-A}}$. These values are presented in Table 6.2. Notably, we observe that when the energy difference between the ferromagnetic and antiferromagnetic states is significant, the machine learning model predicts a higher critical temperature. This correlation arises from the fact that a substantial energy difference implies a larger exchange parameter, hence a higher critical temperature. This behavior is not followed by the $Ir_2Al_1Mn_1$ which could be due to the fact that the machine learning model we use is not accurate enough to predict the Néel temperature for that material.

Compound	$\Delta E_{\mathrm{F-A}}$ (meV/atom)	$T_{\mathrm{C}}^{\mathrm{pred}}$ (K)
$Rh_2Mn_1Sn_1$	9.72	381.62
$Rh_2Ge_1Mn_1$	10.68	399.59
$Ru_2Fe_1Ga_1$	8.69	466.34
$Rh_2Ga_1Mn_1$	2.25	141.35
$Fe_2Mn_1Si_1$	5.83	300.07
$Ir_2Al_1Mn_1$	2.69	373.55
$Fe_2Ge_1Mn_1$	7.28	451.437

Table 6.2: Energy difference between the ferromagnetic and antiferromagnetic configurations. For the ones that have an antiferromagnetic ground-state.

The maximum energy gain that we observe by changing the magnetic configuration is 10.68 meV/atom, found for $Rh_2Ge_1Mn_1$, which is substantial in drive the distance from the convex hull to -8.15 meV/atom from 2.15 meV/atom and the compound is now considered thermodynamically stable. The same analysis has been performed to describe how the tetragonal distortion affects the energy. We calculate the difference in energy when the compound is in a cubic versus a tetragonal lattice, $\Delta E_{\mathrm{C-T}}$. Although we were unable to identify any significant differences for compounds with distances below 8.91 meV/atom, extending this discussion to compounds with distances below k_BT for $T = 300$ K reveals the interesting case of $Co_2Si_1V_1$. The calculated value for introducing a lattice distortion in that compound is 25.51 meV/atom. Remarkably, this energy gain helps reduce the convex hull distance from 39.51 meV/atom to 14

meV/atom, which is very close to the upper bound we defined. The table with the calculated energy differences between the ferromagnetic and antiferromagnetic configurations is presented in the Appendix D.

In the next part of the analysis, we focus on compounds that have been synthesized experimentally but are not predicted to be stable with the use of our workflows for the search of tetragonally distorted or antiferromagnetic configurations. The total number of these compounds is 29 and the distance from the convex hull increases to 283.34 meV/atom. The maximum distance from the convex hull corresponds to the $Ru_2Mn_1Ge_1$. It should be emphasized that from Ref. [148], we are not able to understand whether there was any type of disorder in the material, or if the synthesized compound was stable, as not much materials was grown in order for rigorous experiments to be performed. The rest of the materials are concentrated at distances below 100 meV/atom. The results are presented in Table 6.3.

Compound	IH/FH	Tet	AF1	AF2	T_C^{pred} (K)	T_C^{exp} (K)	δ, (meV/atom)	Ref.
$Au_2Mn_1Zn_1$	FH	✗	✗	✗	265.55	160	8.99	[189]
$Rh_2Mn_1Pb_1$	FH	✗	✓	✗	301.90	338	11.88	[190]
$Ni_2Mn_1Sn_1$	FH	✓	✗	✗	319.29	✗	12.22	[191]
$Pd_2Mn_1Sb_1$	FH	✓	✗	✗	265.34	✗	12.48	[192]
$Ni_2Ga_1Mn_1$	FH	✓	✗	✗	416.89	393	12.94	[193]
$Co_2Si_1V_1$	FH	✓	✗	✗	222.52	✗	14.01	[166]
$Mn_2Fe_1Ga_1$	IF	✗	✗	✓	514.70	✗	19.29	[150]
$Pd_2Al_1Mn_1$	FH	✗	✗	✗	270.71	415	30.67	[194]
$Mn_2Al_1Co_1$	IF	✗	✗	✗	649.96	745	32.67	[195]
$Fe_2Al_1Cr_1$	FH	✓	✗	✗	267.23	260	32.73	[196]
$Fe_2Ge_1Ru_1$	IF	✗	✗	✗	479.69	860	34.97	[197]
$Mn_2Ga_1Ni_1$	IF	✗	✗	✗	595.04	588	34.98	[151]
$Co_2Ge_1Sc_1$	FH	✓	✗	✗	225.79	✗	35.25	[166]
$Co_2Cr_1Ga_1$	FH	✗	✗	✗	425.22	✗	37.44	[198]

$Fe_2Ga_1Ni_1$	IF	✗	✗	✗	779.58	840	38.00	[199]
$Ni_2In_1Mn_1$	FH	✓	✗	✗	312.21	✗	38.87	[200]
$Rh_2Fe_1Sn_1$	FH	✓	✗	✗	475.98	✗	43.25	[148]
$Fe_2Ge_1Ni_1$	IF	✗	✗	✗	712.58	835	47.04	[201]
$Mn_2Ga_1Rh_1$	IF	✗	✗	✗	352.36	✗	47.33	[169]
$Fe_2Sn_1V_1$	FH	✗	✓	✗	237.79	✗	58.80	[202]
$Cu_2Al_1Mn_1$	FH	✓	✗	✗	553.11	(424,605,614)	63.65	[203]
$Fe_2Mn_1Si_1$	IF	✗	✗	✓	300.07	220	64.07	[180]
$Ni_2Mn_1Sb_1$	FH	✗	✗	✗	354.69	✗	67.88	[204]
$Co_2Al_1Cr_1$	FH	✗	✗	✗	328.53	340	68.37	[205]
$Cu_2In_1Mn_1$	FH	✓	✗	✗	457.48	530	76.01	[206]
$Co_2Sn_1V_1$	FH	✗	✗	✗	150.07	105	77.64	[166]
$Pd_2Ge_1Mn_1$	FH	✗	✗	✗	220.56	✗	79.27	[207]
$Fe_2Al_1Cu_1$	IF	✗	✗	✗	807.18	875	80.45	[208]
$Cu_2Mn_1Sn_1$	FH	✗	✗	✗	471.70	✗	99.03	[209]
$Ru_2Mn_1Ge_1$	FH	✗	✗	✗	283.34	296		[210]

Table 6.3: The Heusler compounds, which are predicted to be unstable but have been experimentally synthesized. Their predicted lattice distortion is indicated, as well as the magnetic order. In addition, their predicted critical temperature is provided as well as the relative reference.

A closer examination of the literature may shed light on some of the reasons behind our inability to predict the stability of the studied compounds through ab-initio methods. One potential explanation is the presence of structural disorder, which has been reported for the majority of the compounds studied here. When dealing with a disordered structure, the contribution of entropy to the Gibbs free energy increases, and this entropy contribution tends to stabilise these compounds. Disorder has been documented for $Mn_2Fe_1Ga_1$, $Fe_2Al_1Cr_1$, $Fe_2Ge_1Ru_1$, and $Mn_2Ga_1Ni_1$ as reported in references [150, 151, 196, 197].

Furthermore, for several of these compounds, a different less ordered crystal structure

was discovered, specifically the $B2$ crystal structure, which has CsCl as the prototypical material. Here, $B2$ is an ordered body-centered-cubic (bcc) structure formed by two interpenetrating simple cubic sublattices. A derivative of the $B2$ lattice is the $L2_1$ structure used here to model the Full and Inverse Heuslers. Structures that crystallise on the $B2$-type are reported for $Pd_2Al_1Mn_1$ [194], $Fe_2Al_1Cr_1$ [196], $Fe_2Ga_1Ni_1$ [199], and $Ni_2In_1Mn_1$ [200]. Interestingly, $Fe_2Ni_1Ga_1$, has a transition from the ordered Inverse Heusler at low temperatures, to the less ordered $B2$-type at higher temperatures. In summary, the disorder reported in these structures might explain our inability to predict their thermodynamic stability.

Next, we proceed by presenting the compounds that have not yet been experimentally synthesized, and their corrected distance from the convex hull lies below the threshold of 8.91 meV/atom defined before. The total number of these structures is 93, where the majority of them, 63% are predicted to lie below 1 meV/atom away from the convex hull. Two histograms, with respect to their predicted critical temperature, $T_{\mathrm{C}}^{\mathrm{pred}}$, and their corrected distance from the convex hull, δ', are presented in Figure 6.9.

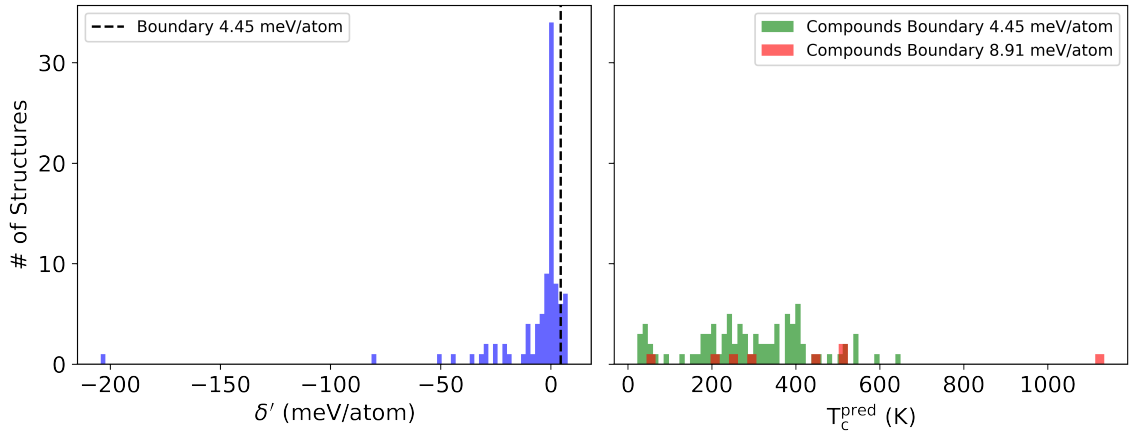

Figure 6.9: Histograms of the corrected distance from the convex hull, δ', and the predicted critical temperature, $T_{\mathrm{C}}^{\mathrm{pred}}$, for the compounds predicted to lie below the energy threshold, and never synthesized before. The average value for the critical temperature predicted is 303 K, slightly above room temperature. However, there are compounds that are predicted to have robust ferromagnetism such as $Co_2Fe_1Zn_1$ with a predicted critical temperature of 1050 K respectively. The histogram of the critical temperatures for the compounds that considered stable with the boundary of 4.75 meV/atom is denoted with green color and those added with the extended boundary of 8.91 meV/atom is presented with red.

Here, 49 out of 93 compounds are predicted to lie below the AFLOW-calculated

convex hulls, thus exhibiting negative corrected distance from the convex hull. The system corresponding to the lowest corrected distance is the $Co_2Hf_1Mn_1$, which is 204.28 meV/atom below the calculated convex hull. This compound is predicted to exhibit type 1 antiferromagnetic order, with opposite magnetic moments at the Manganese atoms. A subset of the complete catalog consisted from the 10 structures that correspond to those with the lowest corrected distance from the convex hull, denoted as δ' is presented. The results are shown in Table 6.4. The complete catalog of the compounds that are not yet experimentally synthesized, but are calculated to be thermodynamically stable can be found in the Appendix D.

Compound	IH/FH	Tet	AF1	AF2	T_C^{pred} (K)	δ' (meV/atom)
$Co_2Hf_1Mn_1$	FH	✓	✓	✗	266.45	-204.28
$Pt_2Cr_1Mn_1$	FH	✓	✗	✗	389.17	-80.10
$Fe_2Mn_1Ni_1$	IF	✓	✗	✗	541.41	-50.80
$Mn_2Ge_1Li_1$	IF	✗	✗	✓	381.88	-43.25
$Mn_2Ge_1Tc_1$	IF	✗	✗	✓	412.79	-35.85
$Mn_2Ir_1Zn_1$	IF	✓	✗	✗	283.92	-30.73
$Pt_2Mn_1Zn_1$	FH	✓	✓	✗	336.91	-29.32
$Mn_2Co_1Os_1$	FH	✓	✓	✗	324.15	-28.93
$Pt_2Cr_1Zn_1$	FH	✓	✓	✗	172.30	-25.72
$Mn_2Cr_1Pt_1$	FH	✓	✗	✗	319.79	-24.55

Table 6.4: The Heusler compounds predicted to have the largest distance below the convex hull. Their predicted lattice distortion is indicated, as well as the magnetic order. Furthermore, their predicted Curie/Néel temperature is presented. To the best of our knowledge, these compounds have never been synthesized.

A large portion of the materials predicted to be stable are found in the tetragonal distorted configuration, more quantitatively 50 out of 93. Structural instabilities of this kind are widely reported in the literature [211]. The reason behind this occurrence is that structural deformation lifts the degeneracy of the *d*-electron bands, reducing the energy of the system by electron redistribution. Furthermore, sometimes tetragonal distortion suppresses the magnetic moment of the material, resulting in a distorted nonmagnetic ground-state. The energy gain from this lattice distortion is of the order

of $\sim 10^2$ meV/atom for some compounds, for example $Mn_2Ir_1Zn_1$, $Pt_2Cr_1Mn_1$, and $Fe_2Mn_1Ni_1$. In Table 6.5 we present the energy difference between the cubic and tetragonal distortion, ΔE_{C-T}, also the magnetic moment of the tetragonal-distorted compounds shown in Table 6.4. Furthermore, for the structures that their ground state is found to be antiferromagnetic we present the energy difference between the ferromagnetic and antiferromagnetic state, $\Delta E_{\mathrm{A-F}}$.

Compound	m (μ_b/f.u.)	$\Delta E_{\mathrm{C-T}}$ (meV/atom)	$\Delta E_{\mathrm{A-F}}$ (meV/atom)	δ' (meV/atom)
$Co_2Hf_1Mn_1$	0.00	4.41	223.81	-204.28
$Pt_2Cr_1Mn_1$	1.10	172.10	✗	-80.10
$Fe_2Mn_1Ni_1$	0.65	149.68	✗	-50.80
$Mn_2Ir_1Zn_1$	1.09	85.38	✗	-30.73
$Pt_2Mn_1Zn_1$	0.00	15.22	65.43	-29.32
$Mn_2Co_1Os_1$	0.00	49.84	77.63	-28.93
$Pt_2Cr_1Zn_1$	0.00	69.85	37.84	-25.72
$Mn_2Cr_1Pt_1$	1.01	57.83	✗	-24.55

Table 6.5: The tetragonally distorted predicted Heusler compounds. Their magnetic moment per formula unit, m, the energy difference between the cubic and the tetragonal distortion, $\Delta E_{\mathrm{C-T}}$ and the corrected distance from the convex hull, δ' are presented.

As evident in Table 6.5, modifications to the lattice structure can result in a substantial difference in energy. Consequently, structures that were once considered thermodynamically unstable can be re-evaluated as stable. As an example, consider $Pt_2Cr_1Mn_1$, whose cubic cell is 92 meV/atom above the convex hull, suggesting initial instability. This is predicted to achieve thermodynamic stability through a tetragonal distortion. Another example is the $Fe_2Mn_1Ni_1$ with an energy distance of 98.88 meV/atom above the convex hull for the cubic phase, but ultimately stabilising through distortion with an energy level of 50.80 meV/atom below the tie plane. Furthermore, for the ones that are found to have an antiferromagnetic ground state, we observe large energy differences between the ferromagnetic and antiferromagnetic ground state energies. The largest one is calculated for $Co_2Hf_1Mn_1$ with value of 223.81 meV/atom. For this compound, the opposite magnetic moments are located in the manganese atoms.

The complete catalog of the energy differences between the ferromagnetic and antiferromagnetic compounds as well as between the ferromagnetic and antiferromagnetic compounds are presented in the Appendix D.

Non-cubic crystals exhibit a natural inclination toward directional magnetization magnetocrystalline anisotropy, that is not found in cubic materials. This property is associated with the tetragonal alteration of the crystal axes. Studies have shown that tetragonally distorted Heusler compounds, containing heavy transition metals and characterized by low magnetic moments, hold promise for displaying significant magnetocrystalline anisotropy [212]. This property makes them attractive candidates for spintronics applications. For instance, $Fe_2Mn_1Ni_1$ is a tetragonally distorted ferromagnetic material with a low magnetic moment. Another interesting compound is the $Ti_2Ga_1Pd_1$ which is a low magnetic moment antiferromagnet and includes palladium (Pd), which is a heavy transition metal. We recommend further investigation of the entire list of proposed tetragonally distorted materials, as presented in Appendix D, regarding their magnetocrystalline anisotropy.

6.3.2 Band Structure Calculations

Next a series of band structure and density of states calculations are conducted. These calculations provide valuable insights into the materials' type and electronic structure. Band structure calculations are carried out for compounds that have not been experimentally synthesized and are located within a threshold of 10 meV/atom away from the convex hull. Applying this criterion results in a total of 94 calculations.

In order to ensure high precision in our calculations, we utilize a Monkhorst-Pack [98] k-point mesh with 20,000 k-points per reciprocal atom, N_{KPPRA}. The determination of the high-symmetry path within the Brillouin zone was achieved by the Python Materials Genomics (pymatgen) [93] library, which uses the paths described in Ref. [99]. Our computational workflow consists of an initial self-consistent field (SCF) calculation to attain well-converged charge densities, followed by a non-self-consistent field (non-SCF) calculation along the high symmetry path to compute the

material's band structure and density of states (DOS). The number of bands used in the calculations is defined by Equation (6.6) and it is VASP's default number increased by 100.

$$max\left(\frac{N_{\text{electrons}}}{2}+\frac{N_{\text{ions}}}{2}, N_{\text{electrons}}\times 0.6\right)+100, \tag{6.6}$$

where $N_{\text{electrons}}$ is the number of electrons in the system and N_{ions} is the number of ions.

The graphs of band structures show that almost all of the materials studied are, in fact, metals. For the materials that exhibit an antiferromagnetic ground state and there is not a structural deformation that breaks the symmetry of the crystal, we observe a degeneracy in the bands as it should be expected. A sample of the bandstructure graphs is presented for an antiferromagnet of type 1 and type 2, in Figure 6.10 and 6.11, Type 1 ($Pt_2Mn_1Zn_1$) and Type 2 ($Fe_2Ge_1Mn_1$), respectively.

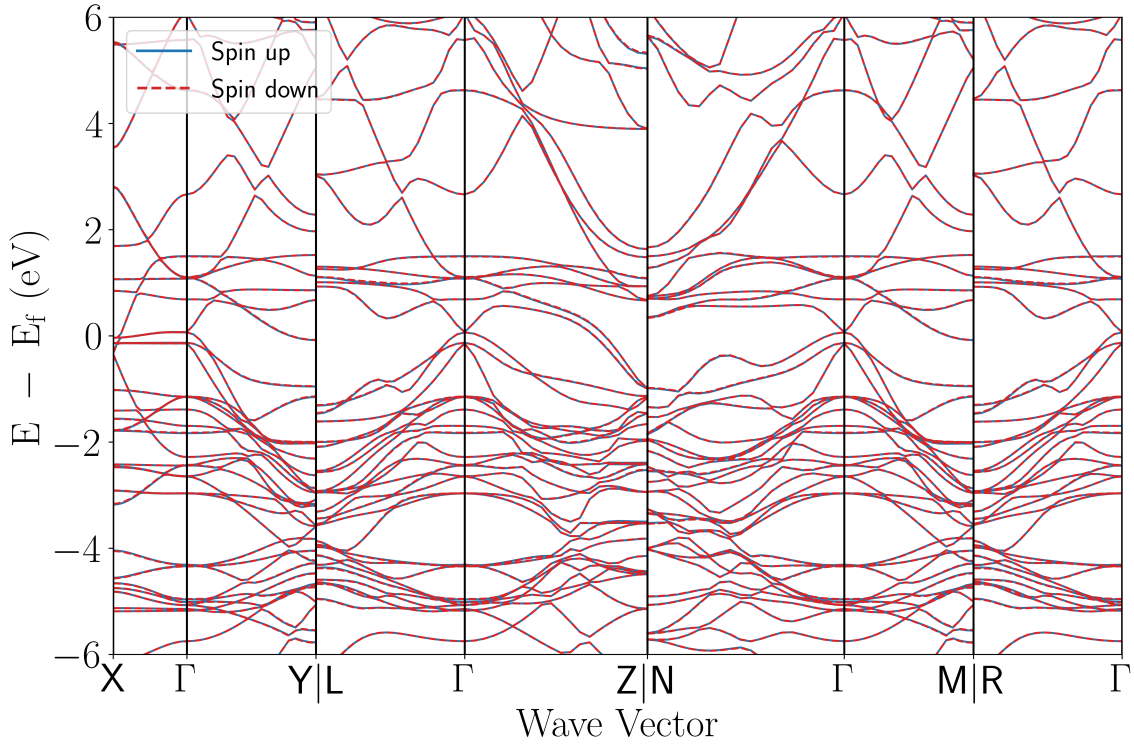

Figure 6.10: Spin-polarised electronic band structure of the full Heusler $Pt_2Mn_1Zn_1$. Solid blue and red dashed lines represent the bands of the up and down spin channels, respectively.

Although, for the vast majority of compounds studied, band degeneracy is observed as it should be in the absence of spin-orbit coupling, in the case of $Rh_2Cr_1Zn_1$ this

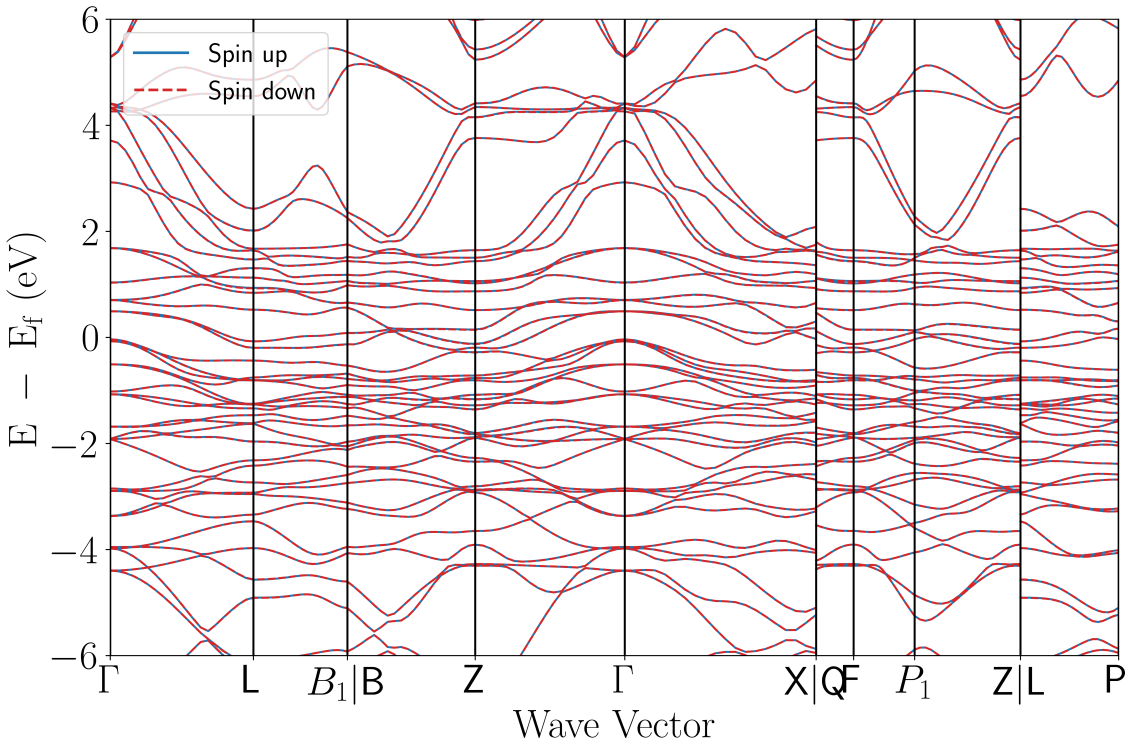

Figure 6.11: Spin polarised electronic band structure of the full Heusler $Fe_2Ge_1Mn_1$. Solid blue and red dashed lines represent the bands of up and down spin channels, respectively.

degeneracy is lifted. This can be observed from the band structure where a shift in bands is observed. This occurence could be explained by the fact that a structural distortion breaks the crystal symmetry and hence the lifts degeneracy in the band structure. In Figure 6.12 we present a bandstructure plot regarding the $Rh_2Cr_1Zn_1$ compound.

However, this behavior changes when it comes to tetragonally distorted Heusler compounds. In these cases, the band degeneracy is generally lifted, and the magnitude is analogous to the calculated magnetization value. This means that as the magnetization increases, the band degeneracy becomes more pronounced.

As can been observed from the bandstructures the majority of the Heusler alloys calculated are metals. However, in the case of $Co_2Mn_1Si_1$ (see Figure 6.13), half-metallicity is observed. Interestingly, the material acts as a metal for electrons with one spin configuration and as a semiconductor for those with the opposite orientation. This property is described to be found in the Heusler alloy family [213]. This interesting family of materials are expected to be used in spin electronics. In the following figures,

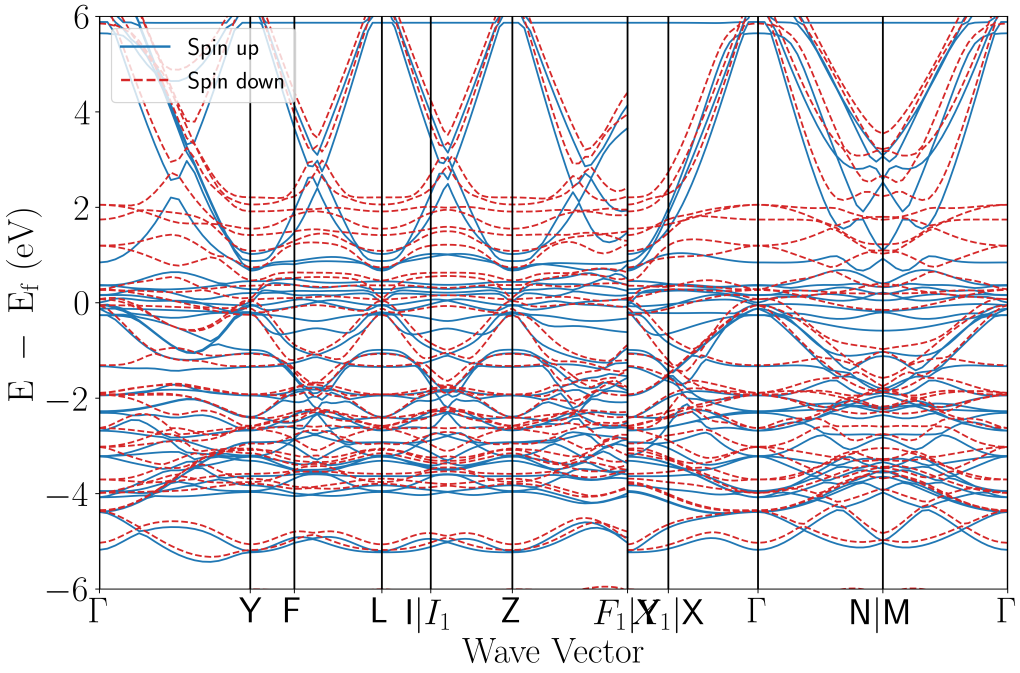

Figure 6.12: Spin polarised electronic band structure of $Rh_2Cr_1Zn_1$ full Heusler. Solid blue and red dashed lines represent the bands of up and down spin channels, respectively.

the calculated band structure graph and the DOS are presented to illustrate this phenomenon. For the rest of the Heusler compounds the calculated bandstructures and DOS graphs can be found in this github repository.

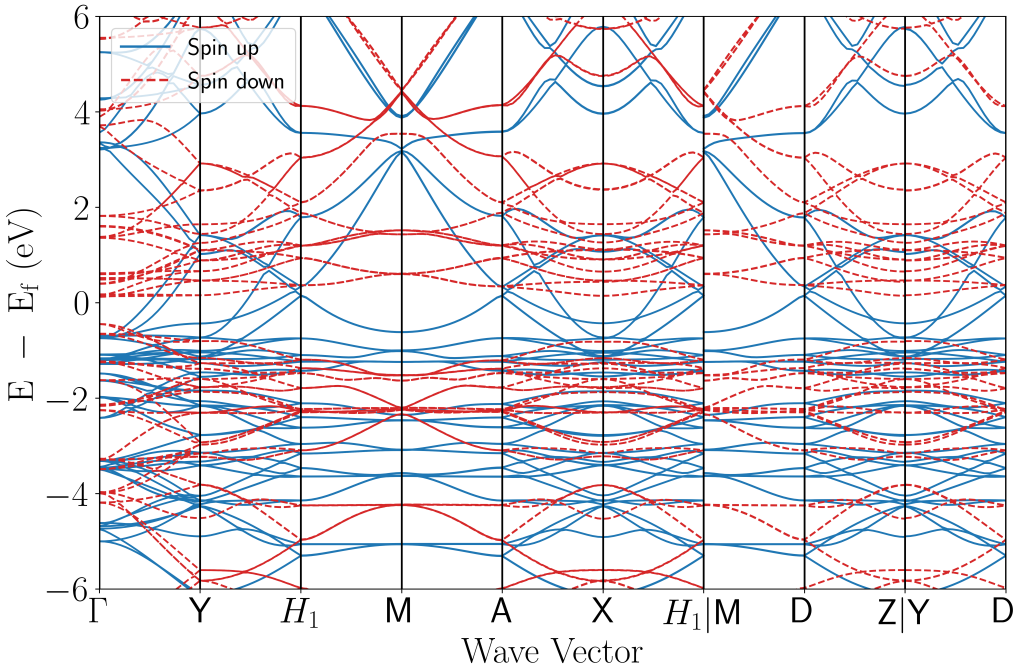

Figure 6.13: Spin-polarized electronic band structure of $Co_2Mn_1Si_1$ full Heusler. The solid blue lines and red dashed lines represent the bands for up and down spin channels, respectively.

6.4 Conclusions and Discussion

In this chapter, we have conducted a high-throughput analysis on the Heusler compounds family. Inspired by the work of Sanvito et al. [6], our study aimed to identify tetragonally distorted compounds, to correct their distances from the convex hull, and to re-evaluate their stability. Additionally, we have explored various magnetic orders.

We began with a candidate pool of approximately 700 compounds, each having an energy distance of less than 100 meV/atom from the convex hull. We have demonstrated that by modifying their lattice or magnetic configuration, their distances from the convex hull gets reduced. Ultimately, we identified 124 compounds with energy distances below the threshold of 17.81 meV/atom, boundary 1, which is increased to 182 if we take into account the second energy boundary. These structures, which have not yet been synthesized experimentally, encompass both ferromagnetic and antiferromagnetic materials, with an average predicted critical temperature of 303 K based on our trained model. The list of materials created by these compounds is anticipated to be synthesized in the future.

Chapter 7

Conclusions and Future Work

7.1 Conclusions

The work presented in this thesis covers two distinct paths in the area of theoretical discovery of materials. In the first three chapters, we explore the more modern, data-informed materials discovery route. Here, we developed and applied tools designed to accelerate the throughput of proposed and screened candidate materials. Additionally, we incorporated already available methods, e.g., Enumlib crystal structure enumeration library, towards this goal. By combining these methods, we successfully implemented, benchmarked, and ultimately established an end-to-end workflow for predicting ternary-phase diagrams. These materials discovery workflows, coupled with property prediction models, are expected to play a crucial role in uncovering materials with intriguing properties.

In the last chapter of the thesis, a more traditional approach is pursued. Such approaches are commonly known as combinatorial searches, wherein an interesting material serves as the starting point. The crystal structure of this material is then utilized as a prototype, initiating an exhaustive search where the material is systematically decorated in a combinatorial fashion with appropriate elements. Subsequently, the created candidates undergo screening based on their thermodynamic stability. At this stage, materials deemed most feasible for synthesis are selected, and comprehensive studies based on their properties follow. The ultimate goal is to identify the most

possible experimentally realizable materials, which are then synthesized and further studied in the laboratory.

A variety of interesting results and outcomes have been extracted from this work, which will be summarized in the following paragraphs. However, the general conclusion is that computational materials science plays a crucial role in materials discovery. Both approaches, one more general than the other in terms of the materials studied, contribute to this understanding. The first method aims to focus on specific interesting triplets of elements, where for the selection of these ternary systems, data-driven methods are employed to assess the property of interest and exhaustively search a variety of different materials candidates. Meanwhile, the second method targets a specific family of materials by exploring all possible combinations of appropriate elements. Both approaches have successfully uncovered thermodynamically stable materials, where some of them exhibit interesting properties, indicating a promising future for such studies in revealing the potential of functional materials.

The journey towards implementing an end-to-end data-driven materials discovery workflow commences in Chapter 3, where we assess the utility of existing data extracted from ab initio calculations. The key focus is to assess the potential effectiveness of a machine-learning model trained on these data within the context of materials discovery workflows. The existence of numerous repositories containing ab initio results from calculations raises the question of whether these databases offer sufficient and accurate data that models trained with them are capable of accurately assess the energy, hence the stability, of candidate materials. Consequently, we explore whether models trained with such databases, when integrated into materials design workflows, are capable of accurately predicting the thermodynamic stability of materials candidates.

Since the workflow is built towards uncovering thermodynamically stable ternary intermetallics, we explore the idea of training models with the use of data extracted from their constituent binaries. These models will be employed towards the energy prediction of ternary compounds. We then use them to predict the energy of created ternaries by exploiting the similarity between binary and ternary compounds made of

transition metals.

To test the hypothesis, we trained SNAP models and benchmarked their accuracy for different ternary systems. We began with the Cu-Ag-Au ternary system, as this noble metal system provides enough simplicity to demonstrate the concept we explored. After establishing the training workflow with this system, we progressed to more challenging ternary systems, such as Ti-Mo-Pt and Cd-Hf-Rh. These systems involve early, mid, and late-transition metal elements, introducing increased complexity to the local chemical environment from which our model learns. While models trained with data from these systems show a higher energy prediction error, it remains insignificant when compared to the depth of the convex hull. This suggests that they are valuable tools for materials discovery workflows.

Interestingly, we were able to establish that machine learning interatomic potentials, trained with readily available data consisting only of energy-structure pairs extracted from binaries, can predict the energy of ternary materials when they are near or at their equilibrium. Remarkably, for materials candidates that are away from their equilibrium, these models can be used to accurately order their energy. This characteristic renders them powerful screening tools in high-throughput materials discovery workflows and suggests their potential use as a preliminary, layer-1 screening solution for phase-diagram prediction algorithms. Additionally, we can conclude that the potential of such trained force fields and the wealth of information within freely available databases should be fully leveraged in materials discovery efforts.

In the following two chapters, Chapter 4 and Chapter 5, we worked towards building a ternary convex hull prediction workflow and applied it to study various systems, such as CuAgAu and MoTaW. Some of these systems contained magnetic elements, specifically AlFeNi, BiFeZr, and BiFeTa. The approach we followed for these two projects is relatively similar. For a specific ternary system, we create a catalogue of candidate materials, which is subsequently screened using a machine learning interatomic potential (MLIAP). The choice of MLIAP dictates the limitations of our approach. In the first case, we employed SNAP, as discussed in the previous paragraphs, which

accurately predicts the energy of ternary systems when they are near or at equilibrium. In Chapter 5, we utilized a universal graph deep learning potential based on representing crystals and molecules as mathematical graphs, namely M3GNet.

For both approaches, we identified that ternary compounds created by decorating binary structures with the chosen elements provide a useful approximation for constructing the materials catalogue that will be used in the screening step. In the final part of the workflow, we conduct high-throughput DFT calculations to generate a ternary phase diagram with ab initio accuracy. Overall, the constructed workflows leverage data that are byproducts of ternary convex hull construction to search for novel ternary compounds. This is done in parallel to increasing the throughput of existing workflows and avoiding compromises in accuracy.

The first workflow, based on the SNAP potential, was employed in the search for thermodynamically stable compounds in the CuAgAu and MoTaW ternary systems. It successfully identified two novel ternaries in the Au-rich region of the ternary phase diagram, aligning with the finite temperature phase diagram for that system. Subsequently, it was applied to study the MoTaW ternary system, chosen for the performance of AFLOW there. For this system, the workflow identified six novel ternary structures in the center and near the TaW binary region, surpassing the two phases identified by AFLOW. This highlights its capability to identify multiple stable and metastable phases throughout the entire phase diagram in accordance with the experimental finite temperature phase diagram, consistently outperforming the AFLOW encyclopedia method of predicting ternary phase diagrams.

Overall, this study highlights the usefulness of readily available data. Workflows based on the byproducts of ab initio ternary phase diagram explorations are capable of predicting reasonable materials candidates. This work emphasizes the fact that there is still room for exploration in already-searched materials systems.

In Chapter 5, we employed M3GNet, a universal graph deep learning interatomic potential, to study ternary convex hulls containing magnetic elements. M3GNet utilizes the graph representation of molecules and solids, along with 3-body interactions, to

create a force field accurate enough for use as a screening tool. While its ability to guide structure relaxation towards the correct path reduced the throughput compared to the previous workflow, it enables the screening of a larger volume of candidate structures. However, the increased prediction error necessitates sampling more structures for DFT calculations. Despite this, the workflow surpasses known ab initio ternary prediction workflows, such as the AFLOW encyclopedia method, in predicting novel ternaries by being able to scan a larger space of materials.

The M3GNet-based workflow is compared with the SNAP-based workflow using the MoTaW ternary system. It systematically tracks the quality of predictions made by the latter and eventually surpasses it by predicting a variety of novel stable ternaries. Subsequently, the M3GNet workflow was applied to study ternary systems containing magnetic elements, specifically AlFeNi, BiFeTa, and BiFeZr. It successfully identified some novel stable and metastable ternaries in the AlFeNi system. However, it did not uncover any new phases in the bismuth-based ternaries. One possible explanation for this could be attributed to the poor alloying ability that bismuth exhibits with the rest of the elements in the periodic table.

In summary, we have introduced an end-to-end phase diagram prediction algorithm that harnesses the capabilities of machine-learning interatomic potentials as surrogates for DFT, enabling the efficient exploration of numerous candidate structures. These studies exemplify the seamless integration of machine-learning tools with prototype generation techniques, creating a pipeline capable of significantly reducing the need for ab initio calculations and, ultimately, generating ternary phase diagrams with DFT-level accuracy. Workflows of this nature exhibit valuable characteristics that, once complemented with accurate property predictors, such as critical temperature in the case of magnetic materials, are of great importance for the targeted search of functional materials.

In the final section of this thesis, we focused solely on a specific family of materials, in contrast to the previously discussed workflow. Heusler alloys are known to harbor materials with interesting properties, and in our case, we concentrated on exploring

them for tetragonally distorted and antiferromagnetic compounds. For this reason, we implemented two distinct workflows to accommodate the change in lattice or magnetic configuration. Subsequently, we moved on to discussing different approximations regarding the distance from the convex hull, based on available literature regarding disorder in these compounds. This study resulted in the correction of the distance from the convex hull for compounds that exhibit different ground state. Furthermore, machine learning models were trained with data extracted from the scientific literature to provide an estimation for the critical temperature of the explored compounds.

The results of this study are summarized in three tables. The number of compounds experimentally synthesized and those identified as stable by the workflows provide an estimate of the accuracy of the implemented workflow in making predictions. Compounds that are known to have been synthesized experimentally but were not predicted as stable by our workflows offer insights into the limitations of the high-throughput frameworks employed and underscore the role of disorder in predicting materials under ambient conditions. Ultimately, the comprehensive catalogue of compounds that fall below the energy threshold and are classified as stable serves as a valuable resource for those interested in the synthesis of novel Heusler compounds.

To sum up, in this thesis, we discuss a variety of tools and methods to create a machine-learning-assisted workflow used for the prediction of ternary phase diagrams. Additionally, we employ more traditional approaches to extensively explore a specific family of materials known as Heusler alloys. Beyond a materials design study, this thesis serves as a comparative analysis between these two approaches, presenting their limitations and advantages in each chapter. Furthermore, we demonstrated that data-driven methods and high-throughput ab initio calculations can be employed for the exploration and identification of novel materials. In the next section, we will explore potential future work, including the development of a more accurate workflow and the investigation of interesting properties of the predicted tetragonal Heusler compounds.

7.2 Future Work

In the last part of this thesis, we discuss potential directions for future research, considering the findings and limitations of the current work. We explore ways to improve the methodologies developed in this thesis and leverage them to expand research into possible areas of interest. Our objective is to contribute to a deeper understanding in the field of materials discovery and potentially identify functional materials of interest.

As discussed earlier, one of the limitations of the considered ternary phase diagram workflow lies in the fact that the interatomic potential employed is not accurate enough to predict the energy value of structures away from equilibrium but rather to order them energetically. This can be addressed by employing an active learning-like strategy to train the model by introducing similar structures in the training set. However, training a MLIAP with the use of active learning is often an expensive procedure. In the case of our workflow, we perform DFT calculations to validate our predictions by constructing the ternary phase diagram of the studied system.

Structures sampled along the relaxation path of these calculations can then be added to the training set of the machine learning potential. Doing that will enrich the training set with chemical environments far from equilibrium but still reasonable, as they were constructed by utilizing the binary compounds. Such a trained MLIAP may offer improved accuracy for energy prediction and the potential for atomic relaxation, as the variety of chemical environments contained in the dataset is, by definition, more diverse. Importantly, this step does not incur additional cost in the proposed workflow, as it leverages data already available from the previous step.

Such a trained potential can then be employed to re-evaluate the energy of the created materials and re-order their energy. This might be able to uncover predicted materials that had their energy wrongly ordered during the first energy screening. Furthermore, we can use it to estimate the entropy-forming ability, as introduced in [214], which serves as a descriptor of configurational entropy. Calculating this descriptor involves determining the number of different configurations that can be

formed for a specific stoichiometry, a byproduct of our workflow, and accurately predicting their energy.

So far, we have built a workflow to predict the ternary phase diagrams with ab initio accuracy. Employing such workflows alongside property predictors, such as the random forest regressor we used to predict the critical temperature in Chapter 6, creates a workflow that can be used for the search of thermodynamically stable compounds with targeted properties. Following the same idea to increase the prediction accuracy, we could fine-tune M3GNet with the use of data extracted from AFLOWLib for the class of materials that we are mostly interested in, in our case transition metals. This would result in a more accurate force field to be used in our workflow.

In the last part of our work, we explore Heusler alloys to identify potentially stable tetragonally-distorted compounds. It is reported that materials crystallize into non-cubic structures show a directional preference for magnetization, a phenomenon absent in cubic materials. This effect, known as magnetocrystalline anisotropy, refers to the fact that it requires more energy to magnetize a compound in a specific direction than it does in others. For this reason, high throughput magnetocrystalline anisotropy calculations can be employed to assess how strong this phenomenon is for these compounds. Combining that information with the distance from the convex hull can help us provide compounds that exhibit this property but are also experimentally realizable.

Appendices

Appendix A

PCA plot for Cu and Au

Principal Component Analysis (PCA) is a dimensionality reduction method used to analyze large datasets. It aids in improving interpretability with minimal information loss. In our case, the PCA algorithm was utilized to visualize the local chemical environments sampled during the relaxation of a given structure. Subsequently, they were compared with those sampled during the training process. This provides us with insights into the response of the trained model when it comes to predicting the energies of unseen chemical environments. Therefore, it would be beneficial to briefly present the basic concepts behind this method.

The way in which PCA reduces the dimensionality of the given dataset (in our case, the local chemical environment is translated to a vector of coefficients known as Bispectrum Components, B_i) is by fitting an ellipsoid to the data, where each of the axes represents a Principal Component. The algorithm to calculate the principal components begins by defining a matrix $\mathbf{X}$, where the number of rows, denoted n, corresponds to the different observables of the experiment (in our case, each of the different structures), and p represents the number of columns corresponding to the features of these vectors, which in our case is equal to 56. Furthermore, the mean of the columns of the matrix $\mathbf{X}$ is shifted to zero by subtracting the mean value.

To calculate the transformation of $\mathbf{w}_{(k)}$ that maps the rows of $\mathbf{X}$, denoted as $\mathbf{x}_{(i)}$, to the vector of the principal components $t_{k(i)} = \mathbf{x}_{(i)} \cdot \mathbf{w}_{(k)}$ for $i = 1, \ldots, n$ and $k = 1, \ldots, l$, this is done in a way that maximizes the variance for the new vector of components,

ensuring that the information remains unchanged through this transformation. Then we proceed to calculate the coefficient $\mathbf{w}_{(1)}$ that will lead us to the principal components $t_{k(i)}$.

$$\mathbf{w}_{(1)} = \arg\max_{\|\mathbf{w}\|=1} \left\{ \|\mathbf{X}\mathbf{w}\|^2 \right\} = \arg\max_{\|\mathbf{w}\|=1} \left\{ \mathbf{w}^\mathsf{T}\mathbf{X}^\mathsf{T}\mathbf{X}\mathbf{w} \right\} \tag{A.1}$$

to get the unit vector $\mathbf{w}_{(1)}$ we calculate.

$$\mathbf{w}_{(1)} = \arg\max \left\{ \frac{\mathbf{w}^\mathsf{T}\mathbf{X}^\mathsf{T}\mathbf{X}\mathbf{w}}{\mathbf{w}^\mathsf{T}\mathbf{w}} \right\} \tag{A.2}$$

Once the coefficients $\mathbf{w}_{(1)}$ are calculated. Then the first principal component can be calculated by $t_{1(i)} = \mathbf{x}_{(i)} \cdot \mathbf{w}_{(1)}$. To calculate the remaining k components, one has to subtract the $k-1$ components from the matrix $\mathbf{X}$ and perform a procedure similar to before. The matrix $\hat{\mathbf{X}}$ is calculated from Equation (A.3).

$$\hat{\mathbf{X}}_k = \mathbf{X} - \sum_{s=1}^{k-1} \mathbf{X}\mathbf{w}_{(s)}\mathbf{w}_{(s)}^\mathsf{T} \tag{A.3}$$

The weights, $\mathbf{w}_{(k)}$, are calculated using Equation (A.2). The matrix that corresponds to the full principal component decomposition is given by $\mathbf{T} = \mathbf{X}\mathbf{W}$. This transformation maps an original space of p variables to a new space of p variables. However, not all the components are needed always, in our case the first two components are visualised , calculated from the $\mathbf{T}_2 = \mathbf{X}\mathbf{W}_2$.

In our case, the analysis is conducted separately for each species. For all the structures in the training set, one must calculate the bispectrum components for each of the atoms contained in the crystal structure. Then, the bispectrum components corresponding to the same atom species are summed element-wise. Subsequently, this resulting vector (one vector per species and structure) is used to form the matrix $\mathbf{X}$ and calculate the bispectrum components. The results for the elements Au and Cu are shown in Figures A.1.

In the cases of Au and Cu (shown in Figure A.1), the relaxation process begins in a region that is better sampled in the training set. However, having an inaccurate

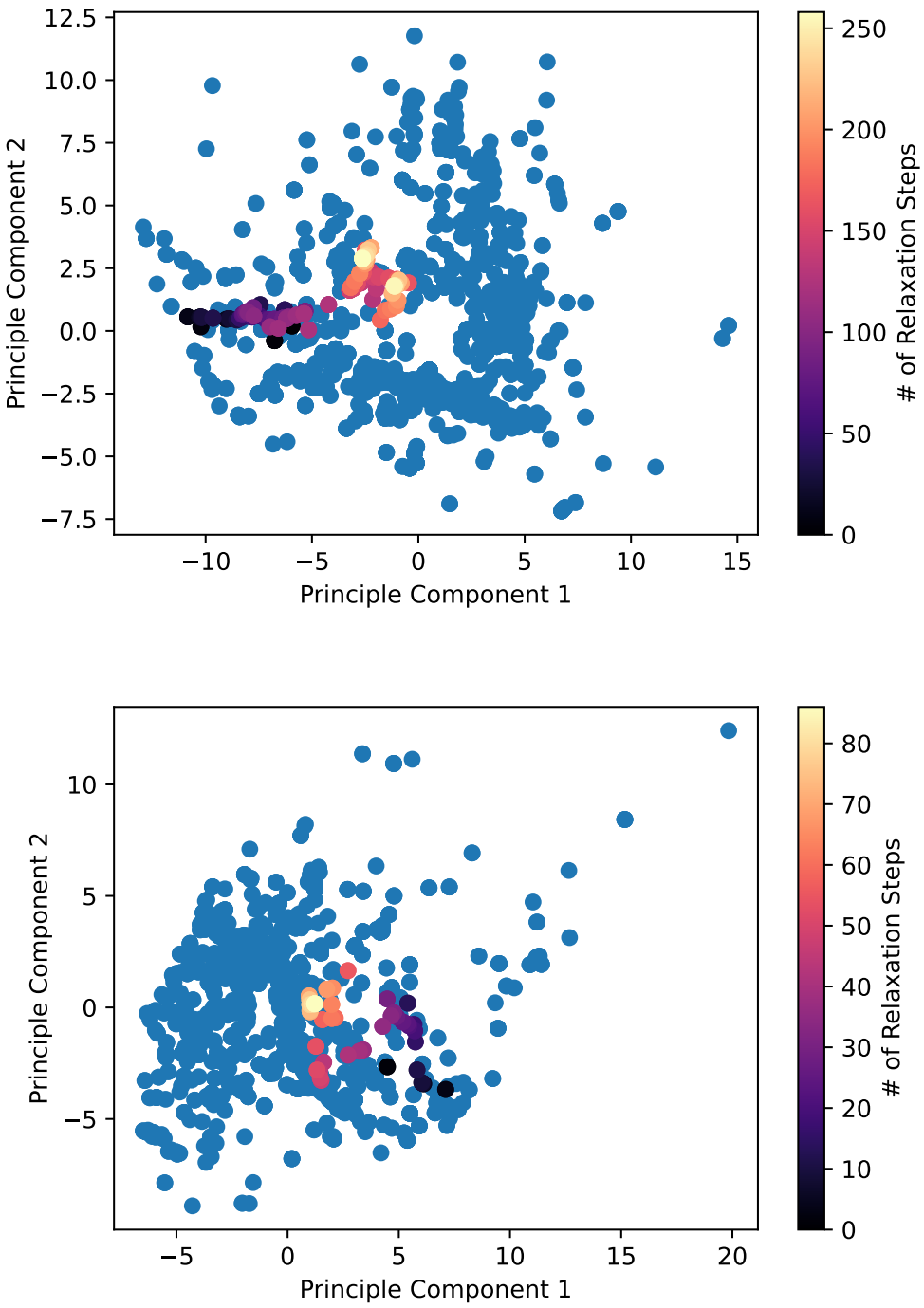

Figure A.1: Principal Components Analysis plot for the first two components for the local chemical environments of Au (upper panel) and Cu (lower panel) sampled in the training set (blue circles). The colored circles denote the local chemical environments of Au encountered through the relaxation path.

prediction for the Ag element (shown in 3.7) implies that the prediction of the total energy for the ternary structure will also be inaccurate. This underscores that in the case of ternary structures, achieving accurate predictions for all species is essential to ensure an accurate total energy prediction.

Appendix B

Candidates Selection for the AgAu

The Ag-Au binary system exhibits five distinct stable binary intermetallics across numerous stoichiometries, namely Ag_2Au_2, Ag_1Au_3, and Ag_3Au_1. Furthermore, a large number of metastable structures are energetically close to these stable configurations, resulting in a deeper calculated convex hull compared to those of the other two systems, namely Ag-Cu and Au-Cu. A narrower energy window for selecting structures from this convex hull is necessary to ensure equal sampling across all systems, preventing bias toward any particular binary. This energy window ensures a selection of 25 binary structures from the AgAu binary phase diagram.

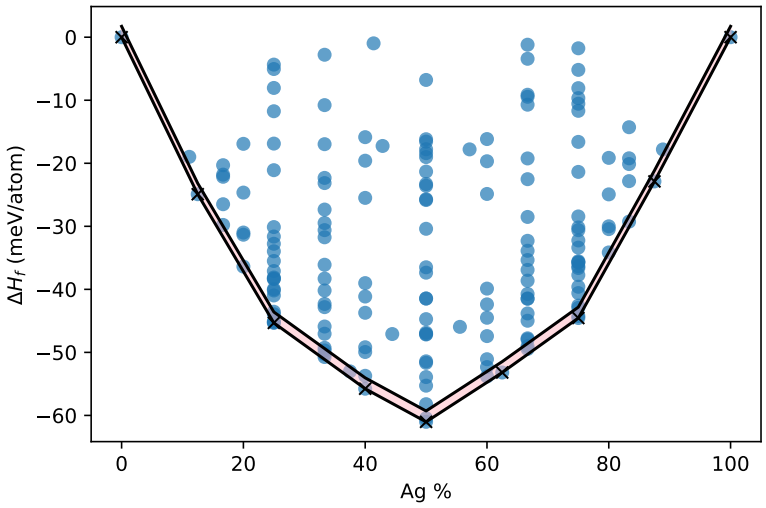

Figure B.1: The energy window used for selecting the required number of crystal structures in the Ag-Au binary system includes those within the pink-shaded region. These 25 structures are added to the primary pool of the parent compounds.

Appendix C

Convex hull analysis Mo-Ta-W

For the Mo-Ta-W ternary system, we scanned the binary convex hull of the consituents, namely Mo-Ta, Ta-W,and Mo-W and we selected the compounds with formation enthalpy closest to the calculated convex hull. The energy window is adjusted for each of the binary phase diagrams so that a similar number of compounds were selected. The energy window is a hyperparameter of the model and is employed to avoid oversampling of a specific binary. In the Figure C.1 the structures selected from each binary phase diagram are selected, as well as the energy window used.

In this case the Mo-Ta binary is the one with the deeper hull with depth of 170 meV/atom. This binary corresponds to those that exhibit the largest number of stable binary intermetallics with six stable compounds across different compositions. An energy window capable of selecting ~ 50 compounds per binary is chosen. The energy window is narrower as we move to deeper binary phase diagrams. Subsequently, the same procedure as before was followed, and we used the AFLOW-SYM [115] tool to select the unique structures prior decorating them.

Utilizing the AFLOW-SYM tool results in 28 unique structures. Following this step, these compounds will be decorated with the stoichiometries of interest and subsequently relaxed using an ensemble of SNAP models trained on the entire database consisting of data extracted from the phase diagrams of the three binary systems, namely Mo-W, Mo-Ta, and Ta-W. The structures with the predicted lowest energy then proceed to the DFT step.

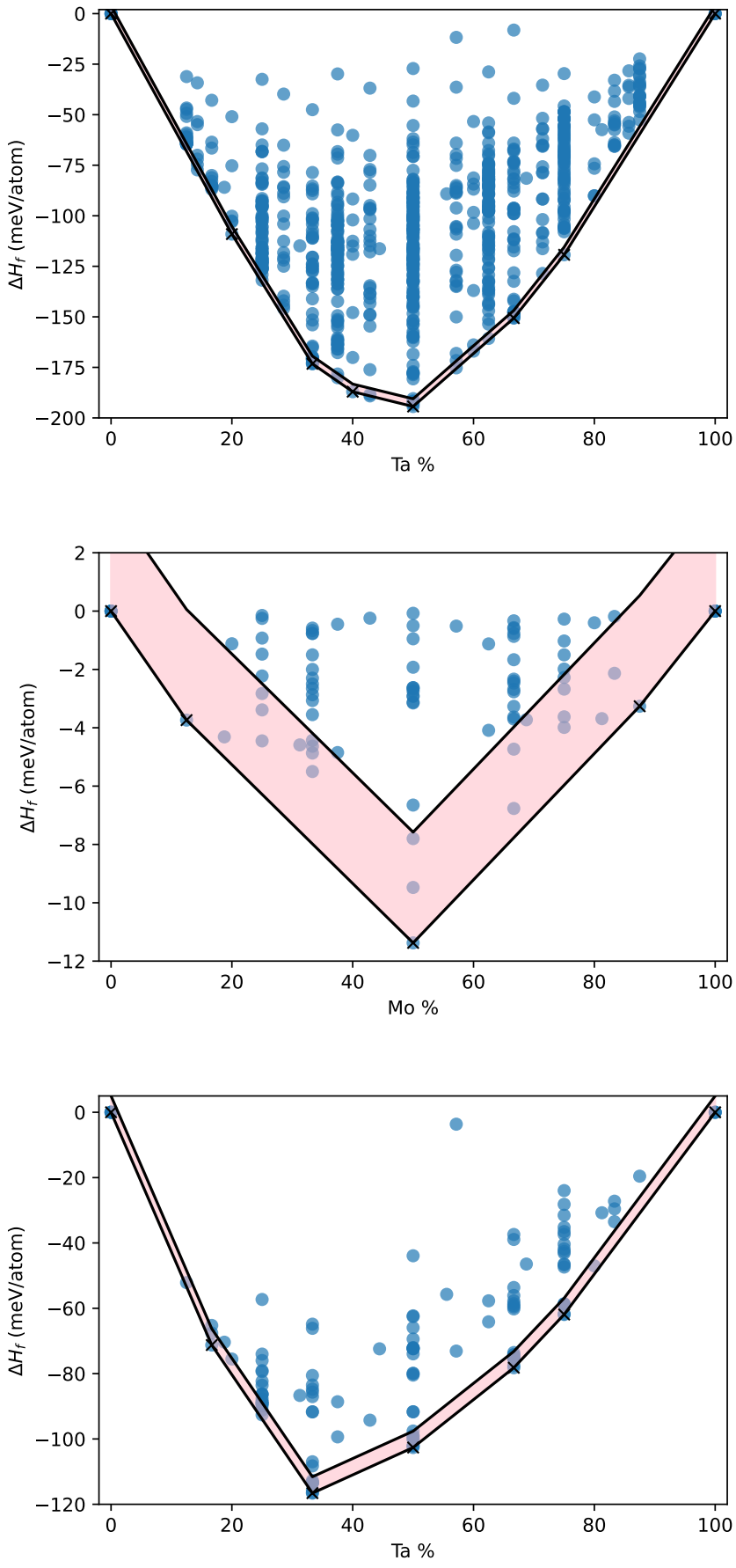

Figure C.1: The energy window employed for the selection of the necessary number of crystal structures for the Mo-Ta (upper), Mo-W (middle),and W-Ta (lower) binaries. The structures selected as parent structures are the ones inside the pink area.

Appendix D

Heusler Alloys

The list of the calculated differences between the cubic and tetragonally distorted structures for compounds that are experimentally synthesized and lie below the energy threshold of 17.81 meV/atom is presented below.

Compound	$\Delta E_{\mathrm{C-T}}$ (meV/atom)
$Rh_2Mn_1Sn_1$	-89.07
$Rh_2Ge_1Mn_1$	-1.50
$Ru_2Fe_1Ga_1$	-10.63
$Co_2Al_1Zr_1$	0.65
$Rh_2Ga_1Mn_1$	-82.35
$Co_2Mn_1Ti_1$	0.93
$Co_2Al_1Ta_1$	0.58
$Co_2Sc_1Sn_1$	0.35
$Ru_2Ge_1V_1$	0.33
$Mn_2Ga_1V_1$	0.34
$Ru_2Cr_1Ge_1$	0.22
$Rh_2In_1Mn_1$	0.14
$Ru_2Al_1Mn_1$	0.08
$Fe_2Co_1Ge_1$	0.03

Compound	$\Delta E_{\mathrm{C-T}}$ (meV/atom)
$Rh_2Al_1Fe_1$	-105.81
$Pd_2Mn_1Sn_1$	-0.95
$Ir_2Ga_1Mn_1$	-37.41
$Co_2Ge_1Ti_1$	-11.47
$Fe_2Co_1Si_1$	-102.31
$Ru_2Cr_1Si_1$	-1.14
$Mn_2Ge_1Ru_1$	-113.10
$Mn_2Pd_1Pt_1$	-33.84
$Mn_2Fe_1Ge_1$	-84.48
$Rh_2Al_1Mn_1$	-113.67
$Co_2Al_1Nb_1$	-60.20
$Co_2Al_1Fe_1$	-237.21
$Ni_2Al_1Mn_1$	-8.95
$Co_2Al_1Mn_1$	0.01
$Co_2Mn_1Si_1$	0.09
$Co_2Al_1V_1$	-31.18
$Co_2Fe_1Ge_1$	-55.59
$Co_2Al_1Ti_1$	-2.49
$Pd_2In_1Mn_1$	-3.65
$Co_2Fe_1Si_1$	-65.45
$Co_2Ge_1Mn_1$	-81.65
$Ru_2Mn_1Si_1$	-0.33
$Co_2Mn_1Sn_1$	0.25
$Mn_2Al_1V_1$	-117.57
$Fe_2Mn_1Si_1$	-0.18
$Ru_2Mn_1V_1$	-119.75

Compound	$\Delta E_{\mathrm{C-T}}$ (meV/atom)
$Ir_2Al_1Mn_1$	-69.59
$Co_2Ga_1V_1$	-2.53
$Co_2Ga_1Nb_1$	-17.59
$Co_2Fe_1Ga_1$	-181.79
$Mn_2Co_1Ga_1$	-138.86
$Co_2Ga_1Mn_1$	-1.41
$Co_2Ga_1Hf_1$	-0.04
$Co_2Mn_1Sb_1$	0.03
$Co_2Ga_1Ti_1$	-6.46
$Fe_2Ge_1Mn_1$	-0.08
$Au_2Al_1Mn_1$	-0.14
$Au_2Mn_1Zn_1$	-0.63
$Rh_2Mn_1Pb_1$	-19.81
$Ni_2Mn_1Sn_1$	0.84
$Pd_2Mn_1Sb_1$	2.60
$Ni_2Ga_1Mn_1$	2.74
$Co_2Si_1V_1$	25.51

Table D.1: The energy difference, $\Delta E_{\mathrm{C-T}}$, between the cubic and tetragonally distorted structures for the compounds that are experimentally synthesized and lie below the energy threshold.

From Table D.1 we observe that a large number of the compounds have large negative energy differences, meaning that a cubic cell is strongly favored with respect to the tetragonally distorted. The maximum value we calculate for introducing a tetragonally distortion in the lattice for those experimentally synthesized and predicted stable, is 25.51 meV/atom for the $Co_2Si_1V_1$, which helps to reduce the convex hull distance from 39.51 meV/atom to 14 meV/atom and to consider it stable.

Next, the complete list of Heusler compounds predicted to be stable, according

to the criteria introduced in Chapter 6, is presented below. It is important to note that, to the best of our knowledge, none of these compounds have been experimentally synthesized. The compounds are sorted in decreasing order based on their corrected distance from the convex hull, δ_{corr}.

Additionally, we provide predictions of the critical temperature $T_{\text{C}}^{\text{pred}}$ using the model referenced in [3]. This catalogue offers concise details regarding the stability of each specific compound, which may be valuable for researchers interested in experimental studies.

Compound	IH/FH	Tet	AF1	AF2	$T_{\text{C}}^{\text{pred}}$ (K)	δ' (meV/atom)
$Rh_2Mn_1Zn_1$	FH	✗	✗	✓	190.36	-21.76
$Ti_2In_1Zn_1$	FH	✓	✗	✗	356.03	-20.06
$Mn_2Pd_1Rh_1$	FH	✗	✗	✓	237.70	-18.45
$Fe_2Ge_1V_1$	FH	✗	✓	✗	404.69	-12.73
$Pd_2Hg_1Mn_1$	FH	✓	✓	✗	275.16	-11.09
$Mn_2Ir_1Ru_1$	FH	✗	✓	✗	337.58	-10.29
$Mn_2Co_1Ru_1$	FH	✓	✓	✗	248.88	-9.56
$Rh_2Mn_1Si_1$	FH	✗	✓	✗	207.87	-9.41
$Rh_2Mg_1Mn_1$	FH	✗	✗	✓	399.99	-8.46
$Rh_2Cr_1Li_1$	FH	✗	✓	✗	260.20	-7.13
$Mn_2Os_1Si_1$	IF	✗	✗	✓	319.26	-6.06
$Pt_2Li_1Mn_1$	FH	✗	✗	✓	236.96	-5.80
$Pt_2Mg_1Mn_1$	FH	✓	✓	✗	270.77	-5.11
$Pd_2Mg_1Mn_1$	FH	✗	✓	✗	385.66	-5.04
$Pt_2Cr_1Cu_1$	FH	✓	✗	✗	209.73	-4.57
$Pt_2Cd_1Mn_1$	FH	✓	✓	✗	351.00	-3.91
$Pt_2In_1Mn_1$	FH	✓	✗	✗	299.86	-3.09
$Pd_2Cd_1Mn_1$	FH	✓	✓	✗	300.53	-3.01
$Fe_2Ge_1Nb_1$	FH	✗	✓	✗	234.44	-2.77
$Mn_2Si_1Tc_1$	IF	✗	✗	✓	384.74	-2.55

Compound	IH/FH	Tet	AF1	AF2	T_C^{pred} (K)	δ' (meV/atom)
$Co_2V_1Zn_1$	FH	✓	✗	✗	268.42	-1.76
$Be_2Mn_1Pt_1$	FH	✓	✗	✗	400.57	-1.60
$Rh_2Li_1Mn_1$	FH	✓	✗	✓	400.61	-1.59
$Ru_2Cr_1Sn_1$	FH	✓	✗	✓	232.94	-1.47
$Co_2Ta_1Zn_1$	FH	✓	✗	✗	415.09	-1.40
$Pd_2Mn_1Zn_1$	FH	✓	✗	✗	187.59	-1.30
$Fe_2Sb_1Ti_1$	FH	✗	✓	✗	205.81	-0.87
$Be_2Ir_1Mn_1$	FH	✓	✗	✗	388.09	-0.62
$Co_2Hf_1In_1$	FH	✓	✗	✗	225.08	-0.58
$Be_2Co_1Ir_1$	FH	✓	✗	✗	207.93	-0.55
$Mn_2Ge_1Ti_1$	FH	✓	✗	✗	374.01	-0.53
$Pd_2Cu_1Fe_1$	FH	✓	✗	✗	519.04	-0.42
$Au_2Mn_1Pd_1$	IF	✓	✓	✗	287.05	-0.25
$Sc_2Cd_1Tl_1$	FH	✓	✗	✗	63.85	-0.17
$Co_2Ge_1Zn_1$	FH	✓	✗	✗	191.33	-0.09
$Fe_2Be_1V_1$	FH	✓	✗	✗	181.06	-0.09
$Pd_2Li_1Mn_1$	FH	✓	✗	✗	407.93	-0.08
$Mn_2Fe_1Si_1$	IF	✓	✗	✗	182.57	-0.04
$Ru_2Cr_1Ga_1$	FH	✓	✗	✗	152.22	-0.02
$Fe_2Ga_1Ir_1$	IF	✗	✗	✗	587.97	0.00
$Co_2In_1Zr_1$	FH	✗	✗	✗	239.36	0.00
$Mn_2Ga_1Ir_1$	IF	✗	✗	✗	351.37	0.00
$Rh_2Fe_1Zn_1$	FH	✗	✗	✗	505.93	0.00
$Rh_2Fe_1Ga_1$	FH	✗	✗	✗	515.38	0.00
$La_2Cd_1Tl_1$	FH	✗	✗	✗	58.61	0.00
$Mn_2Co_1Cr_1$	FH	✗	✗	✗	445.99	0.00
$Ru_2Si_1V_1$	FH	✗	✗	✗	175.05	0.00

Compound	IH/FH	Tet	AF1	AF2	T_C^{pred} (K)	δ' (meV/atom)
$Ir_2Fe_1Ga_1$	FH	✗	✗	✗	394.05	0.00
$Ru_2Sn_1V_1$	FH	✗	✗	✗	236.37	0.00
$Y_2Ga_1Li_1$	FH	✗	✗	✗	85.44	0.00
$Co_2In_1Ti_1$	FH	✗	✗	✗	305.28	0.00
$Ru_2Al_1Cr_1$	FH	✗	✗	✗	135.18	0.00
$Rh_2Mn_1Ti_1$	FH	✗	✗	✗	211.81	0.00
$Mn_2Al_1Nb_1$	FH	✗	✗	✗	458.68	0.00
$Zn_2Co_1Mn_1$	FH	✓	✗	✗	400.71	0.08
$Co_2Ga_1Ta_1$	FH	✗	✗	✗	391.62	0.09
$Mn_2Al_1Ti_1$	FH	✗	✗	✗	543.89	0.47
$Cu_2Mn_1Pt_1$	FH	✓	✗	✗	262.82	0.56
$Fe_2Ir_1Rh_1$	FH	✗	✓	✗	649.73	1.09
$Ir_2In_1Zr_1$	FH	✓	✗	✗	30.42	1.27
$La_2Hg_1Tl_1$	FH	✗	✗	✗	25.63	1.29
$Ni_2Mn_1Zn_1$	FH	✓	✗	✗	539.17	1.33
$Y_2Hg_1Tl_1$	FH	✓	✗	✗	22.51	1.53
$Sc_2Hg_1Tl_1$	FH	✗	✗	✗	43.06	1.58
$La_2Ag_1Tl_1$	FH	✗	✗	✓	36.76	1.62
$Co_2Nb_1Zn_1$	FH	✗	✓	✗	356.88	2.00
$Mn_2Ga_1Ti_1$	FH	✗	✗	✗	483.62	2.16
$Ir_2Mn_1Zn_1$	FH	✗	✗	✓	379.11	2.16
$La_2Ag_1Hg_1$	FH	✓	✗	✗	36.33	2.96
$Rh_2Bi_1Mg_1$	FH	✓	✗	✗	39.13	3.96
$La_2Cd_1Hg_1$	FH	✓	✗	✗	48.23	3.96
$Co_2Be_1Ta_1$	FH	✓	✗	✗	331.70	4.12
$Co_2Ga_1Zr_1$	FH	✓	✗	✗	237.13	4.17
$Zn_2Ir_1Mn_1$	FH	✓	✗	✗	283.14	4.39

Compound	IH/FH	Tet	AF1	AF2	T_C^{pred} (K)	δ' (meV/atom)
$Fe_2Ga_1Ti_1$	FH	✓	✗	✗	504.78	5.41
$Ru_2Mn_1Nb_1$	FH	✗	✗	✗	241.40	6.15
$Co_2Fe_1Zn_1$	FH	✓	✗	✗	1134.93	6.98
$Ru_2Mn_1Ta_1$	FH	✗	✗	✗	288.01	7.09
$Mn_2Ru_1Si_1$	IF	✓	✗	✓	512.74	7.30
$Mn_2Ga_1Nb_1$	FH	✓	✗	✗	445.90	7.48
$Fe_2Al_1Mn_1$	FH	✗	✓	✗	197.52	7.54
$Hf_2Os_1V_1$	FH	✓	✗	✗	44.28	7.66
$Ti_2Ga_1Pd_1$	FH	✓	✗	✗	389.17	9.13
$Mn_2Ga_1Zn_1$	FH	✓	✗	✗	469.43	9.24
$Ta_2Fe_1Os_1$	FH	✓	✗	✗	182.05	9.82
$Os_2Mn_1Si_1$	FH	✗	✗	✓	345.14	10.17
$Zn_2Mn_1Pt_1$	FH	✓	✗	✗	254.72	10.24
$Ir_2Fe_1Mn_1$	FH	✓	✗	✗	402.29	10.30
$Rh_2Fe_1Mg_1$	FH	✗	✗	✗	343.47	10.60
$Fe_2Nb_1Sn_1$	FH	✗	✓	✗	226.07	10.69
$Rh_2Cr_1Zn_1$	FH	✗	✗	✓	156.12	10.91
$Be_2Co_1Rh_1$	FH	✓	✗	✗	228.01	11.25
$Mn_2Ir_1Si_1$	IF	✗	✗	✓	329.55	11.44
$Au_2Mn_1Pd_1$	FH	✓	✗	✗	287.05	11.52
$Rh_2Hf_1Mn_1$	FH	✗	✗	✗	258.12	12.02
$Rh_2Mn_1Zr_1$	FH	✗	✗	✗	318.48	12.32
$Ir_2Cr_1Ga_1$	FH	✓	✗	✗	116.83	13.26
$Rh_2Mn_1Sc_1$	FH	✗	✗	✗	352.71	13.69
$Mn_2Cr_1Ga_1$	FH	✓	✗	✗	633.11	13.85
$Ti_2Al_1Ir_1$	IF	✗	✗	✗	105.31	14.29
$Cu_2Mn_1Pd_1$	FH	✓	✗	✗	267.76	14.44

Compound	IH/FH	Tet	AF1	AF2	T_C^{pred} (K)	δ' (meV/atom)
$Pt_2Cu_1Mn_1$	FH	✓	✗	✗	332.74	14.64
$Be_2Co_1Mn_1$	FH	✓	✗	✗	466.91	14.74
$La_2Ag_1Cd_1$	FH	✗	✗	✗	81.04	14.86
$Sc_2Hg_1In_1$	FH	✓	✗	✗	85.51	15.11
$Rh_2Be_1Fe_1$	FH	✗	✗	✗	432.06	15.12
$Cd_2La_1Y_1$	FH	✗	✗	✓	80.06	15.50
$Co_2Cr_1Si_1$	FH	✗	✗	✗	176.24	16.47
$Fe_2Co_1Ti_1$	IF	✗	✗	✗	801.75	16.48
$Rh_2Fe_1In_1$	FH	✗	✗	✗	389.40	16.55
$Be_2Mn_1Rh_1$	FH	✗	✗	✗	458.90	16.89
$Al_2Ir_1Mn_1$	FH	✓	✓	✗	381.50	16.98
$Ni_2Ge_1Mn_1$	FH	✗	✗	✗	392.57	17.33
$La_2Ag_1Zn_1$	FH	✗	✗	✓	80.67	17.37
$Ru_2Al_1Fe_1$	FH	✓	✗	✓	450.50	17.92
$Pd_2Cu_1Mn_1$	FH	✗	✗	✗	200.33	18.13
$Mn_2Al_1Hf_1$	FH	✗	✗	✗	161.87	18.36
$Pt_2Cu_1Fe_1$	FH	✓	✗	✗	417.46	19.78
$La_2Ag_1Sn_1$	FH	✓	✗	✗	77.13	20.16
$Mn_2Co_1Si_1$	IF	✗	✗	✗	455.60	20.25
$Ti_2Os_1V_1$	FH	✗	✗	✓	122.38	20.60
$Pt_2Ga_1Mn_1$	FH	✓	✗	✗	285.19	21.51
$Co_2Be_1Fe_1$	FH	✓	✗	✗	845.40	21.65
$Ru_2Fe_1Ta_1$	FH	✗	✗	✗	350.35	21.83
$Os_2Mn_1Ta_1$	FH	✗	✗	✗	320.75	21.98
$Pd_2Au_1Fe_1$	FH	✓	✗	✗	334.64	22.49
$Mn_2Co_1Ni_1$	FH	✗	✗	✗	391.37	22.97
$Zr_2Co_1Fe_1$	FH	✓	✗	✗	216.03	23.33

Compound	IH/FH	Tet	AF1	AF2	T_C^{pred} (K)	δ' (meV/atom)
$Cu_2Au_1Mn_1$	FH	✓	✗	✗	253.84	23.89
$Fe_2Ta_1Ti_1$	FH	✗	✗	✗	212.79	24.09
$Ir_2Mn_1Sn_1$	FH	✗	✓	✗	353.99	24.17
$La_2Hg_1Zn_1$	FH	✓	✗	✗	51.67	24.39
$Be_2Cr_1Pt_1$	FH	✓	✗	✗	113.01	24.57
$Zn_2Mn_1Rh_1$	FH	✓	✗	✗	258.76	24.65
$Ti_2Co_1Ni_1$	FH	✗	✓	✗	256.23	24.91
$Ti_2Mn_1Ru_1$	FH	✗	✗	✗	304.80	24.92
$Ir_2Mg_1Mn_1$	FH	✗	✗	✓	250.38	25.00
$Rh_2Be_1Mn_1$	FH	✓	✗	✓	360.52	25.92
$Ir_2Al_1Fe_1$	FH	✗	✗	✗	396.12	26.31
$Co_2Mg_1Sn_1$	FH	✗	✓	✗	208.68	26.44
$Pd_2Fe_1Li_1$	FH	✗	✗	✗	260.40	26.73
$Hg_2La_1Y_1$	FH	✓	✗	✓	26.79	27.28
$Cu_2Mn_1Pt_1$	IF	✓	✓	✗	262.82	27.59
$Fe_2Ir_1Si_1$	IF	✗	✗	✗	460.09	28.28
$Co_2Fe_1Ti_1$	FH	✗	✗	✗	897.83	28.29
$Fe_2Ru_1Si_1$	IF	✗	✗	✗	486.73	28.51
$Ir_2Be_1Mn_1$	FH	✓	✗	✓	393.31	28.63
$Ir_2Mn_1Si_1$	FH	✗	✓	✗	355.09	28.90
$Al_2Co_1Ni_1$	FH	✓	✗	✗	148.77	28.90
$Fe_2Ti_1V_1$	FH	✓	✗	✗	139.90	28.97
$Mn_2Al_1Cr_1$	FH	✗	✗	✗	604.99	29.28
$Au_2Cu_1Mn_1$	FH	✓	✗	✓	282.40	29.35
$Co_2Hf_1Ti_1$	FH	✗	✗	✗	308.89	29.81
$La_2Ag_1Pb_1$	FH	✗	✗	✗	32.04	29.90
$Al_2Cr_1Ir_1$	FH	✓	✗	✗	97.49	30.35

Compound	IH/FH	Tet	AF1	AF2	T_C^{pred} (K)	δ' (meV/atom)
$Mn_2Rh_1Ru_1$	FH	✗	✓	✗	236.98	30.43
$Fe_2Ru_1V_1$	IF	✗	✗	✗	484.53	30.47
$Co_2Be_1Nb_1$	FH	✗	✓	✗	266.33	31.49
$Pt_2Al_1Mn_1$	FH	✓	✓	✗	292.71	31.73
$Au_2Li_1Mn_1$	FH	✓	✗	✓	195.91	32.54
$Al_2Ir_1V_1$	FH	✗	✗	✗	69.04	32.59
$Mn_2Ge_1Os_1$	IF	✗	✗	✗	273.96	33.52
$Mn_2Al_1Os_1$	IF	✗	✗	✓	300.31	33.61
$Ir_2Mn_1Ti_1$	FH	✗	✗	✗	347.39	34.21
$Cu_2Mn_1Ni_1$	IF	✓	✗	✗	545.73	34.28
$Ba_2Ga_1Zn_1$	FH	✗	✗	✗	81.72	34.33
$Rh_2Cu_1Mn_1$	FH	✓	✗	✓	214.76	34.42
$Ni_2Cu_1Fe_1$	FH	✓	✗	✗	624.39	34.45
$Al_2Fe_1Ni_1$	FH	✓	✓	✗	349.79	34.65
$Ru_2Fe_1V_1$	FH	✗	✗	✗	401.52	34.71
$Au_2Mg_1Mn_1$	FH	✗	✗	✗	250.94	34.76
$Co_2Ge_1V_1$	FH	✓	✗	✗	273.27	35.18

Table D.2: The complete catalog of Heusler compounds predicted to be thermodynamically stable according to our criteria, yet not experimentally synthesized, is presented up to of 35.62 meV/atom away from the convex hull. When the 8.91 meV/atom boundary is taken into account, the specific compounds are added and correspond to those above the red line. For each compound, we indicate its Heusler type (Inverse (IH) or Full (FH)), predicted lattice distortion (Tetragonal distortion (Tet)), and magnetic ordering (Antiferromagnet 1 (AF1) or Antiferromagnet 2 (AF2)) in case they correspond to an antiferromagnetic ground-state. Additionally, we present the predicted Curie temperature, T_C^{pred}, and the corrected distance from the convex hull (δ').

Next, we present the energy differences between the cubic and tetragonally distorted lattice, as well as between the antiferromagnetic and ferromagnetic ground state energies when the ground state of the studied compound corresponds to an antiferromagnetic state.

Compound	$\Delta E_{\mathrm{C-T}}$ (meV/atom)	$\Delta E_{\mathrm{A-F}}$ (meV/atom)
$Rh_2Mn_1Zn_1$	-44.84	27.09
$Ti_2In_1Zn_1$	114.09	✗
$Mn_2Pd_1Rh_1$	-179.71	24.60
$Fe_2Ge_1V_1$	-5.08	16.23
$Pd_2Hg_1Mn_1$	37.58	13.25
$Mn_2Ir_1Ru_1$	-33.19	57.65
$Mn_2Co_1Ru_1$	7.66	73.97
$Rh_2Mn_1Si_1$	-88.99	9.77
$Rh_2Mg_1Mn_1$	-0.23	29.68
$Rh_2Cr_1Li_1$	-0.11	12.78
$Mn_2Os_1Si_1$	-225.42	6.22
$Pt_2Li_1Mn_1$	-3.64	8.43
$Pt_2Mg_1Mn_1$	13.71	28.67
$Pd_2Mg_1Mn_1$	-9.32	10.18
$Pt_2Cr_1Cu_1$	98.60	✗
$Pt_2Cd_1Mn_1$	59.63	21.84
$Pt_2In_1Mn_1$	49.54	✗
$Pd_2Cd_1Mn_1$	20.16	13.86
$Fe_2Ge_1Nb_1$	-8.77	18.84
$Mn_2Si_1Tc_1$	-185.47	24.14
$Co_2V_1Zn_1$	9.73	✗
$Be_2Mn_1Pt_1$	1.60	✗
$Rh_2Li_1Mn_1$	0.16	24.52
$Ru_2Cr_1Sn_1$	0.23	12.47
$Co_2Ta_1Zn_1$	3.72	✗
$Pd_2Mn_1Zn_1$	20.49	✗
$Fe_2Sb_1Ti_1$	-0.16	15.10

Compound	$\Delta E_{\mathrm{C-T}}$ (meV/atom)	$\Delta E_{\mathrm{A-F}}$ (meV/atom)
$Be_2Ir_1Mn_1$	0.62	✗
$Co_2Hf_1In_1$	0.58	✗
$Be_2Co_1Ir_1$	0.55	✗
$Mn_2Ge_1Ti_1$	0.53	✗
$Pd_2Cu_1Fe_1$	26.58	✗
$Au_2Mn_1Pd_1$	78.38	3.39
$Sc_2Cd_1Tl_1$	0.17	✗
$Co_2Ge_1Zn_1$	0.21	✗
$Fe_2Be_1V_1$	0.09	✗
$Pd_2Li_1Mn_1$	0.61	✗
$Mn_2Fe_1Si_1$	0.04	✗
$Ru_2Cr_1Ga_1$	0.02	✗
$Fe_2Ga_1Ir_1$	-133.85	✗
$Co_2In_1Zr_1$	-2.24	✗
$Mn_2Ga_1Ir_1$	-143.21	✗
$Rh_2Fe_1Zn_1$	-67.75	✗
$Rh_2Fe_1Ga_1$	-84.09	✗
$La_2Cd_1Tl_1$	-0.16	✗
$Mn_2Co_1Cr_1$	-125.27	✗
$Ru_2Si_1V_1$	-8.62	✗
$Ir_2Fe_1Ga_1$	-112.46	✗
$Ru_2Sn_1V_1$	-4.86	✗
$Y_2Ga_1Li_1$	-0.32	✗
$Co_2In_1Ti_1$	-17.48	✗
$Ru_2Al_1Cr_1$	-194.16	✗
$Rh_2Mn_1Ti_1$	-150.73	✗
$Mn_2Al_1Nb_1$	-1.95	✗

Compound	$\Delta E_{\mathrm{C-T}}$ (meV/atom)	$\Delta E_{\mathrm{A-F}}$ (meV/atom)
$Zn_2Co_1Mn_1$	53.90	✗
$Co_2Ga_1Ta_1$	-15.08	✗
$Mn_2Al_1Ti_1$	-10.53	✗
$Cu_2Mn_1Pt_1$	79.81	✗
$Fe_2Ir_1Rh_1$	-52.90	52.44
$Ir_2In_1Zr_1$	83.35	✗
$La_2Hg_1Tl_1$	-0.08	✗
$Ni_2Mn_1Zn_1$	9.28	✗
$Y_2Hg_1Tl_1$	0.42	✗
$Sc_2Hg_1Tl_1$	-0.27	✗
$La_2Ag_1Tl_1$	-0.12	0.12
$Co_2Nb_1Zn_1$	-15.03	2.02
$Mn_2Ga_1Ti_1$	-0.27	✗
$Ir_2Mn_1Zn_1$	-8.92	13.92
$La_2Ag_1Hg_1$	0.12	✗
$Rh_2Bi_1Mg_1$	24.55	✗
$La_2Cd_1Hg_1$	0.26	✗
$Co_2Be_1Ta_1$	10.52	✗
$Co_2Ga_1Zr_1$	0.53	✗
$Zn_2Ir_1Mn_1$	38.05	✗
$Fe_2Ga_1Ti_1$	0.03	✗
$Ru_2Mn_1Nb_1$	-157.68	✗
$Co_2Fe_1Zn_1$	0.21	✗
$Ru_2Mn_1Ta_1$	-230.10	✗
$Mn_2Ru_1Si_1$	0.04	0.46
$Mn_2Ga_1Nb_1$	0.02	✗
$Fe_2Al_1Mn_1$	-0.16	8.37

Compound	$\Delta E_{\mathrm{C-T}}$ (meV/atom)	$\Delta E_{\mathrm{A-F}}$ (meV/atom)
$Hf_2Os_1V_1$	24.63	✗
$Ti_2Ga_1Pd_1$	84.77	✗
$Mn_2Ga_1Zn_1$	59.97	✗
$Ta_2Fe_1Os_1$	0.05	✗
$Os_2Mn_1Si_1$	-1.72	8.18
$Zn_2Mn_1Pt_1$	22.30	✗
$Ir_2Fe_1Mn_1$	73.80	✗
$Rh_2Fe_1Mg_1$	-117.06	✗
$Fe_2Nb_1Sn_1$	-12.70	33.04
$Rh_2Cr_1Zn_1$	-14.50	11.08
$Be_2Co_1Rh_1$	0.49	✗
$Mn_2Ir_1Si_1$	-87.12	1.98
$Au_2Mn_1Pd_1$	60.74	✗
$Rh_2Hf_1Mn_1$	-324.49	✗
$Rh_2Mn_1Zr_1$	-304.74	✗
$Ir_2Cr_1Ga_1$	66.75	✗
$Rh_2Mn_1Sc_1$	-136.88	✗
$Mn_2Cr_1Ga_1$	17.26	✗
$Ti_2Al_1Ir_1$	-0.36	✗
$Cu_2Mn_1Pd_1$	66.79	✗
$Pt_2Cu_1Mn_1$	37.28	✗
$Be_2Co_1Mn_1$	0.06	✗
$La_2Ag_1Cd_1$	-0.17	✗
$Sc_2Hg_1In_1$	0.33	✗
$Rh_2Be_1Fe_1$	-125.31	✗
$Cd_2La_1Y_1$	-0.01	0.14
$Co_2Cr_1Si_1$	-8.50	✗

Compound	$\Delta E_{\mathrm{C-T}}$ (meV/atom)	$\Delta E_{\mathrm{A-F}}$ (meV/atom)
$Fe_2Co_1Ti_1$	-168.36	✗
$Rh_2Fe_1In_1$	-71.28	✗
$Be_2Mn_1Rh_1$	-6.89	✗
$Al_2Ir_1Mn_1$	0.49	34.08
$Ni_2Ge_1Mn_1$	-9.95	✗
$La_2Ag_1Zn_1$	-0.39	0.15
$Ru_2Al_1Fe_1$	0.29	7.89
$Pd_2Cu_1Mn_1$	-0.01	✗
$Mn_2Al_1Hf_1$	-6.78	✗
$Pt_2Cu_1Fe_1$	50.07	✗
$La_2Ag_1Sn_1$	0.19	✗
$Mn_2Co_1Si_1$	-86.16	✗
$Ti_2Os_1V_1$	-2.43	16.80
$Pt_2Ga_1Mn_1$	44.96	✗
$Co_2Be_1Fe_1$	0.19	✗
$Ru_2Fe_1Ta_1$	-151.02	✗
$Os_2Mn_1Ta_1$	-110.55	✗
$Pd_2Au_1Fe_1$	57.23	✗
$Mn_2Co_1Ni_1$	-1.16	✗
$Zr_2Co_1Fe_1$	19.02	✗
$Cu_2Au_1Mn_1$	46.42	✗
$Fe_2Ta_1Ti_1$	-0.23	✗
$Ir_2Mn_1Sn_1$	-11.69	58.95
$La_2Hg_1Zn_1$	0.83	✗
$Be_2Cr_1Pt_1$	1.39	✗
$Zn_2Mn_1Rh_1$	20.23	✗
$Ti_2Co_1Ni_1$	-45.52	0.11

Compound	$\Delta E_{\mathrm{C-T}}$ (meV/atom)	$\Delta E_{\mathrm{A-F}}$ (meV/atom)
$Ti_2Mn_1Ru_1$	-1.57	✗
$Ir_2Mg_1Mn_1$	-39.69	22.57
$Rh_2Be_1Mn_1$	0.42	22.30
$Ir_2Al_1Fe_1$	-135.02	✗
$Co_2Mg_1Sn_1$	-0.34	0.89
$Pd_2Fe_1Li_1$	-2.21	✗
$Hg_2La_1Y_1$	0.22	0.02
$Cu_2Mn_1Pt_1$	37.24	1.91
$Fe_2Ir_1Si_1$	-130.73	✗
$Co_2Fe_1Ti_1$	-0.30	✗
$Fe_2Ru_1Si_1$	-142.68	✗
$Ir_2Be_1Mn_1$	0.25	10.13
$Ir_2Mn_1Si_1$	-116.12	56.43
$Al_2Co_1Ni_1$	0.10	✗
$Fe_2Ti_1V_1$	0.70	✗
$Mn_2Al_1Cr_1$	-1.55	✗
$Au_2Cu_1Mn_1$	0.46	0.41
$Co_2Hf_1Ti_1$	-1.12	✗
$La_2Ag_1Pb_1$	-0.14	✗
$Al_2Cr_1Ir_1$	0.23	✗
$Mn_2Rh_1Ru_1$	-83.66	9.16
$Fe_2Ru_1V_1$	-117.72	✗
$Co_2Be_1Nb_1$	-3.35	1.19
$Pt_2Al_1Mn_1$	11.93	1.79
$Au_2Li_1Mn_1$	0.07	3.29
$Al_2Ir_1V_1$	-2.40	✗
$Mn_2Ge_1Os_1$	-89.11	✗

Compound	$\Delta E_{\mathrm{C-T}}$ (meV/atom)	$\Delta E_{\mathrm{A-F}}$ (meV/atom)
$Mn_2Al_1Os_1$	-0.10	49.75
$Ir_2Mn_1Ti_1$	-79.01	✗
$Cu_2Mn_1Ni_1$	52.61	✗
$Ba_2Ga_1Zn_1$	-0.26	✗
$Rh_2Cu_1Mn_1$	16.45	5.95
$Ni_2Cu_1Fe_1$	47.26	✗
$Al_2Fe_1Ni_1$	0.32	2.58
$Ru_2Fe_1V_1$	-79.09	✗
$Au_2Mg_1Mn_1$	-0.94	✗
$Co_2Ge_1V_1$	37.92	✗

Table D.3: The complete catalog of Heusler compounds predicted up to a distance of 35 meV/atom away from the convex hull. The compounds added when the boundary of 8.91 meV/atom is taken into account are those above the red line. For each compound, we present the energy difference between the cubic and the tetragonally distorted structure, $\Delta E_{\mathrm{C-T}}$ (meV/atom). As well as the energy differences between the antiferromagnetic and ferromagnetic ground state, $\Delta E_{\mathrm{A-F}}$ (meV/atom), when an antiferromagnetic ground state is found.

Here, in Table D.3 we observe that for a number of structures the tetragonal distorted structure is strongly favored against the cubic one. Some examples are the $Ti_2In_1Zn_1$, that exhibits and energy difference of 114.09 meV/atom, the Pt-rich alloys of $Pt_2Cr_1Cu_1$, $Pt_2Cd_1Mn_1$, and $Pt_2In_1Mn_1$ with energy differences of 98.60, 59.63, and 49.54 meV/atom. Furthermore, there are structures that the antiferromagnetic ground state is strongly favored comprared to the ferromagnetic, for example the Mn-rich alloys $Mn_2Ir_1Ru_1$ and $Mn_2Co_1Ru_1$ with energy values of 57.65 and 73.97 meV/atom, respectivelly.

Bibliography

1. Ashby, M. Materials–a brief history. *Philosophical magazine letters* **88,** 749–755 (2008).

2. Coey, J. M. *Magnetism and magnetic materials* (Cambridge university press, 2010).

3. Nelson, J. & Sanvito, S. Predicting the Curie temperature of ferromagnets using machine learning. *Physical Review Materials* **3,** 104405 (2019).

4. Curtarolo, S. *et al.* The high-throughput highway to computational materials design. *Nature Materials* **12,** 191–201 (2013).

5. Armiento, R., Kozinsky, B., Fornari, M. & Ceder, G. Screening for high-performance piezoelectrics using high-throughput density functional theory. *Physical Review B* **84,** 014103 (2011).

6. Sanvito, S. *et al.* Accelerated discovery of new magnets in the Heusler alloy family. *Science Advances* **3,** e1602241 (2017).

7. Choudhary, K. & Garrity, K. Designing high-TC superconductors with BCS-inspired screening, density functional theory, and deep-learning. *npj Computational Materials* **8,** 244 (2022).

8. Bardeen, J., Cooper, L. N. & Schrieffer, J. R. Microscopic theory of superconductivity. *Physical Review* **106,** 162 (1957).

9. Choudhary, K. *et al.* The joint automated repository for various integrated simulations (JARVIS) for data-driven materials design. *npj computational materials* **6,** 173 (2020).

10. Bartók, A. P., Payne, M. C., Kondor, R. & Csányi, G. Gaussian Approximation Potentials: The Accuracy of Quantum Mechanics, without the Electrons. *Physical Review Letter* **104,** 136403 (13 2010).

11. Drautz, R. Atomic cluster expansion for accurate and transferable interatomic potentials. *Physical Review B* **99,** 014104 (2019).

12. Shapeev, A. V. Moment tensor potentials: A class of systematically improvable interatomic potentials. *Multiscale Modeling & Simulation* **14,** 1153–1173 (2016).

13. Chen, C. & Ong, S. P. A universal graph deep learning interatomic potential for the periodic table. *Nature Computational Science* **2,** 718–728 (2022).

14. Domina, M., Patil, U., Cobelli, M. & Sanvito, S. The Jacobi-Legendre potential. *arXiv preprint arXiv:2208.10292* (2022).

15. Stanev, V. *et al.* Machine learning modeling of superconducting critical temperature. *npj Computational Materials* **4,** 29 (2018).

16. Liang, H., Stanev, V., Kusne, A. G. & Takeuchi, I. CRYSPNet: Crystal structure predictions via neural networks. *Physical Review Materials* **4,** 123802 (2020).

17. Zunger, A. Inverse design in search of materials with target functionalities. *Nature Reviews Chemistry* **2,** 0121 (2018).

18. Martin, R. M. *Electronic structure: basic theory and practical methods* (Cambridge university press, 2020).

19. Hohenberg, P. & Kohn, W. Inhomogeneous Electron Gas. *Phys. Rev.* **136,** B864–B871 (3B 1964).

20. Kohn, W. & Sham, L. J. Self-Consistent Equations Including Exchange and Correlation Effects. *Physical Review* **140,** A1133–A1138 (4A 1965).

21. Kohn, W. v-Representability and density functional theory. *Physical review letters* **51,** 1596 (1983).

22. Levy, M. Universal variational functionals of electron densities, first-order density matrices, and natural spin-orbitals and solution of the v-representability problem. *Proceedings of the National Academy of Sciences* **76,** 6062–6065 (1979).

23. Levy, M. Electron densities in search of Hamiltonians. *Physical Review A* **26,** 1200 (1982).

24. Levy, M. Density functional methods in physics. *The inhomogeneous electron gas,* 32–94 (1985).

25. Lieb, E. *Physics as Natural Philosophy ed A Shimony and H Feshbach* 1982.

26. Born, M. & Heisenberg, W. Zur quantentheorie der molekeln. *Original Scientific Papers Wissenschaftliche Originalarbeiten,* 216–246 (1985).

27. Perdew, J. P., Burke, K. & Ernzerhof, M. Generalized Gradient Approximation Made Simple. *Phys. Rev. Lett.* **77,** 3865–3868 (18 1996).

28. Kresse, G. & Furthmüller, J. Efficiency of ab-initio total energy calculations for metals and semiconductors using a plane-wave basis set. *Computational Materials Science* **6,** 15–50 (1996).

29. Kresse, G. & Hafner, J. Ab initio molecular dynamics for liquid metals. *Physical review B* **47,** 558 (1993).

30. Kresse, G. & Joubert, D. From ultrasoft pseudopotentials to the projector augmented-wave method. *Physical review b* **59,** 1758 (1999).

31. Kresse, G. & Furthmüller, J. Efficient iterative schemes for ab initio total-energy calculations using a plane-wave basis set. *Physical review B* **54,** 11169 (1996).

32. Alpaydin, E. *Introduction to machine learning* (MIT press, 2020).

33. Hastie, T. *et al.* Overview of supervised learning. *The elements of statistical learning: Data mining, inference, and prediction,* 9–41 (2009).

34. Kubat, M. & Kubat, J. *An introduction to machine learning* (Springer, 2017).

35. Sutton, R. S. & Barto, A. G. *Reinforcement learning: An introduction* (MIT press, 2018).

36. Shapeev, A. V. Moment tensor potentials: A class of systematically improvable interatomic potentials. *Multiscale Modeling & Simulation* **14,** 1153–1173 (2016).

37. Spectral neighbor analysis method for automated generation of quantum-accurate interatomic potentials. *Journal of Computational Physics* **285,** 316–330 (2015).

38. Li, X.-G. *et al.* Quantum-accurate spectral neighbor analysis potential models for Ni-Mo binary alloys and fcc metals. *Physical Review B* **98,** 094104 (2018).

39. Chen, C. *et al.* Accurate force field for molybdenum by machine learning large materials data. *Physical Review Materials* **1,** 043603 (2017).

40. Lunghi, A. & Sanvito, S. A unified picture of the covalent bond within quantum-accurate force fields: From organic molecules to metallic complexes' reactivity. *Science Advances* **5,** eaaw2210 (2019).

41. Attarian, S., Morgan, D. & Szlufarska, I. Thermophysical properties of FLiBe using moment tensor potentials. *Journal of Molecular Liquids* **368,** 120803 (2022).

42. Shapeev, A. V., Podryabinkin, E. V., Gubaev, K., Tasnádi, F. & Abrikosov, I. A. Elinvar effect in β-Ti simulated by on-the-fly trained moment tensor potential. *New Journal of Physics* **22,** 113005 (2020).

43. Tikhonov, A. N. *On the solution of ill-posed problems and the method of regularization* in *Doklady akademii nauk* **151** (1963), 501–504.

44. Everitt, B. S. & Skrondal, A. The Cambridge dictionary of statistics (2010).

45. Garnett, R. *Bayesian optimization* (Cambridge University Press, 2023).

46. Curry, H. B. The method of steepest descent for non-linear minimization problems. *Quarterly of Applied Mathematics* **2,** 258–261 (1944).

47. LeSar, R. *Introduction to computational materials science: fundamentals to applications* (Cambridge University Press, 2013).

48. Zhou, Y., Kirkpatrick, W. & Deringer, V. L. Cluster fragments in amorphous phosphorus and their evolution under pressure. *Advanced Materials* **34,** 2107515 (2022).

49. Deringer, V. L., Caro, M. A. & Csányi, G. A general-purpose machine-learning force field for bulk and nanostructured phosphorus. *Nature communications* **11,** 5461 (2020).

50. Jones, J. E. On the Determination of Molecular Fields. II. From the Equation of State of a Gas. *Proceedings of the Royal Society of London. Series A, Containing Papers of a Mathematical and Physical Character* **106,** 463–477 (1924).

51. Morse, P. M. Diatomic molecules according to the wave mechanics. II. Vibrational levels. *Physical review* **34,** 57 (1929).

52. Ziegler, J. F. & Biersack, J. P. in *Treatise on Heavy-Ion Science: Volume 6: Astrophysics, Chemistry, and Condensed Matter* 93–129 (Springer, 1985).

53. Prodan, E. & Kohn, W. Nearsightedness of electronic matter. *Proceedings of the National Academy of Sciences* **102,** 11635–11638 (2005).

54. Bartók-Pirtay, A. *The Gaussian Approximation Potential: an interatomic potential derived from first principles quantum mechanics* (Springer Science & Business Media, 2010).

55. Bartók, A. P., Kondor, R. & Csányi, G. On representing chemical environments. *Physical Review B* **87,** 184115 (2013).

56. Behler, J. & Parrinello, M. Generalized Neural-Network Representation of High-Dimensional Potential-Energy Surfaces. *Physical Review Letter* **98,** 146401 (14 2007).

57. Varshalovich, D. A., Moskalev, A. N. & Khersonskii, V. K. *Quantum theory of angular momentum* (World Scientific, 1988).

58. Drautz, R. Atomic cluster expansion for accurate and transferable interatomic potentials. *Physical Review B* **99,** 014104 (2019).

59. Shimizu, K. *et al.* Phase stability of Au-Li binary systems studied using neural network potential. *Physical Review B* **103,** 094112 (2021).

60. Ibarra-Hernández, W. *et al.* Structural search for stable Mg–Ca alloys accelerated with a neural network interatomic model. *Physical Chemistry Chemical Physics* **20,** 27545–27557 (2018).

61. Hajinazar, S., Shao, J. & Kolmogorov, A. N. Stratified construction of neural network based interatomic models for multicomponent materials. *Physical Review B* **95,** 014114 (2017).

62. Kim, K. *et al.* Machine-learning-accelerated high-throughput materials screening: Discovery of novel quaternary Heusler compounds. *Physical Review Materials* **2,** 123801 (2018).

63. Schmidt, J., Chen, L., Botti, S. & Marques, M. A. Predicting the stability of ternary intermetallics with density functional theory and machine learning. *The Journal of Chemical Physics* **148,** 241728 (2018).

64. Gubaev, K., Podryabinkin, E. V., Hart, G. L. & Shapeev, A. V. Accelerating high-throughput searches for new alloys with active learning of interatomic potentials. *Computational Materials Science* **156,** 148–156 (2019).

65. Pickard, C. J. & Needs, R. J. Ab initio random structure searching. *Journal of Physics: Condensed Matter* **23,** 053201 (2011).

66. Pickard, C. J. & Needs, R. J. High-Pressure Phases of Silane. *Physical Review Letters* **97,** 045504 (4 2006).

67. Errea, I. *et al.* High-Pressure Hydrogen Sulfide from First Principles: A Strongly Anharmonic Phonon-Mediated Superconductor. *Physical Review Letters* **114,** 157004 (15 2015).

68. Pickard, C. J. Ephemeral data derived potentials for random structure search. *Physical Review B* **106,** 014102 (2022).

69. Oganov, A. R., Lyakhov, A. O. & Valle, M. How Evolutionary Crystal Structure Prediction Worksand Why. *Accounts of Chemical Research* **44,** 227–237 (2011).

70. Oganov, A. R. & Glass, C. W. Crystal structure prediction using ab initio evolutionary techniques: Principles and applications. *The Journal of chemical physics* **124** (2006).

71. Oganov, A. R. & Ono, S. Theoretical and experimental evidence for a post-perovskite phase of MgSiO3 in Earth's D layer. *Nature* **430,** 445–448. ISSN: 0028-0836 (2004).

72. Li, Q. *et al.* Superhard Monoclinic Polymorph of Carbon. *Physical Review Letters* **102,** 175506 (2009).

73. Ma, Y. *et al.* Transparent dense sodium. *Nature* **458,** 182–185 (2009).

74. Curtarolo, S. *et al.* AFLOW: An automatic framework for high-throughput materials discovery. *Computational Materials Science* **58,** 218–226 (2012).

75. Curtarolo, S. *et al.* AFLOWLIB.ORG: A distributed materials properties repository from high-throughput ab initio calculations. *Computational Materials Science* **58,** 227–235 (2012).

76. Hart, G. L. & Forcade, R. W. Algorithm for generating derivative structures. *Physical Review B* **77,** 224115 (2008).

77. Hart, G. L. & Forcade, R. W. Generating derivative structures from multilattices: Algorithm and application to hcp alloys. *Physical Review B* **80,** 014120 (2009).

78. Hart, G. L., Nelson, L. J. & Forcade, R. W. Generating derivative structures at a fixed concentration. *Computational Materials Science* **59,** 101–107 (2012).

79. Mehl, M. J. *et al.* The AFLOW Library of Crystallographic Prototypes: Part 1. *Computational Materials Science* **136,** S1–S828 (2017).

80. Hicks, D. *et al.* The AFLOW Library of Crystallographic Prototypes: Part 2. *Computational Materials Science* **161,** S1–S1011 (2019).

81. Hicks, D. *et al.* The AFLOW Library of Crystallographic Prototypes: Part 3. *Computational Materials Science* **199,** 110450 (2021).

82. He, J., Naghavi, S. S., Hegde, V. I., Amsler, M. & Wolverton, C. Designing and Discovering a New Family of Semiconducting Quaternary Heusler Compounds Based on the 18-Electron Rule. *Chemistry of Materials* **30,** 4978–4985 (2018).

83. Vegard, L. Die konstitution der mischkristalle und die raumfüllung der atome. *Zeitschrift für Physik* **5,** 17–26 (1921).

84. Zunger, A., Wei, S.-H., Ferreira, L. & Bernard, J. E. Special quasirandom structures. *Physical review letters* **65,** 353 (1990).

85. DeHoff, R. *Thermodynamics in materials science* (CRC Press, 2006).

86. Barber, C. B., Dobkin, D. P. & Huhdanpaa, H. The quickhull algorithm for convex hulls. *ACM Transactions on Mathematical Software (TOMS)* **22,** 469–483 (1996).

87. Toher, C., Oses, C., Hicks, D. & Curtarolo, S. Unavoidable disorder and entropy in multi-component systems. *npj Computational Materials* **5,** 69 (2019).

88. He, J., Rabe, K. M. & Wolverton, C. Computationally accelerated discovery of functional and structural Heusler materials. *MRS Bulletin* **47,** 559–572 (2022).

89. Balluff, J., Diekmann, K., Reiss, G. & Meinert, M. High-throughput screening for antiferromagnetic Heusler compounds using density functional theory. *Physical Review Materials* **1,** 034404 (2017).

90. Hayes, F. H., Lukas, H. L., Effenberg, G. & Petzow, G. A Thermodynamic Optimisation of the Cu–Ag–Pb System. *Z. Metallkd.* **77,** 749–754 (1986).

91. Feynman, R. P. There's plenty of room at the bottom. *Resonance* **16,** 890–905 (2011).

92. Pizzi, G., Cepellotti, A., Sabatini, R., Marzari, N. & Kozinsky, B. AiiDA: automated interactive infrastructure and database for computational science. *Computational Materials Science* **111,** 218–230 (2016).

93. Ong, S. P. *et al.* Python Materials Genomics (pymatgen): A robust, open-source python library for materials analysis. *Computational Materials Science* **68,** 314–319 (2013).

94. Jain, A. *et al.* Commentary: The Materials Project: A materials genome approach to accelerating materials innovation. *APL Materials* **1** (2013).

95. Saal, J. E., Kirklin, S., Aykol, M., Meredig, B. & Wolverton, C. Materials Design and Discovery with High-Throughput Density Functional Theory: The Open Quantum Materials Database (OQMD). *Journal of The Minerals* **65,** 1501–1509 (2013).

96. Oses, C. *et al.* AFLOW-CHULL: Cloud-Oriented Platform for Autonomous Phase Stability Analysis. *Journal of Chemical Information and Modeling* **58,** 2477–2490 (2018).

97. Calderon, C. E. *et al.* The AFLOW standard for high-throughput materials science calculations. *Computational Materials Science* **108,** 233–238 (2015).

98. Monkhorst, H. J. & Pack, J. D. Special points for Brillouin-zone integrations. *Physical Review B* **13,** 5188–5192 (12 1976).

99. Setyawan, W. & Curtarolo, S. High-throughput electronic band structure calculations: Challenges and tools. *Computational Materials Science* **49,** 299–312 (2010).

100. Minotakis, M., Rossignol, H., Cobelli, M. & Sanvito, S. Machine-Learning Surrogate Model for Accelerating the Search of Stable Ternary Alloys. *arXiv* (2023).

101. Plimpton, S. Fast parallel algorithms for short-range molecular dynamics. *Journal of Computational Physics* **117,** 1–19 (1995).

102. Pedregosa, F. *et al.* Scikit-learn: Machine Learning in Python. *Journal of Machine Learning Research* **12,** 2825–2830 (2011).

103. Bergstra, J., Bardenet, R., Bengio, Y. & Kégl, B. *Algorithms for Hyper-Parameter Optimization* in *Advances in Neural Information Processing Systems* (eds Shawe-Taylor, J., Zemel, R., Bartlett, P., Pereira, F. & Weinberger, K.) **24** (Curran Associates, Inc., 2011).

104. Bergstra, J., Yamins, D. & Cox, D. *Making a Science of Model Search: Hyperparameter Optimization in Hundreds of Dimensions for Vision Architectures* in *Proceedings of the 30th International Conference on Machine Learning* (eds Dasgupta, S. & McAllester, D.) **28** (Atlanta, Georgia, USA, 2013), 115–123.

105. Coello, C. A. C., Ozaki, Y., Tanigaki, Y., Watanabe, S. & Onishi, M. Multiobjective tree-structured parzen estimator for computationally expensive optimization problems. *Proceedings of the 2020 Genetic and Evolutionary Computation Conference,* 533–541 (2020).

106. Akiba, T., Sano, S., Yanase, T., Ohta, T. & Koyama, M. *Optuna: A Next-generation Hyperparameter Optimization Framework* in *Proceedings of the 25th ACM SIGKDD International Conference on Knowledge Discovery and Data Mining* (2019).

107. Ntukogu, T. O. & Cadoff, I. B. Tie line compositions of ternary Cu–Ag–Au alloys within miscibility gap. *Materials Science and Technology* **2,** 528–533 (1986).

108. Kusoffsky, A. Thermodynamic evaluation of the ternary Ag–Au–Cu system—including a short range order description. *Acta Materialia* **50,** 5139–5145 (2002).

109. Van der Oord, C., Sachs, M., Kovács, D. P., Ortner, C. & Csányi, G. Hyperactive learning for data-driven interatomic potentials. *npj Computational Materials* **9,** 168 (2023).

110. Wang, R. *et al.* Machine learning guided discovery of ternary compounds involving La and immiscible Co and Pb elements. *npj Computational Materials* **8,** 258 (2022).

111. Sun, H. *et al.* Machine Learning-Guided Discovery of Ternary Compounds Containing La, P, and Group 14 Elements. *Inorganic Chemistry* **61,** 16699–16706 (2022).

112. Jain, A. *et al.* Commentary: The Materials Project: A materials genome approach to accelerating materials innovation. *APL Materials* **1,** 011002 (2013).

113. Rossignol, H., Minotakis, M., Cobelli, M. & Sanvito, S. Machine-Learning-Assisted Construction of Ternary Convex Hull Diagrams. *arXiv preprint arXiv:2308.15907* (2023).

114. Kusoffsky, A. Thermodynamic evaluation of the ternary Ag–Au–Cu system—including a short range order description. *Acta materialia* **50,** 5139–5145 (2002).

115. Hicks, D. *et al.* AFLOW-SYM: platform for the complete, automatic and self-consistent symmetry analysis of crystals. *Acta Crystallographica Section A: Foundations and Advances* **74,** 184–203 (2018).

116. Prince, A. Phase diagrams of ternary gold alloys. *Institute of Metals,* 7–42 (1990).

117. Barber, C. B., Dobkin, D. P. & Huhdanpaa, H. The quickhull algorithm for convex hulls. *ACM Transactions on Mathematical Software (TOMS)* **22,** 469–483 (1996).

118. Taylor, R. H. *et al.* A RESTful API for exchanging materials data in the AFLOWLIB. org consortium. *Computational materials science* **93,** 178–192 (2014).

119. Deringer, V. L. *et al.* Gaussian process regression for materials and molecules. *Chemical Reviews* **121,** 10073–10141 (2021).

120. Rostoker, W. A Study of Ternary Phase Diagrams of Tungsten and Tantalum. *Battelle Memorial Inst. Defense Metals Information Center, Columbus, Ohio* (1963).

121. Chen, C., Ye, W., Zuo, Y., Zheng, C. & Ong, S. P. Graph Networks as a Universal Machine Learning Framework for Molecules and Crystals. *Chemistry of Materials* **31,** 3564–3572 (2019).

122. Nikolov, S. *et al.* Data-driven magneto-elastic predictions with scalable classical spin-lattice dynamics. *npj Computational Materials* **7,** 153 (2021).

123. Domina, M., Cobelli, M. & Sanvito, S. Spectral neighbor representation for vector fields: Machine learning potentials including spin. *Physical Review B* **105** (June 2022).

124. He, K., Zhang, X., Ren, S. & Sun, J. Deep Residual Learning for Image Recognition. *arXiv.* eprint: 1512.03385 (2015).

125. Gasteiger, J., Groß, J. & Günnemann, S. Directional message passing for molecular graphs. *arXiv preprint arXiv:2003.03123* (2020).

126. Eleno, L., Frisk, K. & Schneider, A. Assessment of the Fe–Ni–Al system. *Intermetallics* **14,** 1276–1290 (2006).

127. Zhang, L. *et al.* Thermodynamic properties of the Al–Fe–Ni system acquired via a hybrid approach combining calorimetry, first-principles and CALPHAD. *Acta Materialia* **57,** 5324–5341 (2009).

128. Chumak, I., Richter, K. W. & Ipser, H. The Fe–Ni–Al phase diagram in the Al-rich (¿50at.% Al) corner. *Intermetallics* **15,** 1416–1424 (2007).

129. Newkirk, J., Black, P. & Damjanovic, A. The refinement of the Co2Al5 structures. *Acta Crystallographica* **14,** 532–533 (1961).

130. Douglas, A. The structure of Co2Al9. *Acta Crystallographica* **3,** 19–24 (1950).

131. Sina, H., Corneliusson, J., Turba, K. & Iyengar, S. A study on the formation of iron aluminide (FeAl) from elemental powders. *Journal of Alloys and Compounds* **636,** 261–269 (2015).

132. Raghavan, V. Al-Fe-Ni (aluminum-iron-nickel). *Journal of Phase Equilibria and Diffusion* **31,** 455–458 (2010).

133. Goldbeck, O. K. v. IRON—Binary Phase Diagrams, 22–23 (1982).

134. Arias, D. & Abriata, J. P. The FeZr (Iron-Zirconium) system. *Bulletin of Alloy Phase Diagrams* **9,** 597–604 (1988).

135. Okamoto, H. The Bi-Zr (Bismuth-Zirconium) system. *Bulletin of Alloy Phase Diagrams* **11,** 295–297 (1990).

136. Garg, S. P. & Krishnamurthy, N. The Bi-Ta (bismuth-tantalum) system. *Journal of Phase Equilibria* **13,** 269–270 (1992).

137. Okamoto, H. Fe-Ta (Iron-Tantalum). *Journal of Phase Equilibria and Diffusion* **34,** 165–166 (2013).

138. Ishida, K. & Nishizawa, T. The bico (bismuthcobalt) system. *Journal of Phase Equilibria* **12,** 346–348 (1991).

139. Osamura, K. The BiPbSn (Bismuth-Lead-Tin) system. *Bulletin of Alloy Phase Diagrams* **9,** 274–281 (1988).

140. Heusler, F. & Take, E. The nature of the Heusler alloys. *Transactions of the Faraday Society* **8,** 169–184 (1912).

141. Carrete, J., Li, W., Mingo, N., Wang, S. & Curtarolo, S. Finding Unprecedentedly Low-Thermal-Conductivity Half-Heusler Semiconductors via High-Throughput Materials Modeling. *Physical Review X* **4,** 011019 (2014).

142. Klimczuk, T. *et al.* Superconductivity in the Heusler family of intermetallics. *Physical Review B* **85,** 174505 (2012).

143. Pušelj, M. & Ban, Z. The crystal structure of TiCuHg2. *Croatica Chemica Acta* **41,** 79–83 (1969).

144. Nowotny, H. & Sibert, W. Ternäre Valenzverbindungen in den Systemen Kupfer (Silber)-Arsen (Antimon, Wismut)-Magnesium. *International Journal of Materials Research* **33,** 391–394 (1941).

145. Graf, T., Felser, C. & Parkin, S. S. Simple rules for the understanding of Heusler compounds. *Progress in Solid State Chemistry* **39,** 1–50 (2011).

146. Masumoto, H. & Watanabe, K. New Compounds of the Clb, Cl Types of RhMnSb, IrMnSn and IrMnAl, New L21 (Heusler) Type of Ir2MnAl and Rh2MnAl Alloys, and Magnetic Properties. *Journal of the Physical Society of Japan* **32,** 281–281 (1972).

147. Yoshimura, K., Yamada, M., Mekata, M., Shimizu, T. & Yasuoka, H. Nuclear magnetic relaxation in the metallic localized moment system Ir2MnGa. *Journal of the Physical Society of Japan* **57,** 409–412 (1988).

148. Yin, M. & Nash, P. Standard enthalpies of formation of selected Rh2YZ Heusler compounds. *Journal of Alloys and Compounds* **650,** 925–930 (2015).

149. Ganesan, V. & Girirajan, K. Lattice parameter and thermal expansion of cscl and csbr by x-ray powder diffraction. i. thermal expansion of cscl from room temperature to 90 k. *Pramana* **27,** 469–474 (1986).

150. Kalache, A. *et al.* Tunable magnetic properties in tetragonal Mn-Fe-Ga Heusler films with perpendicular anisotropy for spintronics applications. *Physical Review Materials* **2,** 084407 (2018).

151. Paul, S., Kundu, A., Sanyal, B. & Ghosh, S. Anti-site disorder and improved functionality of Mn2NiX (X= Al, Ga, In, Sn) inverse Heusler alloys. *Journal of Applied Physics* **116** (2014).

152. Breiman, L. Random Forests. *Machine Learning* **45,** 5–32 (2001).

153. Byland, J. *et al. Novel database driven method for discovering new Co-based ferromagnets* in *APS March Meeting Abstracts* **2021** (2021), Y36–013.

154. Yako, H. *et al.* Magnetic properties of Mn-rich Rh2Mn1+xSn1x Heusler alloys. *Physica B: Condensed Matter* **407,** 311–315 (2012).

155. Adachi, Y. *et al.* Pressure effect on the Curie temperature of the Heusler alloys Rh2MnZ (Z = Sn, Ge). *Journal of Alloys and Compounds* **383,** 37–39 (2004).

156. Kanomata, T. *et al.* Magnetic properties of ferromagnetic Heusler alloy Co2ZrAl. *Journal of Alloys and Compounds* **393,** 26–33 (2005).

157. Buschow, K. & Van Engen, P. Magnetic and magneto-optical properties of Heusler alloys based on aluminium and gallium. *Journal of Magnetism and Magnetic Materials* **25,** 90–96 (1981).

158. Carbonari, A., Pendl Jr, W., Attili, R. & Saxena, R. Magnetic hyperfine fields in the Heusler alloys Co2 YZ (Y= Sc, Ti, Hf, V, Nb; Z= Al, Ga, Si, Ge, Sn). *Hyperfine Interactions* **80,** 971–976 (1993).

159. Mizusaki, S. *et al.* Appearance of ferromagnetism in Heusler alloy Ru2Mn1-xVxGe. *Journal of Physics: Conference Series* **200,** 052017 (2010).

160. Klewe, C., Meinert, M., Schmalhorst, J. & Reiss, G. Negative spin polarization of Mn2VGa probed by tunnel magnetoresistance. *Journal of Physics: Condensed Matter* **25,** 076001 (2013).

161. Kusakari, Y., Kanomata, T., Fukushima, K. & Nishihara, H. Magnetic properties of Heusler alloys Ru2xFexCrGe. *Journal of Magnetism and Magnetic Materials* **310.** Proceedings of the 17th International Conference on Magnetism, e607–e609 (2007).

162. Jha, S. *et al.* Mössbauer measurement of the hyperfine magnetic field AT sp site in Heusler alloys Rh2 Mn Z (Z=In and Sb). *Hyperfine Interactions* **28,** 491–494 (1986).

163. Siewierska, K. *et al.* Structural, magnetic and electronic properties of L2 1 - ordered Ru2–xMn1+xAl Heusler alloy thin films. *Journal of Magnetism and Magnetic Materials* **579,** 170853 (2023).

164. Kumar Roul, R., Kumar Jana, A., Manivel Raja, M., Arout Chelvane, J. & Narayana Jammalamadaka, S. Evidence for vortex state in Fe2CoGe thin films using FORC and magnetic imaging. *Journal of Magnetism and Magnetic Materials* **566,** 170318 (2023).

165. Yako, H., Shima, T. & Doi, M. Magnetocaloric Effect in Pd2-xNixMn1.47Sn0.53 Heusler Alloy. *2017 IEEE International Magnetics Conference (INTERMAG),* 1–1 (2017).

166. Carbonari, A. W., Pendl, W., Attili, R. N. & Saxena, R. N. Magnetic hyperfine fields in the Heusler alloys Co2 YZ (Y=Sc, Ti, Hf, V, Nb; Z=Al, Ga, Si, Ge, Sn). *Hyperfine Interactions* **80,** 971–976 (1993).

167. Asvini, V., Saravanan, G., Kalaiezhily, R. K., Raja, M. M. & Ravichandran, K. Effect of film thickness on soft magnetic behavior of Fe2CoSi Heusler alloy for spin transfer torque device applications. *AIP Conference Proceedings* **1942,** 130051 (2018).

168. Hiroi, M., Matsuda, K. & Rokkaku, T. Magnetic properties and a metal-semiconductor crossover in Heusler compounds Ru2xFexCrSi. *Physical Review B* **76,** 132401 (2007).

169. Kreiner, G. *et al.* New Mn2-based Heusler Compounds. *Zeitschrift für anorganische und allgemeine Chemie* **640,** 738–752 (2014).

170. Aryal, A. *et al.* Synthesis, structural, and magnetic properties of Heusler-type Mn2- x Fe1+ x Ge (0.0 x 1.0) alloys. *Journal of Magnetism and Magnetic Materials* **538,** 168307 (2021).

171. Umetsu, R. Y., Okubo, A. & Kainuma, R. Magnetic and chemical order-disorder transformations in Co2Fe(Ga1xSix) and Co2Fe(Al1ySiy) Heusler alloys. *Journal of Applied Physics* **111,** 073909 (2012).

172. Sutou, Y., Ohnuma, I., Kainuma, R. & Ishida, K. Ordering and martensitic transformations of Ni2AlMn heusler alloys. *Metallurgical and Materials Transactions A* **29,** 2225–2227 (1998).

173. Webster, P. Magnetic and chemical order in Heusler alloys containing cobalt and manganese. *Journal of Physics and Chemistry of Solids* **32,** 1221–1231 (1971).

174. Ahmed, S., Boyer, C. & Niewczas, M. Magnetic and structural properties of Co2MnSi based Heusler compound. *Journal of Alloys and Compounds* **781,** 216–225 (2019).

175. Yin, M., Chen, S. & Nash, P. Enthalpies of formation of selected Co2YZ Heusler compounds. *Journal of Alloys and Compounds* **577,** 49–56 (2013).

176. Jassim, I., Neumann, K.-U., Visser, D., Webster, P. & Ziebeck, K. The magnetic structure of the Heusler alloy Pd2xAgxMnIn. *Physica B: Condensed Matter* **180,** 145–146 (1992).

177. Kanomata, T., Kikuchi, M., Yamauci, H. & Kaneko, T. Magnetic Properties of New Heusler Alloys Ru2MnZ (Z=Si, Ge, Sn and Sb). *Japanese Journal of Applied Physics* **32,** 292 (1993).

178. Zhang, S. *et al.* Photoinduced terahertz radiation and negative conductivity dynamics in Heusler alloy Co2MnSn film. *Opt. Lett.* **42,** 3080–3083 (2017).

179. Meinert, M., Schmalhorst, J.-M., Reiss, G. & Arenholz, E. Ferrimagnetism and disorder of epitaxial Mn2xCoxVAl Heusler compound thin films. *Journal of Physics D: Applied Physics* **44,** 215003 (2011).

180. Pimentel, B. *et al.* Cubic to hexagonal tuning in Fe2Mn(Si1x Ge x) Heusler alloys. *Journal of Alloys and Compounds* **893,** 162236 (2022).

181. Masumoto, H. & Watanabe, K. New compounds of the Clb, Cl types of RhMnSb, IrMnSn and IrMnAl, New L21 (Heusler) type of Ir2MnAl and Rh2MnAl alloys, and magnetic properties. *Journal of the Physical Society of Japan* **32,** 281–281 (1972).

182. Ziebeck, K. & Webster, P. A neutron diffraction and magnetization study of Heusler alloys containing Co and Zr, Hf, V or Nb. *Journal of Physics and Chemistry of Solids* **35,** 1–7 (1974).

183. Wang, Y. *et al.* Magnetism, phase transition, and magnetocaloric effects of Co2Nb0.8Ga1.2 and Co2Nb1.2Ga0.8 Heusler alloys. *Physics Letters A* **471,** 128790 (2023).

184. Umetsu, R. Y. *et al.* Half-metallic properties of Co2(Cr1xFex)Ga Heusler alloys. *Physical Review B* **72,** 214412 (2005).

185. Umetsu, R. Y. *et al.* Site preference and magnetic properties of Mn2CoGa heusler alloy. *2015 IEEE Magnetics Conference (INTERMAG),* 1–1 (2015).

186. Okubo, A., Umetsu, R. Y., Kainuma, R. & Ishida, K. Magnetic properties and phase stability of Co2(Ti1xMnx)Ga Heusler alloys. *Journal of Physics: Conference Series* **200,** 062018 (2010).

187. Manea, A. *et al.* Heusler bulk materials as targets for pulsed laser deposition: growth and characterisation. *Journal of Crystal Growth* **275,** e1787–e1792 (2005).

188. Plant, J. S. Magnetic order and coupling in Heusler alloys Au2(Mn, Z)2. *Journal of Physics F: Metal Physics* **9,** 545 (2001).

189. Bacon, G. E. & Plant, J. S. Magnetic order in the AuMn alloy derivatives Au2(Mn,Z)2 where Z is Al, Cu, Ga, In or Zn. *Journal of Physics F: Metal Physics* **3,** 2003 (2001).

190. Jha, S., Black, R. D., Julian, G. M., Blue, J. W. & Liu, D. C. Hyperfine magnetic field at Cd impurity site in L21 Heusler alloys Rh2MnGe and Rh2MnPb by TDPAC technique. *Journal of Applied Physics* **50,** 7507–7509 (1979).

191. Kamarád, J. *et al.* Pressure study of magnetism in off-stoichiometric Ni2MnSn-based alloys. *Journal of Magnetism and Magnetic Materials* **539,** 168345 (2021).

192. Schaf, J., Dang, K. L., Veillet, P. & Campbell, I. A. Extended and local effects of cold work in Heusler alloys. *Journal of Physics F: Metal Physics* **13,** 1311 (2000).

193. Prasad, R., Raja, M. M. & Phanikumar, G. Structure and magnetic properties of Ni2(Mn,Co)Ga Heusler alloys rapidly solidified by melt-spinning. *Intermetallics* **25,** 42–47 (2012).

194. Webster, P. & Tebble, R. Magnetic and chemical order in Pd 2 MnAl in relation to order in the Heusler alloys Pd 2 MnIn, Pd 2 MnSn, and Pd 2 MnSb. *Journal of Applied Physics* **39,** 471–473 (1968).

195. Benea, D., Gavrea, R., Coldea, M., Isnard, O. & Pop, V. Half-metallic compensated ferrimagnetism in the Mn-Co-V-Al Heusler alloys. *Journal of Magnetism and Magnetic Materials* **475,** 229–233 (2019).

196. LUO, H. Z. *et al.* DISORDER ENHANCED MAGNETIC MOMENT IN Fe2CrAl RIBBONS. *Functional Materials Letters* **1,** 115–120 (2008).

197. Chakraborty, S. *et al.* Large saturation moment and high ferromagnetic transition temperature in a structurally disordered inverse Heusler alloy Fe2RuGe. *arXiv preprint arXiv:2306.14831* (2023).

198. Tsunekawa, M. *et al.* Soft X-ray photoemission study of Co2(Cr1xFex)Ga Heusler compounds. *Japanese Journal of Applied Physics* **54,** 082401 (2015).

199. Zhang, Y., X.K. Xi, F. M., W.H. Wang, E. L. & J.L. Chen, G. W. The structural and magnetic properties of Fe2xNiGa1+x Heusler alloys. *Physica B: Condensed Matter* **462,** 93–96 (2015).

200. Dubenko, I. *et al.* Magnetocaloric effects in Ni–Mn–X based Heusler alloys with X=Ga, Sb, In. *Journal of Magnetism and Magnetic Materials* **321,** 754–757 (2009).

201. Kratochvílová, M. *et al.* Systematic experimental search for Fe2 YZ Heusler compounds predicted by ab-initio calculation. *Intermetallics* **131,** 107073 (2021).

202. Yin, M., Nash, P. & Chen, S. Enthalpies of formation of selected Fe2YZ Heusler compounds. *Intermetallics* **57,** 34–40 (2015).

203. Dubois, B. & Chevereau, D. Decomposition of the Heusler alloy Cu2MnAl at 360°C. *Journal of Materials Science* **14,** 2296–2302 (1979).

204. Buschow, K., Engen, P. v. & Jongebreur, R. Magneto-optical properties of metallic ferromagnetic materials. *Journal of Magnetism and Magnetic Materials* **38,** 1–22 (1983).

205. Srivastava, Y., Vajpai, S. K. & Srivastava, S. Structure and magnetic properties of Co2(Cr1xFex)Al, (0x1) Heusler alloys prepared by mechanical alloying. *Journal of Magnetism and Magnetic Materials* **433,** 141–147 (2017).

206. Kondo, K., Saito, Y., Sato, K. & Katayama, T. Electrical Resistivity of In-Heusler Cu2.0Mn0.94In1.0 Single Crystal. *Transactions of the Japan Institute of Metals* **19,** 301–302 (1978).

207. Yin, M. & Nash, P. Enthalpies of formation of selected Pd2YZ Heusler compounds. *Intermetallics* **58,** 15–19 (2015).

208. Gasi, T. *et al.* Iron-based Heusler compounds Fe2YZ: Comparison with theoretical predictions of the crystal structure and magnetic properties. *Physical Review B* **87,** 064411 (2013).

209. Uhl, E. & Sobczak, R. Magnetism of Cu2(Mn1xNix)Sn Heusler alloys. *Solid State Communications* **39,** 655–659 (1981).

210. Kanomata, T., Kikuchi, M. & Yamauchi, H. Magnetic properties of Heusler alloys Ru2MnZ (Z= Si, Ge, Sn and Sb). *Journal of alloys and compounds* **414,** 1–7 (2006).

211. Suits, J. Structural instability in new magnetic heusler compounds. *Solid State Communications* **18,** 423–425 (1976).

212. Wollmann, L., Chadov, S., Kübler, J. & Felser, C. Magnetism in tetragonal manganese-rich Heusler compounds. *Physical Review B* **92,** 064417 (2015).

213. Ram, M., Saxena, A., Aly, A. E. & Shankar, A. Half-metallicity in new Heusler alloys Mn 2 ScZ (Z = Si, Ge, Sn). *Royal Society of Chemistry Advances* **10,** 7661–7670 (2020).

214. Sarker, P. *et al.* High-entropy high-hardness metal carbides discovered by entropy descriptors. *Nature Communications* **9,** 4980 (2018).